Development and Applications of Diffuse Reflectance Infrared Fourier Transform Spectroscopy (DRIFTS) in Protonic Ceramic Cells

by

Zixian Wang

B.S., Kansas State University, 2018
M.S., Kansas State University, 2020

AN ABSTRACT OF A DISSERTATION

submitted in partial fulfillment of the requirements for the degree

DOCTOR OF PHILOSOPHY

The Tim Taylor Department of Chemical Engineering
Carl R. Ice College of Engineering

KANSAS STATE UNIVERSITY
Manhattan, Kansas

2026

Abstract

Protonic ceramic cells (PCCs) are emerging as a versatile platform for power generation, hydrogen production, and electrochemical synthesis at intermediate temperatures (300–600 °C). While substantial progress has been achieved in materials development and cell performance, a fundamental understanding of proton transfer, hydration processes, and catalytic reaction mechanisms remains limited, particularly under realistic operating conditions. Addressing this gap is essential for rational design of electrodes and electrolytes with improved cell efficiency, product selectivity/yield, and long-term durability. This research proposal aims to establish diffuse reflectance infrared Fourier transform spectroscopy (DRIFTS) as a mechanistic and kinetic probe for key surface processes in PCCs. The proposed work systematically applies Operando DRIFTS to three representative scientific questions:

(i) Time-resolved DRIFTS is used to quantify surface and near-surface proton kinetics in protonic ceramic electrolytes, enabling extraction of exchange rates, activation energies, and kinetic asymmetry among hydration, dehydration, and H_2O/D_2O isotope exchange processes;

(ii) The impact of nickel oxide in $BaZr_{0.1}Ce_{0.7}Y_{0.1}Yb_{0.1}O_{3-\delta}$ protonic electrolyte on hydration behavior and isotope exchange dynamics is investigated using DRIFTS to clarify how Ni incorporation alters local proton transport environments and kinetics;

(iii) DRIFTS is employed to elucidate catalytic reaction pathways during CO_2 methanation in protonic ceramic electrochemical cells, with an emphasis on identifying surface intermediate and structure-activity relationships that govern methane selectivity;

By integrating with complementary DRIFTS measurements and material characterizations, this research seeks to bridge the gap between macroscopic performance and microscopic proton behavior in PCCs. The outcomes will provide qualitative and quantitative insights into surface

hydration and catalytic mechanisms of PCCs, offering guidance for materials optimization and cell design.

Development and Applications of Diffuse Reflectance Infrared Fourier Transform Spectroscopy (DRIFTS) in Protonic Ceramic Cells

by

Zixian Wang

B.S., Kansas State University, 2018
M.S., Kansas State University, 2020

A DISSERTATION

submitted in partial fulfillment of the requirements for the degree

DOCTOR OF PHILOSOPHY

The Tim Taylor Department of Chemical Engineering
Carl R. Ice College of Engineering

KANSAS STATE UNIVERSITY
Manhattan, Kansas

2026

Approved by:

Major Professor
Bin Liu

Copyright

Abstract

Protonic ceramic cells (PCCs) are emerging as a versatile platform for power generation, hydrogen production, and electrochemical synthesis at intermediate temperatures (300–600 °C). While substantial progress has been achieved in materials development and cell performance, a fundamental understanding of proton transfer, hydration processes, and catalytic reaction mechanisms remains limited, particularly under realistic operating conditions. Addressing this gap is essential for rational design of electrodes and electrolytes with improved cell efficiency, product selectivity/yield, and long-term durability. This research proposal aims to establish diffuse reflectance infrared Fourier transform spectroscopy (DRIFTS) as a mechanistic and kinetic probe for key surface processes in PCCs. The proposed work systematically applies Operando DRIFTS to three representative challenges:

(i) Time-resolved DRIFTS is used to quantify surface and near-surface proton kinetics in protonic ceramic electrolytes, enabling extraction of exchange rates, activation energies, and kinetic asymmetry among hydration, dehydration, and H_2O/D_2O isotope exchange processes; (ii) The impact of nickel in $BaZr_{0.1}Ce_{0.7}Y_{0.1}Yb_{0.1}O_{3-\delta}$ protonic electrolyte on hydration behavior and isotope exchange dynamics is investigated using DRIFTS to clarify how Ni incorporation alters local proton transport environments and kinetics. (iii) DRIFTS is employed to elucidate catalytic reaction pathways during CO_2 methanation in protonic ceramic electrochemical cells, with an emphasis on identifying surface intermediate and structure-activity relationships that govern methane selectivity;

By integrating with complementary DRIFTS measurements and material characterizations, this research seeks to bridge the gap between macroscopic performance and microscopic proton behavior in PCCs. The outcomes will provide qualitative and quantitative insights into surface

hydration and catalytic mechanisms of PCCs, offering guidance for materials optimization and cell design.

Table of Contents

List of Figures

List of Tables

Acknowledgements

I would like to express my deepest gratitude to all the professors, colleagues, friends, and collaborators whom I had the privilege of working with during my time at Kansas State University and Idaho National Laboratory

I would like to express my sincere appreciation to my major professor, Prof. Bin Liu, and my graduate committee members, Dr. Dong Ding, Prof. Chuancheng Duan, and Prof. James Edgar, for their invaluable guidance, encouragement, and unwavering support throughout my doctoral studies. I would also like to sincerely thank Prof. Larry Erickson for his mentorship during my master's studies. I am grateful to all of you for fostering an inspiring research environment, generously sharing your knowledge and expertise, and encouraging my growth as a researcher. Your mentorship has made these years truly unforgettable and has profoundly influenced both my personal and professional development.

I would also like to express my sincere gratitude to my colleagues and mentors at Idaho National Laboratory, where I had the opportunity to complete my research internship. I am especially grateful to Prof. Meng Li, Dr. Haixia Li, Prof. Haiyan Zhao, Dr. Wenjuan Bian, Dr. Yuqing Meng, Dr. Wanhua Wang, Dr. Wei Tang, Dr. Hao Deng, Dr. Yuchen Zhang, and Dr. Zeyu Zhao for their generous support, insightful discussions, and willingness to share their expertise.

My deepest appreciation goes to my parents, Xi Ouyang and Lixin Wang. When I was still a high school student who had never traveled abroad, they courageously supported my decision to leave home and pursue my undergraduate education in the United States. Their unconditional love, unwavering trust, and countless sacrifices gave me the opportunity to chase my dreams across the world. Every step of my academic journey has been built upon their support and encouragement.

To my beloved husband, Fan Liu, we first met at Kansas State University and shared some of the happiest years of our graduate school lives together. We have explored breathtaking natural landscapes and vibrant cities across the United States, creating countless cherished memories along the way. More importantly, during the most challenging moments of graduate school, whether facing setbacks in research or difficulties in life, we continually encouraged one another, celebrated every achievement together, and reminded each other never to give up. Thank you for always believing in me and for being the light that illuminated my path whenever I lost my direction.

I would also like to express my heartfelt gratitude to my dearest friends, Xiaofang Liu, Xuhui Pan, and Ke Li. Thank you for your unwavering encouragement, friendship, and support throughout every stage of my journey. I sincerely hope that the friendship we have built over the years will continue to grow stronger and that the years ahead will bring us many more cherished memories together.

Finally, I would like to thank everyone who has been part of this journey. Whether through mentorship, collaboration, friendship, encouragement, or simply by sharing life's everyday moments, each of you has left a meaningful mark on my life. I will always treasure these experiences and carry them with me as I begin the next chapter of my career.

Chapter 1 - Objectives of my Ph. D work

The overarching objective of this Ph.D. research is to establish diffuse reflectance infrared Fourier transform spectroscopy (DRIFTS) as a platform for investigating proton transport processes and catalytic reaction mechanisms in protonic ceramic electrochemical systems. Although protonic ceramic materials have demonstrated excellent electrochemical performance for fuel cells, electrolysis cells, and membrane reactors, the fundamental relationships among surface proton chemistry, bulk proton transport, and catalytic reactions remain insufficiently understood due to the lack of experimental techniques capable of directly probing these dynamic processes under realistic operating conditions.

To address this challenge, this dissertation combines operando DRIFTS with complementary techniques including electrochemical conductivity relaxation (ECR), isotope exchange, SEM, TEM, X-ray diffraction (XRD), X-ray Photoelectron Spectroscopy (XPS), X-ray Absorption Spectroscopy (XAS) and density functional theory (DFT) calculations to establish relationships between microscopic surface chemistry and macroscopic electrochemical performance. Through this integrated approach, the dissertation seeks to provide mechanistic insights that guide the rational design of protonic ceramic materials and electrochemical devices.

Specifically, this Ph.D. research consists of three interconnected objectives.

The first objective is to establish a quantitative DRIFTS-based kinetic framework for investigating proton transport in protonic ceramic electrolytes. This aims to directly monitor the evolution of surface hydroxyl species during hydration and dehydration, quantify proton exchange kinetics through H_2O/D_2O isotope exchange, determine the associated activation behavior, and correlate local proton dynamics with bulk proton transport under realistic operating conditions.

The second objective is to understand how nickel oxide, a widely used sintering aid for proton-conducting electrolytes, influences hydration behavior and proton exchange kinetics beyond its conventional processing role. Emphasis is placed on revealing the effects of nickel incorporation on reversible hydration capacity, hydroxyl formation, isotope exchange kinetics, and the temperature dependence of proton transport, thereby providing mechanistic guidance for optimizing electrolyte compositions and fabrication strategies while maintaining both manufacturability and electrochemical performance.

The third objective is to use the DRIFTS methodology in catalytic reaction investigations by elucidating the reaction intermediate and mechanistic pathways governing CO_2 methanation in protonic ceramic electrolysis systems. This work focuses on identifying high-performance catalysts for intermediate-temperature CO_2 hydrogenation, understanding the surface reaction pathways responsible for enhanced CO_2 conversion and CH_4 selectivity, and establishing structure–activity relationships that provide design principles for future protonic ceramic catalytic systems.

Overall, this dissertation aims to advance the fundamental understanding of proton-related processes and catalytic reactions in protonic ceramic electrochemical systems by integrating operando spectroscopy with electrochemical, structural, and computational characterization techniques. The knowledge generated throughout this work not only establishes DRIFTS as a powerful mechanistic characterization platform but also provides scientific guidance for the design of next-generation protonic ceramic fuel cells, electrolysis cells, and membrane reactors for efficient energy conversion and chemical production.

Chapter 2 - Fundamentals of Protonic Ceramic Cells and DRIFTS

2.1 Operating principles for PCCs

Protonic Ceramic Cells (PCCs) are solid energy conversion and storage devices with a three-layer structure, consisting of two porous electrodes and a dense proton-conducting electrolyte sandwiched between them. As shown in Figure 2.1, PCCs can work reversibly in two modes: as protonic ceramic fuel cells (PCFCs, Figure 2.1 a, b, and c) for power generation, and as protonic ceramic electrolysis cells (PCECs, Figure 2.1 d, e, and f) for affordable hydrogen production[1] and chemical synthesis[2]. The main applications of PCCs can be classified according to their electrochemical conversion processes and target products.

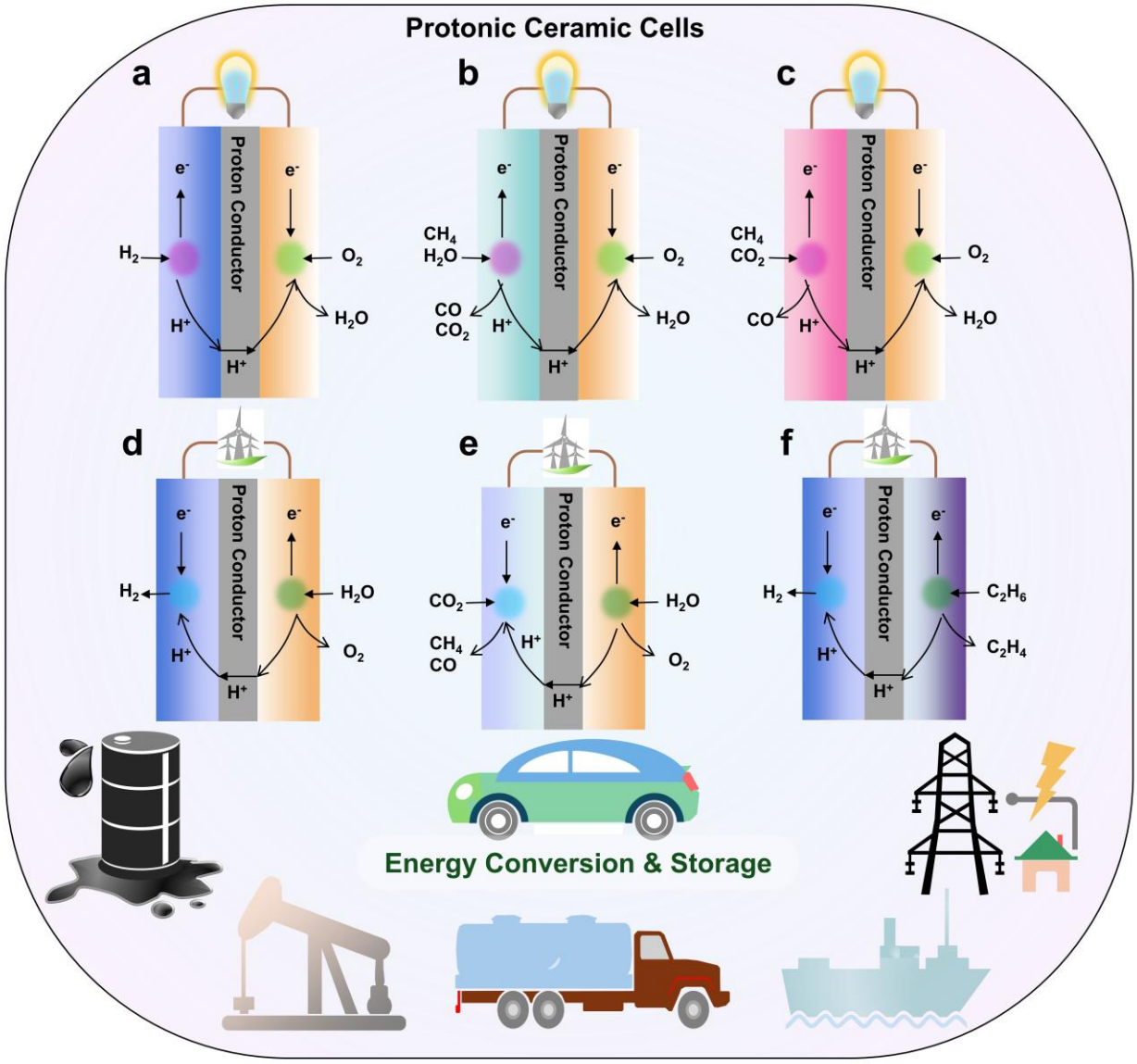

Figure 2.1. Schematic diagrams of PCCs operated in fuel cells and electrolysis modes for energy conversion and storage

PCFCs can convert chemical energy from fuels into electricity. The overall reactions in PCFCs involve the formation of water at the oxygen electrode through the combination of protons, oxygen, and electrons (Equation 1). Hydrogen (H_2) is typically the primary fuel (Figure 2.1a), producing protons by the hydrogen oxidation reaction (HOR), shown in Equation 2. Alternatively,

methane can be used with steam (Figure 2.1b, steam methane reforming (SMR), Equation 3) or carbon dioxide (Figure 2.1c, dry reforming of methane (DRM) as fuels (Equation 4)) [3]. Although the specific overall reactions in PCFCs vary depending on the supplied fuels, the general process always involves the HOR at the hydrogen electrode and the oxygen reduction reaction (ORR) at the oxygen electrode.

PCC working in the fuel cell mode:

Oxygen electrode: $O_2 + 4H^+ + 4e^- \rightarrow 2H_2O$ (1)

Hydrogen electrode/fuel electrode:

(I) Hydrogen-PCFCs (H_2 as fuel)

$2H_2 \rightarrow 4H^+ + 4e^-$ (2)

(II) SMR-PCFCs (CH_4 and H_2O as fuels)

$CH_4 + H_2O \rightarrow CO + 6H^+ + 6e^-$ (3)

(III) DRM-PCFCs (CH_4 and CO_2 as fuels)

$CH_4 + CO_2 \rightarrow 2CO + 4H^+ + 4e^-$ (4)

In the reversible mode of PCFCs, PCECs perform water electrolysis to produce affordable hydrogen by using an applied external voltage (Figure 2.1d). Steam is introduced at the oxygen electrode, where it undergoes the oxygen evolution reaction (OER). This is the adsorption and decomposition of steam into protons (H^+), electrons (e^-), and oxygen (O_2), as shown in Equation 5. Protons migrate through the dense proton-conducting electrolyte to the hydrogen electrode,

combining with electrons to form pure hydrogen, i.e., the hydrogen evolution reaction (HER), shown in Equation 6.

Co-conversion of CO_2 and H_2O can also be realized in PCECs (Figure 2.1e). Water electrolysis and the electrochemical hydrogenation of CO_2 occur at the oxygen electrode (Equation 7) and hydrogen electrode (also referred to as the CO_2 electrode), respectively (Equation 8, and Equation 9). CO_2 can be converted into CO, CH_4, and even ethanol, based on applied catalysts and operating temperatures. PCECs can also be used to synthesize value-added chemicals[2, 4]. For example, an electrochemical dehydrogenation reaction can take place when an alkane (such as C_2H_6) is fed into the system, producing an alkene (C_2H_4) and pure H_2 (Figure 2.1f, Equation 10 and Equation 11).

PCC working in the electrolysis mode:

(I) Hydrogen production

Oxygen electrode: $2H_2O \rightarrow 4H^+ + O_2 + 4e^-$ (5)

Hydrogen electrode: $4H^+ + 4e^- \rightarrow 2H_2$ (6)

(II) Co-conversion of CO_2 and H_2

Oxygen electrode: $2H_2O \rightarrow 4H^+ + 2O_2 + 2e^-$ (7)

CO_2 electrode:

$1/2CO_2 + 4H^+ + 4e^- \rightarrow 1/2CH_4 + H_2O$ (8)

$$2CO_2 + 4H^+ + 4e^- \rightarrow 2CO + 2H_2O \quad (9)$$

(III) Electrochemical dehydrogenation (C_2H_6)

Dehydrogenation electrode: $C_2H_6 \rightarrow 2H^+ + C_2H_4 + 2e^-$ (10)

Hydrogen electrode: $2H^+ + 2e^- \rightarrow H_2$ (11)

As depicted in Figure 2.1, PCCs enable low-cost hydrogen production, facilitate CO_2 conversion to mitigate emissions from human activities, and support efficient energy storage and distribution systems and devices, such as power grids and residential applications[5, 6]. Furthermore, their integration with functional catalysts drives the synthesis of high-value chemicals, such as ethylene, which is a crucial feedstock in chemical engineering. However, critical challenges remain, including the need to ensure high performance and long-term durability, and to achieve scalability for widespread implementation. Addressing these issues is essential for unlocking the full transformative potential of PCCs.

2.2 Basics of Protonic Ceramic electrolytes

Protonic ceramic electrolytes are the key functional component of PCCs, including PCFCs and PCECs. Their primary function is to selectively transport protons from the fuel electrode to the oxygen electrode while preventing direct contact between the fuel and oxidant gases. In addition, the electrolyte must effectively block electronic conduction to avoid internal short-circuiting and maintain high energy conversion efficiency. Compared with conventional oxygen-ion conducting electrolytes, proton-conducting ceramics enable water formation at the cathode in fuel cell operation, thereby reducing fuel dilution and allowing efficient operation at intermediate temperatures (300–600 °C).

Most proton-conducting electrolytes currently employed in PCCs are based on perovskite-type oxides with the general formula ABO_3 (Figure 2.2).[7] In this crystal structure, the A-site is occupied by relatively large alkaline-earth or rare-earth cations, whereas the B-site consists of smaller transition-metal cations coordinated by corner-sharing BO_6 octahedra.[7] One of the greatest advantages of the perovskite structure is its excellent compositional flexibility. Partial substitution at either the A-site or B-site enables systematic tuning of oxygen vacancy concentration, lattice distortion, hydration behavior, chemical stability, and proton transport properties, providing a highly versatile platform for electrolyte design.[7]

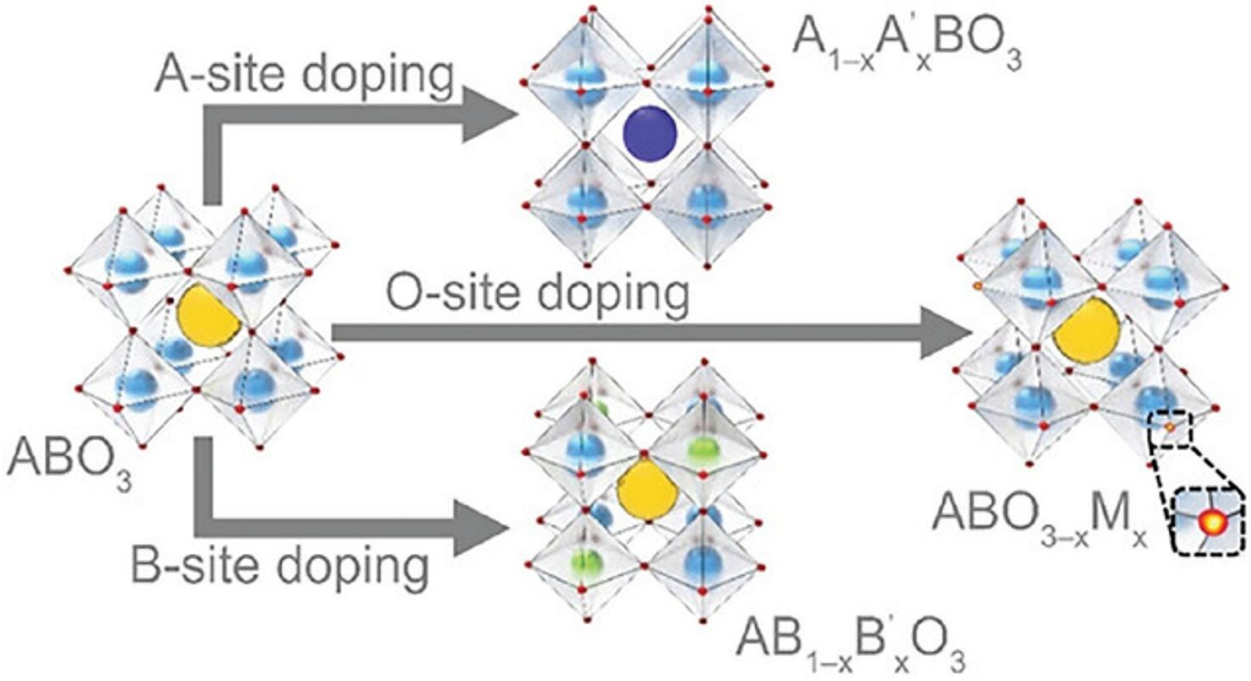

Figure 2.2. Schematic illustration of element substitution strategies in ABO_3-type perovskite oxides, including A-site, B-site, and oxygen-site doping.[8]

The discovery of proton conduction in acceptor-doped perovskite oxides by Takahashi and Iwahara in 1980 marked the beginning of protonic ceramic electrolyte research (Figure 2.3).[9] Subsequent studies demonstrated that acceptor-doped $SrCeO_3$ and $BaCeO_3$ exhibit significant

proton conductivity under humidified atmospheres at intermediate temperatures.[10, 11] Since then, considerable research efforts have focused on developing proton-conducting electrolytes with improved proton conductivity, thermal and chemical stability, and processing characteristics. Among the available material systems, barium cerates generally exhibit superior proton conductivity but suffer from poor chemical stability in CO_2- and H_2O-containing environments.[12] In contrast, barium zirconates possess excellent chemical stability but typically require higher sintering temperatures and exhibit lower proton conductivity.[12] Consequently, mixed cerate–zirconate compositions, such as $BaZr_xCe_{1-x}O_3$-based electrolytes, have become one of the most widely investigated electrolyte families because they provide a favorable balance between proton conductivity, chemical stability, and sinterability.[13]

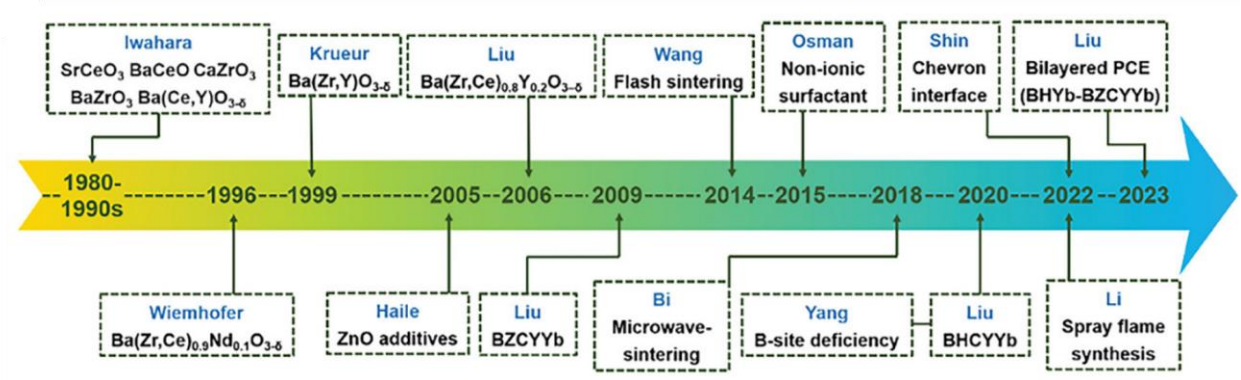

Figure 2.3. Historical overview of remarkable innovations in the preparation route, structural design, or chemical component of perovskite-based Proton-conducting electrolytes.[14]

To achieve high electrochemical performance, protonic ceramic electrolytes should satisfy several fundamental requirements. From a practical perspective, the electrolyte should be readily fabricated into dense, gas-tight membranes while maintaining excellent compatibility with

electrode materials. More importantly, it should possess high proton conductivity together with negligible electronic conductivity, thereby minimizing ohmic losses and preventing internal electronic leakage. The electrolyte must also remain chemically and mechanically stable under both oxidizing and reducing atmospheres encountered during long-term cell operation.

The microstructure of the electrolyte plays an important role in determining its transport properties. Proton conduction occurs through both the crystal lattice (bulk conduction) and grain boundaries, with the total ionic resistance consisting of contributions from each transport pathway.[10] Grain boundaries often exhibit lower proton conductivity than the grain interior because of defect segregation, space-charge effects, and impurity accumulation. Therefore, dense electrolytes with large grains are generally preferred, as they reduce grain boundary resistance and improve overall proton transport.[10] In addition to microstructure optimization, decreasing electrolyte thickness is an effective strategy for reducing ohmic resistance. For example, Bae et al.[15] fabricated a $BaCe_{0.55}Zr_{0.3}Y_{0.15}O_{3-\delta}$ electrolyte with a thickness of approximately 1 μm by pulsed laser deposition, achieving a peak power density exceeding 1 W cm^{-2} at 600 °C owing to the substantially reduced electrolyte resistance. Although composition and microstructure largely determine the macroscopic transport performance of protonic ceramic electrolytes, proton conduction fundamentally originates from hydration chemistry. Acceptor doping creates oxygen vacancies that incorporate water molecules under humidified conditions to generate mobile protonic defects. Consequently, the hydration behavior, proton concentration, and local proton environment directly govern proton transport kinetics and overall electrolyte performance.

Among the various proton-conducting perovskites developed to date, acceptor-doped barium zirconate–cerate electrolytes with the general composition $BaZr_{1-x-y}Ce_xM_yO_{3-\delta}$ (M = Y, Yb, etc.) are widely regarded as the state-of-the-art proton-conducting electrolytes because they

provide an excellent balance of proton conductivity, chemical stability, and sinterability.[11, 16, 17] In particular, $BaZr_{0.4}Ce_{0.4}Y_{0.1}Yb_{0.1}O_{3-\delta}$ (BZCYYb4411)[18] and $BaZr_{0.1}Ce_{0.7}Y_{0.1}Yb_{0.1}O_{3-\delta}$ (BZCYYb1711)[19] have emerged as benchmark electrolyte compositions for intermediate-temperature protonic ceramic cells. These two electrolyte systems constitute the primary materials investigated throughout this dissertation, with BZCYYb4411 serving as the model electrolyte for the fundamental studies of hydration and proton transfer presented in Chapters 3, while BZCYYb1711 is employed to investigate the influence of Ni on hydration behavior and proton transport kinetics in Chapter 4.

2.3 Why choose DRIFTS for PCC characterizations?

Over the past few decades, significant advancements have been made in the development of PCC materials, particularly in designing effective electrocatalysts and electrolytes. Two key areas advancing overall PCC performance are electrode/catalyst integration and reactor engineering (Figure 2.4). The integration of electrocatalysts and the electrode/electrolyte interfaces is critical for reducing resistance, enhancing charge transfer, and improving reaction kinetics. However, the complex interactions, particularly under dynamic operating conditions, are not yet fully understood. Addressing these challenges requires systematic cell modification/optimization, which in turn depends on the support of advanced characterization techniques. In this regard, DRIFTS plays a crucial role, offering unique capabilities to probe surface species and reaction mechanisms in PCCs.

The principle of DRIFTS is rooted in the interaction of IR radiation with the material surface. An IR beam is generated and directed toward the sample, and in advanced setups, synchrotron radiation (SR) can be employed to enhance IR intensity and sensitivity, particularly

for *operando* investigations. When the IR beam interacts with the sample surface, it is diffusely scattered instead of passing through the material. This scattering can capture information from sub-surface regions of the sample. The sample is housed in a specialized cell with a heating stage to control temperature and a gas flow system ("gas in" and "gas out") to introduce reactants (right side of Figure 2.4). More importantly, the external voltage can be applied to further simulate PCC operational conditions (such as charging and discharging). The absorption peaks in the spectrum correspond to specific chemical interactions or species. For example, -OH peaks indicate hydroxyl groups, providing observations of hydration behavior. Variations in peak intensity, shape, or position can reveal dynamic processes such as proton transfer, adsorption, or desorption during a specific reaction. The combination of DRIFTS results with other advanced tools, such as synchrotron radiation and computational modeling, enhances its utility for studying complex material systems like PCCs, thus providing critical insights into reaction mechanisms and supporting material performance optimization (Figure 2.4).

DRIFTS enables the direct probing of surface species evolution during reactions, allowing researchers to capture information about proton hydration, carbonate formation, adsorbed CO/CO_2, and other intermediates under conditions relevant to PCC operation. Table **2.1** summarizes key functional groups and their typical vibrational peak positions observed in DRIFTS studies, which link surface chemistry to electrochemical performance.

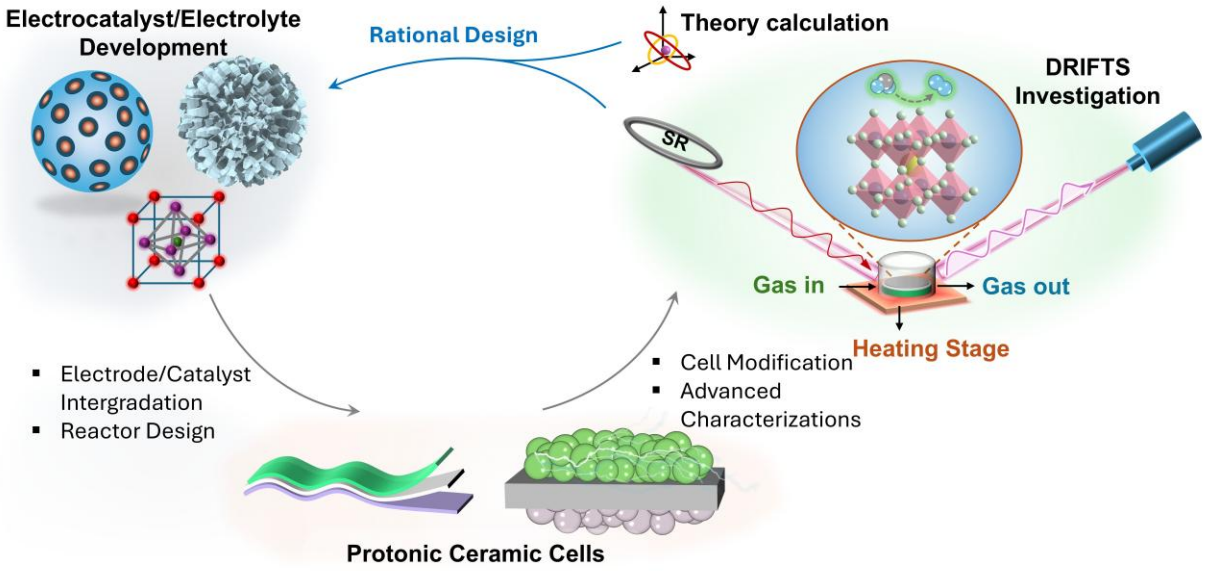

Figure 2.4. DRIFTS's role in the workflow of PCC development and optimization.

Table 2.1. Summary of DRIFTS peak ranges for key functional groups and chemical bonds relevant to PCC studies

Functional Groups/Chemical Bonds	Wavenumber (cm^{-1})	References
Hydroxyl group (–OH) stretching vibration	3800–3200	[20-26]
Olefins (C═C–H)	3030–3180	[27, 28]
Methane (CH_4)	3016, 1306	[27, 29]
Paraffins(–CH_2)	2855, 2926, 2955	[27, 30]
Deuterated hydroxyl (–OD) group stretching vibration	2500	[31]
Carbon Dioxide (O=C=O) stretching vibration	2353	[32]
Dicarbonyls	2120–2000	[33-35]
Carbon monoxide (CO)	2115–2060	[33, 34]

Carbonyls	2000–1900	[33, 36, 37]
Formyl (–CHO)	1750	[32]
Hydronium (H_3O^+) ions	1700	[26]
Water molecules (H–O–H) bending vibration	1630	[38]
Hydrogen–oxygen–deuterium (H–O–D) bending vibration	1650-1400	[39, 40]
Bicarbonates	1610, 1212	[38]
Formate ($HCOO^-$) species	1540	[41]
Carbon–carbon double bond (C=C) stretching vibration	1515	[42]
Carbonates (CO_3^{2-})	1456, 857,718	[43]
Hydroxymethyl (–CHOH)	1440–1400	[42]
Metal–hydroxyl (M–OH) bending vibration	1430, 1427	[26]
Deuterium–oxygen–deuterium (D–O–D) bending vibration	1150–1400	[39, 40]
Methoxy (CH_3O^-)	1046	[27, 44]

DRIFTS serves as a powerful tool for studying the three key components of PCCs: protonic electrolyte, oxygen electrode, and hydrogen electrode (Figure 2.5). Firstly, it contributes significantly to the advancement of protonic electrolyte development by providing valuable information about proton behavior and material properties. The discovery of proton conduction in

$SrCeO_3$-based perovskites by Iwahara et al. in 1981 initiated decades of research into protonic ceramics[45]. Proton conduction was later found in various doped perovskite oxides. $BaCe_{0.4}Zr_{0.4}Y_{0.1}Yb_{0.1}O_{3-\delta}$ (BCZYYb4411) has since become one of the most widely used groups of electrolyte materials for PCCs, striking a balance between protonic conductivity, sinterability, and chemical stability (mainly CO_2 and H_2O tolerance)[18, 46]. BZCYYb7111 showed barium carbonate formation under CO_2 exposure at 500 °C, while BZCYYb4411 maintained a stable perovskite phase, reflecting its superior chemical stability[18, 46]. DRIFTS is capable of detecting carbonate-related species and thus can be effectively used to identify carbonate formation and assess the CO_2 tolerance of protonic electrolytes. For example, Sozal et al. showed that the DRIFTS spectra of BCZYYb4411 remained essentially unchanged before and after exposure to 5% CO_2, suggesting good CO_2 tolerance of BCZYYb4411[47]. By understanding these interactions, researchers can make informed decisions on how to further modify the electrolyte composition to improve overall cell performance.

Secondly, the design of oxygen electrodes is crucial for enhancing the performance of PCCs. In PCCs, the oxygen electrode functions in two modes: (i) facilitating the ORR during fuel cell mode and (ii) enabling the OER in the electrolysis mode, both of which are potential rate-limiting steps Steam electrolysis places higher demands on the oxygen electrode, such as high steam tolerance and thermal/chemical stability. Traditional oxygen electrode materials such as $La_{0.8}Sr_{0.2}CoO_{3-\delta}$ (LSC)[48, 49], $La_{0.4}Sr_{0.6}Co_{0.2}Fe_{0.8}O_{3-\delta}$ (LSCF)[50, 51], and $Ba_{0.5}Sr_{0.5}Co_{0.8}Fe_{0.2}O_{3-\delta}$ (BSCF)[52, 53], which have been widely used in oxygen ion-based SOCs, have limited proton conductivity when applied to PCECs. As a result, researchers have paid much more attention to triple-conducting materials that simultaneously conduct protons (H^+), oxygen ions (O^{2-}), and electrons (e^-), such as $BaCo_{0.4}Fe_{0.4}Zr_{0.1}Y_{0.1}O_{3-\delta}$ (BCFZY4411)[54-57], $PrBa_{0.8}Ca_{0.2}Co_2O_{5+\delta}$

(PBCC)[58, 59], $PrBa_{0.5}Sr_{0.5}Co_{1.5}Fe_{0.5}O_{5+\delta}$ (PBSCF)[46, 60], and $PrNi_{0.5}Co_{0.5}O_{3-\delta}$ (PNC)[23, 61, 47, 62]. When the oxygen electrode is exposed to steam, the hydration reaction occurs and generates abundant proton defects (Equation 12):

$$H_2O + V_O^{\cdot\cdot} + O_O^{\times} \leftrightarrow 2OH_O^{\cdot} \quad (12)$$

However, understanding the behavior of protons within the oxygen electrode is still challenging. Here, DRIFTS can help probe proton hydration at the oxygen electrode. It allows researchers to monitor the hydroxyl (-OH) stretching vibrations at the surface, providing real-time observation of proton behavior during electrochemical operation.

Lastly, the hydrogen electrode is vital in facilitating electrochemical reactions such as the HER and HOR. The typical material used for the hydrogen electrode is a Ni-based cermet; these are composites of metallic nickel and ceramic proton-conducting oxides, such as BCZYYb. However, Ni-based materials have drawbacks, such as carbon deposition when using hydrocarbons (e.g., methane, CH_4) as fuel[63]. To address these issues, additional reforming or catalytic layers are often integrated into the hydrogen electrode to facilitate related catalytic reactions. Other strategies, such as modifying the material composition with metals like Pd[64, 65], Ru[66], or Co[67], have also been employed. DRIFTS can effectively probe intermediates and predict reaction pathways in these catalytic reactions, facilitating the development of efficient and stable catalysts, which can then be integrated with the hydrogen electrode in PCCs.

Moreover, DRIFTS measurements under electrochemical load (i.e., constant current or voltage) can offer realistic insights into the reaction environments in PCCs. These measurements are especially important for evaluating electrochemical processes on the surface, as they occur under actual working conditions. Although implementing this remains technically challenging,

operando DRIFTS configurations capable of applying external voltages are under development, representing a promising avenue for future mechanistic investigations.

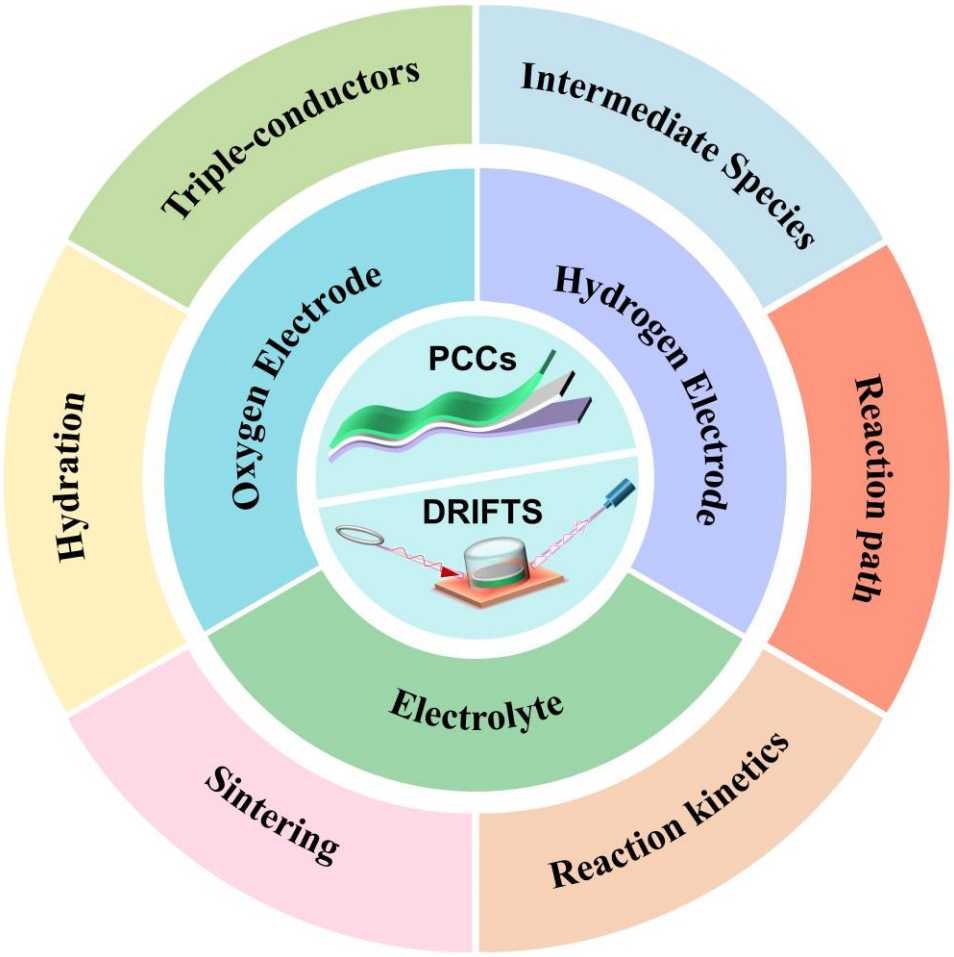

Figure 2.5. Key aspects of DRIFTS on PCCs: oxygen electrode, electrolyte, and hydrogen electrode.

2.4 Working principles of DRIFTS

DRIFTS is an analytical technique that derives information from the frequency changes of photons after they interact with a substance. The foundational work of Michelson[68] and the Michelson–Morley[69] experiments in the 19th century paved the way for the development of infrared (IR) spectroscopy. These interferometric concepts not only enabled the early exploration

of IR light–matter interactions but also became the cornerstone for the later development of Fourier transform infrared (FTIR) spectroscopy by establishing interferometric principles. The Perkin–Elmer Infracord, introduced in 1957, was the first low-cost spectrophotometer capable of recording infrared spectra, covering a wavelength range of 2.5 to 15 μm (corresponding to a wavenumber range of 4,000 to 660 cm^{-1})[70]. It is worth noting that although infrared spectroscopy laid the essential foundation for the development of FTIR spectroscopy, its practical realization was inseparable from subsequent technological advancements, particularly the emergence of digital computation and the development of fast Fourier transform algorithms. The 1960s and 1970s saw significant advancements in computer technology, enabling the practical application of FTIR spectroscopy. These efforts ultimately led, in 1969, to Digilab Inc. releasing the first commercial infrared spectrometer capable of performing fast Fourier transform calculations[71]. In 1996, Fan et al. demonstrated the application of *in situ* DRIFTS to study both adsorbed and desorbed species on high-surface-area anodes and cathodes in direct methanol/oxygen fuel cells, further expanding the scope of this technique[72]. More recently, DRIFTS has also seen rapid and widespread development in electrochemical energy systems, such as lithium-ion batteries[73], proton exchange membrane (PEM) fuel cells[74], and solid-state batteries[75]. This review primarily focuses on the application of DRIFTS in the study of PCCs. By enabling surface-sensitive characterization, DRIFTS offers valuable insights into proton uptake mechanisms in oxygen electrodes, hydration behavior in proton-conducting electrolytes, and surface reactions relevant to catalyst development. These insights collectively support material optimization and contribute to enhancing the overall performance of PCC systems[23, 41, 76].

In a DRIFTS instrument (Figure 2.6), the core component is the interferometer, which consists of two mutually perpendicular mirrors. One is fixed, while the other is movable[77]. The

broadband source produces IR radiation and emits a beam, which is then split by a beam splitter into two paths: one reflects off the fixed mirror, while the other reflects off the moving mirror. The reflected beams then recombine at the beam splitter, with the resultant interference pattern dependent on the relative path lengths of the two beams. This modulated beam exits the interferometer and is focused on a detector[78]. The signal, known as the interferogram, represents the intensity of the recombined beams as a function of the position of the moving mirror[78]. The detector amplifies and transforms the signal into a readable one, which is then sent to a computer for Fourier transformation[79].

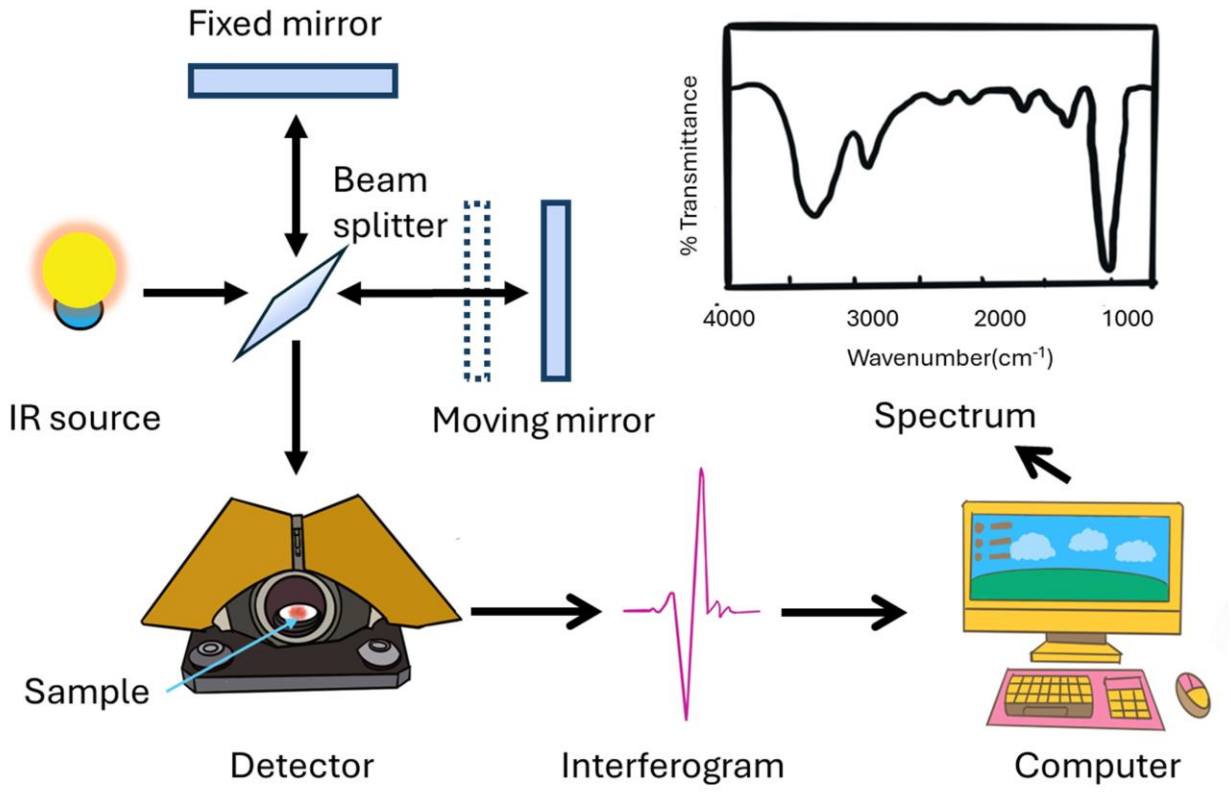

Figure 2.6. Schematic diagram of a typical DRIFTS system, illustrating IR beam generation, interferometer processing, signal detection, and data output.

To obtain a DRIFTS spectrum, the interferogram must be converted through Fourier transformation[79]. This process involves two essential steps: first, generating interferograms with and without the sample in the beam, and second, transforming these interferograms into spectra representing the source with and without sample absorption. The ratio of these two spectra yields the sample's IR transmission spectrum. The values produced by the interferogram, which function over time, are referred to as the time domain. To generate the frequency domain, which is then Fourier analyzed to produce a spectrum, the time domain undergoes Fourier transformation.

DRIFTS has always been and continues to be a crucial spectroscopic method for obtaining structural information about organic molecules[77]. It primarily focuses on the characterization of functional groups within the mid-IR range (4,000–400 cm^{-1}), making it particularly useful for investigating the surface properties of materials and understanding their chemical behavior in various applications. Table **2.1** presents a summary of DRIFTS peak ranges for key functional groups, intermediates, and products relevant to PCC studies. It includes representative vibrational modes and typical wavenumber ranges (cm^{-1}). These assignments support the identification of surface species such as hydroxyls, carbonates, and adsorbed CO/CO_2, which are critical for elucidating the reaction mechanisms and degradation pathways during PCC operation.

The DRIFTS system mainly consists of an IR optical path, a sample holder with a high-temperature chamber, and a temperature control system. Figure 2.7a presents a real photograph of the Nicolet™ iS50 FTIR spectrometer equipped with a Praying Mantis™ diffuse reflectance accessory and its high-temperature reaction chamber. As shown in the figure, the sample is placed inside the chamber, which functions as the sample holder. The chamber is connected to a temperature controller via a thermocouple to ensure precise temperature regulation. A cooling

system is also integrated, allowing coolants to circulate through water tubes to prevent overheating of the outer chamber wall. Figure 2.7a further illustrates the gas inlet and outlet pathways that enable *operando* gas flow during measurements. In the DRIFTS system's interior, the IR beam passes through a series of mirrors (shown in Figure 2.7b) and is directed to the sample surface, with the diffusely reflected signal collected and returned to the spectrometer for analysis.

The high-temperature chamber is enclosed by a standard dome with one glass observation window and two windows for the infrared. IR-transparent window materials such as ZnSe, CaF_2, and KBr are commonly employed to isolate the sample environment while permitting infrared radiation to pass through. ZnSe offers good mid-IR transmission and moderate thermal stability, making it suitable for *operando* studies up to ~250–300 °C, but ZnSe absorbs strongly starting around 700 cm^{-1}, so any spectral features below this will be lost[80]. CaF_2 provides broader spectral coverage and can tolerate slightly higher temperatures (~400 °C), though it is sensitive to moisture[81, 82]. Potassium bromide (KBr) exhibits excellent IR transparency but is highly hygroscopic and thus limited to dry, low-temperature environments[80]. At elevated temperatures, thermal radiation from both the sample and the window materials can increase the background signal and reduce spectral clarity, especially when using materials with temperature-dependent transmission properties. Therefore, appropriate window selection is essential to ensure accurate and stable DRIFTS measurements under realistic PCC operating conditions.

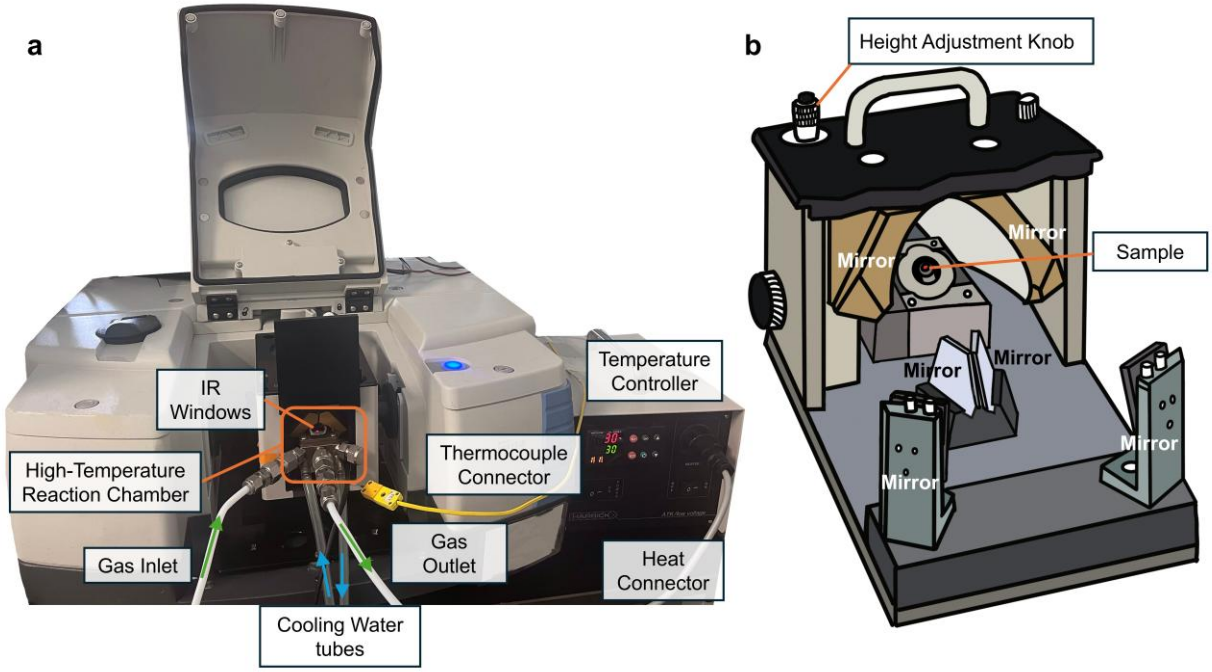

Figure 2.7. (a) Digital photo and (b) illustration of interior of DRIFTS equipment

In a DRIFTS experiment, the spectrometer records the diffuse reflectance signal of the sample, directly outputting intensity values, typically in arbitrary units (a.u.). This intensity represents the reflected light signal detected by the system, which results from the combined scattering and absorption characteristics of the sample. The experiment begins by recording a reference spectrum to determine the initial intensity I_o, typically using a non-absorbing sample or, more commonly, a mirror[83]. Next, the signal I_{cat}, corresponding to the catalyst free of adsorbates (e.g., after pretreatment in inert gas or under vacuum), is measured[83]. The intensity I_{cat} is generally an order of magnitude lower than I_o, and the absolute reflectance of the infinitely thick layer is defined as Equation. 13[84]:

$$R_\infty = I_{cat}/I_o. \quad (13)$$

Following this, the signal $I_{cat+ads}$ is recorded for the catalyst in the presence of adsorbates. The reflectance of the sample with adsorbates is then defined as:

$$R = I_{cat+ads}/I_o. \quad (14)$$

The relative reflectance, R', commonly measured when no mirror spectrum is collected, is calculated as:

$$R' = I_{cat+ads}/I_{cat}. \quad (15)$$

Since measuring absolute reflectance is often challenging, DRIFTS experiments typically focus on measuring the relative reflectance (R'), using a standard reference material such as KBr. Relative reflectance is derived by normalizing the experimentally measured intensity, which captures the effect of surface adsorbates on the optical properties. The absolute reflectance of the sample can be calculated (Equation 16)

$$R_\infty = R/R' \quad (16)$$

Once the absolute reflectance R_∞ is determined, it is used to calculate the Kubelka–Munk function (Equation 17)

$$F(R_\infty) = (1-R_\infty)^2/(2R_\infty) = K/S \quad (17)$$

K is the molar absorption coefficient, which is proportional to the concentration of absorbing species in the sample (e.g., functional groups). S is the scattering coefficient, which depends on the sample's physical properties, such as particle size and surface roughness. The ratio, K/S, reflects the concentration of absorbing species and can be used for quantitative analysis.

For a solute of absorptivity $k = 2.303\epsilon C$, where ϵ is the molar absorptivity and C the solute concentration in a nonabsorbing matrix, the Kubelka-Munk function $F(R_\infty)$ is directly proportional to C (Equation 18).

$$C = \text{constant} \times F(R_\infty) \quad (18)$$

However, certain conditions are not suitable for applying the Kubelka-Munk theory[85], due to factors such as Fresnel reflection (specular or mirror-like), matrix absorption, and a sample

having nonuniform optical properties. Although signal corrections can be performed even for undiluted samples, the process is difficult, and variations in the sample's micro- or nano-structure can influence the scattering coefficient, complicating comparisons between samples prepared differently. In many cases, calibration curves reveal that the Kubelka–Munk equation does not exhibit linearity with solute concentration, often showing a curved[86] or segmented pattern[87]. Olinger and Griffiths suggested that for strongly absorbing matrices, such as those commonly found in catalytic materials, the most linear correlation between solute concentration and intensity is achieved using $\log(1/R_\infty)$ (Equation 19[86]), denoted "absorbance" by analogy with the absorbance = log 1/T measured in transmission IR:

$$C = \text{constant} \times F(R_\infty) = \text{constant} \times \log(1/R_\infty) \quad (19)$$

DRIFTS is highly surface sensitive, meaning it primarily detects species that are adsorbed or bound to the surface of the material[88, 89]. This is advantageous when studying surface reactions, such as those occurring on the electrodes of PCCs. The sensitivity of DRIFTS can be affected by the signal-to-noise ratio (SNR), which refers to the level of useful signal compared to the background noise[80]. A high SNR enables the detection of low-intensity peaks, which is critical when studying weakly adsorbed species or surface species at low concentrations. High SNR helps distinguish weak, broad peaks from background noise, allowing detection before the species desorbs. And it ensures that even small signals are detectable, preventing surface species at low concentrations from being lost in noise. One of the major advantages of DRIFTS over other infrared spectrometers is their ability to measure spectra with high SNRs; those of 100 or better are routinely measured by DRIFTS[80]. Different materials absorb infrared light at different intensities, depending on their chemical composition, bond types, and vibrational modes. Materials

containing functional groups like –OH or C=O are generally more sensitive to DRIFTS analysis, as they generate stronger signals.

Time-resolved DRIFTS can be used to study the dynamics of surface adsorption and desorption processes, providing valuable information on how the electrolyte, electrodes, and catalyst materials interact during the cell's operation. For example, during the reverse water-gas-shift reaction (RWGS, $CO_2 + H_2 \rightarrow CO + H_2O$), time-resolved DRIFTS can track the appearance and disappearance of surface species, such as formates, carbonates, or hydroxyl groups, as the reaction progresses[32]. Additionally, time resolution allows the tracking of short-lived intermediates that might be critical in the reaction mechanism but could otherwise be missed due to fast reaction rates. By capturing spectra at short time intervals (milliseconds or seconds), one can monitor the real-time evolution of these species and gain information about the reaction mechanism.

DRIFTS is a versatile technique that can be applied to qualitative analysis, quantitative analysis, and kinetics studies[90-93]. For qualitative analysis, the positions of IR absorption peaks reveal the presence of specific functional groups, such as –OH or CO_3^{2-}, within the samples. The qualitative results from DRIFTS must be interpreted cautiously, particularly when determining whether a species participates in the main reaction pathway. While DRIFTS is highly sensitive to surface species and can detect "buffer" species, these may not directly contribute to the main reaction pathway. For example, Meunier employed DRIFTS and identified formates and their reactivity under reaction conditions, but quantitative analysis using gas chromatography (GC) revealed that formates were only minor intermediates and not part of the main reaction pathway[94]. In quantitative analysis, the linear relationship between the Kubelka–Munk function and the concentration of absorbing species enable the precise determination of their quantities.

Furthermore, in kinetics studies, changes in the intensity of absorption peaks during a reaction can provide valuable insights into reaction mechanisms and the dynamic behavior of the system. This combination of qualitative and quantitative capabilities makes DRIFTS an essential tool for material and chemical analysis. However, at the current stage of DRIFTS application in PCC research, the focus remains primarily on qualitative analysis. The potential for future advancements in quantitative analysis is significant and warrants further exploration.

While DRIFTS is a powerful technique, it does have certain limitations. Variations in the electronic structures, color, or molar mass of samples can affect the detected data, making comparisons challenging. For instance, the color of a sample significantly affects the scattering and absorption of infrared light, which directly impacts the intensity of DRIFTS measurements. To address this issue, mixing dark-colored samples with KBr, in a specific ratio, is commonly used. The samples and KBr powder need to be ground to reduce particle size and prevent light scattering. Grinding can be accomplished using a mechanical grinder[80].

Chapter 3 - Probing hydration and proton exchange dynamics in protonic ceramic electrolyte via DRIFTS

3.1. Introduction

PCECs operating at intermediate temperatures (400-600 °C) have emerged as a promising platform for efficient energy conversion and storage, operating in both fuel cell and electrolysis modes. [2, 11, 17, 46] Unlike high-temperature (>650 °C) oxygen-ion-conducting solid oxide cells, PCECs use protonic electrolytes with lower energy barriers and the bulk proton conductivities of 10^{-3}-10^{-2} S cm^{-1} in the 400-600 °C range, [95, 96] enabling lower operating temperatures while maintaining high efficiency, thereby reducing system costs and improving materials' long-term durability. [18, 23, 57, 60, 97]

Proton-conducting ceramic electrolytes are central to PCEC operations. These materials are typically perovskite-structured oxides. Among them, acceptor-doped barium zirconate-based perovskites, generally expressed as $BaZr_{1-x-y}Ce_xM_yO_{3-\delta}$ (M = Y^{3+}, Yb^{3+}, etc.), are widely considered high-performance proton-conducting electrolytes.[11, 16, 17] In particular, $BaZr_{0.4}Ce_{0.4}Y_{0.1}Yb_{0.1}O_{3-\delta}$ (BZCYYb4411)[18] and $BaZr_{0.1}Ce_{0.7}Y_{0.1}Yb_{0.1}O_{3-\delta}$ (BZCYYb1711)[19] are the state-of-the-art candidates, exhibiting a balance of proton conductivity, sinterability, and chemical stability. Protons are incorporated into the lattice via hydration reaction according to Equation 12, where water interacts with oxygen vacancies ($V_O^{\cdot\cdot}$) to generate hydroxyl defects ($OH_O^{\cdot}$).[98, 99] This hydration reaction establishes the population of protonic defects available for proton transport. [100, 101]. Proton migration occurs between adjacent oxygen ions, forming a Grotthuss-type hopping pathway in the lattice,[102, 103] i.e., $OH^- + O^{2-} \rightarrow [O \cdots H \cdots O]^{3-} \rightarrow O^{2-} + OH^-$.[104] This dynamic process allows protons to move continuously through the lattice rather than remaining bound to specific oxygen sites, resulting in appreciable proton mobility at

elevated temperatures. The extent and kinetics of hydration, therefore, directly influence mobile protons and, consequently, proton conductivity in PCECs.[105] . Bulk hydration behavior has been investigated using techniques such as thermogravimetric analysis (TGA)[106] and electrochemical impedance spectroscopy (EIS)[107]. However, these techniques primarily provide bulk-averaged information and offer limited insight into the local evolution of protonic species during hydration. As a result, the dynamic behavior of surface hydroxyl species and their relationship to proton transport on electrolyte remain largely unresolved. Gaining direct insight into surface hydration kinetics is highly desirable for the rational design of next-generation PCEC systems.

DRIFTS provides a surface-sensitive approach for directly monitoring vibrational features and is widely used in heterogeneous catalysis to probe surface intermediates and reaction pathways.[108-111] However, its use in characterizing protonic ceramic materials remains limited.[111] Existing studies have primarily focused on the qualitative identification of surface species . For example, Xie et al.[20] employed DRIFTS to investigate proton uptake behavior in $PrBaCo_2O_{5+\delta}$ (PBC) and $PrBaCo_{1.9}Zn0.1O_{6-\delta}$ (PBCZn10), showing that Zn substitution promotes the formation of surface hydroxyl species under humidified conditions. Shi et al.[112] combined DRIFTS with electrochemical polarization to monitor hydroxyl-related vibrational features on $PrBa_{0.5}Sr_{0.5}Co_{2-x}Fe_xO_{5+\delta}$ (PBSCF) electrodes, providing evidence for the participation of protonic species during electrode reactions. In addition, DRIFTS has been used to investigate CO_2 adsorption and activation on proton-conducting oxides such as $BaZr_{0.8}Y_{0.2}O_{3-\delta}$ (BZY), revealing the formation of surface carbonate and bicarbonate intermediates that facilitate subsequent proton-assisted CO_2 conversion.[113] Recently, our group [103] successfully developed a custom operando DRIFTS platform that operates under high-temperature (up to 750 °C), steam conditions with an applied bias and demonstrated that electrochemical bias can accelerate surface proton-exchange

processes in BZCYYb1711. Despite these advances, several fundamental questions remain unresolved. For example, the kinetic relationship between hydration and dehydration processes in protonic electrolytes was not systematically investigated yet.

While hydration ability of protonic electrolyte can be related with the concentration of protonic defects, H_2O/D_2O isotope exchange, when combined with vibrational spectroscopy, provides a powerful approach for probing the dynamic behavior of protonic species by tracking the interconversion between O-H and O-D groups. For example, Meng et al.[103] monitored the interconversion between O-H and O-D vibrational modes during H_2O/D_2O isotope exchange, probing proton-exchange processes at oxide surfaces. Gao et al.[114] employed in situ Raman spectroscopy to investigate isotope exchange in TiO_2 and revealed key insights into hopping-based proton conduction in simple oxides.[114] Additionally, to complement the surface-sensitive information obtained from DRIFTS, understanding the bulk response during hydration is equally important. Electrochemical conductivity relaxation (ECR) has been extensively used to quantify oxygen transport kinetics in mixed-conducting oxygen electrodes through conductivity responses to step changes in oxygen partial pressure, allowing the determination of surface exchange coefficients (k) and chemical diffusion coefficients (D).[60, 115, 116] However, its application to hydration kinetics and bulk transport processes in proton-conducting oxides remains relatively limited. Recently, Kim et al.[117] analyzed conductivity relaxation following step changes in water vapor activity and demonstrated that hydration involves coupled proton- and vacancy-related transport processes rather than a simple single-step H_2O diffusion mechanism. These findings highlight the complexity of hydration, where conductivity reflects not only proton transport but also defect redistribution and re-equilibration processes within the bulk. However, the extraction of effective diffusion coefficients and their correlation with bulk hydration kinetics to quantify

proton- and vacancy-related equilibration processes remains limited in current ECR studies. Moreover, the relationship between surface hydration reactions and bulk proton transport has not yet been well established.

In this work, we employ *operando* DRIFTS to systematically investigate hydration, dehydration, and H_2O/D_2O isotope exchange in BZCYYb4411 electrolytes across 400-600 °C. By tracking the evolution of -OH and -OD stretching modes during these processes, DRIFTS enables real-time observation of surface exchange dynamics that are inaccessible via purely electrochemical measurements. The analysis showed that proton incorporation into the lattice occurs more readily than proton removal. The isotope exchange experiments reveal asymmetric exchange behavior, where H-to-D substitution occurs more readily than the reverse process. DFT was employed to identify the relationship between local atomic configurations and hydroxyl populations, and to further determine the energetic origin of their exchange behaviors. ECR measurements were analyzed using a two-fold diffusion model to extract the effective proton-related (D_i^H) and vacancy-related (D_v^H) diffusion coefficients, thereby linking surface proton chemistry with macroscopic transport behavior. This combined approach provides a quantitative link between surface hydroxyl chemistry and bulk defect transport and establishes a general framework for interrogating hydration and proton exchange in compositionally complex protonic ceramics.

3.2. Materials and Methods

3.2.1 Materials

The BZCYYb4411 powders were synthesized via a solid-state reactive sintering method using commercial precursors: $BaCO_3$ (Alfa Aesar, 99.8%), CeO_2 (Alfa Aesar, 99.9%), ZrO_2 (Alfa

Aesar, 99.7%), Y_2O_3 (Alfa Aesar, 99.9%), and Yb_2O_3 (Alfa Aesar, 99.9%). Stoichiometric amounts were weighed and homogenized in a Nalgene bottle using ethanol ball milling at 300 rpm for 24 h. The dried mixture was pressed into pellets and calcined at 1100°C in air for 5 h. The resulting pellets were crushed and milled again in ethanol, then calcined to ensure phase purity. Tape casting was used to prepare the electrolyte pellet. BZCYYb4411 powders were first ball-milled in an ethanol: toluene solvent for 24 h. Polyvinyl butyral (binder), butyl benzyl phthalate (plasticizer), and fish oil (dispersant) were then added and ball-milled for an additional 24 h to achieve suitable rheology. The green tape was cast to a thickness of ~300 um and dried at 38 °C for 4 h. After punching 1.27 cm (0.5 in) diameter disks, the electrolyte underwent pre-sintering at 920 °C in air to remove organic components. Final densification of the electrolyte was achieved by sintering at 1500 °C for 5 h in air.

3.2.2 Hydration and dehydration experiments

A dense BZCYYb4411 pellet (diameter: 8 mm, thickness: 300 um) was mounted on the custom sample holder in the high-temperature reaction chamber of DRIFTS. A K-type thermocouple was positioned within 1 cm beneath the cell to monitor and maintain a uniform temperature distribution during measurements. Prior to measurements, the temperature was raised from room temperature to 600 °C at a rate of 2 °C min^{-1}, followed by ~2 h held in flowing dry Ar to ensure complete drying and removal of residual H_2O, thereby establishing a dehydrated reference state.

Time-resolved DRIFTS was used to investigate hydration and dehydration processes under well-defined temperature and gas-switching conditions (Figure 3.1). The DRIFTS spectra were collected with a Thermo Scientific Nicolet iS50 FTIR spectrometer equipped with a customized Praying Mantis^{TM} high-temperature reaction chamber (Harrick Scientific Products). The

electrolyte surface was directly exposed to the gas atmosphere and positioned normal to the incident infrared beam to ensure stable collection of diffuse reflectance signals. Spectra were recorded over the range of 4000-500 cm^{-1} with a resolution of 8 cm^{-1}, averaging 32 scans per measurement to ensure a high signal-to-noise ratio. The background spectrum was collected using standard dried KBr powder before each experiment. This background was then subtracted from the sample spectra to remove system- and environment-related contributions. During all DRIFTS measurements, the heating and cooling rates were set to approximately 2 °C min^{-1} to ensure thermal and ceramic cell stability. Hydration experiments were initiated by switching the gas feed from dry Ar (40 mL/min) to humidified Ar containing 3 % H_2O (40 mL/min), while dehydration experiments were performed by reversing the gas sequence. Water vapor was introduced into the reactor using either an H_2O or D_2O bubbler. Gas switching was performed without interrupting spectral acquisition, thereby enabling continuous monitoring of the transient response of surface hydroxyl species (Figure 3.2). Experiments were performed at temperatures between 500 and 600 °C to evaluate the influence of temperature on hydration dynamics. At each testing temperature, the system was stabilized for approximately 30 min before data collection to ensure thermal equilibrium.

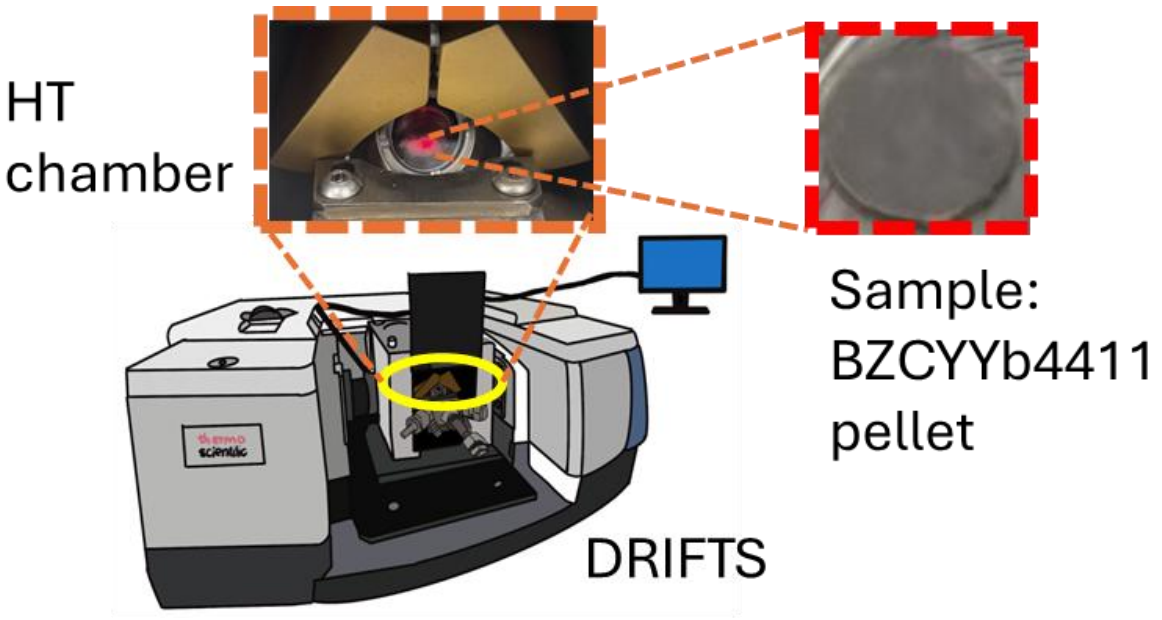

Figure 3.1. Experimental configuration of the operando DRIFTS system used for in situ monitoring of hydroxyl species during hydration, dehydration, and isotope exchange.

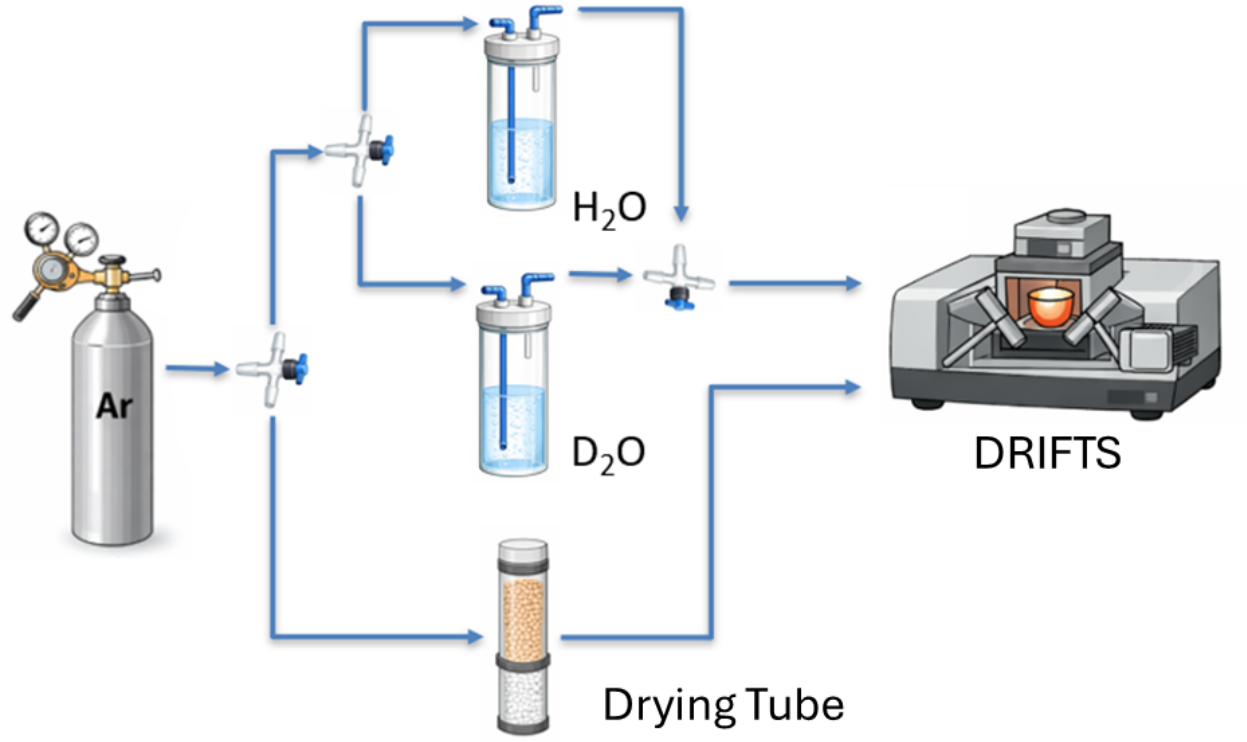

Figure 3.2. Gas-switching setup for controlled hydration and isotope exchange during DRIFTS.

DRIFTS spectra were collected as a function of time following each gas switch, with particular attention to the evolution of O-H stretching vibrations in the 3000-3600 cm^{-1} region, centered at approximately 3400 cm^{-1}. The integrated intensity of the O-H stretching band served as a semi-quantitative measure of surface hydroxyl coverage. Time-dependent changes in band intensity were analyzed to extract characteristic hydration and dehydration time constants, providing insight into surface hydration exchange kinetics.

The centered peak height from raw DRIFTS spectra was first baseline-corrected and then normalized according to:

$$I_{nol}(t) = \frac{I(t)-I_{min}}{I_{max}-I_{min}} \quad (20)$$

where $I(t)$ represents the baseline-corrected peak intensity at time t. The values of $I_{\min}$ and $I_{\max}$ were defined from the steady-state intensities obtained before and after each gas-switching event at a given temperature. Specifically, each kinetic cycle was recorded starting from a stable initial condition and continued until the -OH signal reached a new equilibrium plateau, and the corresponding steady-state intensities were used as normalization bounds. This normalization procedure removes variations due to baseline fluctuations, optical scattering, and absolute intensity differences, thereby allowing direct comparison of the evolution of the intrinsic hydroxyl population across hydration, dehydration, and isotope-exchange processes.

3.2.3 H_2O/D_2O isotope exchange experiments

To further probe protonic species and distinguish between surface and subsurface hydration processes, H_2O/D_2O isotope exchange experiments were conducted on the same DRIFTS platform. The sample was first equilibrated under a humidified Ar atmosphere containing either 3 % H_2O or

3 % D_2O at the target temperature. Isotope exchange was then triggered by switching the gas feed between H_2O/Ar and D_2O/Ar, while maintaining a constant total flow rate (40 mL/min).

Time-resolved DRIFTS spectra were collected during isotope switching to monitor the concurrent decay of O-H stretching bands (3000-3600 cm^{-1}) and the growth of O-D stretching bands in the 2200-2700 cm^{-1} region. Both H_2O-to-D_2O and D_2O-to-H_2O exchange sequences were examined over a temperature range of 300-600 °C. The temporal evolution of O-H and O-D band intensities was analyzed to quantify isotope exchange kinetics and to provide mechanistic insight into proton exchange and transport processes at and beneath the electrolyte surface.

3.2.4 Electrochemical conductivity relaxation (ECR)

ECR measurements were performed under identical gas-switching protocols, including hydration (dry air → 3% H_2O in Air), dehydration (3% H_2O in Air → dry Air), and isotope exchange (3% H_2O in Air ↔ 3% D_2O in Air). BZCYYb4411 powders were synthesized using the same procedure as that used for the DRIFTS samples. The powders were uniaxially pressed and sintered into dense bar-shaped specimens. The final sample dimensions were approximately 10.50 mm in length, 3.08 mm in width, and 2.46 mm in thickness. For electrical measurements, silver wires were wrapped around both ends of the bar to serve as current electrodes. Two additional silver wires were attached approximately 1 mm away from the current electrodes to serve as voltage probes, forming a four-probe configuration. Silver paste was applied to ensure good electrical contact between the silver wires and the sample surface.

3.2.5 Other characterization techniques

The crystal structures of the electrolyte samples were determined using XRD (2008 Bruker D8, CuKα with a scan rate of 10°/ min at room temperature). XRD Rietveld refinement was

conducted using the GSAS-II software package.[118] The morphology of reduced BZCYYb4411 was examined using transmission electron microscopy (TEM) and energy-dispersive X-ray spectroscopy (EDS) (TALOS F200X, Thermo Fisher Scientific). XPS characterization was performed on Thermo Scientific ESCALAB 250Xi with a monochromatic Al Ka source (photon energy of 1486.68 eV) operated at 30 keV and X-ray power of 150 W and a hemispherical energy analyzer. Before spectral acquisition, the sample surface was Ar sputtered for 5 min to remove surface contamination layers, including adsorbed CO_2 and other residual surface species. High-resolution core-level spectra were measured, and data analysis was performed using casaXPS software. The binding energies (BE) of all elements were calibrated using the C 1s peak at 284.8 eV as the reference.

3.2.6 DFT Calculations

DFT calculations were carried out using the Vienna *Ab initio* Simulation Package (VASP).[119-121] Spin polarization was included for all calculations. The projector augmented wave method was employed to describe the core-valence interaction,[122] For Ba, Zr, and Y, their shallow semicore 5s, 4s, and 4s states are explicitly included as valence electrons. The Ce 4f states were included as valence states, whereas the filled Yb 4f states were treated as the frozen core. DFT+U treatments with U_{eff} = 5 eV and 6 eV were applied to the 4*f* states of Ce and Yb, respectively.[123, 124] The generalized gradient approximation Perdew-Burke-Ernzerhof (GGA-PBE) functional was used to describe the exchange-correlation functional.[125, 126] The BZCYYb lattice was approximated with a 2×2×2 supercell that is derived from cubic $BaCeO_3$. The B-site Ce atoms were then substituted with Zr, Y, and Yb, yielding $Ba_8Zr_3Ce_3Y_1Yb_1O_{24}$, mimicking the atomic ratio of BZCYYb4411. Eight B-site configurations were considered, and the most favorable B-site configuration is illustrated in Figure 3.3. The optimized primitive cell lattice is 4.37 Å, close to the

experimental value of 4.31 Å, determined in this work and reported elsewhere. In this configuration, the Ce and Zr atoms are dispersed and occupy the sites in the main diagonal plane. The aliovalent Y and Yb atoms are also separated, occupying the remaining open lattice sites.

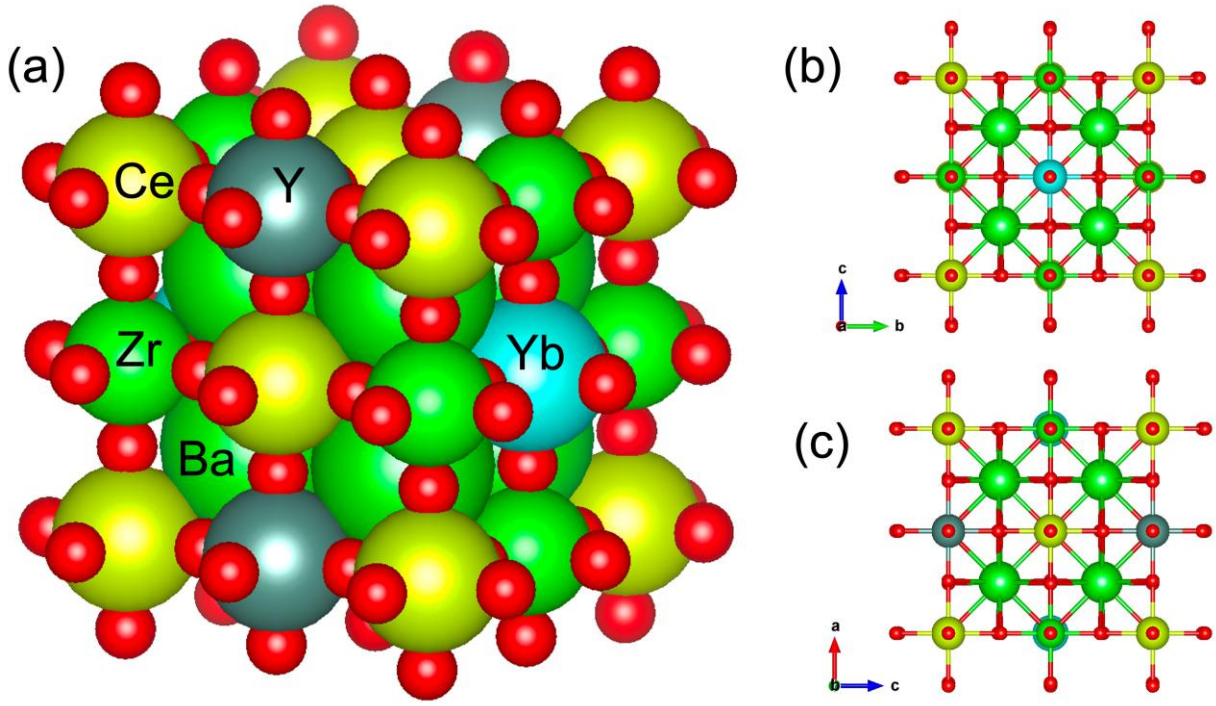

Figure 3.3. Schematic lattice of BZCYYb4411 with the most favorable B-site configuration determined by DFT optimization. (a) The space-filling representation, (b-c) ball-and-stick representation, viewed along the a-axis and b-axis, respectively. (b) and (c) highlight the atomic arrangement of Zr (small green), Ce (yellow), Y (grey), and Yb (turquoise). The Ba and O atoms are displayed in large green spheres and red spheres, respectively.

For phonon calculations, we adopted a higher set of computational parameters, with a plane-wave cutoff energy of 520 eV. Electronic self-consistency was converged to 10^{-5} eV for structural relaxation, and 10^{-7} eV s, and ionic relaxation was continued until the residual forces on

all unconstrained atoms were below 0.02 eV $Å^{-1}$. A 3×3×3 k-point mesh was used to sample the first Brillouin zone in the supercell's reciprocal space.

Three $Ba_8Zr_3Ce_3Y_1Yb_1O_{23}$ bulk models, mimicking the oxygen-deficient BZCYYb4411 lattice, were considered to examine the influence of local dopant arrangement on the H/D isotope effect[127-129]. These included one configuration with adjacent Y and Yb dopants and two configurations with separated Y and Yb dopants, differing in the local position of the oxygen vacancy. Hydrogen-containing structures (BZCYYb4411+H) were generated by placing one H atom near a lattice oxygen in the vacancy-containing environment, followed by structural optimization. The corresponding deuterium-substituted structures (BZCYYb4411+D) were generated from the same local geometries, with the isotope effect introduced through the atomic mass. Vibrational frequencies were computed using the finite-difference method in VASP at the Γ-point with a displacement amplitude of 0.015 Å. The harmonic vibrational free energy was calculated from the phonon frequencies according to:

$$F_{vib}(T) = \sum_i \left[\frac{1}{2}\hbar\omega_i + k_B T ln\left(1 - e^{-\hbar\omega_i/k_B T}\right)\right],$$

where $\hbar$ is the reduced Planck constant, k_B is the Boltzmann constant, ω_i and is the frequency of mode i.[130] The isotope-dependent vibrational free energy difference was then defined as

$$\Delta F_{vib}(T) = F_{vib}^{H}(T) - F_{vib}^{D}(T)$$

$\Delta F_{vib}(T)$ was evaluated over the temperature range of 0-900 K.

3.3. Results and discussion

3.3.1 Phase and microstructures of BZCYYb4411

The phase structure and microstructural characteristics of the BZCYYb4411 electrolyte were first examined. As shown in Figure 3.4a, Rietveld refinement of the X-ray diffraction pattern

demonstrated the formation of a single-phase cubic perovskite structure (space group Pm3m) and a lattice constant of 4.3128(1) Å. TEM images further reveal a dense, defect-free electrolyte microstructure (Figure 3.4b). The corresponding SAED/FFT pattern inserted exhibits diffraction spots that can be indexed to the cubic perovskite structure along the [001] zone axis, with well-resolved reflections corresponding to the (200) and (110) planes. High-resolution TEM images (Figure 3.4c) show clear lattice fringes with interplanar spacings of approximately 0.309 and 0.215 nm, corresponding to the (110) and (200) planes of cubic BZCYYb4411, respectively, consistent with the XRD refinement results (d_{110}=0.31 nm and d_{200}=0.22 nm). In addition, cross-sectional STEM images and EDS elemental mapping of Ba, Zr, Ce, Y, and Yb (Figure 3.4d & Figure 3.5) demonstrate good compositional homogeneity throughout the electrolyte. Even across the grain boundary region (Figure 3.4e-f), no elemental enrichment or depletion observed, indicating nano-scaled chemically uniform grain boundary regions within the dense electrolyte.

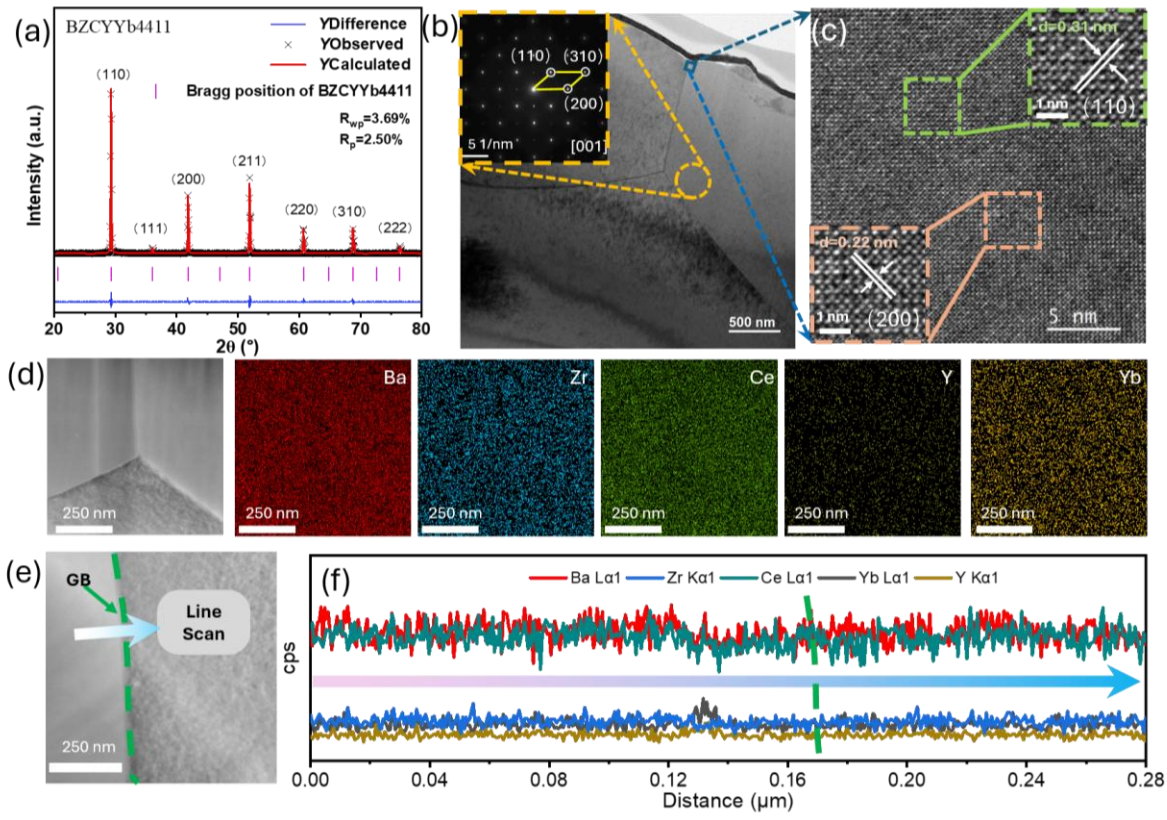

Figure 3.4. The phase and morphology investigation of the synthesized BZCYYb4411 protonic electrolyte. (a) Rietveld refinement of the X-ray diffraction pattern. (b) TEM image and corresponding SAED pattern along the [001] zone axis. (c) High-resolution TEM image showing lattice fringes corresponding to the (110) and (200) planes of BZCYYb4411. (d) Cross-sectional STEM image. (d) STEM-EDS elemental mappings of Ba, Zr, Ce, Y, and Yb, respectively. (e) STEM image showing the grain boundary region selected for elemental line-scan analysis. (f) STEM-EDS line-scan profiles across the grain boundary region, showing the elemental distributions of Ba, Zr, Ce, Y, and Yb.

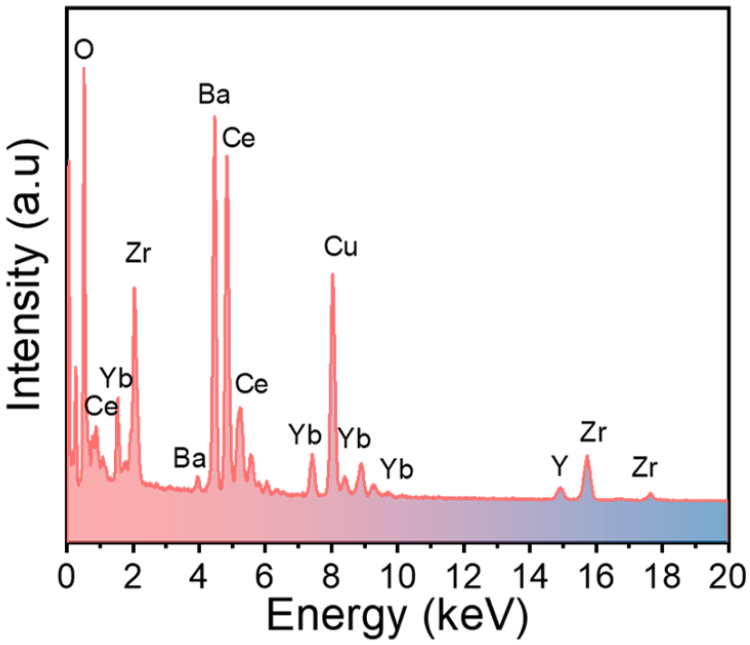

Figure 3.5. Energy-dispersive X-ray spectroscopy (EDS) spectrum of the BZCYYb4411 electrolyte collected from the area used for the elemental mapping shown in Figure 3.4.

3.3.2 Hydration and dehydration kinetics probed by *operando* DRIFTS

Operando DRIFTS measurements were performed to investigate the hydration and dehydration behavior of the BZCYYb4411. Before hydration, the BZCYYb4411 electrolyte exhibits a -OH stretching band centered around ~3416 cm^{-1} [131] treated under dry Ar for 2 h at 600°C (Figure 3.6), and the -OH signals can still be detected at temperatures up to 800 °C (Figure 3.7), indicating the strong intrinsic hydration ability of BZCYYb4411. To elucidate the origin of this behavior, DFT calculations were performed using BZCYYb4411 (100) surface models with difference local B-site cation distributions. The calculations show that oxygen vacancies are preferentially formed at Zr-Yb and Y-Yb pair sites (Figure 3.10a-d), creating favorable local environment for hydration. Further hydration calculations were performed by introducing H_2O at these surface oxygen-vacancy sites and examining the resulting hydrated structures (Figure 3.11). After dissociative water incorporation, the stability of the hydrated state varies with the local cation environment and the resulting proton arrangement. Among the configurations examined, the Zr-$V_O^{\cdot\cdot}$-Yb site exhibits a thermodynamically favorable hydrated configuration with a hydration energy of -0.12 eV, demonstrating that water incorporation can be energetically favored at specific surface vacancy environments. Consistent with this strong hydration tendency upon exposure to humidified Ar gas (3% of H_2O) at 600 °C, the -OH peak grows rapidly within the initial 10 min and gradually approaches a steady intensity as shown in Figure 3.8a. In addition, weak CO_2-related absorption bands near ~2400 cm^{-1} were also observed during the measurement.[32] The intensity of the -OH stretching band progressively decreases after switching the gas atmosphere to dry Ar gas (Figure 3.8b). It is noted that dehydration required approximately 200 min to reach equilibrium, compared to 150 min for hydration, suggesting that dehydration involves additional energetic barriers. In addition, the -OH stretching vibration exhibits a temperature-dependent blue shift

(Figure 3.8a-b and Figure 3.9). For example, as the temperature increases, the center of the -OH stretching band shifts from approximately 3396 cm^{-1} at 500 °C to 3405 cm^{-1} at 550 °C, and further to about 3416 cm^{-1} at 600 °C, which is related to a gradual weakening of hydrogen-bonding interactions.[25]

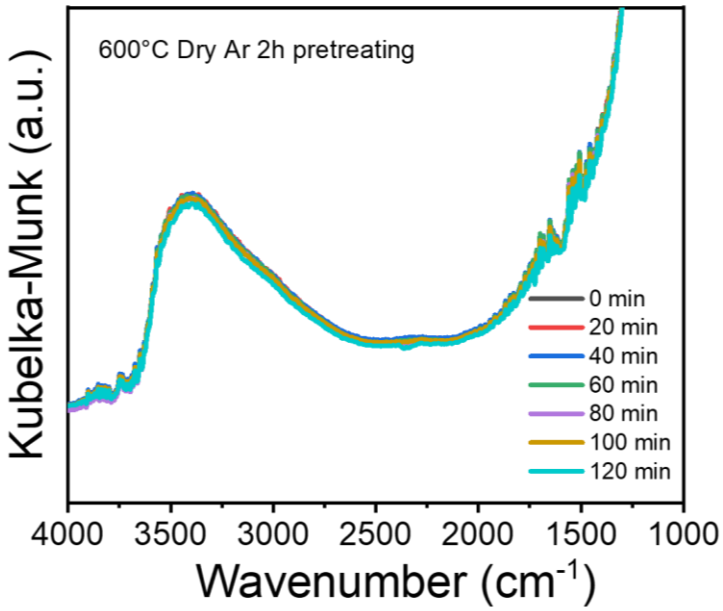

Figure 3.6. DRIFTS collected from the BZCYYb4411 electrolyte pellet at 600 °C under dry air condition. The sample was pre-treated in dry air at 600 °C for at least 2 h to remove physiosorbed or weakly bound water.

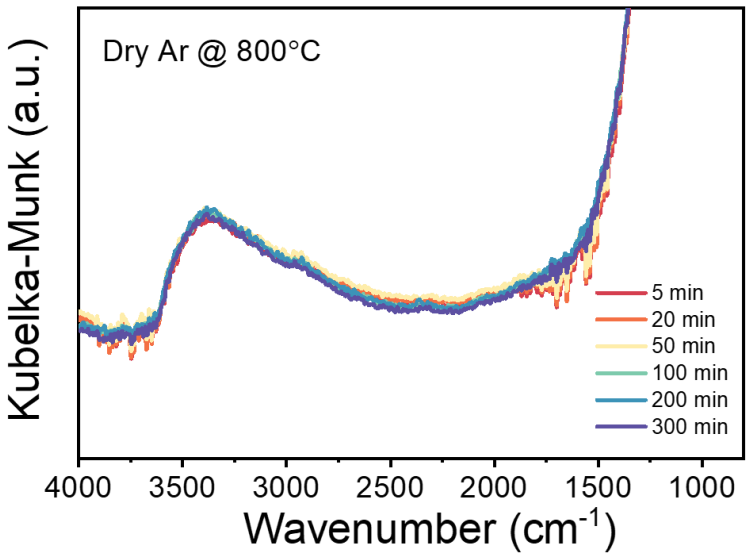

Figure 3.7. DRIFTS spectra collected during prolonged drying at 800 °C under dry Ar condition.

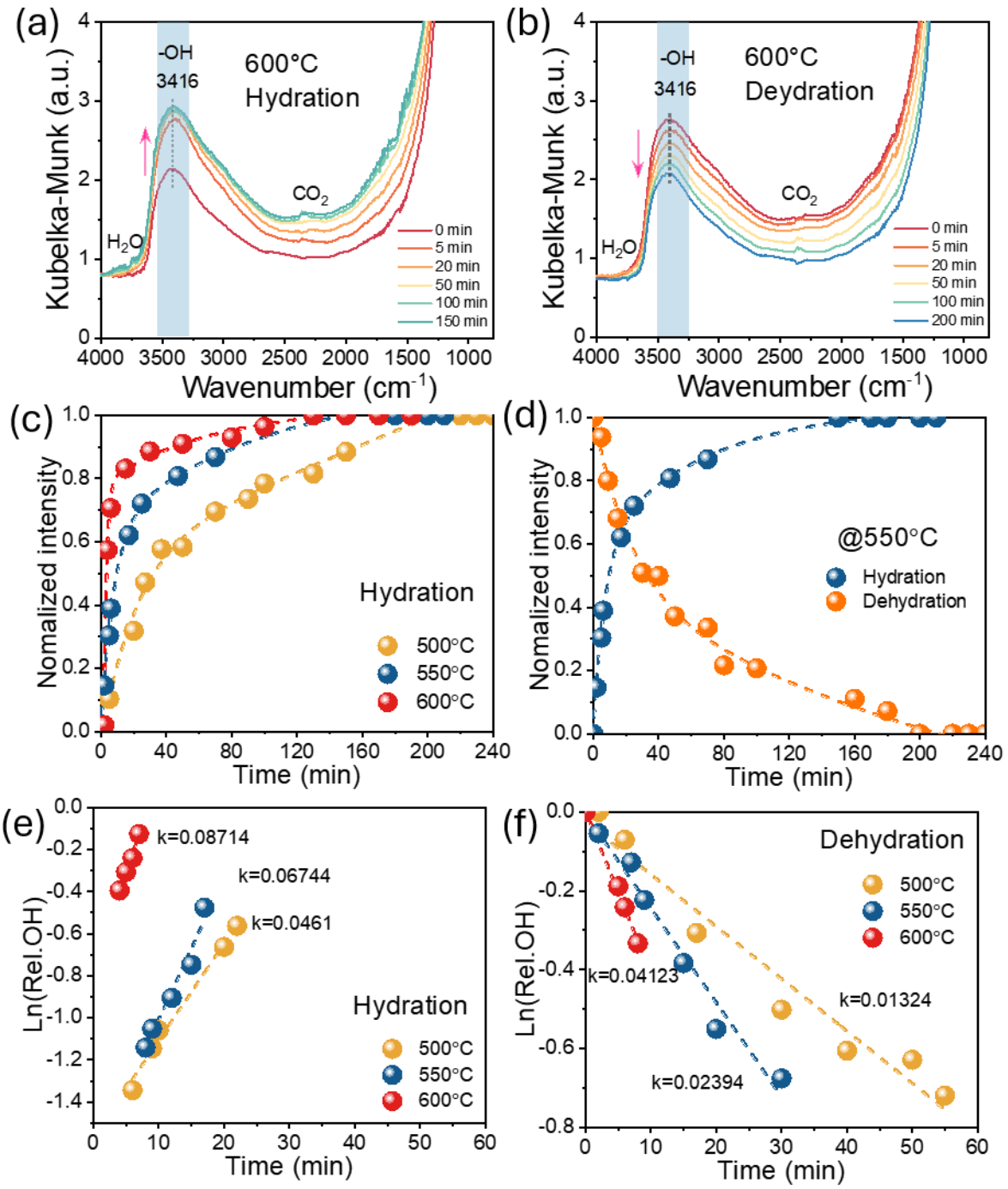

Figure 3.8. Time-resolved DRIFTS spectra collected at 600 °C during (a) hydration and (b) dehydration, showing the evolution of hydroxyl stretching bands, (c) Normalized -OH band intensity as a function of time from 600 °C to 500 °C during hydration, (d) Comparison of normalized -OH band intensity as a function of time in hydration to in dehydration at 550 °C, (e)

The natural logarithm of normalized -OH bands (500-600°C) as a function of exchange time at different time in the hydration process and (f) the natural logarithm of normalized -OH bands (500-600°C) as a function of exchange time at different time in the dehydration process.

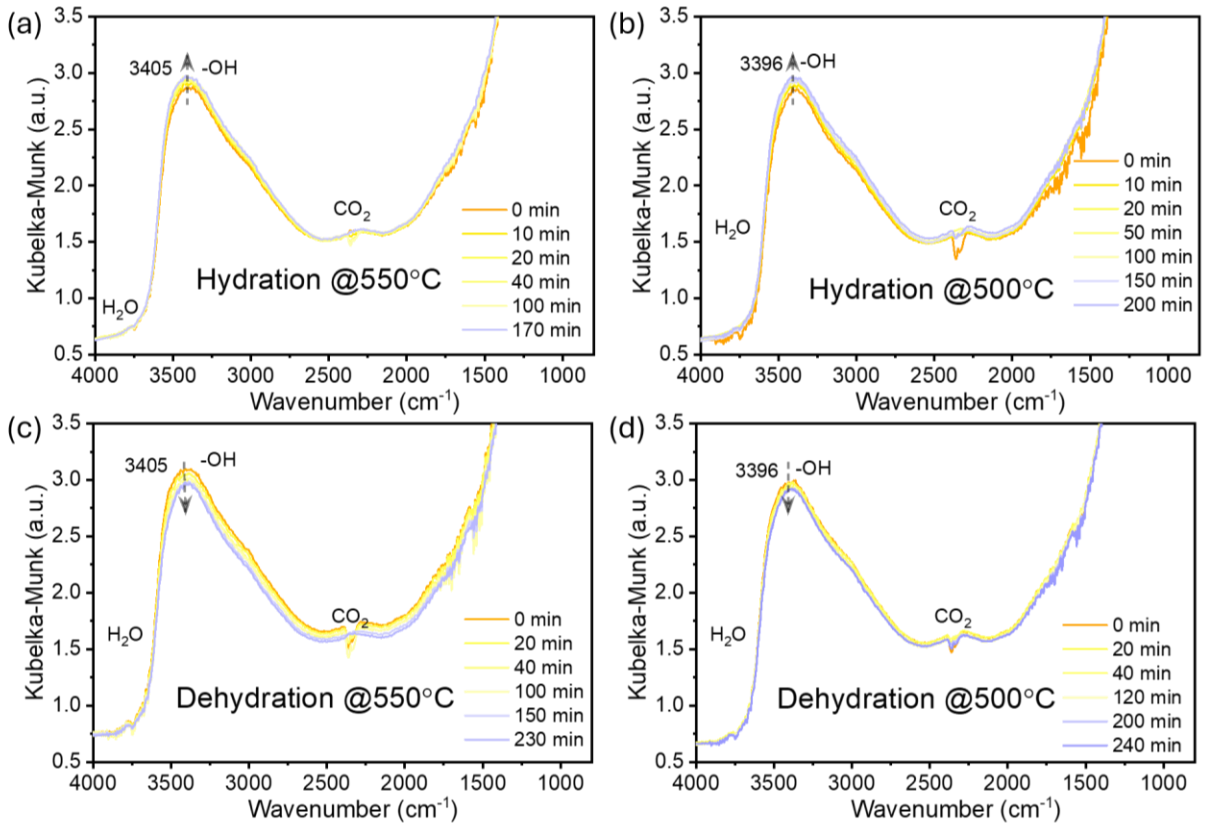

Figure 3.9. Time-resolved DRIFTS spectra collected during hydration upon switching from dry Ar to humidified Ar (3 % H_2O) (a) at 550 °C and (b) at 500 °C; time-resolved DRIFTS spectra collected during dehydration upon switching from humidified Ar (3 % H_2O) to dry Ar (c) at 550 °C and (d) at 500 °C

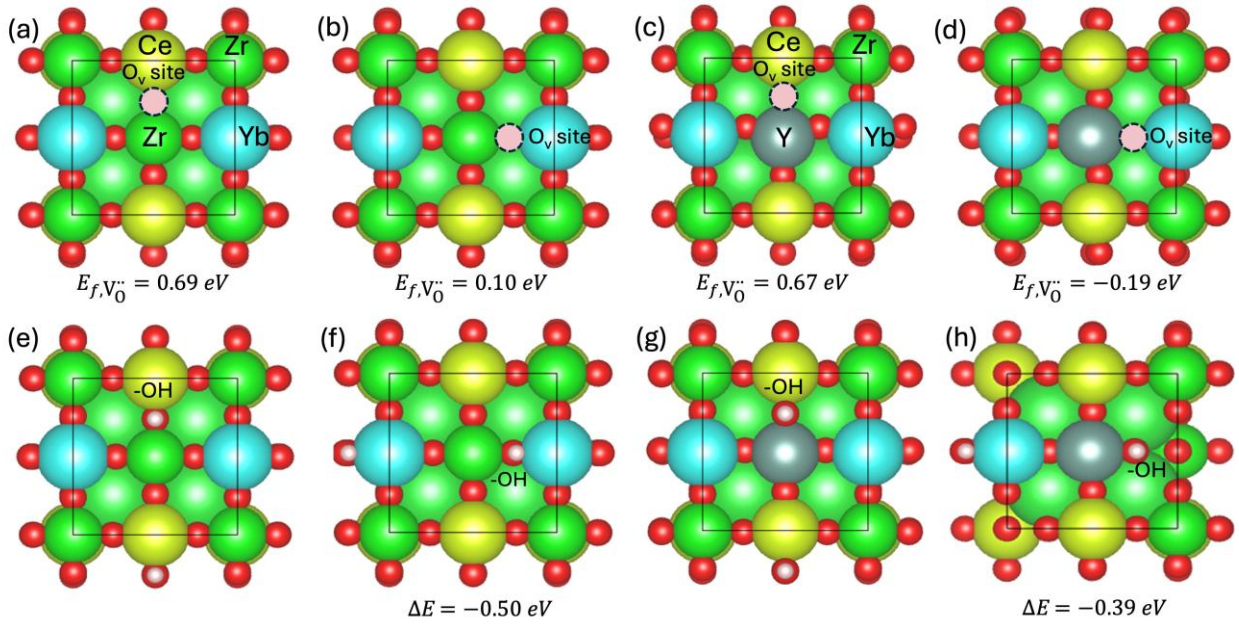

Figure 3.10. (a-b) $\mathbf{V_O^{\cdot\cdot}}$ sites between the Zr-Ce pair and Zr-Yb pair in a (100) facet with a Zr/Ce/Zr/Yb configuration. (c-d) $\mathbf{V_O^{\cdot\cdot}}$ sites between the Zr-Ce pair and Zr-Yb pair in a (100) facet with a Y/Ce/Zr/Yb configuration. (e-f) -OH group occupying the $\mathbf{V_O^{\cdot\cdot}}$ site Zr-Ce pair and Zr-Yb pair. (g-h) -OH group occupying the Ov site Zr-Ce pair and Zr-Yb pair. Color scheme: Zr (small green), Ce (yellow), Y (grey), and Yb (turquoise). Ba and O atoms are displayed as large green and red spheres, respectively. The oxygen vacancy formation energy is defined as: $\boldsymbol{E_{f,V_O^{\cdot\cdot}} = E_{V_O^{\cdot\cdot}} + \frac{1}{2}E_{O_2(g)} - E_{V_O^{\cdot\cdot}-free(100)}}$.

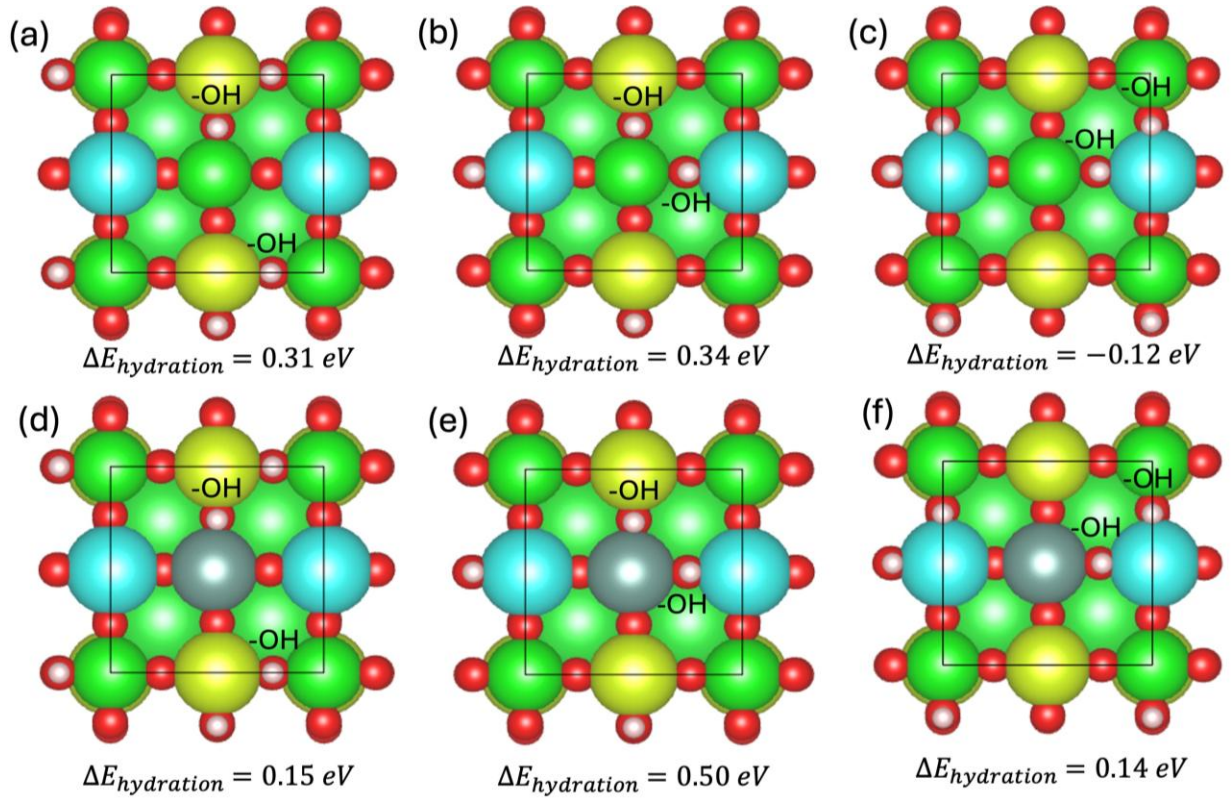

Figure 3.11. (a) Distribution and hydration energy ($\Delta \boldsymbol{E_{hydration}}$) of OH groups after the hydration of the (100) facet with the Zr/Ce/Zr/Yb configuration at the Zr-$\mathbf{V_O^{\cdot\cdot}}$-Ce site. (b-c) Distributions and $\Delta \boldsymbol{E_{hydration}}$ of OH groups after the hydration of the (100) facet with the Zr/Ce/Zr/Yb configuration at the Zr-$\mathbf{V_O^{\cdot\cdot}}$-Yb site. (d) Distribution and $\Delta \boldsymbol{E_{hydration}}$ of OH groups after the hydration of the (100) facet with the Y/Ce/Zr/Yb configuration at the Y-$\mathbf{V_O^{\cdot\cdot}}$-Ce site. (e-f) Distributions and $\Delta \boldsymbol{E_{hydration}}$ of OH groups after the hydration of the (100) facet with the Y/Ce/Zr/Yb configuration at the Y-$\mathbf{V_O^{\cdot\cdot}}$-Yb site. Color scheme: Zr (small green), Ce (yellow), Y (grey), and Yb (turquoise). Ba and O atoms are displayed as large green and red spheres, respectively. The hydration free energy is defined as: $\Delta \boldsymbol{G_{hydration}} = \boldsymbol{E_{hyd-(100)}} - \boldsymbol{\mu_{H_2O(g)}} - \boldsymbol{E_{V_O^{\cdot\cdot}}}$.

Normalization of the -OH band intensity enables direct comparison of hydration and dehydration kinetics across different temperatures (Figure 3.8c & Figure 3.9). Although hydration is thermodynamically favored at lower temperatures due to its exothermic nature, the hydration process proceeds more rapidly at higher temperatures because of accelerated surface reaction and proton transport kinetics.[132, 133] Figure 3.8d provides a direct comparison of the hydration and dehydration, and the dehydration exhibits a noticeably slower decay with an extended tail before reaching equilibrium. This difference might be ascribed to the recombination of lattice hydroxyl defects to regenerate H_2O before desorption can occur.[25]

To quantify the hydration and dehydration kinetics, the natural logarithm of the normalized -OH band intensity, ln(Rel. OH), was plotted as a function of time at each temperature (Figure 3.4e-f). Linear regression analysis shows that the first-order reaction model might be adopted here to describe such kinetic behavior, where the reaction rate is proportional to the instantaneous surface -OH concentration.[114] As shown in Figure 3.8e, the extracted apparent rate constants increase with temperature, rising from 0.0461 min^{-1} at 500 °C to 0.0871 min^{-1} at 600 °C. A similar temperature dependence is observed after switching the gas atmosphere from humidified Ar to dry Ar (Figure 3.8f), and the dehydration rates are approximately 2-3.5 times lower than those for hydration. As shown in Figure 3.12a, the Arrhenius analysis yields an apparent activation energy of 35.8 kJ mol^{-1} for hydration and 63.7 kJ mol^{-1} for dehydration. The significantly higher activation energy for dehydration suggests that removing hydroxyl species requires overcoming additional energetic barriers compared with forming hydroxyls, which is consistent with the slower dehydration kinetics observed in the time-dependent DRIFTS measurements.

To further examine the influence of hydration on surface chemistry, O 1s XPS spectra were analyzed for hydrated and dehydrated samples (Figure 3.12b). The O 1s spectra can be

deconvoluted into a high-binding-energy component associated with surface oxygen species and hydroxyl groups, and a low-binding-energy component corresponding to lattice oxygen.[134] Upon hydration, the relative contribution of the surface oxygen species increased from 58.6% to 67.3%, suggesting an enhanced concentration of surface oxygen-containing species, including hydroxyl groups generated during hydration.

A mechanistic illustration of the asymmetric hydration and dehydration behavior is shown in Figure 3.12d. Thermodynamically, hydration in acceptor-doped protonic ceramics is generally an exothermic process with negative hydration enthalpy, making hydroxyl defect formation energetically favorable. Once water dissociates at the surface, the resulting protonic defects can be stabilized through proton hopping and local lattice reorganization, thereby promoting proton incorporation into the oxide lattice. In contrast, dehydration requires breaking these stabilized hydroxyl configurations and reforming water molecules prior to desorption, leading to a substantially larger energetic barrier. The thermodynamic preference for hydroxyl stabilization therefore provides a fundamental origin for the kinetic asymmetry between hydration and dehydration.

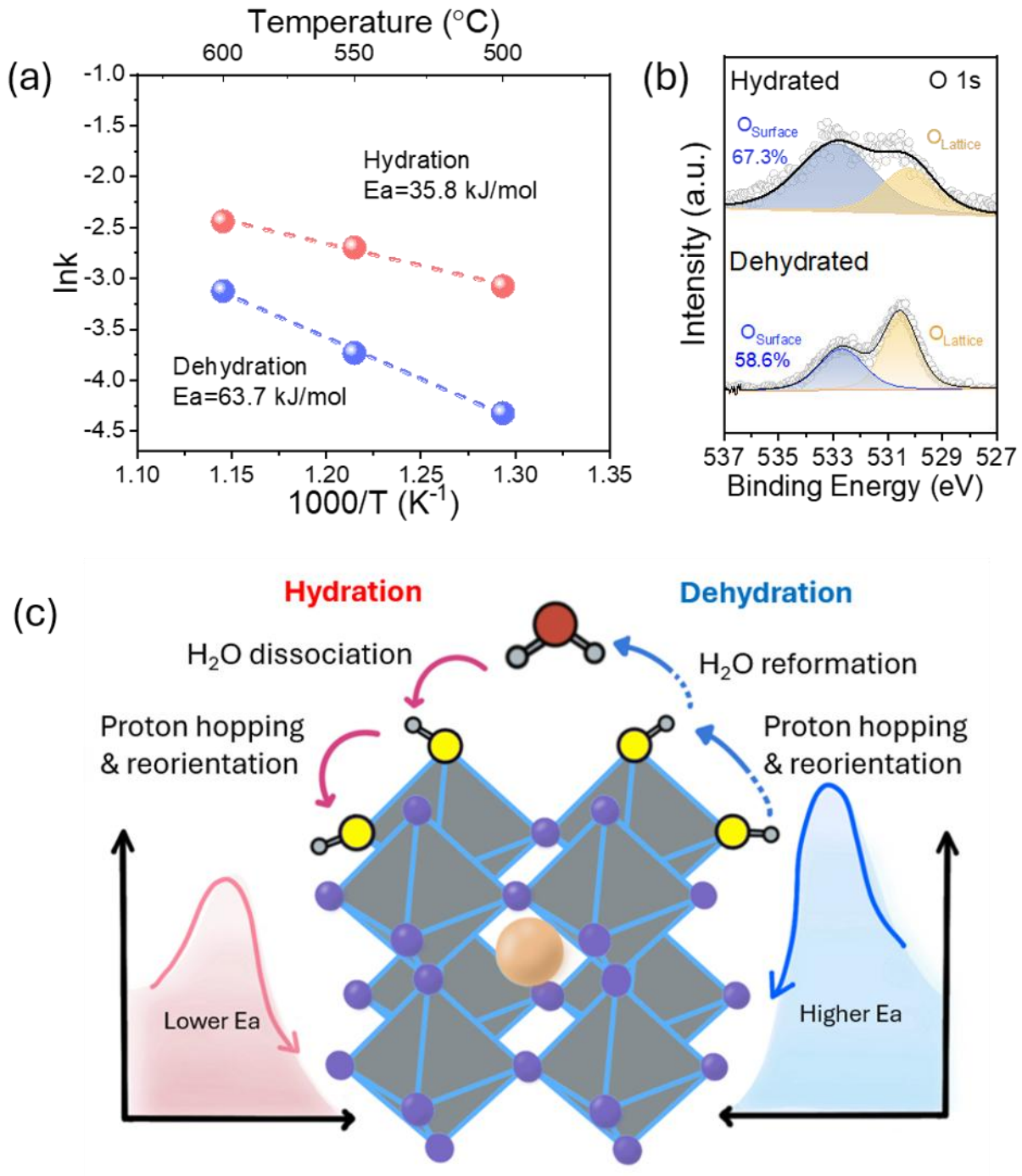

Figure 3.12. Experimental and theoretical analysis of hydration and dehydration processes in BZCYYb4411. (a) temperature-dependent hydration and dehydration kinetics derived from DRIFTS measurements, (b) O 1s XPS spectra demonstrating changes in surface hydroxyl species

upon hydration, and (c) Proposed schematic mechanism illustrating the asymmetric hydration/dehydration behavior.

According to Equation 12, during hydration, the dissociated water fills the available $V_O^{\cdot\cdot}$ site with an OH group, while the remaining H atom is attached to the lattice oxygen (O_O^x). Once water dissociates at the surface, the resulting protonic defects can be stabilized through proton hopping and local lattice reorganization, thereby promoting proton incorporation into the oxide lattice (Figure 3.12c). DFT calculations further reveal a strong energetic preference for hydroxyl stabilization in Yb-containing local environments (Figure 3.10e-h). Specifically, locating the -OH group at the Zr-Yb and Y-Yb oxygen vacancy defects lowers the energy by 0.50 and 0.39 eV, respectively. Such stabilization of the hydroxylated state makes the reverse dehydration process less favorable, as dehydration requires the stabilized protonic species to reorganize and recombine to form H_2O before desorption. This thermodynamic stabilization therefore provides an atomistic rationale for the slower dehydration kinetics observed experimentally.

3.3.3 H_2O/D_2O isotope exchange and proton exchange kinetics

To understand surface proton-exchange behavior, time-resolved DRIFTS experiments involving isotope exchange were performed by switching the feed gas between humidified Ar containing 3% H_2O and humidified Ar containing 3% D_2O, as well as in the reverse direction (Figure 3.13, Figure 3.14,Figure 3.15, and Figure 3.16). Figure 3.13 presents contour plots showing the temporal evolution of the -OH (~3400 cm^{-1}) and -OD (~2500-2524 cm^{-1}) stretching regions during isotope exchange. Red regions indicate higher absorbance intensity, whereas blue regions indicate lower intensity. For $H_2O \rightarrow D_2O$ exchange (Figure 3.13a,c), the gradual disappearance of the -OH band is accompanied by the emergence of the -OD band[103]. Conversely, during $D_2O \rightarrow H_2O$ exchange (Figure 3.13b,d), the -OD band decreases while the O-H band

simultaneously grows, directly visualizing the proton-deuteron exchange process. The isotope exchange kinetics exhibit similar temperature dependence. At 600 °C, both the decay of -OH bands and the growth of -OD bands proceed rapidly, reaching equilibrium within 200 min. In contrast, at 400 °C, the spectral evolution is markedly slower, taking around 3 times as long to approach a steady state. In the reverse D_2O-to-H_2O exchange, the -OD stretching band progressively diminishes while the -OH band recovers with time (Figure 3.13c-d). At the same temperature, the D_2O-to-H_2O exchange reaches equilibrium more rapidly than the H_2O-to-D_2O process, indicating kinetic asymmetry between the two exchange directions. Importantly, the contour plots of isotope-exchange reveal two types of proton populations with distinct exchange rates: (a) labile -OH that exchanges rapidly with D_2O, and (b) more strongly bound -OH. The labile -OH population consists of mobile protons that readily participate in exchange and surface diffusion. While after the system reaches apparent equilibrium, a weak but persistent O–H signal remains observable, suggesting the presence of strongly bound protonic species that exchange more slowly than the dominant proton population. The rapidly exchanging proton species are likely associated with dynamically accessible proton hopping pathways, whereas the residual hydroxyl species may correspond to strongly bound proton configurations requiring additional thermal or electrochemical activation to participate in long-range transport.[25, 135]

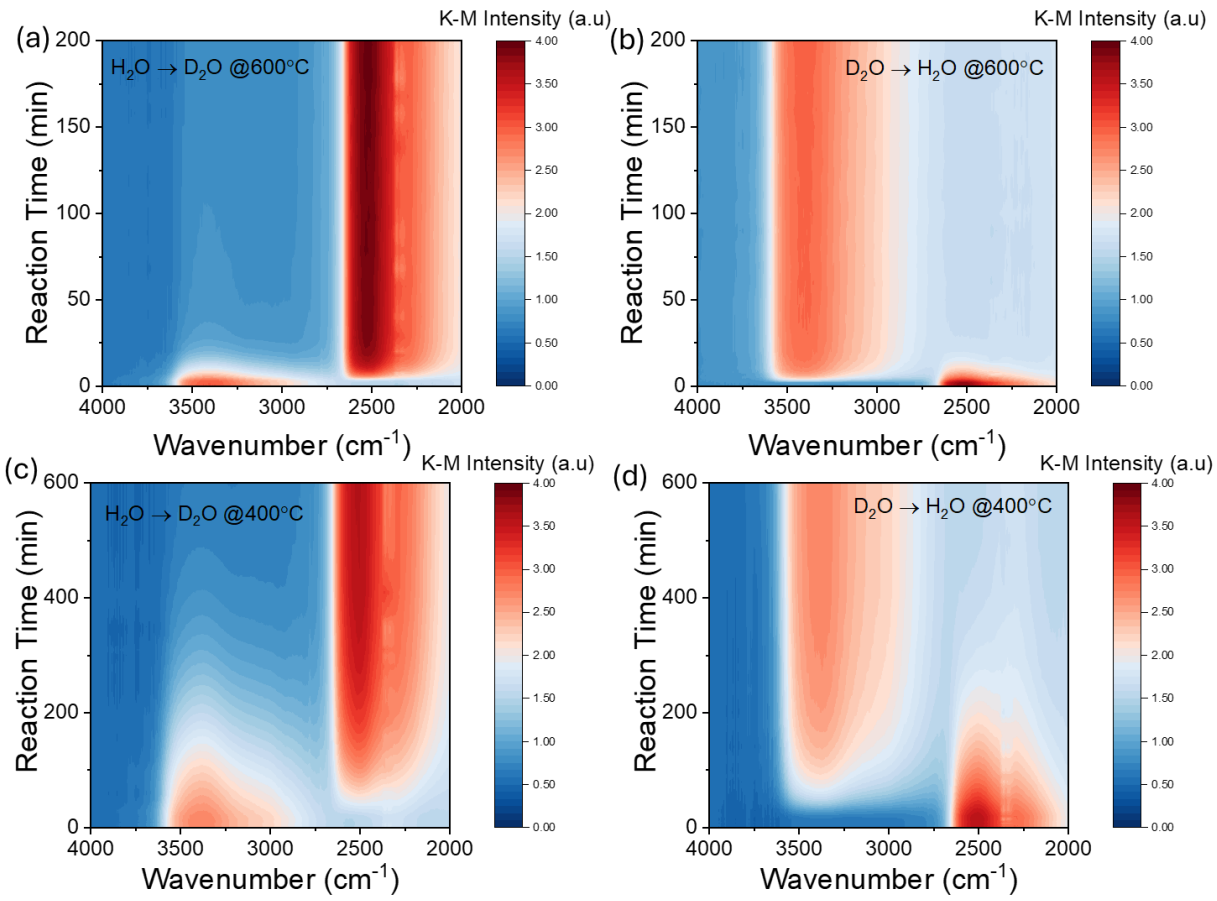

Figure 3.13. 2D spectral map of time-resolved DRIFTS for the BZCYYb4411 electrolyte during isotope exchange (a) from 3% H_2O to 3% D_2O at 600 °C, (b) from 3% D_2O to 3% H_2O at 600 °C, (c) from 3% H_2O to 3% D_2O at 400 °C, and (d) from 3 % D_2O to 3% H_2O at 400 °C.

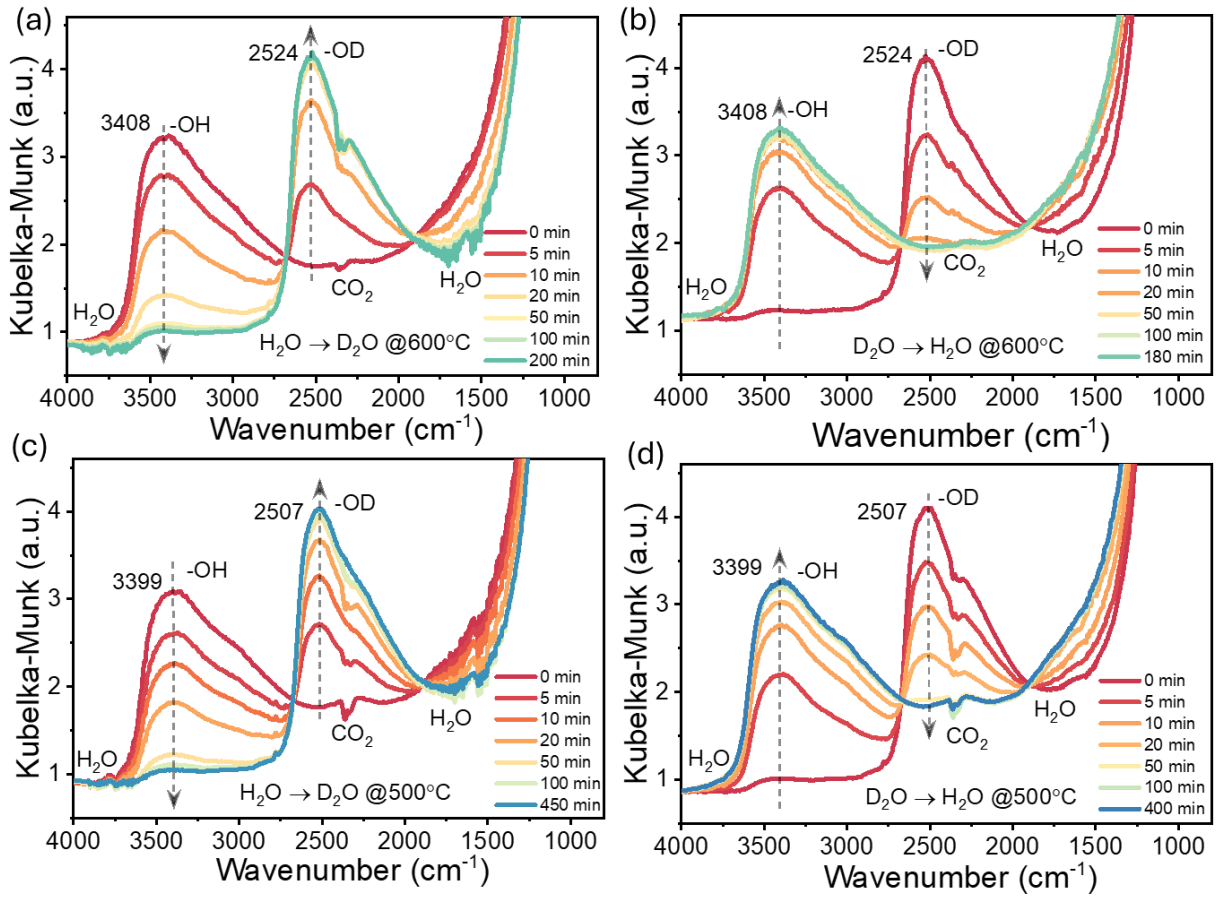

Figure 3.14. DRIFTS of OH and OD bands over time: at 600 °C (a) during gas switching from 3% H_2O-humidified Ar to 3% D_2O-humidified Ar, (b) during gas switching from 3% D_2O-humidified Ar to 3% H_2O-humidified Ar; and at 500 °C (c) during gas switching from 3% H_2O-humidified Ar to 3% D_2O-humidified Ar, (d) during gas switching from 3% D_2O-humidified Ar to 3% H_2O-humidified Ar.

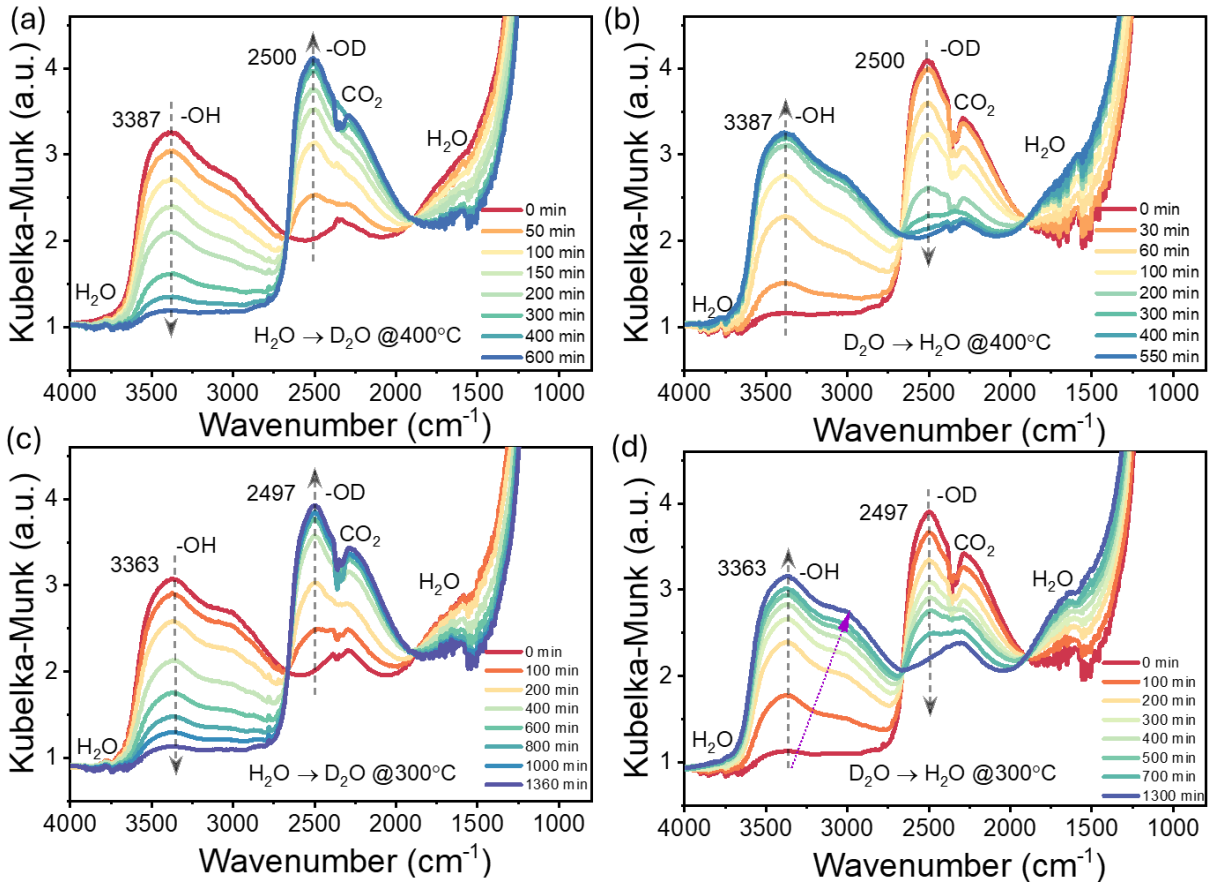

Figure 3.15. DRIFTS of OH and OD bands over time: at 400 °C (a) during gas switching from 3% H_2O-humidified Ar to 3% D_2O-humidified Ar, (b) during gas switching from 3% D_2O-humidified Ar to 3% H_2O-humidified Ar; and at 300 °C (c) during gas switching from 3% H_2O-humidified Ar to 3% D_2O-humidified Ar, (d) during gas switching from 3% D_2O-humidified Ar to 3% H_2O-humidified Ar.

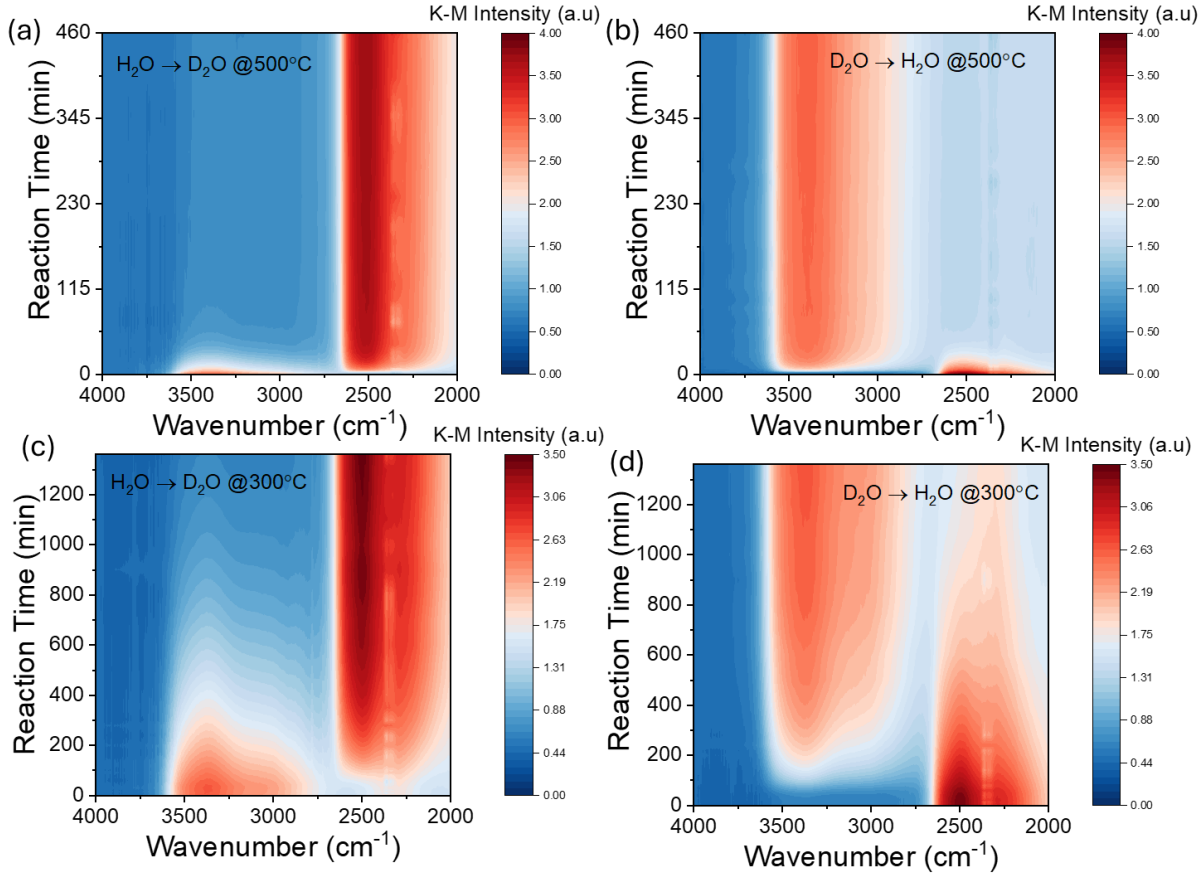

Figure 3.16. 2D spectral map of time-resolved DRIFTS for the BZCYYb4411 electrolyte during isotope exchange (a) from 3% H_2O to 3% D_2O at 500 °C, (b) from 3% D_2O to 3% H_2O at 500 °C, (c) from 3% H_2O to 3% D_2O at 300 °C, and (d) from 3 % D_2O to 3% H_2O at 300 °C.

To compare the temperature-dependent evolution of hydroxyl species during the isotope exchange process, the peak positions of the -OH and -OD stretching bands at different temperatures are summarized in Table 3.1. The observed isotope ratios (ν_{OH}/ν_{OD}) fall in the range of 1.347-1.356, aligning well with the theoretical isotopic factor (1.414 for an H/D species attached to an infinite mass, 1.374 for using reduced masses) [129, 136] for H-D substitution.

Table 3.1. Observed OH/OD vibrations and isotope shift at different temperatures.

Temperature	Vibration		
	OH-stretch cm^{-1}	OD-stretch cm^{-1}	ν_{OH}/ν_{OD}
300°C	3363	2497	1.347
400°C	3387	2500	1.355
500°C	3399	2507	1.356
600°C	3408	2524	1.350

The normalized intensity (Figure 3.17) supports the asymmetric nature of the H_2O-to-D_2O and D_2O-to-H_2O exchange processes. Both exchange directions exhibit a pronounced temperature dependence. At 300 °C, equilibrium is reached after 1,200 min (Figure 3.17a-b). As the temperature increases, the equilibrium time decreases quickly, dropping to below 200 min at 600 °C. At every temperature, D_2O-to-H_2O is consistently faster than H_2O-to-D_2O (Figure 3.17c), which might be due to the stronger O-H bond and the lower mobility of deuterons. Interestingly, the normalized -OH and -OD intensities exhibit a distinct crossover point at each temperature during the isotope exchange process (Figure 3.17d-e). As the temperature increases, the crossover occurs significantly faster (Figure 3.17e). The intersection of normalized -OH and -OD signals from 0.60-0.64 (Figure 3.17f, Figure 3.18, and Figure 3.19), together with the incomplete decay of the -OH band, indicates that only a fraction of the -OH population participates in rapid exchange, while the remaining -OH groups remain relatively stable within the experimental time scale. The

observed deviation supports the presence of kinetically distinct hydroxyl species, consistent with the hypothesis that two types of hydroxyl groups coexist in the material.

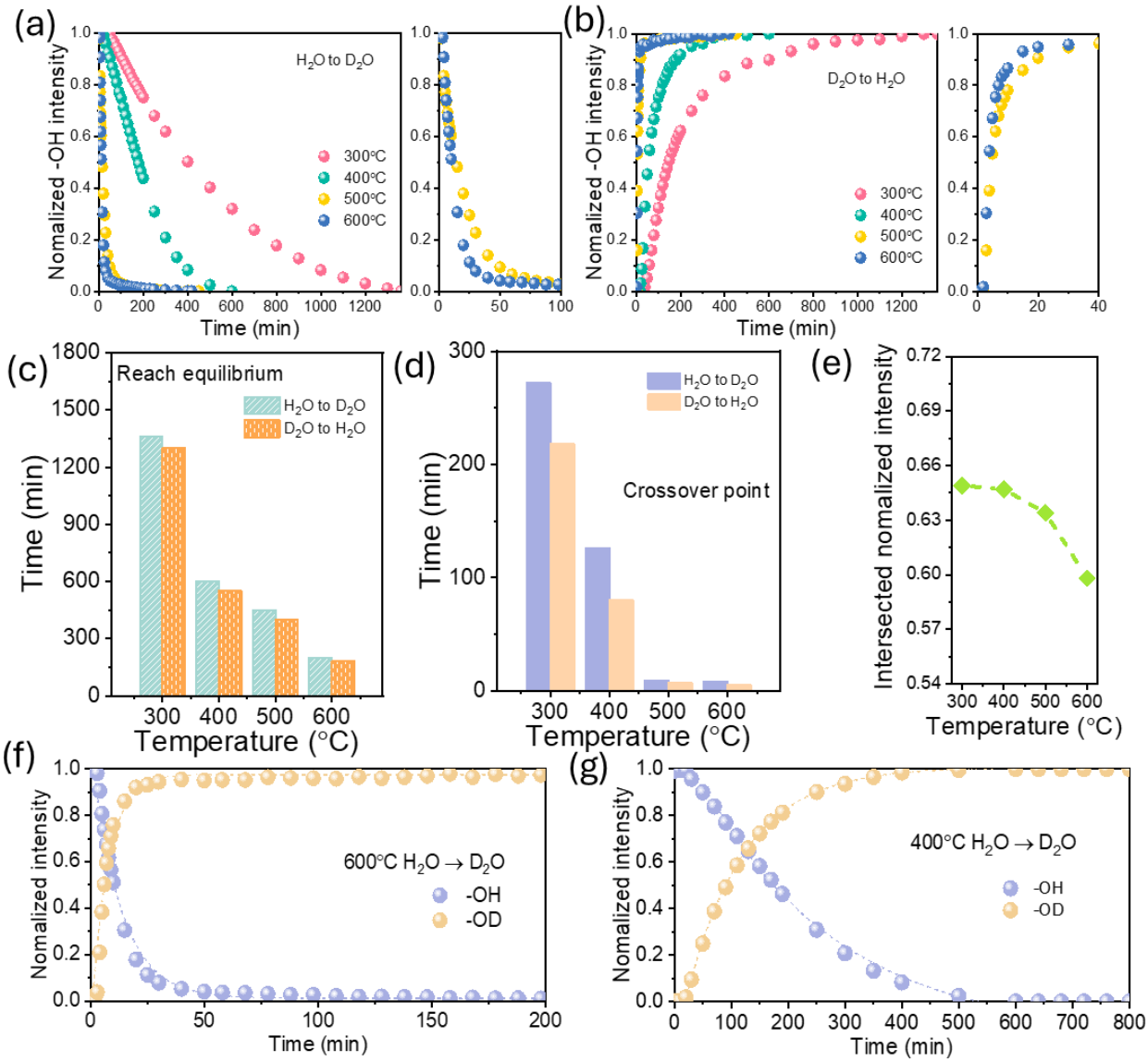

Figure 3.17. Normalized O-H and O-D intensity evolution during isotope exchange at different temperatures. (a) normalized O-H intensity decay during H_2O-to-D_2O exchange. (b) normalized O-H intensity recovery during D_2O-to-H_2O exchange. (c) time required to reach isotopic equilibrium for both exchange directions at different temperatures. (d) crossover times of

normalized O-H and O-D intensities during isotope exchange. (e) Temperature dependence of the crossover intensity between normalized O-H and O-D signals. Representative crossover behavior between normalized O-H and O-D intensities during H_2O-to-D_2O exchange (f) at 600 °C and (g) at 400 °C.

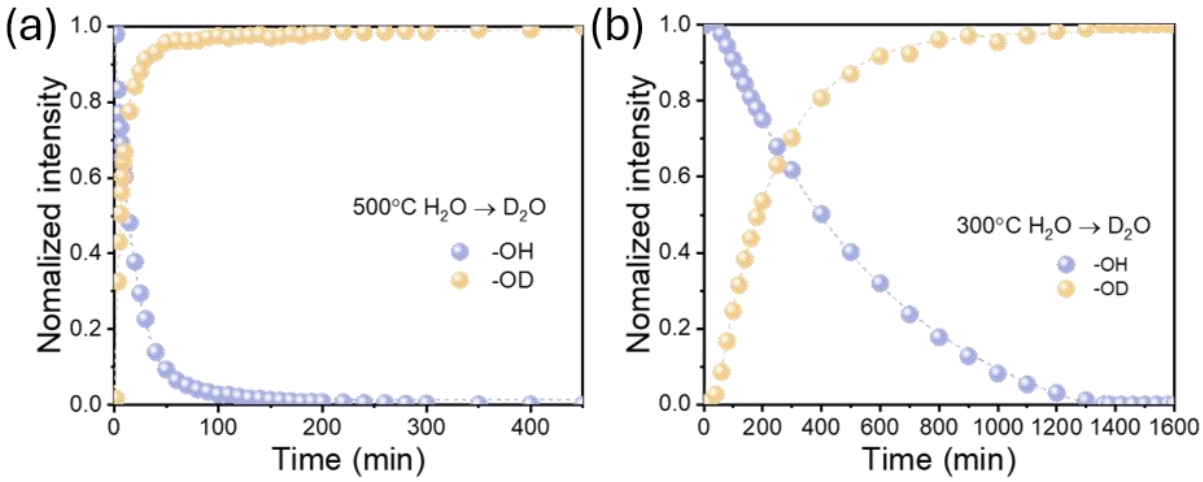

Figure 3.18. Normalized intensities of -OH and -OD bands over time during gas switching from 3% H_2O-humidified air to 3% D_2O-humidified air at 500 °C and 300 °C

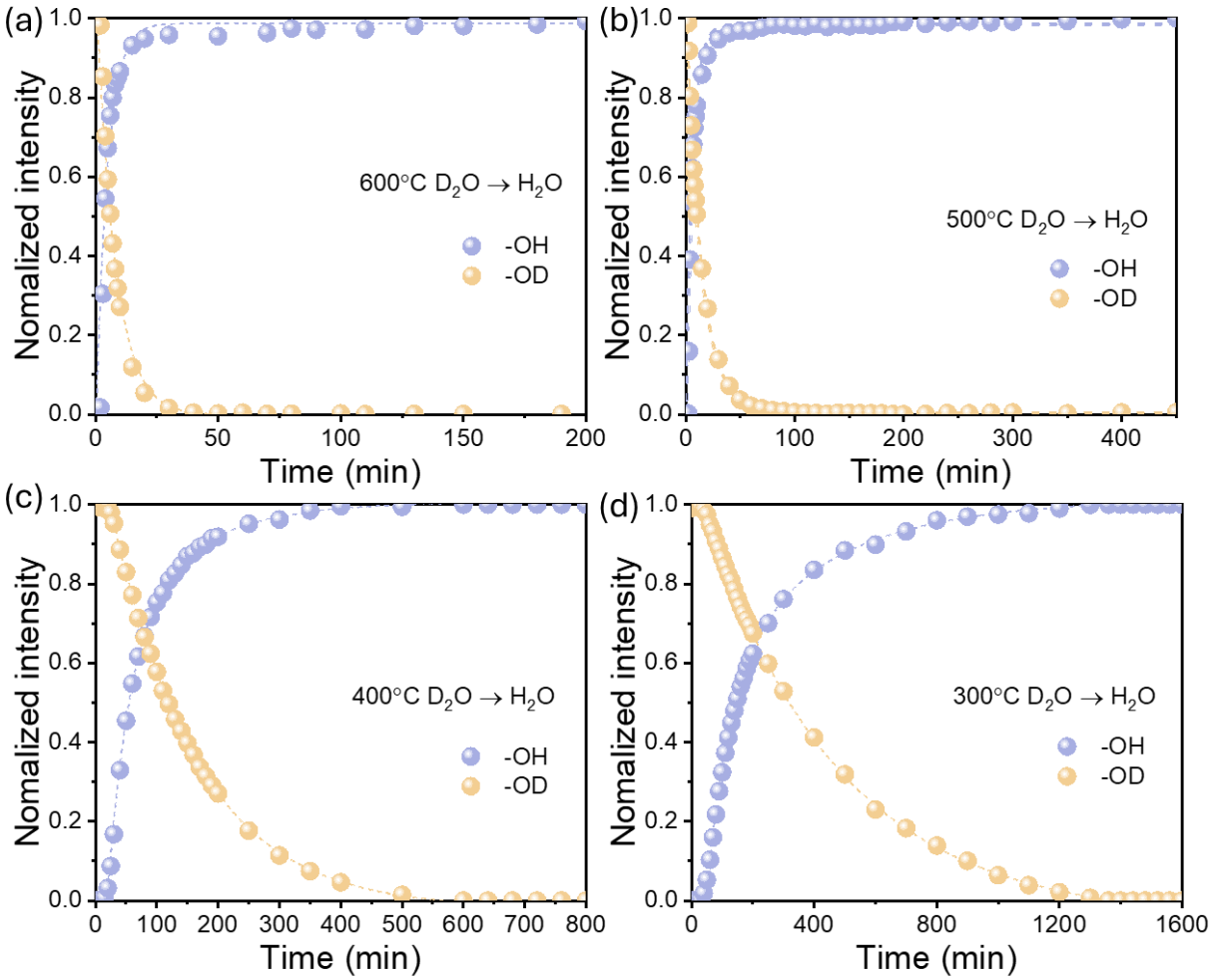

Figure 3.19. Normalized intensities of -OH and -OD bands over time during gas switching from 3% D_2O-humidified air to 3% H_2O-humidified air at 600 °C, 500 °C, 400 °C, and 300 °C

Moreover, a clear kinetic difference is observed between H_2O-to-D_2O, and D_2O-to-H_2O exchange directions. Figure 3.20a-b presents the first-order kinetic analysis of the isotope-exchange process. Linear relationships are observed between ln(Rel. O-H intensity) and time for both $H_2O \rightarrow D_2O$ and $D_2O \rightarrow H_2O$ exchange, enabling the extraction of apparent exchange rate constants. The fitted rate constants reveal distinct kinetic behavior for the two exchange directions, confirming that proton/deuteron substitution proceeds through different exchange rates. As shown in Figure 3.20c, the apparent E_a under the D_2O-to-H_2O process is 65.4 kJ mol^{-1}, which is slightly

higher than that of the H_2O-to-D_2O process (49.9 kJ mol^{-1}). While this difference is consistent with a kinetic isotope effect[127], it also reflects the varying accessibility of the two proton populations.

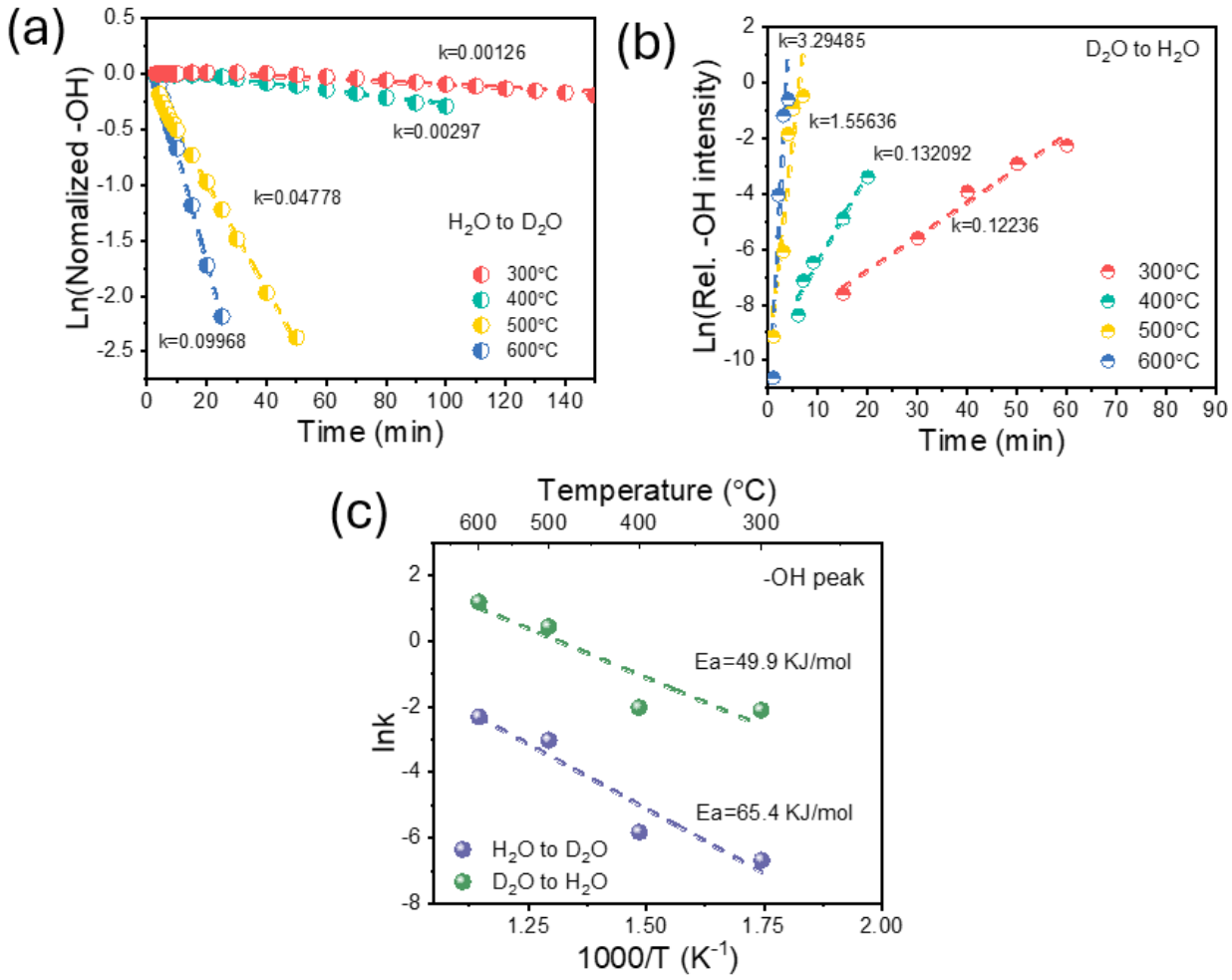

Figure 3.20**.** Kinetic analysis of isotope exchange during proton/deuteron substitution. (a) plots of the natural logarithm of normalized O-H intensity [ln(Rel. O-H)] as a function of time during H_2O-to-D_2O exchange. (b) plots of ln(Rel. O-H) versus time during D_2O-to-H_2O exchange. (c) apparent activation energies (Ea) derived from isotope exchange kinetics for H_2O-to-D_2O and D_2O-to-H_2O processes.

3.3.4 DFT Calculations of H/D Isotope Effect in BZCYYb4411

DFT calculations enable atomistic quantification of isotope effects by resolving how local dopant environments modify the vibrational contribution to the H/D free energy. Fig. 7a-c shows three representative local configurations in BZCYYb arising from the spatial arrangement of Y and Yb dopants. Local Configuration 1 corresponds to H/D located near a Y-Yb dopant pair (Figure 3.21a), whereas local configurations 2 and 3 represent environments without adjacent dopants (Figure 3.21b-c). The calculated $\Delta F_{\mathrm{vib}}(T)$ reveals a clear H/D isotope effect across these local configurations: the D-containing configurations are consistently lower in vibrational free energy than the corresponding H-containing configurations. This behavior is consistent with the larger mass of D, which reduces the associated zero-point and thermal vibrational contributions. The magnitude of the isotope effect depends sensitively on the local dopant-vacancy arrangement. In particular, BZCYYb4411+H/D local configuration 2, where H/D is located between YO_6 and CeO_6 octahedra, yields the smallest $\Delta F_{\mathrm{vib}}(T)$. By contrast, BZCYYb4411+H/D local configurations 1 and 3, where H/D is located between YO_6-YbO_6 octahedra and YbO_6-ZrO_6 octahedra, respectively, give larger and relatively similar values. This site dependence indicates that the local arrangement of Y, Yb, Zr, Ce, and the oxygen vacancy modifies the vibrational characteristics of the proton-containing environment. Such differences likely arise from changes in local O-H bonding geometry, octahedra tilting, and the coupling between the protonic species and the surrounding oxide framework. These results suggest that the H/D isotope effect in BZCYYb4411 is locally environment-dependent rather than completely uniform across the lattice.

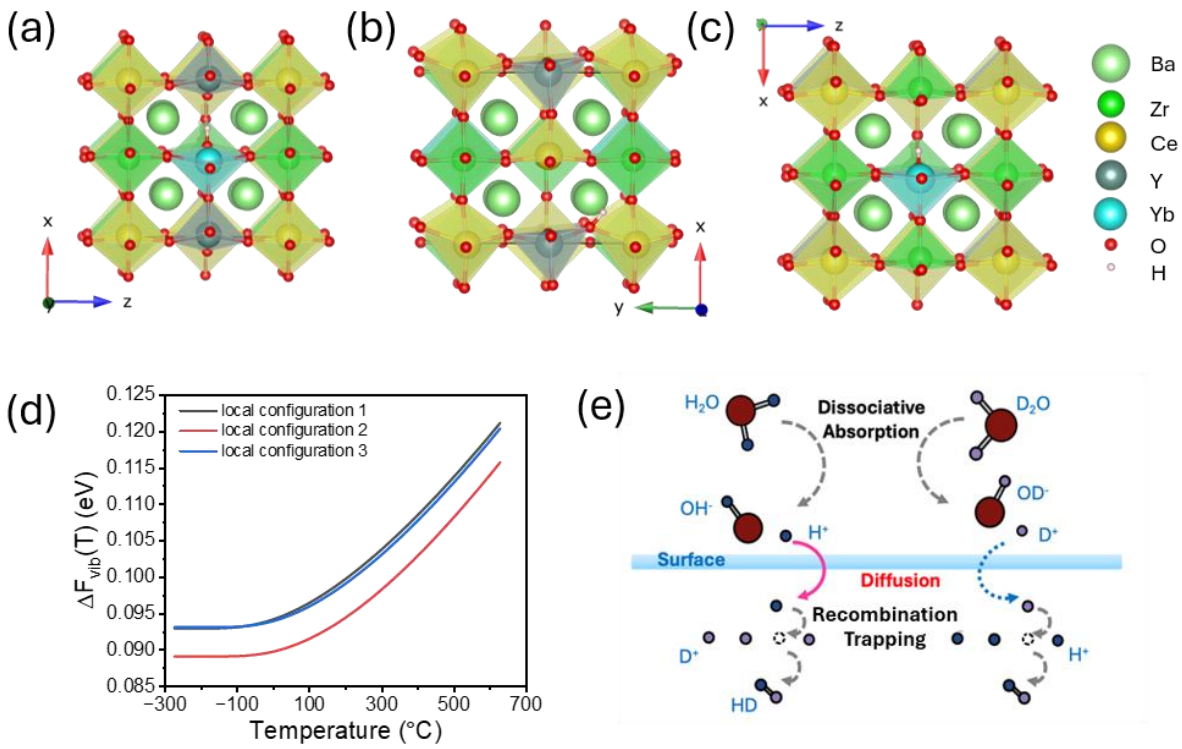

Figure 3.21. (a-c) Atomic structures of BZCYYb4411+H/D with different local dopant environments: (a) BZCYYb4411+H/D local configuration 1, where Y and Yb occupy adjacent B sites to form a Y-Yb dopant pair, and H/D is bonded to a lattice oxygen adjacent to the oxygen vacancy; (b-c) BZCYYb4411+H/D local configurations 2 and 3 without adjacent dopant pairs, where H/D is located between YO_6-YbO_6 octahedra and YbO_6-ZrO_6 octahedra, respectively. (d) temperature-dependent vibrational free-energy difference between H-containing and D-containing structures in three local BZCYYb4411 environments. (e) schematic illustration of the proposed proton exchange mechanism and asymmetric isotope exchange behavior.

A mechanistic illustration is proposed in Figure 3.21e to explain this behavior. Upon dissociative adsorption, water molecules generate surface -OH species and mobile protons (or deuterons), followed by proton diffusion and trapping at oxygen vacancies. Proton diffusion and exchange proceed more readily than deuteron migration due to the kinetic isotope effect. It can be

understood from the difference in zero-point energy between hydrogen and deuterium.[129] According to quantum mechanical considerations, a vibrating particle retains a finite zero-point energy even in its ground state, expressed as Equation 21 and Equation 22:

$$E_{O,H}=\frac{1}{2}\ \mathrm{h}\,\nu_{\mathrm{H}} \tag{21}$$

$$E_{O,D}=\frac{1}{2}\,\mathrm{h}\,\nu_{\mathrm{D}} \tag{22}$$

where represent the vibrational frequencies of hydrogen and deuterium, respectively.[127, 136] Because hydrogen has a lower mass than deuterium, it exhibits a higher vibrational frequency and therefore a larger zero-point energy. As a result, the effective migration barrier for proton transfer is reduced compared with that for deuterons, allowing proton diffusion to proceed more readily than deuteron migration. Consequently, the exchange kinetics are faster during the D_2O-to-H_2O process than H_2O-to-D_2O. Replacement of surface H by D is kinetically hindered and requires a higher activation energy. This directional dependence reflects a kinetic isotope effect governed by proton mobility and vacancy-mediated trapping.

3.3.5 Electrochemical conductivity relaxation (ECR) to probe the bulk hydration properties

To determine how these proton states contribute to macroscopic transport under hydration conditions, electrochemical conductivity relaxation (ECR) measurements were performed to probe

bulk behavior and proton migration kinetics under controlled gas-switching conditions (Figure 3.22).

At 600 °C (Figure 3.22a), the conductivity initially decreases at short times and then gradually increases until reaching equilibrium, exhibiting a non-monotonic relaxation behavior. Similar relaxation responses have been reported for proton-conducting oxides during hydration and are often described using a two-fold relaxation model involving multiple kinetic processes.[117, 133] Such behavior suggests that hydration may involve coupled proton incorporation and defect redistribution rather than a simple single-step H_2O diffusion process. The corresponding residual-sum-of-squares (RSS) contour map (Figure 3.22b) exhibits a distinct minimum centered around these values, indicating a unique and well-defined fitting solution. It should be noted that the physical interpretation of D_{iH} and D_{vH} remains model dependent. The experimental relaxation curve can be well described using the two-fold diffusion model, yielding a hydrogen-related diffusion coefficient D_{iH} =1.08×10^{-6} cm^2 s^{-1} and a vacancy-related diffusion coefficient D_{vH} =1.00×10^{-5} cm^2 s^{-1} at 600 °C. These two coefficients represent characteristic kinetic parameters associated with proton-related and vacancy-related equilibration processes during hydration, respectively, indicating that multiple processes contribute to the observed conductivity evolution. Therefore, these parameters are more appropriately regarded as effective kinetic descriptors of the coupled proton and defect re-equilibration processes during hydration rather than direct microscopic diffusion coefficients.[117]

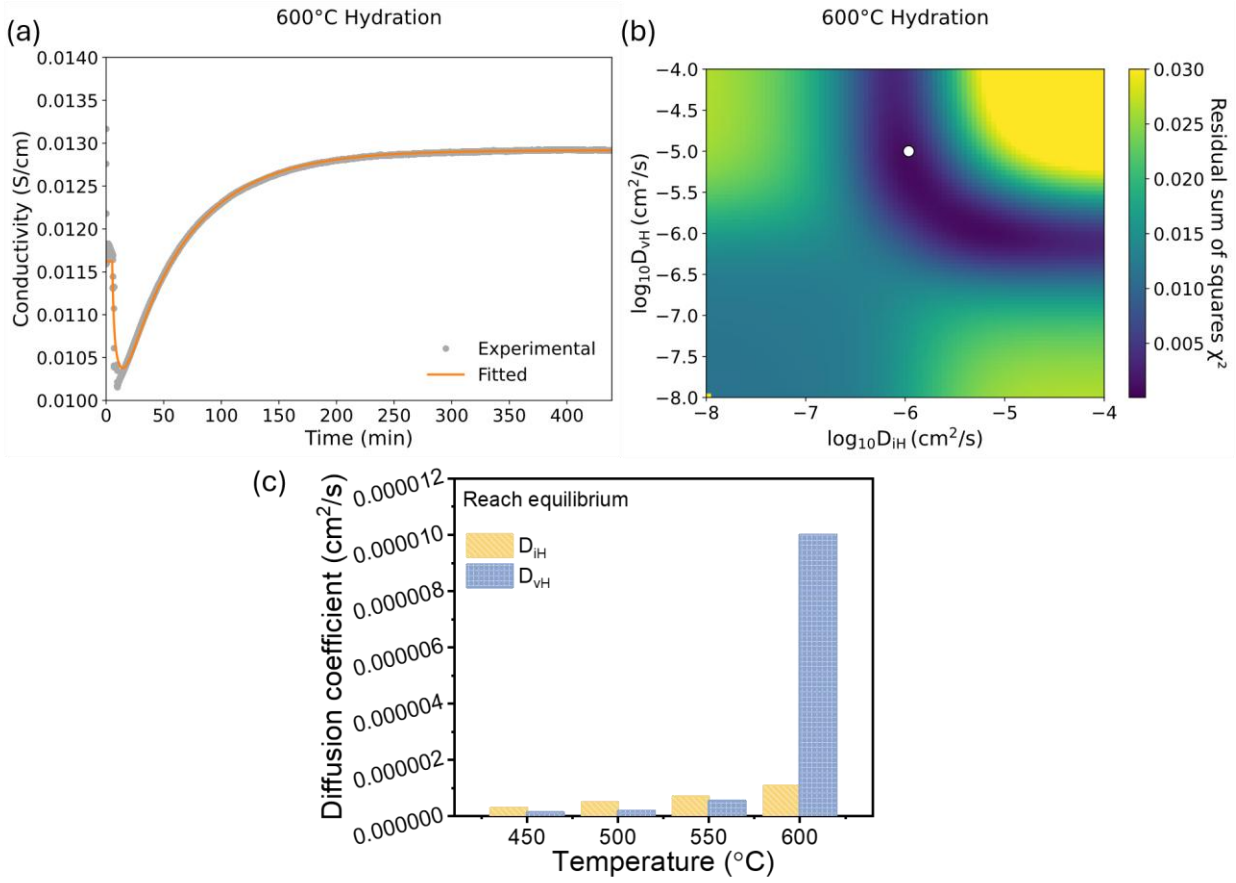

Figure 3.22. (a) Experimental and fitted ECR curves during hydration process at 600 °C, (b) the corresponding residual-sum-of-squares (RSS) contour maps for determination of the optimal diffusion coefficients at 600 °C (The white circles indicate the best-fit values of D_{iH} and D_{vH}), (c) Comparison of D_{iH} and D_{vH} at various temperatures (450 °C-600 °C).

Similar analyses were performed at 550, 500, and 450 °C (Figure 3.23). Figure 3.22c summarizes the effective diffusion coefficients extracted from the two-fold diffusion model. Both D_{iH} and D_{vH} increase with increasing temperature, indicating that the hydration process is strongly thermally activated. While D_{iH} exhibits a gradual increase from 450 to 600 °C, D_{vH} shows a much stronger temperature dependence and increases sharply at 600 °C. This behavior suggests that

defect redistribution processes become significantly faster at elevated temperatures and may contribute to the distinct non-monotonic relaxation behavior observed at 600 °C.

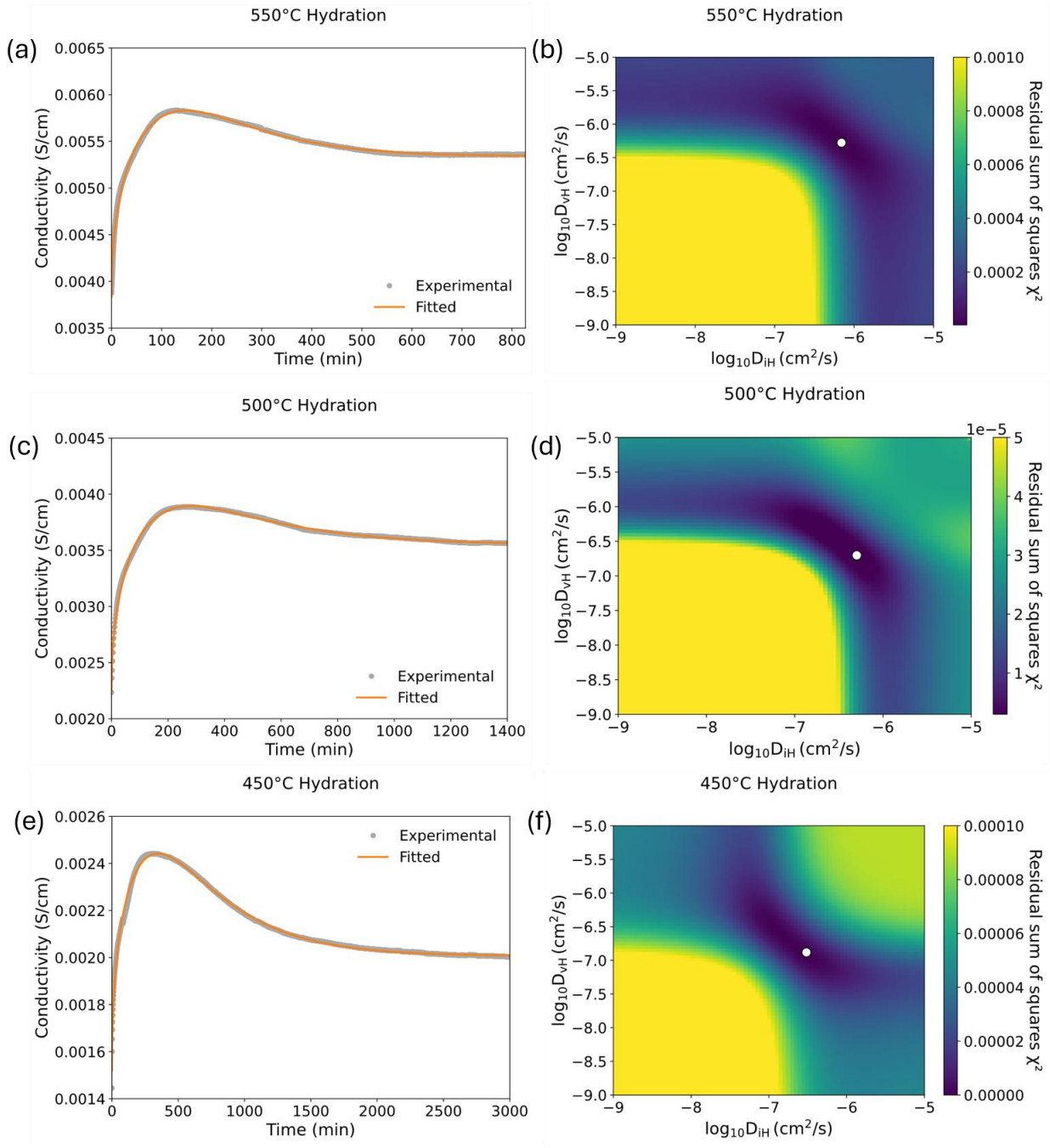

Figure 3.23. Experimental and fitted ECR curves during hydration process at (a) 550 °C, (c) 500 °C, and (e) 450 °C; the corresponding residual-sum-of-squares (RSS) contour maps for

determination of the optimal diffusion coefficients at (b) 550 °C, (d) 500 °C, and (f) 450 °C. The white circles indicate the best-fit values of D_{iH} and D_{vH}.

3.4. Conclusion

In this work, we established a quantitative operando DRIFTS-ECR-DFT framework to investigate hydration, dehydration, and H_2O/D_2O isotope-exchange processes in BZCYYb4411 proton-conducting electrolytes. Time-resolved DRIFTS measurements reveal that both hydration and dehydration follow first-order kinetics, while hydration proceeds substantially faster than dehydration, with activation energies of 35.8 and 63.7 kJ mol^{-1}, respectively. H_2O/D_2O isotope-exchange experiments reveal a clear directional dependence in proton-exchange kinetics, where the replacement of -OH by -OD proceeds more slowly than the reverse substitution of -OD by -OH. The persistence of residual -OH signals and the crossover behavior of normalized -OH and -OD intensities further demonstrate the coexistence of two proton populations: a rapidly exchanging mobile hydroxyl population and a more strongly bound proton population with substantially slower exchange kinetics. DFT calculations further reveal that D-containing configurations consistently possess lower vibrational free energies than their H-containing counterparts and that the magnitude of the isotope effect varies with the local dopant-vacancy arrangement. These results indicate that the H/D isotope effect in BZCYYb4411 is strongly dependent on the local proton environment and is not uniform throughout the lattice. Complementary ECR measurements reveal that bulk hydration kinetics cannot be described by a simple single-step H_2O diffusion process. Instead, conductivity relaxation behavior is consistent

with a two-fold diffusion model involving coupled proton-related and vacancy-related equilibration processes.

Overall, the combined DRIFTS-DFT-ECR approach establishes a quantitative platform for linking surface proton chemistry with macroscopic transport behavior and offers new insights for the rational design of next-generation protonic ceramic electrochemical devices.

Chapter 4 - Investigating Nickel-induced impact in protonic ceramic electrolytes by DRIFTS

4.1. Introduction

Proton-conducting perovskite oxides have attracted extensive attention as electrolytes for protonic ceramic electrochemical devices, including fuel cells, electrolysis cells, and catalytic membrane reactors.[11, 17, 55, 99] Their ability to conduct protons at intermediate temperatures (400-600 °C) enables efficient electrochemical energy conversion and chemical synthesis with reduced thermal losses compared with conventional oxygen-ion conductors.[57] Among the reported materials, the acceptor-doped barium zirconates with the perovskite structure, exhibit high proton conductivity and good chemical stability, making them promising candidates for practical protonic ceramic technologies.[60, 76] However, the poor sinterability of this type of protonic oxides generally requires high sintering temperatures (>1600 °C) to achieve sufficient densification. To overcome this limitation, Nickel oxide (NiO) has been widely employed as a sintering aid. The addition of a small amounts of NiO (typically 1wt%) can significantly enhance densification and promote grain growth.[137-141] For example, Tong et al. [141] demonstrated that the addition of 1 wt% NiO enabled the fabrication of fully dense (>98%) $BaCe_{0.8}Y_{0.2}O_{3-\delta}$ (BCY20) electrolytes at 1400 °C, while NiO-free samples exhibited only ~60% relative density under identical sintering conditions. The improved densification minimizes porosity and grain-boundary resistance, thereby enhancing the overall proton conductivity. Despite these well-established microstructural benefits, the influence of NiO on the fundamental hydration process and proton defect chemistry remains largely unexplored. In these materials, proton conduction originates from the hydration of oxygen vacancies, where water molecules incorporate into the lattice to form mobile hydroxyl defects according to the hydration reaction.

Therefore, understanding how the introduction of NiO affects proton incorporation, exchange, and transport during hydration is fundamentally important for elucidating proton transport mechanisms and optimizing the performance of proton-conducting electrolytes.

For example, Huang et al.[142] also reported that NiO markedly improves densification and grain growth of $Ba(Zr,Ce,Y)O_{3-\delta}$. However, they observed that NiO simultaneously suppresses bulk proton uptake and reduces the effective acceptor concentration. Specifically, thermogravimetric analysis showed that 1 wt% NiO reduced the proton uptake by approximately 50%. Wen *et al.*[137] also reported that increasing the NiO content from 2 to 5 mol% decreased the hydration saturation limit from approximately 0.14 to 0.09 mol fraction (≈35% reduction). They further attributed this behavior to the formation of Yb-Ni point-defect clusters, which suppresses the hydration of oxygen vacancies and consequently reduces the effective proton concentration.[137] While these studies have established that Ni alters bulk hydration behavior and proton defect chemistry, they provide little mechanistic insight into the dynamic evolution of surface hydroxyl species, where hydration, proton exchange, and incorporation are initiated. Consequently, the influence of Ni on surface proton exchange kinetics and reaction pathways remains largely unexplored, and direct experimental evidence is still lacking. Addressing this challenge requires an operando, surface-sensitive spectroscopic technique capable of directly monitoring hydroxyl species under realistic operating conditions.

DRIFTS)

provides surface-sensitive method for probing hydroxyl species and surface intermediates in oxide materials under realistic conditions.[37, 81, 103, 143, 144]. Recently, our group successfully developed a custom *operando* DRIFTS platform capable of operating at high temperatures (up to 750 °C) under steam-containing atmospheres and applied electrochemical bias.[103] In addition, our

recent review systematically summarized and analyzed the application of DRIFTS in protonic ceramic cells, with particular emphasis on probing surface proton processes in proton-conducting electrolytes.[111] Despite these advances, direct spectroscopic investigations of how NiO addition influences proton incorporation, hydroxyl evolution, and isotope exchange kinetics in proton-conducting electrolytes are still lacking. This knowledge gap limits the mechanistic understanding of the interaction between Ni and proton transport, motivating the present operando DRIFTS study.

Here, we investigate the influence of NiO on hydration behavior and surface proton dynamics in $BaZr_{0.1}Ce_{0.7}Y_{0.1}Yb_{0.1}O_{3-\delta}$ using *operando* DRIFTS spectroscopy. By comparing pristine electrolyte (BZCYYb) and 1 wt% NiO-added one (N-BZCYYb), we directly visualize the dynamic evolution of hydroxyl species during hydration, dehydration, and H_2O/D_2O isotope exchange over a wide intermediate-temperature range. DFT calculations further suggest that Ni incorporation perturbs local oxygen coordination and hydroxyl energetics, providing an atomistic basis for the experimentally observed kinetic retardation. The results provide direct spectroscopic evidence that Ni regulates surface proton dynamics beyond its conventional role as a sintering aid, revealing an overlooked coupling between electrolyte processing and proton chemistry.

4.2. Materials and Methods

4.2.1 Material synthesis

The $BaZr_{0.1}Ce_{0.7}Y_{0.1}Yb_{0.1}O_{3-\delta}$ (BZCYYb1711) electrolyte powders were synthesized via the wet-chemistry method. Y_2O_3 and Yb_2O_3 were first dissolved in 20 wt % diluted HNO_3 under continuous stirring at 100 °C to form transparent yttrium and ytterbium nitrate solutions. Subsequently, stoichiometric amounts of $Ba(NO_3)_2$, $Ce(NO_3)_3 \cdot 6H_2O$, and zirconyl nitrate solution (35 wt % in diluted nitric acid) was added to the above solution. Citric acid (CA) and ethylenediaminetetraacetic acid (EDTA) were introduced as the complexing and chelating agents

with a molar ratio of CA:EDTA:total metal cations = 2:2:1. The precursor solution was stirred at room temperature for 3 h to ensure complete complexation, after which the pH was adjusted to approximately 9 using aqueous NH_4OH. The solution was then heated to 250 °C to induce gel formation, followed by drying at 175 °C for 24 h. The obtained precursor was calcined in air at 1450 °C for 5 h to produce BZCYYb1711 powder. Two types of BZCYYb1711 powder samples were investigated. One was pristine BZCYYb1711, while the other contained 1 wt% NiO (N-BZCYYb). For the Ni-containing sample, NiO was added directly to the precursor mixture during the wet-chemistry synthesis prior to gel formation.

4.2.2 Characterizations

Operando diffuse reflectance infrared Fourier transform spectroscopy (DRIFTS) experiments were performed using a high-temperature DRIFTS cell coupled with a Fourier transform infrared spectrometer. The powders were placed on the sample holder inside the high-temperature reaction chamber for DRIFTS measurements. A K-type thermocouple was positioned approximately 1 cm beneath the sample holder to monitor and maintain a uniform temperature distribution during the experiments. Prior to measurements, the samples were heated from room temperature to 600 °C at a rate of 2 °C min^{-1}. The temperature was then held at 600 °C for approximately 2 h under flowing dry Ar to ensure complete removal of residual moisture to establish a dehydrated reference state.

Time-resolved DRIFTS was employed to investigate hydration and dehydration processes under well-defined temperature and gas-switching conditions (Figure 4.1).[129] The DRIFTS spectra were collected using a Thermo Scientific Nicolet iS50 FTIR spectrometer equipped with a customized Praying Mantis™ high temperature reaction chamber (Harrick Scientific Products). Spectra were recorded over the range of 4000-500 cm^{-1} with a resolution of 8 cm^{-1}, averaging 32

scans for each measurement to ensure a high signal-to-noise ratio. The background spectrum was collected using standard KBr powder prior to each experiment. This background was then subtracted from the sample spectra to remove system and environmental contributions. During all DRIFTS measurements, the heating and cooling rates were controlled at around 2 °C min^{-1} to ensure thermal and ceramic cell stability. At each testing temperature, the system was stabilized for approximately 30 min before data collection to ensure thermal equilibrium.

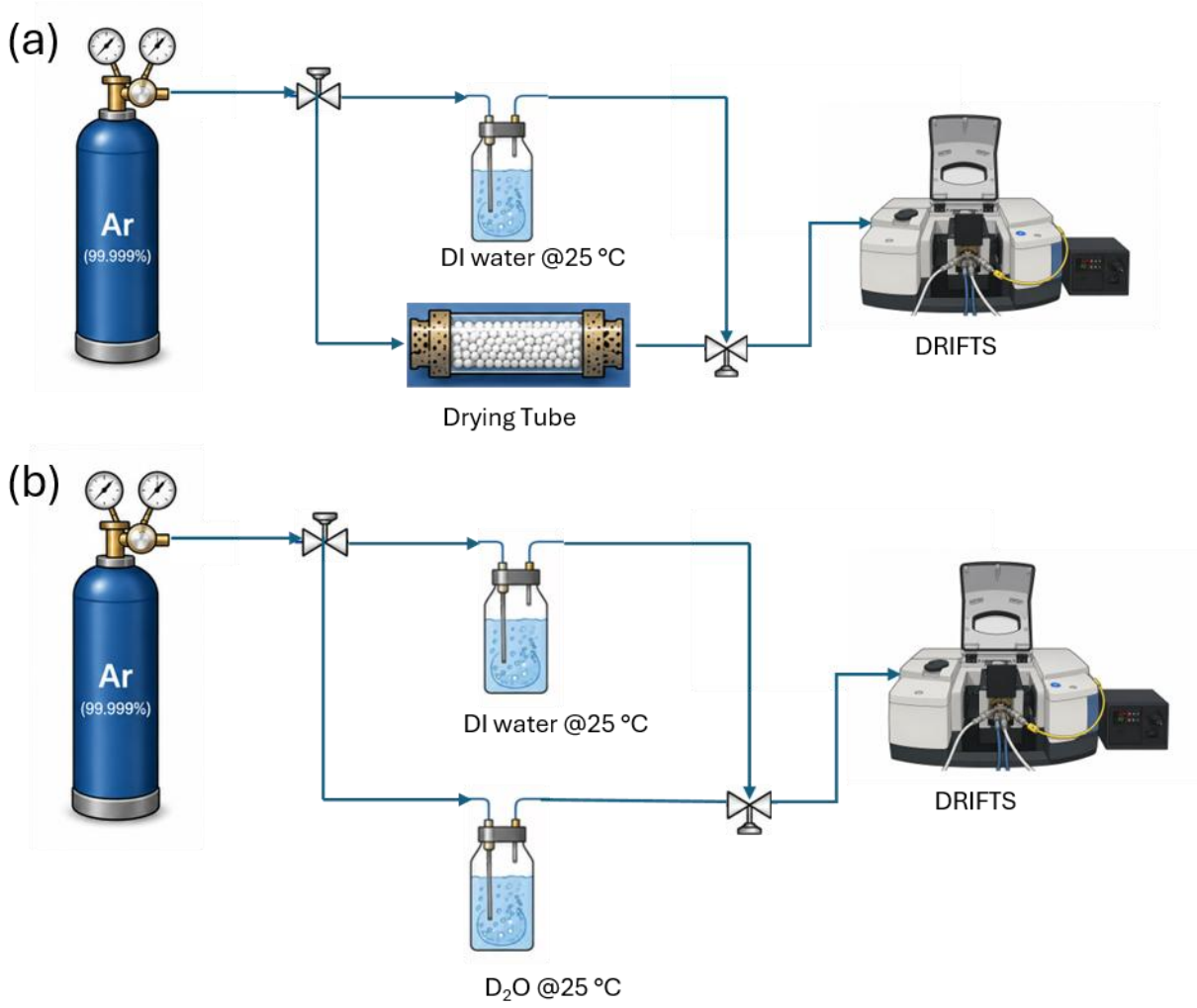

Figure 4.1. Controlled Gas-switching setup before DRIFTS for (a) hydration/dehydration experiments and (b) isotope exchange experiments.

The electrolyte surface was directly exposed to the gas atmosphere and positioned normal to the incident infrared beam to ensure stable diffuse reflectance signal collection. Hydration experiments were initiated by switching the gas feed from humidified Ar containing dry Ar (40 sccm) to 3 % H_2O (40 sccm). Water vapor was introduced into the reactor using an H_2O bubbler. Gas switching was conducted without interrupting spectral acquisition, allowing continuous monitoring of the transient response of surface hydroxyl species. Dehydration experiments were initiated by switching the gas feed from humidified Ar containing 3 % H_2O (40 sccm) to dry Ar (40 sccm).

DRIFTS spectra were collected as a function of time following each gas switch, with particular attention to the evolution of O-H stretching vibrations in the 3000-3600 cm^{-1} region, centered at approximately 3400 cm^{-1}. The normalized intensity of the O-H stretching band was used as a semi-quantitative measure of surface hydroxyl coverage. Time-dependent changes in band intensity were analyzed to extract characteristic hydration and dehydration time constants, providing insight into surface hydration exchange kinetics. Experiments were performed at temperatures between 500 and 600 °C to evaluate the influence of temperature on hydration dynamics.

To further probe protonic species and distinguish surface and sub-surface hydration processes, H_2O/D_2O isotope exchange experiments were conducted using the same DRIFTS platform. The sample was first equilibrated under a humidified Ar atmosphere containing either 3 % H_2O or 3 % D_2O at the target temperature. Isotope exchange was then triggered by switching the gas feed between H_2O/Ar and D_2O/Ar, while maintaining a constant total flow rate.

Time-resolved DRIFTS spectra allowed quantitative comparison of exchange rates between pristine BZCYYb1711 and Ni-added samples. Differences in the crossover time between

-OH and -OD intensities and the time required to reach equilibrium were used to evaluate the influence of nickel on proton exchange kinetics.

The crystal structures of the electrolyte samples were determined using XRD. XRD Rietveld refinement was conducted using the GSAS-II software package.[118] The morphology of reduced BZCYYb4411 was examined using TEM and EDS (TALOS F200X, Thermo Fisher Scientific).

4.2.3 DFT calculations

DFT calculations were performed using the Vienna Ab initio Simulation Package (VASP).[119-121] Spin polarization was included for all calculations. The projector augmented wave (PAW) method was employed to describe the core-valence interaction.[122] For Ba, Zr, and Y, their shallow semicore 5s, 4s, and 4s states are explicitly included as valence electrons. The Ce 4f states were included as valence states, whereas the filled Yb 4f states were treated as the frozen core. DFT+U treatments with Ueff = 5 eV and 6 eV were applied to the 4f states of Ce and Yb, respectively.[123, 124, 145] The generalized gradient approximation Perdew-Burke-Ernzerhof (GGA-PBE) functional was used to describe the exchange-correlation functional.[125, 126] The BZCYYb lattice was approximated using a 2×2×2 supercell derived from cubic $BaCeO_3$. The B-site Ce atoms were then substituted with one Zr, Y, and Yb atom, yielding $Ba_8Zr_1Ce_5Y_1Yb_1O_{24}$, mimicking the atomic ratio of BZCYYb1711.

Four B-site cation configurations were considered, where Zr and Y occupy the same site in every structure, while Yb exchanges positions with Ce, including Yb adjacent to both Zr and Y (Figure 4.2a), Yb separated from Zr and Y (Figure 4.2b), Yb adjacent to Zr but far from Y (Figure 4.2c), and Yb adjacent to Y but far from Zr (Figure 4.2d). The lattice in Figure 4.2a represents a

Zr-Yb-Y clustered configuration with the largest average bond length distortion. The B-site cations are the most dispersed in Figure 4.2b.

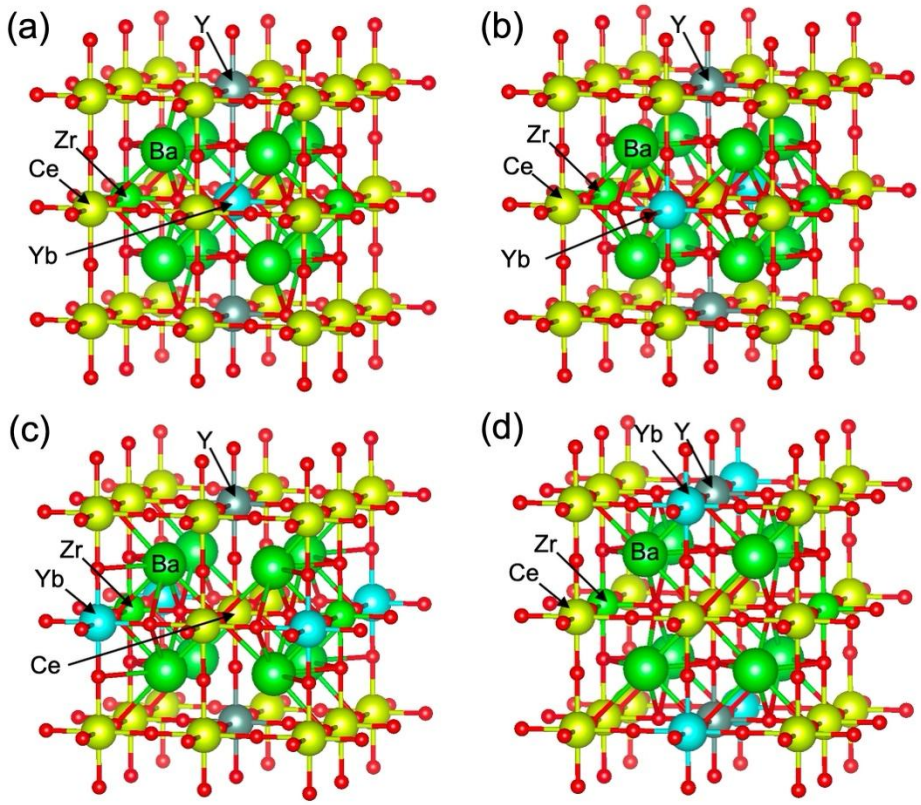

Figure 4.2. Schematic lattice of BZCYYb1711 displaying four B-site cation arrangements. Color scheme: Zr (small green), Ce (yellow), Y (grey), and Yb (turquoise). The Ba and O atoms are displayed in large green spheres and red spheres, respectively. The arrows are used to indicate the location of each set of B-site cations.

4.3. Results and Discussion

4.3.1 Phase and microstructures of pristine and 1 wt% NiO-added BZCYYb1711

To evaluate whether the addition of NiO induces structural changes in BZCYYb, Rietveld refinement and electron microscopy analyses were performed. As shown in Figure 4.3a, pristine

BZCYYb1711 is well indexed to a single-phase cubic perovskite structure with the $Pm\bar{3}m$ space group, yielding a lattice parameter of a =b =c = 4.3025(4) Å. The N-BZCYYb similarly retains the cubic perovskite structure without an obvious crystalline NiO secondary phase detectable by XRD (Figure 4.3b). Compared with pristine BZCYYb1711, the 1 wt% NiO-added sample exhibits a slight left or right shift of the characteristic diffraction peak toward higher 2θ (Figure 4.4), consistent with the decreased lattice parameter obtained from Rietveld refinement (a = b = c = 4.2989(7) Å). This modest lattice contraction suggests that Ni may partially interact with or be incorporated into the perovskite lattice, rather than remaining entirely as a separate crystalline NiO phase. The refined average crystal structures derived from the Rietveld analysis are inserted in Figure 4.3a & b.

The local structure and elemental distribution of the 1 wt% NiO-added BZCYYb1711 were further examined by TEM. Figure 4.3e shows a well-crystallized BZCYYb1711 particle, while the selected-area electron diffraction pattern acquired along the [001] zone axis (Figure 4.3f) exhibits sharp and well-defined diffraction spots. The reflections can be indexed to the cubic perovskite structure, including the (110), (200), and (310) planes, with d-spacings of 3.042, 2.151, and 1.361 Å, respectively, consistent with the XRD Rietveld refinement results (a=4.2989 Å). High-resolution TEM imaging (Figure 4.3g-i) further reveals highly ordered lattice fringes, confirming the high crystallinity of the NiO-added sample. STEM-EDS particlessl mapping (Figure 4.3j) shows that Ba, Ce, Y, Yb, and Zr are broadly distributed throughout the examined particle. Notably, the Ni signal is also distributed across the BZCYYb1711 particle without obvious formation of large Ni-rich segregated domains, further confirming that NiO has been doped into the B site of the electrolyte.

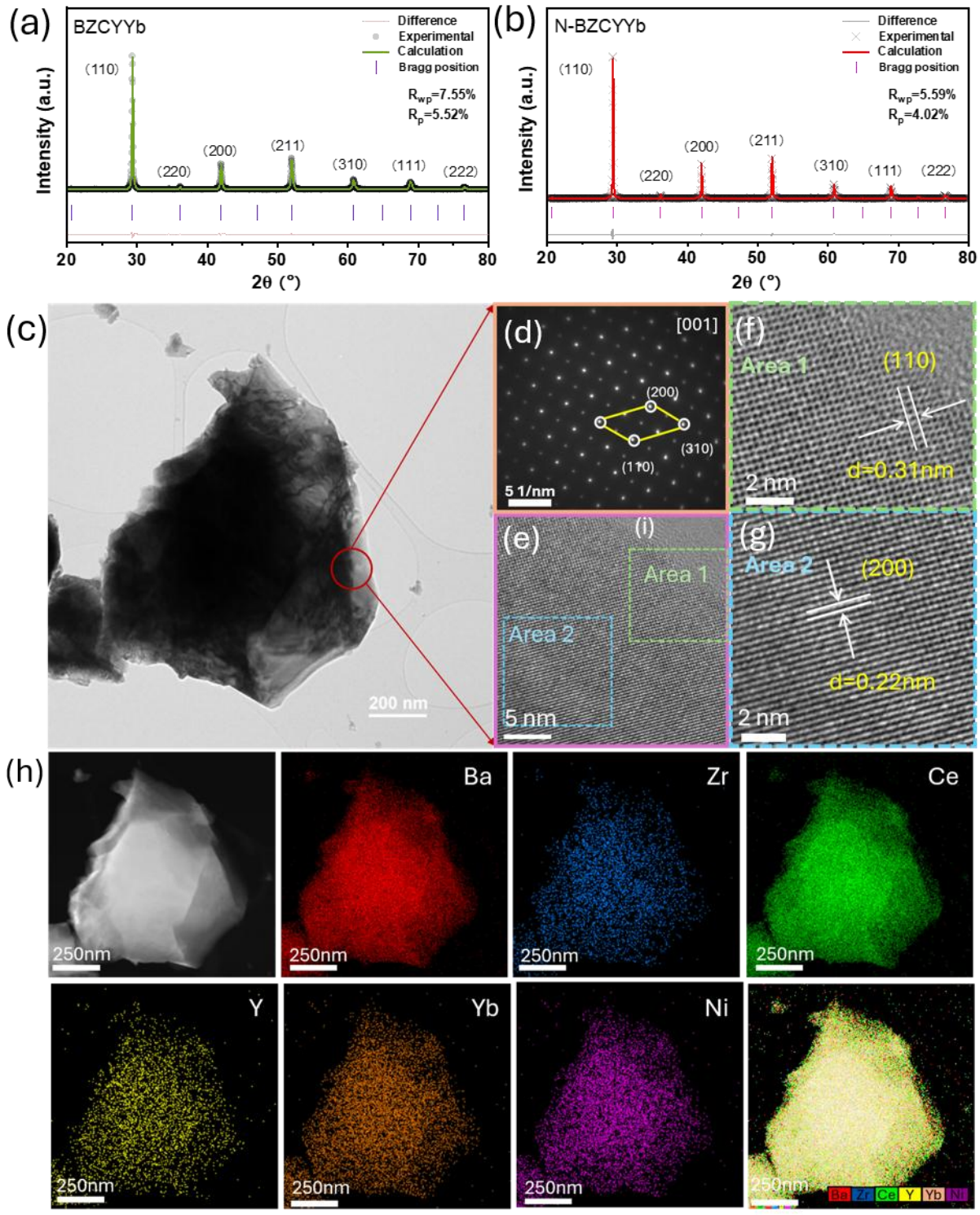

Figure 4.3. Crystal structure and microstructural characterization of pristine and N-BZCYYb. (a) Rietveld refinement of pristine BZCYYb. (b) Rietveld refinement of N-BZCYYb**.** Insets show the refined average cubic perovskite structure. (c) Refined average cubic perovskite structure of

pristine BZCYYb derived from the Rietveld refinement. (d) Refined average cubic perovskite structure of N-BZCYYb derived from the Rietveld refinement. (e) Bright-field TEM image of N-BZCYYb. (f) Selected-area electron diffraction (SAED) pattern indexed along the [001] zone axis. (g) High-resolution TEM image. (h) Enlarged HRTEM image from Area 1 showing lattice fringes with an interplanar spacing of approximately 0.31 nm, corresponding to the (110) plane. (i) Enlarged HRTEM image from Area 2 showing lattice fringes with an interplanar spacing of approximately 0.22 nm, corresponding to the (200) plane. (j) HAADF-STEM image and corresponding EDS elemental maps of Ba, Ce, Ni, Y, Yb, and Zr for the **N**-BZCYYb sample, showing a homogeneous elemental distribution.

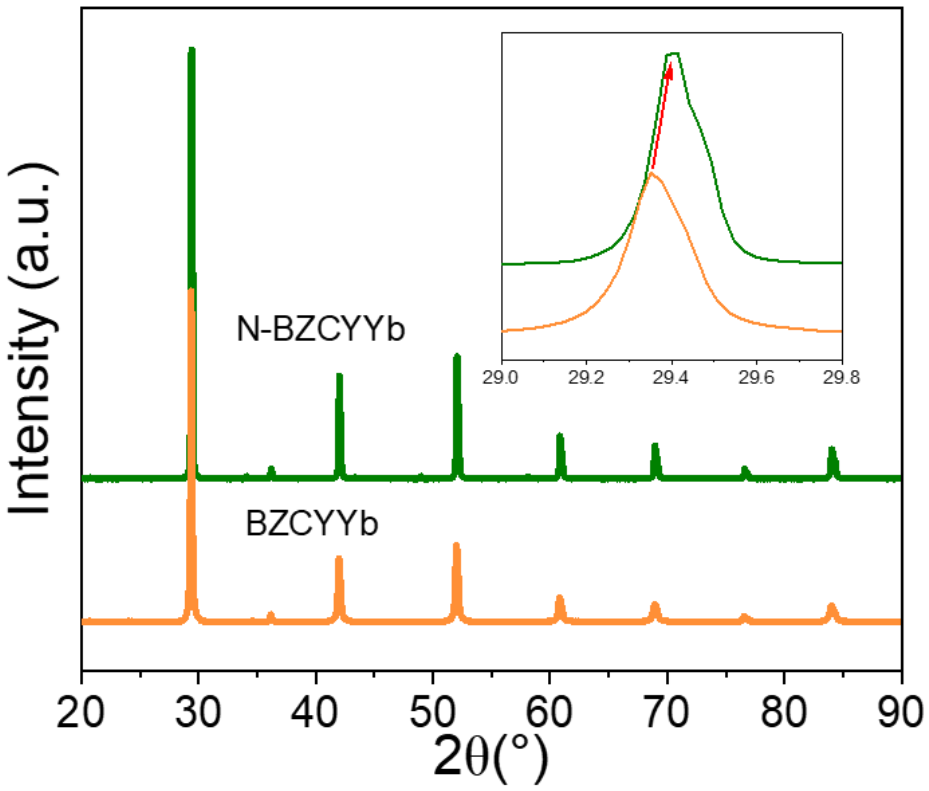

Figure 4.4. X-ray diffraction (XRD) pattern of the pristine BZCYYb and N-BZCYYb electrolyte.

4.3.2 Hydration & dehydration behavior

The hydration and dehydration behavior of pristine BZCYYb and N-BZCYYb were investigated using time-resolved *operando* DRIFTS following the switch from humidified Ar to dry Ar at 500 and 600°C. Figure 4.5a shows the hydration behavior of pristine BZCYYb at 500 °C. Upon exposure to humidified Ar, a broad O-H stretching band centered at approximately 3356 cm^{-1} rapidly develops and continuously increases before reaching a quasi-equilibrium state (~15 min). This evolution reflects continuous water dissociation and proton incorporation, leading to the progressive formation of hydroxyl species. A similar O-H stretching band is observed for the N-BZCYYb sample at approximately 3407 cm^{-1} (Figure 4.5b), but the band reaches equilibrium after approximately 50 min. A similar hydration behavior is observed at 600 °C for both samples (Figure 4.6). The hydration equilibrium time of N-BZCYYb is approximately 2.5 times longer than that of pristine BZCYYb, while the dehydration equilibrium time is approximately 2 times longer. These results demonstrate that Ni significantly retards both the hydration and dehydration processes, resulting in substantially slower equilibration dynamics.

As dehydration proceeds, the intensity of the O-H band continuously decreases and reaches a nearly steady spectral profile within approximately 90 min (Figure 4.5c). The O-H band of N-BZCYYb is centered at a slightly higher wavenumber (~3407 cm^{-1}) compared with BZCYYb (3356 cm^{-1}) and reaches equilibrium after approximately 250 min. It should be noted that the time required for N-BZCYYb to reach equilibrium is more than 2.7 times that of pristine BZCYYb (Figure 4.5c-d). In addition, the O-H band of the Ni-added sample remains more symmetric throughout the dehydration process. The corresponding 2D contour plots of the operando DRIFTS

spectra (Figure 4.7-Figure 4.8) provide a more intuitive visualization of the spectral evolution during hydration and dehydration.

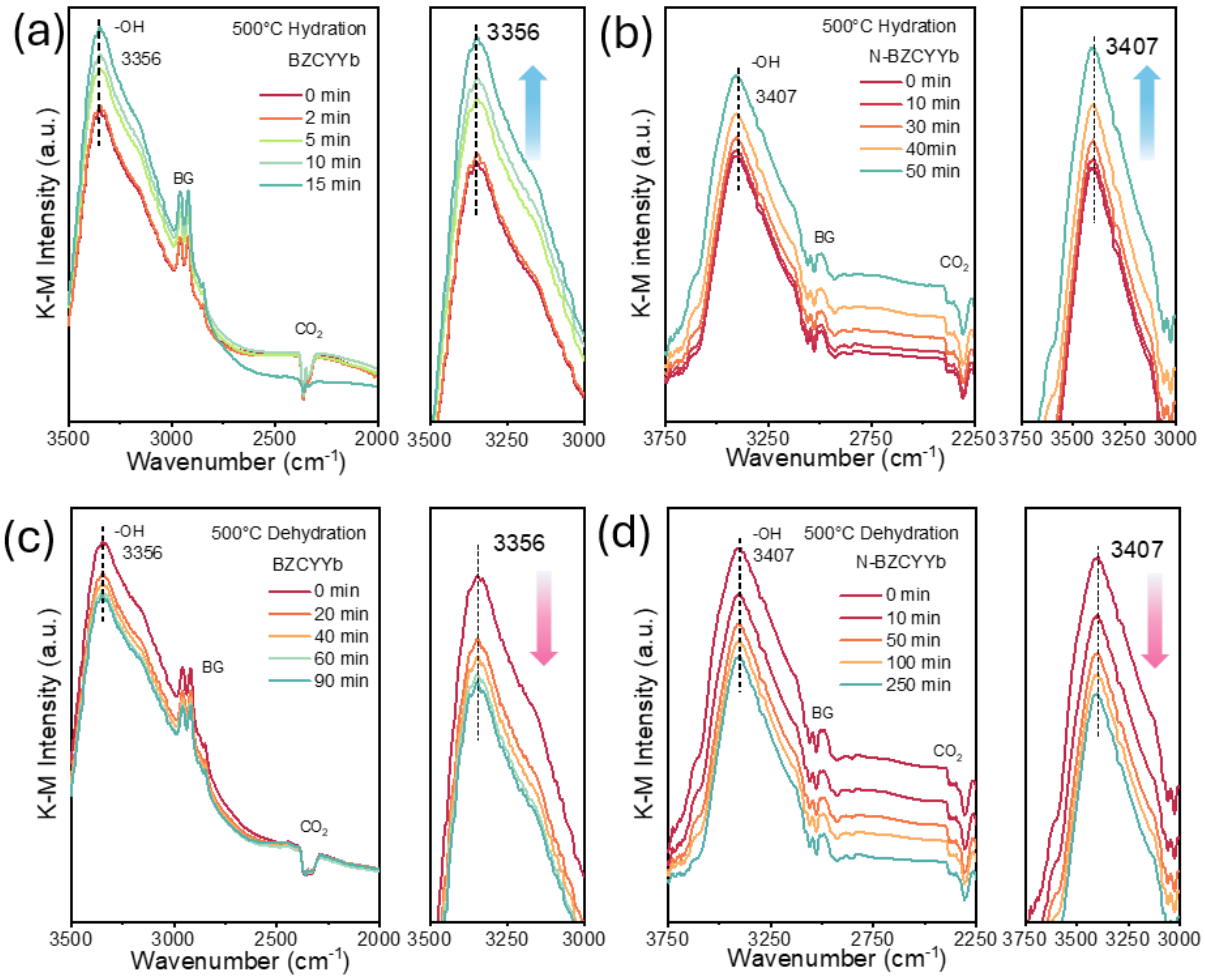

Figure 4.5. Time-resolved operando DRIFTS spectra of (a) pristine BZCYYb during hydration at 500 °C, (b) N-BZCYYb during hydration at 500 °C, (c) N-BZCYYb during dehydration at 600 °C, (d) pristine BZCYYb during dehydration at 500 °C, and (h) N-BZCYYb1711 during dehydration at 500 °C.

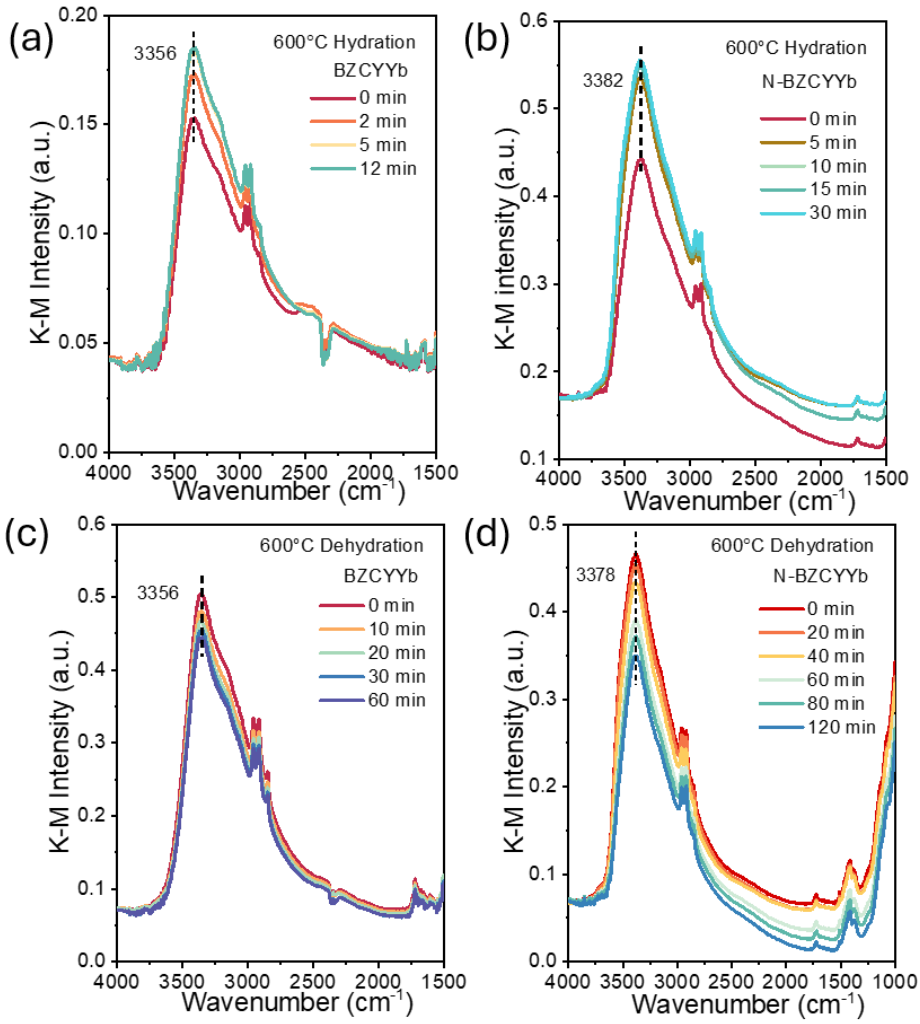

Figure 4.6. Time-resolved operando DRIFTS spectra of (a) pristine BZCYYb during hydration at 600 °C, (b) N-BZCYYb during hydration at 600 °C, (c) N-BZCYYb during dehydration at 600 °C, (d) pristine BZCYYb during dehydration at 600 °C, and (h) N-BZCYYb during dehydration at 600 °C.

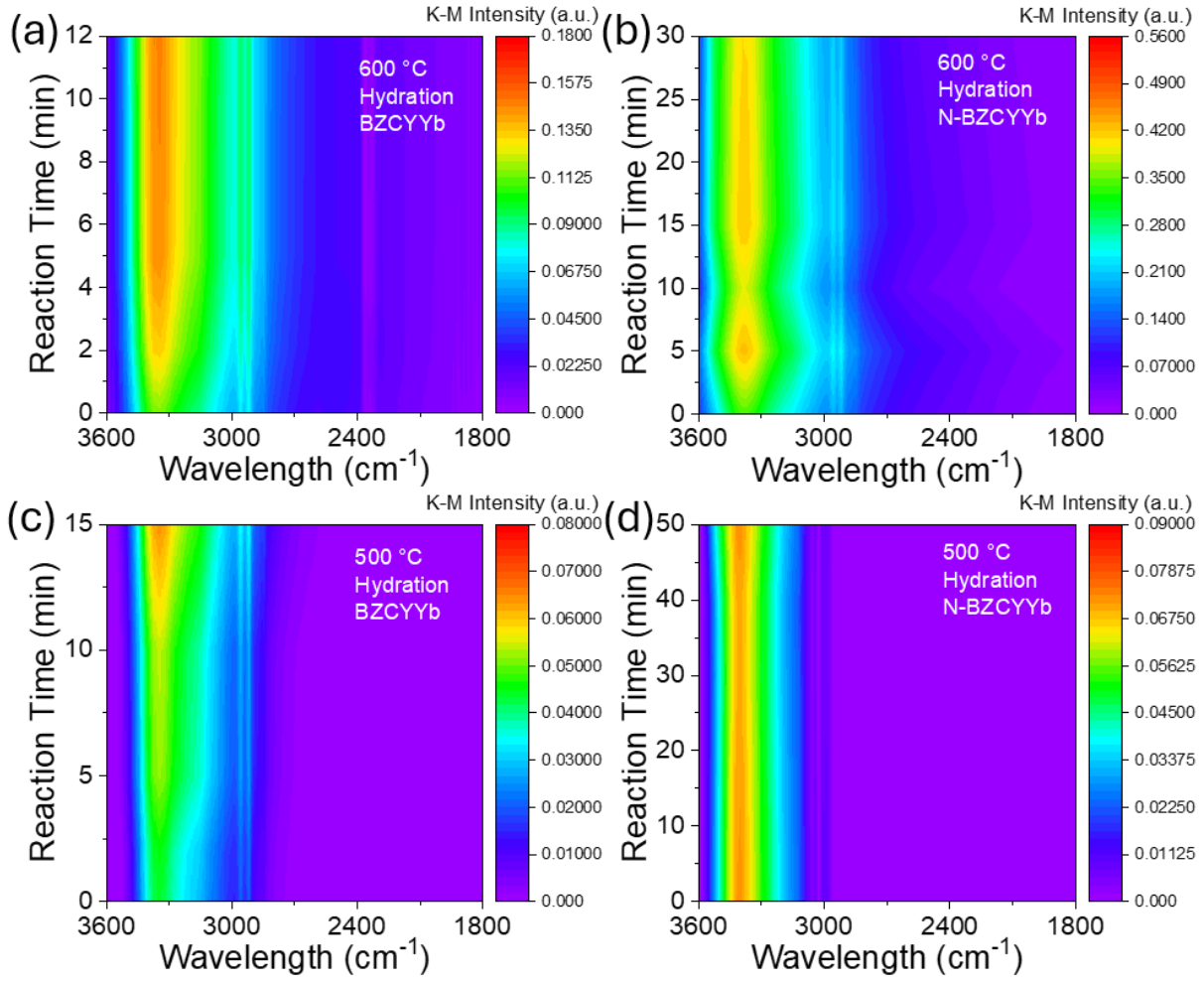

Figure 4.7. Time-resolved operando DRIFTS investigation of hydration in pristine BZCYYb and N-BZCYYb. (a) 2D contour plot of operando DRIFTS spectra for pristine BZCYYb at 600 °C. (b) 2D contour plot of operando DRIFTS spectra for N-BZCYYb at 600 °C. (c) 2D contour plot of operando DRIFTS spectra for pristine BZCYYb at 500 °C. (d) 2D contour plot of operando DRIFTS spectra for N-BZCYYb at 500 °C.

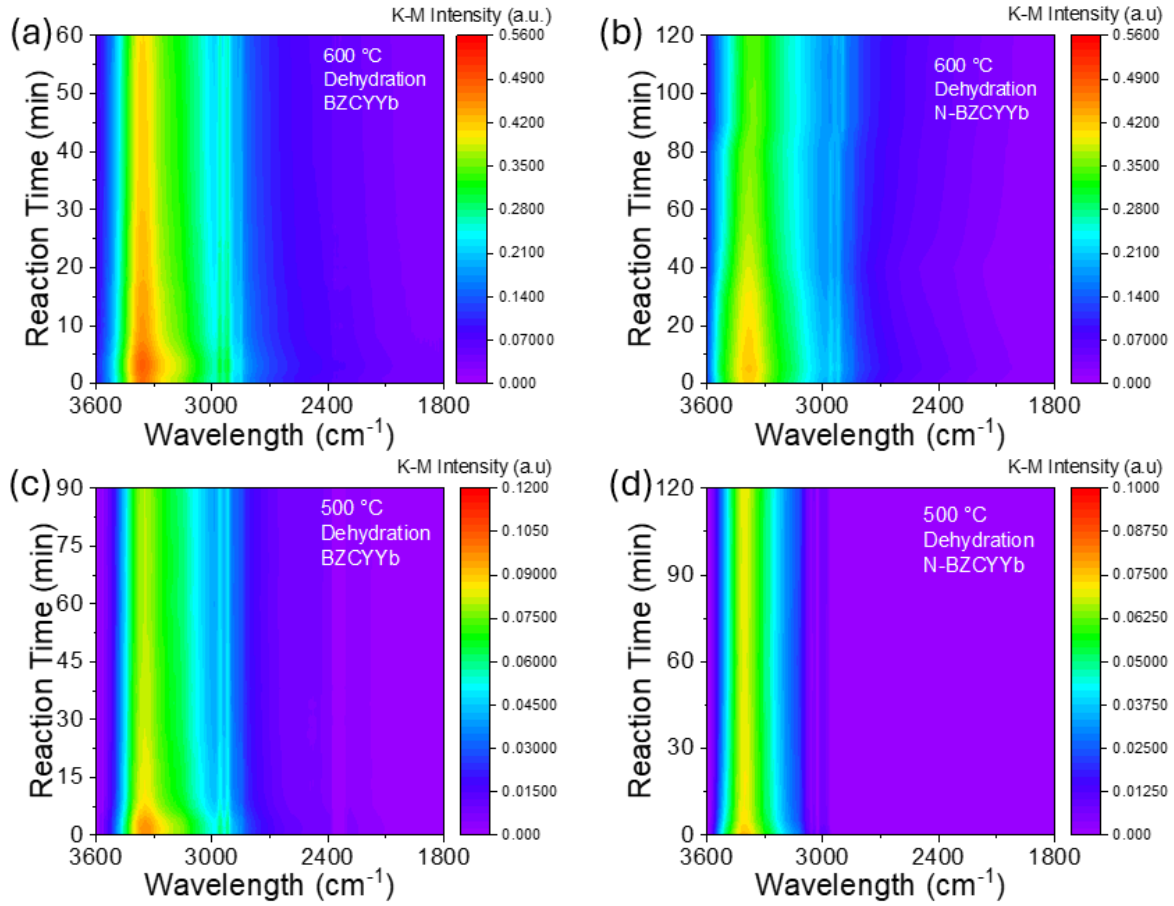

Figure 4.8. Time-resolved operando DRIFTS investigation of dehydration in pristine BZCYYb and N-BZCYYb. (a) 2D contour plot of operando DRIFTS spectra for pristine BZCYYb at 600 °C. (b) 2D contour plot of operando DRIFTS spectra for N-BZCYYb at 600 °C. (c) 2D contour plot of operando DRIFTS spectra for pristine BZCYYb at 500 °C. (d) 2D contour plot of operando DRIFTS spectra for N-BZCYYb at 500 °C.

4.3.3 Proton-deuteron exchange dynamics

To directly probe the influence of Ni on surface proton exchange dynamics, DRIFTS measurements were performed during H_2O/D_2O isotope exchange at 500 °C.[129] As shown in Figure 4.9a-b, upon switching the atmosphere from H_2O to D_2O, the O-H stretching band gradually

decreased, accompanied by the simultaneous growth of the O-D band, indicating the continuous replacement of surface hydroxyl species by deuteroxyl species. Notably, the evolution of the vibrational bands proceeded noticeably more slowly in the Ni-added sample. The time required to reach isotope exchange equilibrium for N-BZCYYb was approximately 5.4 times longer than that of pristine BZCYYb at 500 °C. The reverse isotope exchange ($D_2O \rightarrow H_2O$) at 500 °C are shown in Figure 4.9c-d.There is a slower increase in the O-H band and a slower decrease in the O-D band for N-BZCYYb. The equilibration time of N-BZCYYb was approximately four times longer than that of pristine BZCYYb, indicating that the kinetic retardation induced by Ni is independent of the isotope exchange direction. Similar trends were also observed at 600 and 450 °C (Figure 4.10-Figure 4.11), demonstrating that Ni consistently suppresses proton/deuteron exchange kinetics over the investigated temperature range.

To quantitatively compare the exchange behavior, the normalized intensities of the O–H and O-D bands were extracted as a function of time (Figure 4.9e and Figure 4.12). During $H_2O \rightarrow D_2O$ exchange, pristine BZCYYb1711 exhibited a rapid decrease in O-H intensity accompanied by a rapid increase in O-D intensity, whereas both processes became significantly slower after Ni addition. Likewise, during $D_2O \rightarrow H_2O$ exchange, the recovery of O-H species and the disappearance of O-D species were both delayed in the Ni-added sample. Interestingly, the normalized O-H and O-D intensities exhibit distinct crossover points for the two samples at each temperature during the isotope exchange process. For example, the crossover occurs at approximately 40 min at 600 °C, 63 min at 500 °C, and 70 min at 450 °C. As the temperature decreases, the crossover is progressively delayed.

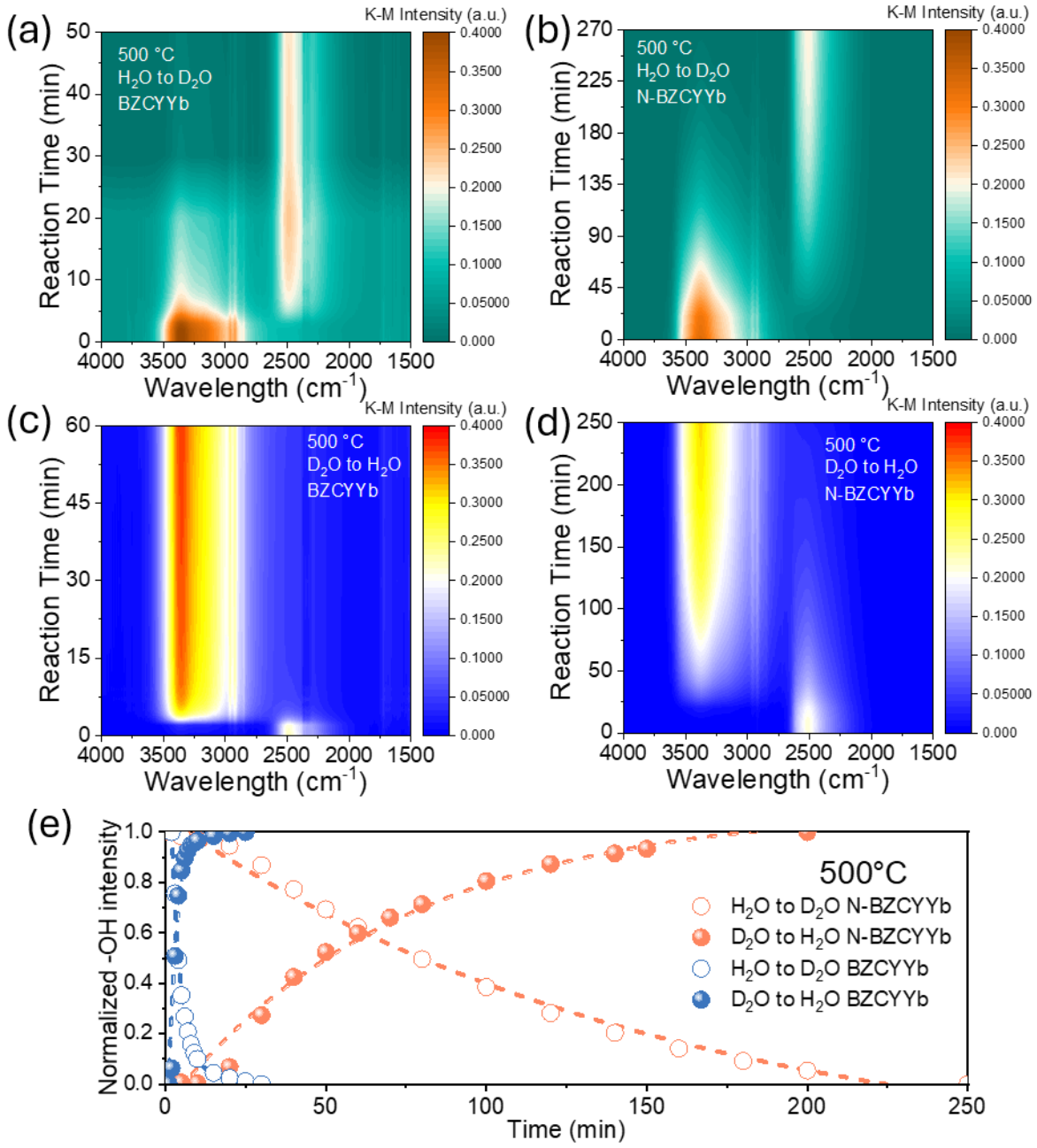

Figure 4.9. Time-resolved operando DRIFTS investigation of proton/deuteron exchange in pristine and N-BZCYYb. (a) 2D contour plot of operando DRIFTS spectra during $H_2O \rightarrow D_2O$ isotope exchange for pristine BZCYYb at 500 °C. (b) 2D contour plot of operando DRIFTS spectra during $H_2O \rightarrow D_2O$ isotope exchange for N-BZCYYb at 500 °C. (c) 2D contour plot of operando DRIFTS spectra during $D_2O \rightarrow H_2O$ isotope exchange for pristine BZCYYb at 500 °C. (d) 2D contour plot

of operando DRIFTS spectra during $D_2O \rightarrow H_2O$ isotope exchange for N-BZCYYb at 500 °C. (e) Normalized O-D band intensity during $D_2O \rightarrow H_2O$ isotope exchange.

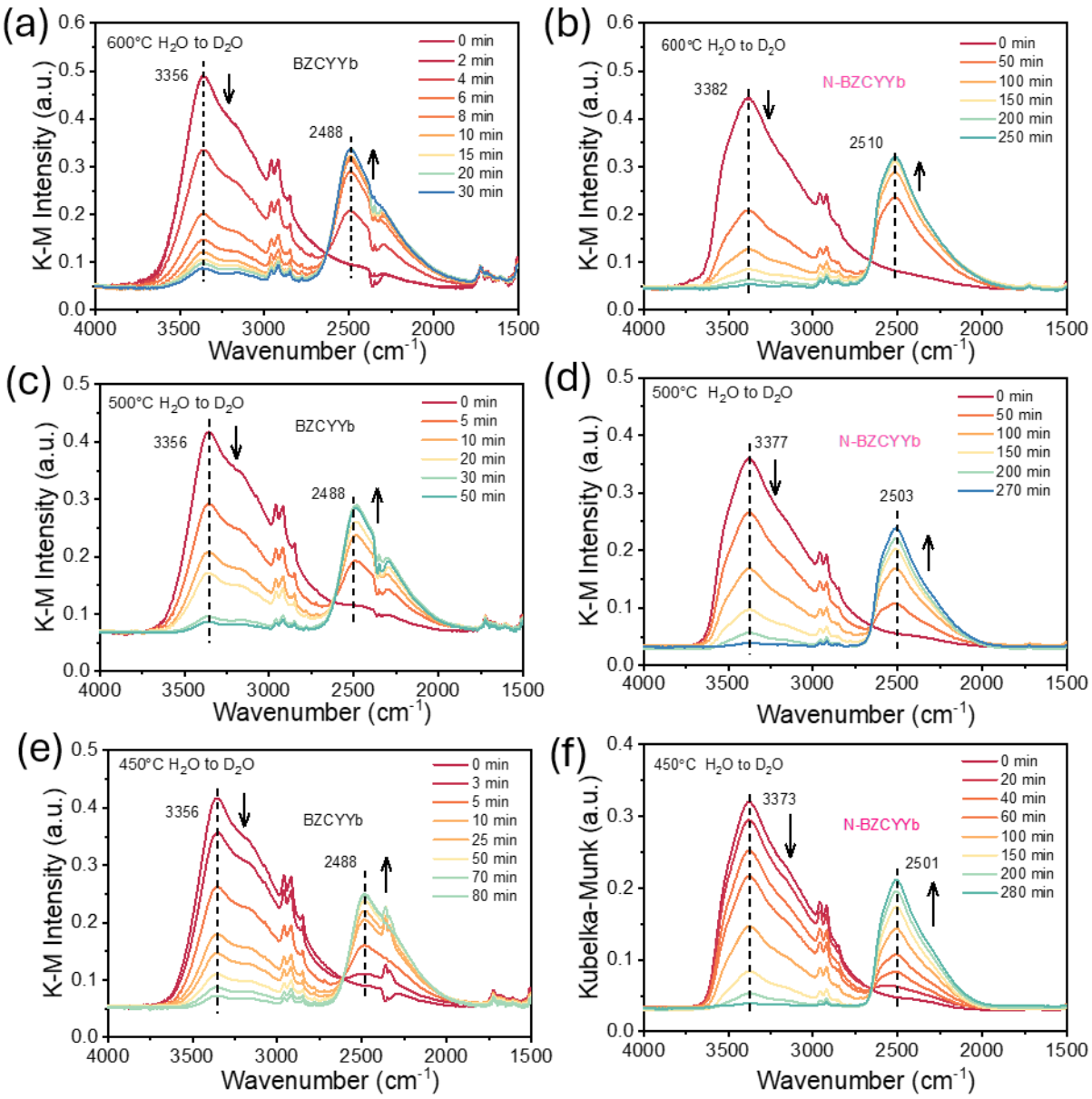

Figure 4.10. Time-resolved operando DRIFTS investigation of proton/deuteron exchange in pristine and N-BZCYYb. DRIFTS spectra (a) during $H_2O \rightarrow D_2O$ isotope exchange for pristine BZCYYb1711 at 600 °C. (b) DRIFTS spectra during $H_2O \rightarrow D_2O$ isotope exchange for N-BZCYYb at 600 °C. (c) during $H_2O \rightarrow D_2O$ isotope exchange for pristine BZCYYb at 500 °C. (d)

DRIFTS spectra during $H_2O \rightarrow D_2O$ isotope exchange for N-BZCYYb at 500 °C. (e) during $H_2O \rightarrow D_2O$ isotope exchange for pristine BZCYYb at 450 °C. (f) DRIFTS spectra during $H_2O \rightarrow D_2O$ isotope exchange for N-BZCYYb at 450 °C.

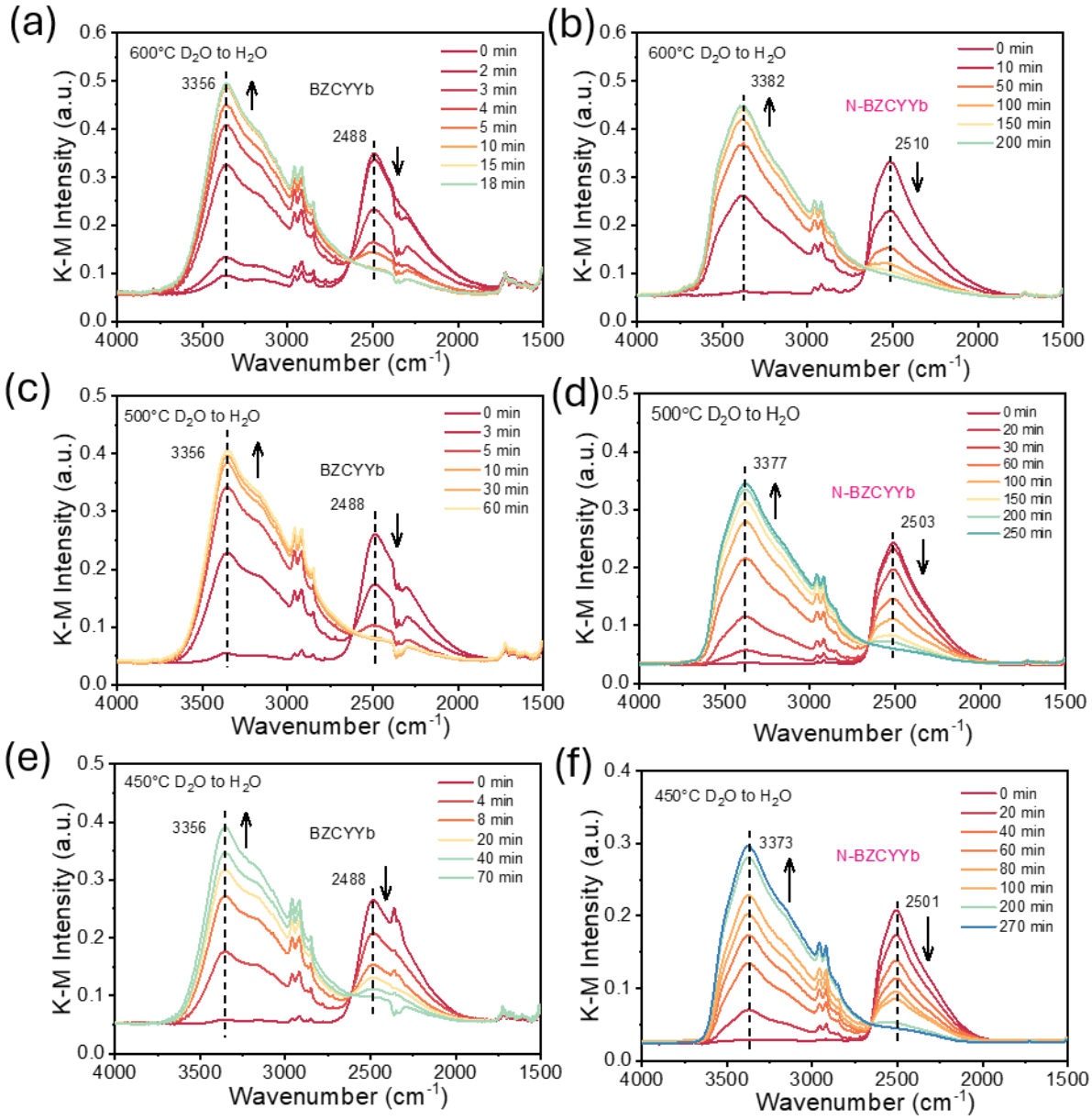

Figure 4.11. Time-resolved operando DRIFTS investigation of proton/deuteron exchange in pristine and N-BZCYYb. DRIFTS spectra (a) during $D_2O \rightarrow H_2O$ isotope exchange for pristine BZCYYb at 600 °C. (b) DRIFTS spectra during $D_2O \rightarrow H_2O$ isotope exchange for N-BZCYYb at

600 °C. (c) during $D_2O \rightarrow H_2O$ isotope exchange for pristine BZCYYb at 500 °C. (d) DRIFTS spectra during $D_2O \rightarrow H_2O$ isotope exchange for N-BZCYYb at 500 °C. (e) during $D_2O \rightarrow H_2O$ isotope exchange for pristine BZCYYb at 450 °C. (f) DRIFTS spectra during $D_2O \rightarrow H_2O$ isotope exchange for N-BZCYYb at 450 °C.

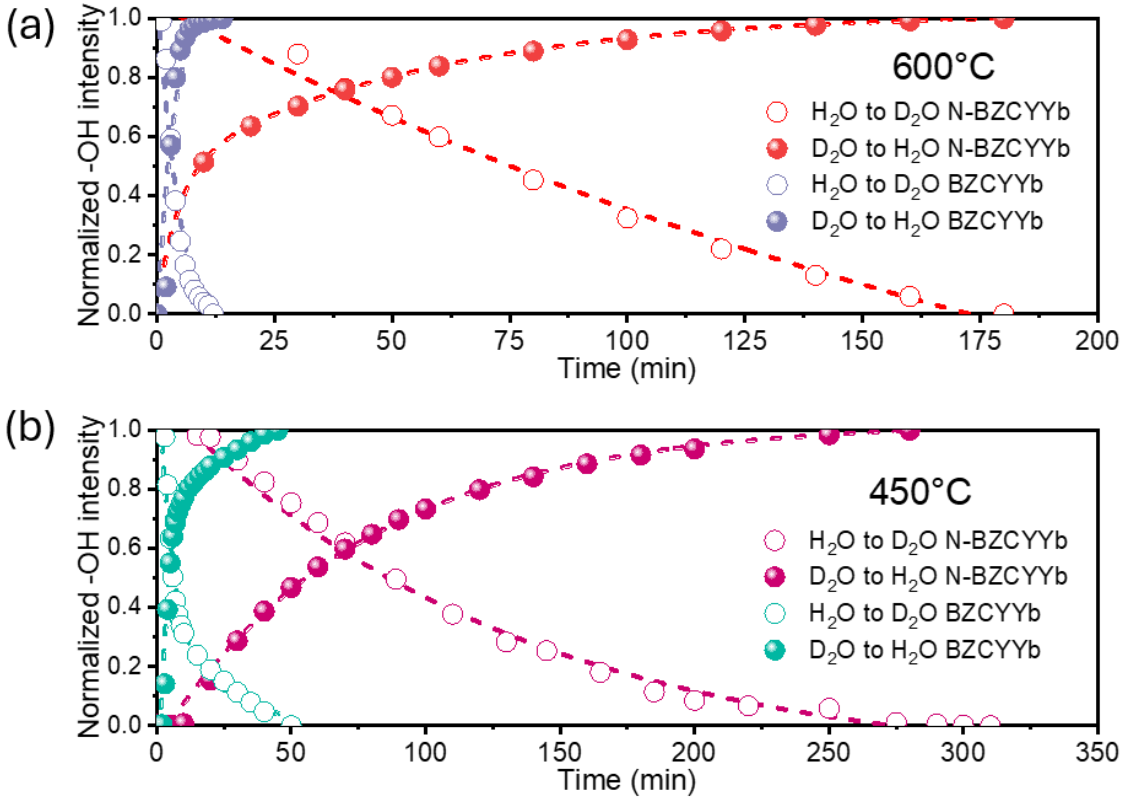

Figure 4.12. (a) Normalized O-H band intensity during $H_2O \rightarrow D_2O$ isotope exchange. (b) Comparison of proton/deuteron exchange kinetics in pristine BZCYYb and N-BZCYYb.

4.3.4 Quantitative analysis and mechanistic interpretation

Figure 4.13a-b present the kinetic analysis of the isotope-exchange process. The excellent linear relationships between ln(Rel. -OH intensity) and time demonstrate that both $H_2O \rightarrow D_2O$ and

$D_2O \rightarrow H_2O$ exchange follow first-order kinetics (R^2 values are listed in Table 4.1), enabling the extraction of the apparent exchange rate constants at 450, 500, and 600 °C. These rate constants provide the basis for quantitatively comparing the isotope-exchange kinetics under different temperatures and exchange directions.

Table 4.1. Coefficients of determination (R^2) for first-order kinetic fitting of $H_2O \rightarrow D_2O$ isotope exchange in pristine BZCYYb and N-BZCYYb.

Temperature	BZCYYb (R^2)	N-BZCYYb (R^2)
600 °C	0.998	0.999
500 °C	0.971	0.998
450 °C	0.992	0.993

The extracted rate constants reveal a pronounced difference in the $H_2O \rightarrow D_2O$ isotope-exchange kinetics between pristine and N-BZCYYb (Figure 4.13c). For pristine BZCYYb1711, the exchange rate constant decreases markedly with decreasing temperature from 600 to 450 °C. In contrast, N-BZCYYb exhibits substantially lower rate constants over the entire temperature range, with only a relatively small variation among 450 °C, 500 °C, and 600 °C (inset of Figure 4.13c). For example, at 450 °C, the rate constant of pristine BZCYYb1711 is approximately 0.07 min^{-1}, whereas that of N-BZCYYb remains at approximately 0.011 min^{-1}, corresponding to an approximately 6.4-fold difference. These results quantitatively demonstrate that Ni addition substantially retards the $H_2O \rightarrow D_2O$ isotope-exchange process and strongly modifies the temperature dependence of surface proton exchange dynamics. This trend is in excellent agreement

with the DRIFTS observations presented in Figure 4.9, where delayed evolution of both -OH and -OD bands was observed after Ni addition.

To further evaluate the kinetic barrier associated with isotope exchange, Arrhenius analysis was performed using the extracted rate constants. As shown in Figure 4.13c, the apparent activation energy of proton/deuteron exchange decreases from 54.75 to 9.70 kJ mol^{-1} after Ni adding. Considering the substantially lower exchange rate constants of N-BZCYYb, the reduced apparent activation energy does not indicate faster proton transfer. Instead, it suggests that Ni alters the rate-limiting process governing proton/deuteron exchange, resulting in distinct exchange kinetics and a much weaker temperature dependence.

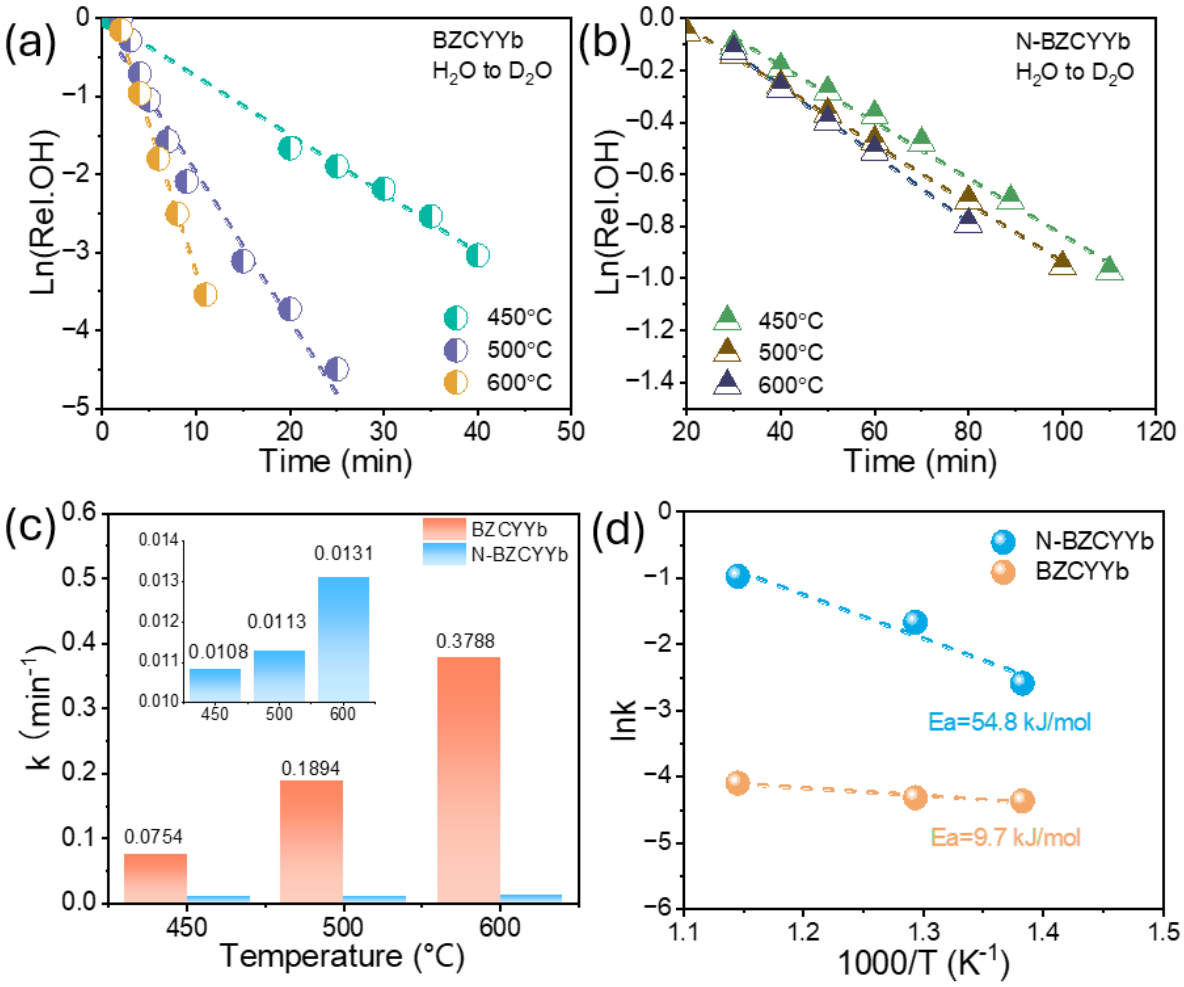

Figure 4.13. Rate constants for $H_2O \rightarrow D_2O$ isotope exchange of (a) pristine BZCYYb and (b) N-BZCYYb. (c) Apparent activation energies of pristine BZCYYb and N-BZCYYb. (d) Comparison of $H_2O \rightarrow D_2O$ isotope-exchange rate constants for pristine BZCYYb and N-BZCYYb at different temperatures.

4.3.5. DFT modeling

The (100) facet of the BZCYYb1711 lattice with dispersed cations (Figure 4.2) was chosen for hydration and dehydration modeling. The B-termination was adapted, where the B-site cations

are exposed in the top layer (Figure 4.14a-d). The oxygen vacancy formation energies obtained from DFT calculations according to $E_{f,V_O^{\cdot\cdot}} = E_{V_O^{\cdot\cdot}} + \frac{1}{2}E_{O_2(g)} - E_{V_O^{\cdot\cdot}-free(100)}$ are -0.23 eV and -0.24 eV, for removing the lattice oxygen between the Y-Zr and Y-Yb pairs (Figure 4.14a-b), respectively. For comparison, the $E_{f,V_O^{\cdot\cdot}}$ corresponding to the (100) facet with Y^{3+} in the sublayers (Figure 4.14c-d) are between 2-3 eV.

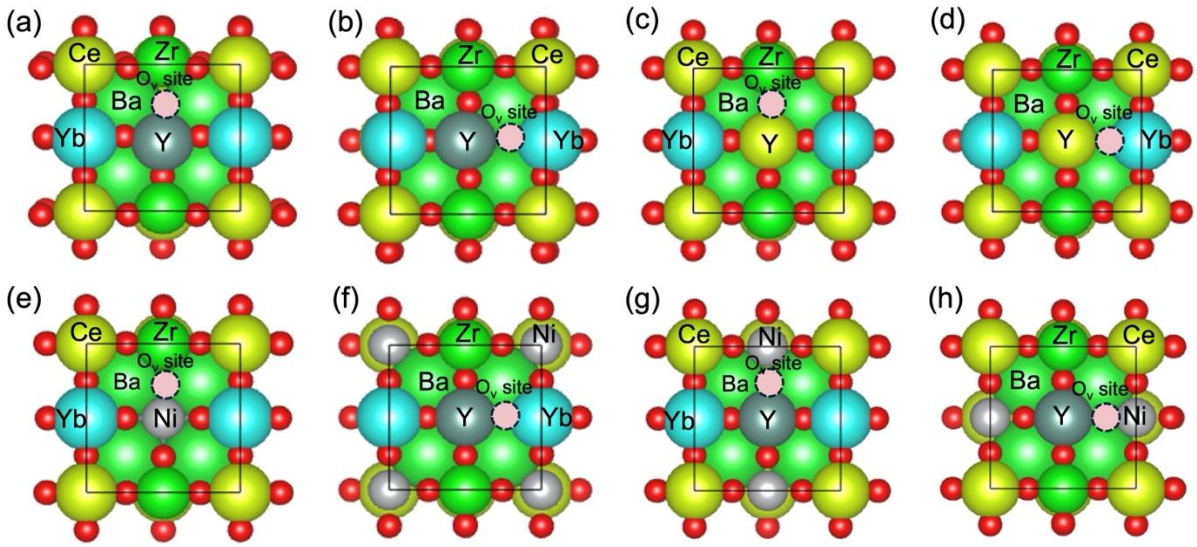

Figure 4.14. The (100) facets of BZCYYb1711 (a-b) with the Y in the top layer and an oxygen vacancy (indicated by the dashed circle); (c-d) with the Ni dopant and an oxygen vacancy. Color scheme: Zr (small green), Ce (yellow), Y (grey), Yb (turquoise), and Ni (small grey). The Ba and O atoms are displayed in large green spheres and red spheres, respectively.

Each original B-site cation was replaced by a Ni atom to indicate that the NiO are incorporated into the BZCYYb lattice. Next, the $E_{f,V_O^{\cdot\cdot}}$ for the most energetically favored oxygen vacancy sites, as illustrated in Figure 4.13e-h, are -0.73 eV, -1.93 eV, -1.10 eV, and -0.54 eV, respectively. These values strongly indicate that the Ni atom will further destabilize the surface lattice oxygen atoms, including those not directly connected to Ni (Figure 4.14f).

The hydrated surfaces with and without the Ni dopant are illustrated in Figure 4.15. The hydration energies were calculated according to $\Delta E_{hydration} = E_{hyd-(100)} - E_{H_2O(g)} - E_{V_O^{\cdot\cdot}}$. On the surface without Ni (Figure 4.15a), the DFT-calculated $\Delta E_{hydration}$ is -2.42 eV. For the surface with a Ni dopant, $\Delta E_{hydration}$ becomes -1.96 eV (Figure 4.15b), -1.59 eV (Figure 4.15c), -1.70 eV (Figure 4.15d), and -2.04 eV (Figure 4.15e), respectively. The hydration energies of the B-termination show consistent trends that can help predict surface behavior and the impact of Ni on surface hydration. While the most favorable hydration sites differ between the Ce and Y surfaces, some general observations appear to apply to both. For example, Ni doping appears to facilitate the formation of oxygen vacancies, but hydration becomes more difficult than on the Ni-free surfaces.

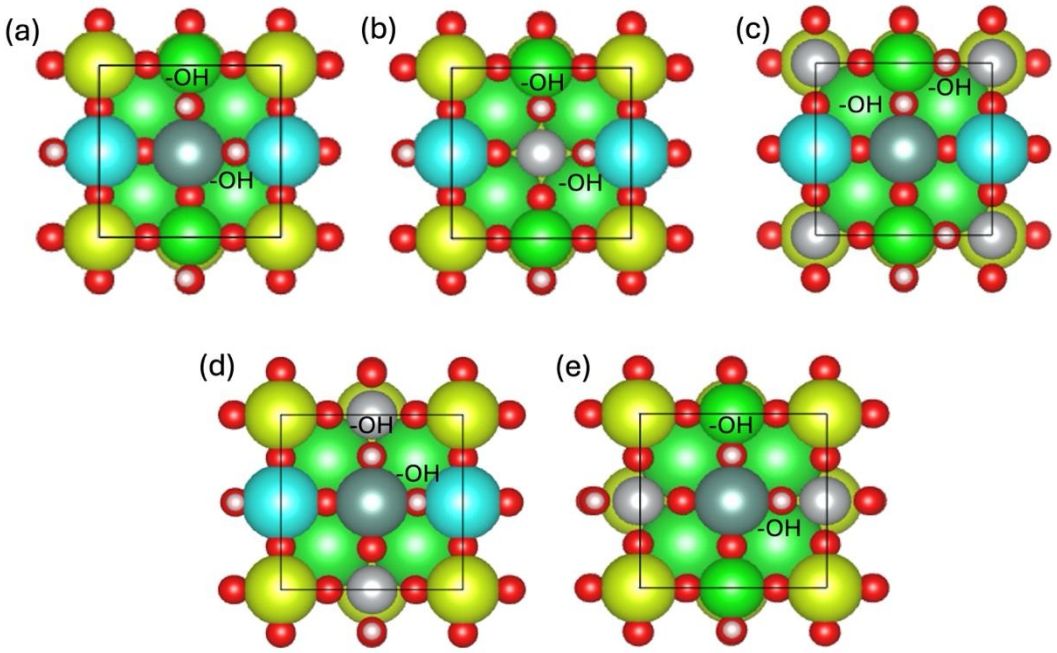

Figure 4.15. Hydrated (100) facets of BZCYYb1711 (a) with the Y in the top layer and no Ni dopant,); (b-e) with a Ni atom replacing a unique surface B-site cation. Color scheme: Zr (small

green), Ce (yellow), Y (grey), Yb (turquoise), and Ni (small grey). The Ba and O atoms are displayed in large green spheres and red spheres, respectively.

4.4. Conclusion

In this work, *operando* DRIFTS combined with H2O/D2O isotope exchange was employed to investigate the influence of Ni on surface proton dynamics in BZCYYb proton-conducting electrolytes. Compared with pristine BZCYYb, the N-BZCYYb exhibited slower hydration equilibration, prolonged dehydration equilibration, and significantly slower proton-deuteron exchange kinetics. Quantitative kinetic analysis further revealed lower isotope-exchange rate constants and a lower apparent activation energy (from 54.75 to 9.70 kJ mol^{-1}) after Ni addition, suggesting that Ni alters the rate-limiting process governing proton/deuteron exchange and leads to distinct exchange kinetics with a weaker temperature dependence. By examining the local coordination structures involving the Ni dopant, DFT calculations revealed that Ni destabilizes the lattice oxygen atoms. This work reveals an overlooked role of sintering additives in coupling electrolyte processing with proton transport chemistry and highlights *operando* vibrational spectroscopy as a powerful approach for elucidating proton processes in proton-conducting oxides.

Chapter 5 - Linking interfacial structure and catalytic reaction pathways in rationally designed CO_2 methanation catalysts via DRIFTS

5.1. Introduction

The electrocatalytic conversion of captured carbon dioxide (CO_2) and generated hydrogen (H_2) into valuable chemicals represents a promising strategy for carbon utilization and intermittent energy storage.[146, 147] This process-intensified "Power-to-Chemicals" mode can be effectively integrated into regulated energy distribution markets.[148-150] By utilizing the H_2 generated on-site, this approach eliminates the need for off-site hydrogen storage and transportation. Moreover, the resulting products, such as methane, which have more than three times the volumetric energy density of hydrogen, can be readily stored and distributed through existing natural gas infrastructure, reducing capital investment and enhancing overall system efficiency.[151, 152]

Intermediate temperature (IT) (300-600°C) and high temperature (HT) (>600°C) electrochemical CO_2 conversions, based on solid oxide cells, emerge as high-efficiency technologies, using abundant, low-cost transition metals as electrocatalysts.[153-155] Currently, most research focuses on CO_2 electrolysis or co-electrolysis with steam in HT cells (i.e., solid oxide electrolysis cells, or SOECs) for CO production. [156-161] Protonic ceramic electrochemical cells (PCECs) have recently been demonstrated as a viable alternative platform that operates within the IT range, benefiting from the lower activation energy of proton conduction relative to oxygen-ion conduction.[56, 162, 163] Therefore, IT-PCECs offer more favorable thermodynamic and kinetic conditions for CO_2 methanation,[161, 162] which is a highly exothermic process (ΔH_{298K}=-165.4 kJ/mol).

Traditionally, the CO_2 electrode of PCECs is designed as a Ni-based cermet, where the ceramic phase has the same composition as the protonic electrolyte, forming a half-cell structure. This configuration provides strong mechanical support, high catalytic activity, and relatively low manufacturing cost.[164, 165] However, $BaCeO_3$-based proton conductors are highly susceptible to carbonation, which severely compromises long-term stability. Substituting Ce partially or fully with Zr has proven effective in addressing this limitation.[18, 46] $BaZr_{0.4}Ce_{0.4}Y_{0.1}Yb_{0.1}O_{3-\delta}$ (BZCYYb4411), a state-of-the-art protonic conductor that combines excellent chemical durability with improved electrochemical performance, has been proposed.[2, 166] Pan *et al.*[166] directly employed BZCYYb4411-Ni as the CO_2 electrodes, demonstrating the concept of co-electrolysis of steam and CO_2 in PCEC for the generation of methane. More recently, Miao *et al.* [167] used density functional theory (DFT) to elucidate the coking-resistant mechanism during CO_2 hydrogenation, highlighting the critical roles of hydration and dissociation processes in BZCYYb4411-Ni. Another major challenge for CO_2 hydrogenation in PCECs is to tune product selectivity. For instance, Wang *et al.*[161] achieved > 99% CO selectivity with the BZCYYb4411-Ni electrode at 650 °C. However, they sacrificed the intrinsic advantage of PCECs working at IT for hydrocarbon production, underscoring the need for alternative electrode compositions or surface modifications to replace or improve the catalytic activity of conventional Ni-ceramic catalysts.

Valuable insights on catalysts selection can be drawn from the extensive body of research on thermally driven CO_2 methanation,[134, 164, 168-170] although additional requirements, such as high electronic conductivity and robust physical/chemical compatibility must also be met. Ceria-based oxides have attracted considerable attention owing to their redox flexibility and oxygen storage capacity.[171-176] For example, Ye *et al.*[163] and Chen *et al.*[177] selectively impregnated CeO_2 onto Ni-based supports, enhancing CH_4 selectivity by facilitating C-H bond formation. Built on this

concept, Mei *et al.* showed that the formate (HCOO*) and carboxyl (COOH*) intermediates can be strongly stabilized on CeO_2 surfaces through bidentate adsorption configurations.[178] Gao *et al.* [179] revealed that oxygen vacancies at the Ni-CeO_2 interface serve as preferential CO_2 adsorption and activation sites, where strong metal-support interactions facilitate CO_2 dissociation and stabilize interfacial reaction intermediate species. DFT calculations showed that the reduced CeO_2 (111) surface stabilizes activated bent bidentate CO_2 intermediates through electron transfer from nearby Ce^{3+} species to the adsorbed CO_2 molecule.[180] In addition, metal nanoparticles tend to nucleate at oxygen vacancies and vacancy clusters on a CeO_2 surface and bind more strongly to vacancy sites than to stoichiometric sites.[181] These mechanistic insights have led to growing interest in transferring CeO_2-based catalyst designs to solid oxide electrochemical systems for CO_2 conversion. Ding *et al*.[123] engineered Ir-O interactions in Sm-doped CeO_2 electrodes and successfully achieved tunable selectivity for CO and CH_4.[123] More recently, the CeO_2-based encapsulated architecture in SOECs has been proposed to create abundant metal-oxide interfaces and enable a dual-site mechanism in which CO_2 is activated as carbonate species at oxygen-vacancy-rich interfaces and subsequently reduced to CO on adjacent metal sites.[182] In our previous work, applying the Ni-Ru arched on Sm-doped CeO_2 as the on-cell reformer layer has also been shown to promote the activities of dry reforming and steam reforming of methane. [32] [183] Although these previous efforts collectively demonstrate that CeO_2-supported Ni has been used in solid oxide cell systems with validated CO_2 electrochemical performance, [184, 185] selective CH_4 formation in the IT range remains a big challenge. Additionally, fundamental insights into the catalytic CO_2 methanation pathways and the surface/bulk electronic structures remain limited, underscoring the need for *operando* characterization to elucidate the relationship between interfacial structure and reaction pathways.

In this work, a Pr-doped CeO_2-based Ni-supported catalyst, which could be potentially implemented in PCECs (Figure 5.1) as an on-cell hydrogenation layer, was developed for CO_2 methanation. The catalyst achieved > 3.5-fold higher CO_2 conversion at 400 °C when compared with traditional BZCYYb4411-Ni electrode. Long-term testing at 500 °C and 400 °C for >400 h demonstrated excellent catalyst stability under realistic operating conditions. Comprehensive *Operando* characterizations, such as DRIFTS, Near-Ambient Pressure X-ray Photoelectron Spectroscopy (NAP-XPS), and XAS, have been used to elucidate the underlying catalytic mechanisms. It is revealed that Pr doping increases oxygen vacancies and strengthens metal-support interactions at the Ni-CeO_2 interface, thereby promoting CO_2 activation and formate-mediated pathways. These findings provide fundamental understanding of how defect chemistry and interfacial interactions govern CO_2 hydrogenation pathways, guiding the design of future catalysts.

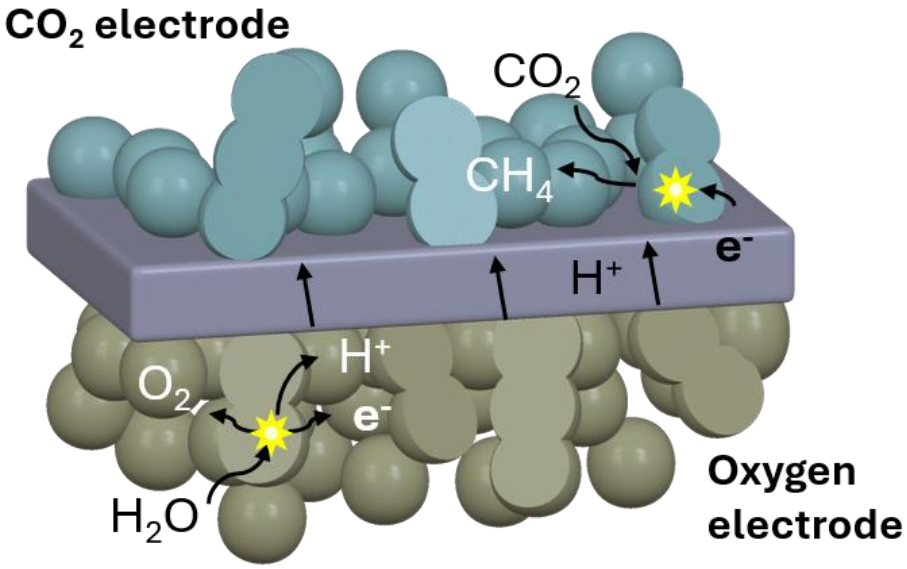

Figure 5.1. An illustration figure for steam and CO_2 co-electrolysis in PCECs to produce methane.

5.2. Experimental

5.2.1. Material and Catalyst Preparation

CO_2 methanation catalysts. A series of CeO_2-supported Ni catalysts (denoted as Ce-Ni*x*, where x = 0.2, 0.5, and 1, representing the molar ratio of Ce:Ni=1:x) were synthesized by a conventional sol-gel method. Briefly, stoichiometric amounts of $Ce(NO_3)_3 \cdot 6H_2O$ (≥99.9%, Sigma-Aldrich) and $Ni(NO_3)_2 \cdot 6H_2O$ (≥99.9%, Sigma-Aldrich) were dissolved in deionized (DI) water under continuous magnetic stirring to form a transparent precursor solution. Ethylenediaminetetraacetic acid (EDTA, ≥99%, Sigma-Aldrich) and citric acid monohydrate (CA, ≥99.5%, Sigma-Aldrich) were subsequently introduced as complexing and chelating agents, with the molar ratio of EDTA : CA : total metal ions fixed at 2:2:1 to ensure homogeneous distribution of metal cations. The pH of the solution was adjusted to ≈9 by dropwise addition of ammonium hydroxide. The solution was then heated on a hotplate to ~250 °C under vigorous stirring until it gradually transformed into a viscous gel via solvent evaporation and organic polymerization. The as-formed gel was transferred to a drying oven and maintained at 175 °C for 24 h to remove residual moisture and volatiles, yielding a solid black precursor. This dried gel was gently ground into a fine powder using an agate mortar and then calcined in air at 600 °C for 5 h at a heating rate of 5 °C min^{-1}. The resulting Ce-Ni_x powders were collected and stored in a desiccator for further use.

La-doped and Pr-doped CeO_2-supported Ni catalysts were synthesized using the same sol-gel procedure as mentioned above, with modifications to incorporate the dopants into the support oxide. La_2O_3(≥99.9%, Sigma-Aldrich) and Pr_6O_{11} (≥99.9%, Sigma-Aldrich) were used as the La and Pr precursor, respectively. Since both oxides are insoluble in DI water, they were first dissolved in diluted nitric acid solutions under mild heating to form clear nitrate solutions. These

nitrate solutions were then mixed with $Ce(NO_3)_3 \cdot 6H_2O$ and $Ni(NO_3)_2 \cdot 6H_2O$ precursors in the desired stoichiometric ratios. The same chelation, gelation, drying, and calcination steps as described above were followed to obtain the doped catalyst powders. The final compositions of the doped catalysts were $La_{0.2}Ce_{0.8}$-$Ni_{0.2}$ and Pr_yCe_{1-y}-Ni (y = 0.2, 0.5, 0.8). All prepared powders were finely ground prior to subsequent characterization and catalytic testing.

Traditional CO_2 electrode (BZCYYb4411-Ni). BZCYYb4411 powders were synthesized via solid-state reaction method. Stoichiometric amounts of $BaCO_3$ (99.8%, Alfa Aesar), ZrO_2 (99.9%, Alfa Aesar), CeO_2 (99.9%, Alfa Aesar), Y_2O_3 (99.9%, Alfa Aesar), and Yb_2O_3 (99.9%, Alfa Aesar) were weighed and mixed by ball milling in ethanol for 24 h. The powder was dried, ground into a fine powder, and calcined in air at 1100 °C for 10 h. The grinding and calcination process was repeated twice to ensure phase purity and homogeneity. The BZCYYb4411 powder was then mixed with NiO at a weight ratio of 4:6 and subsequently sintered at 1450 °C for 5 h to simulate the conventional BZCYYb4411-Ni electrode for CO_2 hydrogenation.

5.2.2. Characterizations

The as-fired catalysts were reduced under 10 % H_2 balanced with Ar (H_2:Ar = 1:9) at 600 °C for 2 h. The crystal structures of as-fired and reduced samples were determined using X-ray diffraction (XRD) (2008 Bruker D8, Cu$K\alpha$ with a scan rate of 10°/ min at room temperature). XRD Rietveld refinement was conducted using the GSAS-II software package.[118] The morphology of reduced $Pr_{0.5}Ce_{0.5}$-Ni powder was examined using TEM and energy-dispersive X-ray spectroscopy (EDS) (TALOS F200X, Thermo Fisher Scientific). The surface morphology of the catalysts was examined using a scanning electron microscope (SEM, JEOL 6700F).

Operando NAP-XPS experiments provide valuable information on the surface electronic structure of the catalysts under realistic reaction conditions, which were performed with a lab-

based SPECS system fitted with an *in situ* cell and a Phoibos-HSA3500 analyzer. The system utilized an Al K-alpha source operated at 60 W and 15 kV. The powdered sample was loaded on carbon tapes and evacuated overnight under ultra-high vacuum. The C 1s, O 1s, Ce 3d, Pr 3d and Ni 2p regions were selected for spectra collection. The samples were first reduced under pure H_2 (2.66 mbar). Subsequently, a CO_2/H_2 mixture with the ratio of 1:1 was introduced, and XPS spectra were collected at 450 °C, 350 °C, and 27 °C. All temperatures were maintained within ±5 °C.

Soft XAS measurements were performed to probe the electronic structure and local chemical environment of the catalysts. The experiments were performed on the SXR beamline at the Australian Synchrotron, part of ANSTO. XAS experiments at the O K-edge, Ni L_3/L_2, and Pr/Ce M_5/M_4 were performed at the SXR beamline of the Australian Synchrotron. Samples were mounted with carbon tape. The XAS data were collected using multiple detection modes to obtain depth-resolved information. Total fluorescence yield (TFY) mode was employed to probe bulk-sensitive signals, while electron yield-based modes, including drain current (DC) and channeltron detection, were used to obtain surface and near-surface information. The drain current signal corresponds to a probing depth of approximately 10-20 nm, whereas the channeltron detector is more surface-sensitive. Data reduction and analysis was performed using the QANT macro package in Igor Pro. All spectra were calibrated using an in-line reference material, and the data were normalized by setting the pre-edge to 0 and the post-edge to 1.

Operando DRIFTS was performed using a Thermo Fisher iS50 FTIR spectrometer equipped with the Praying Mantis high-temperature reaction chamber (Figure 5.2).[111] [103] The gas flow (H_2, CO_2, and Ar) was controlled by mass flow controllers over a range of 0-100 sccm. The temperature was regulated using an external heating system, allowing the sample to be heated from room temperature to 700 °C. CO_2-Temperature-Programmed Desorption (CO_2-TPD) tests were

performed on a PrismaPlus mass spectrometer. Before testing, the samples (100 mg) were pretreated with 10% H_2 (10 ml min^{-1}, H_2:Ar = 1:9) from 25 °C to 600 °C with a heating rate of 10 °C min^{-1}, then holding at 600 °C for ~2 h and finally cooled to 25 °C. CO_2 adsorption was performed in pure CO_2 (10 ml min^{-1}) for 120 min, and the sample was then purged with Ar for 120 min to remove the adsorbed CO_2. Then, CO_2 desorption was performed at a heating rate of 10 °C min^{-1}, detected by a mass spectrometer. H_2-temperature-programmed reduction (H_2-TPR) tests were performed on a ChemBET Pulsar. Before testing, 100 mg of the catalyst was pretreated in a U-shaped quartz tube with N_2 (100 sccm) at 140 °C for 1.5 h to remove moisture and impurities, then cooled to 25 °C. H_2-TPR was performed in 10% H_2 (H_2:Ar = 1:9) with a heating rate of 10 °C min^{-1}.

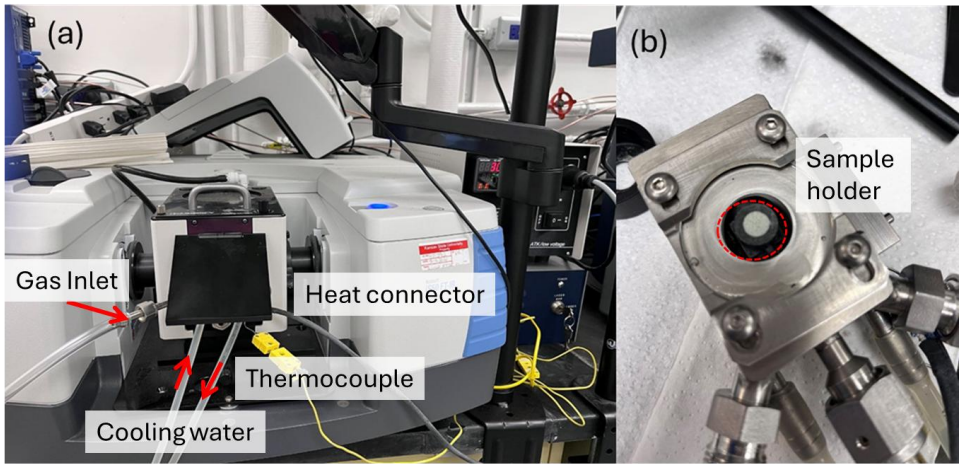

Figure 5.2. Photographs of the *Operando* DRIFTS experimental setup[103, 111], including (a) the DRIFTS spectrometer with gas flow system and (b) the high-temperature reaction cell with the catalyst sample loaded in the sample holder.

5.2.3. Catalyst Testing

CO_2 methanation experiments were conducted in a continuous-flow quartz fixed-bed tubular reactor (inner diameter: 0.28 inch) operated at atmospheric pressure. For each test, 150 mg of catalyst was loaded into the reactor. A K-type thermocouple was positioned near the catalyst bed to precisely monitor the reaction temperature. Prior to testing, the catalyst was reduced in a 10% H_2/N_2 gas mixture (total flow rate: 100 sccm) by heating to 600 °C at a rate of 10 °C min^{-1} and holding at 600 °C for 2 h. After reduction, a feed gas mixture of CO_2 and H_2 (H_2/CO_2 molar ratio =1 or 4) was introduced at a total flow rate of 20 sccm. Meanwhile, 15 sccm of N_2 was introduced into the outlet stream as a purge gas and internal standard. The outlet gas composition was analyzed from online gas chromatography (Agilent 7890A, USA) to determine CO_2 conversion and CH_4/CO selectivity under different testing conditions. The reaction temperature decreased from 600 to 350 °C in 50 °C intervals at a rate of 10 °C min^{-1}. At each temperature, the system was held for approximately 15 min before data collection to ensure steady-state conditions.

The CO_2 conversion (X_{CO_2}), CH_4 selectivity (S_{CH_4}), and CH_4 yield (Y_{CH_4}) during catalytic evaluation were calculated based on the following equations:

$$X_{CO_2}(\%) = (F_{CO_2,in} - F_{CO_2,out}) / F_{CO_2,in} \times 100\% \quad (23)$$

$$S_{CH_4}(\%) = F_{CH_4,out} / (F_{CH_4,out} + F_{CO,out}) \times 100\% \quad (24)$$

$$Y_{CH_4}(\%) = X_{CO_2} \times S_{CH_4} \times 100\%$$

where $F_{CO_2,in}$ and $F_{CO_2,out}$ are the respective molar flow rates of CO_2 at the reactor inlet and outlet, and $F_{CH_4,out}$ and $F_{CO,out}$ are the molar flow rates of CH_4 and CO at the reactor outlet.

5.3. Results and discussion

5.3.1. Rationally designed electrocatalysts for CO_2 methanation

The crystalline structures of the as-synthesized Ce-Ni_x (x = 0.2, 0.5, 1), $La_{0.2}Ce_{0.8}$-Ni, and Pr_yCe_{1-y}-Ni (y = 0.2, 0.5, 1) catalysts were evaluated by XRD, and the results are presented in Figure 5.3a-b, Figure 5.4, Figure 5.5, Figure 5.6, Figure 5.7, Figure 5.8, and Figure 5.9). The XRD Rietveld refinement results for the reduced Ce-Ni (Figure 5.3a) show that it consists of a fluorite-type CeO_2 phase (space group $Fm\bar{3}m$, a = b = c = 5.41 Å) and a Ni phase (space group $Fm\bar{3}m$, a = b = c = 3.52 Å). The refined weight fraction of metallic Ni is ~18.2%, which is slightly lower than the theoretical value of 25.4 wt%, suggesting that a small fraction of Ni might still be incorporated into the CeO_2 lattice. Similarly, $Pr_{0.5}Ce_{0.5}$-Ni consists of a Pr-doped CeO_2 phase and a metallic Ni phase (Figure 5.3**b**). The lattice expansion of the oxide support observed upon Pr incorporation (a = b = c = 5.44 Å) could be attributed to the substitution of Ce^{4+} (0.97 Å) by the larger Pr^{3+} (1.13 Å). While the Ni content in $Pr_{0.5}Ce_{0.5}$ -Ni (23.9 wt%) approaches the theoretical value (25.4 wt%), reflecting that less Ni has been incorporated into the lattice, or Pr doping is more favorable for the exsolution of Ni after reduction.

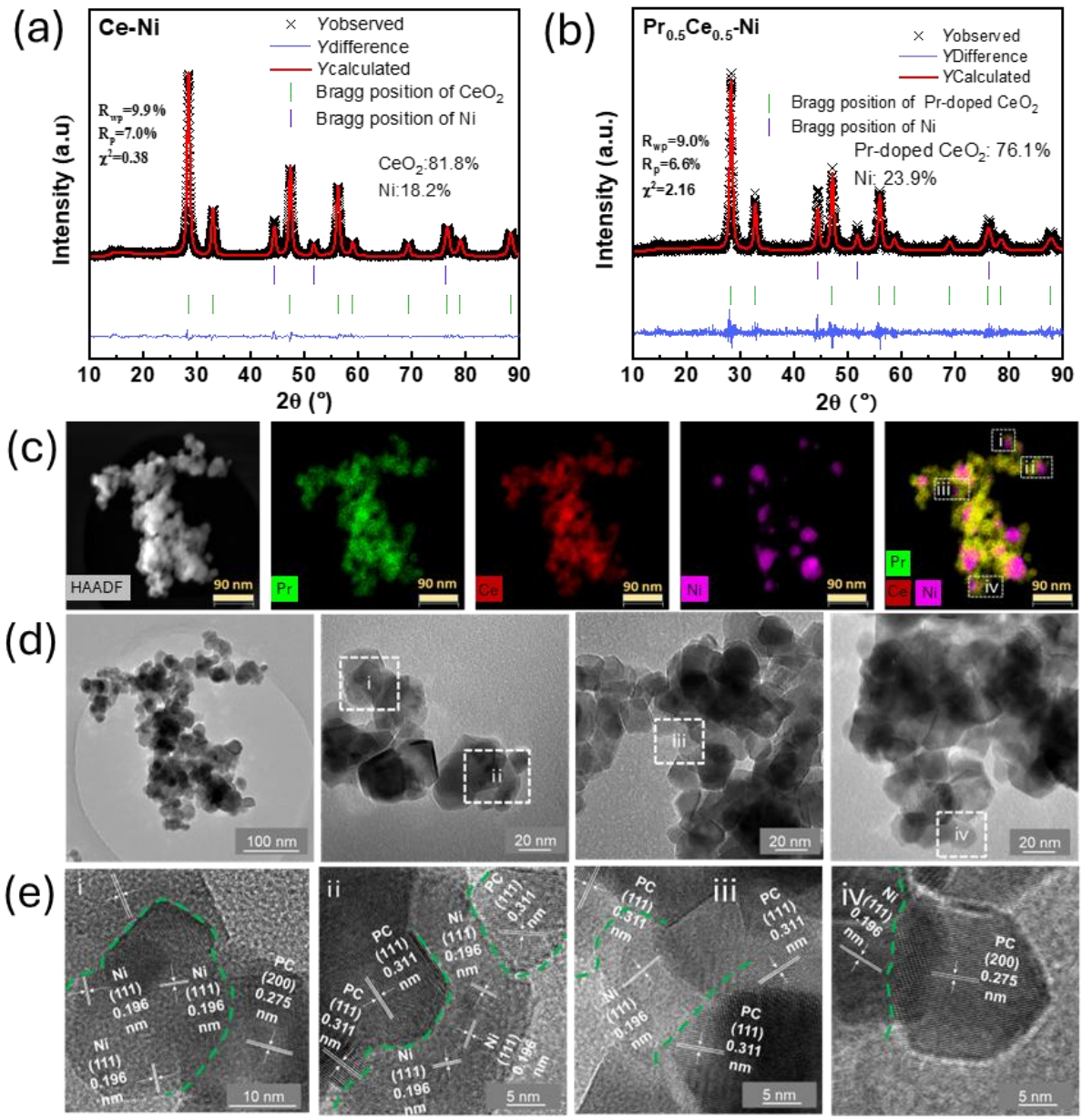

Figure 5.3. XRD Rietveld refinement results of (a) reduced Ce-Ni and (b) reduced $Pr_{0.5}Ce_{0.5}$-Ni; (c) High-angle annular dark-field (HAADF-STEM) image and EDS mapping of reduced $Pr_{0.5}Ce_{0.5}$-Ni catalyst; (d) TEM images of the reduced $Pr_{0.5}Ce_{0.5}$-Ni catalyst at different magnifications; (e) High-resolution TEM (HRTEM) images of the corresponding regions (i-iv) in (d), showing lattice fringes of metallic Ni and Pr-doped CeO_2. PC: Pr-doped CeO_2.

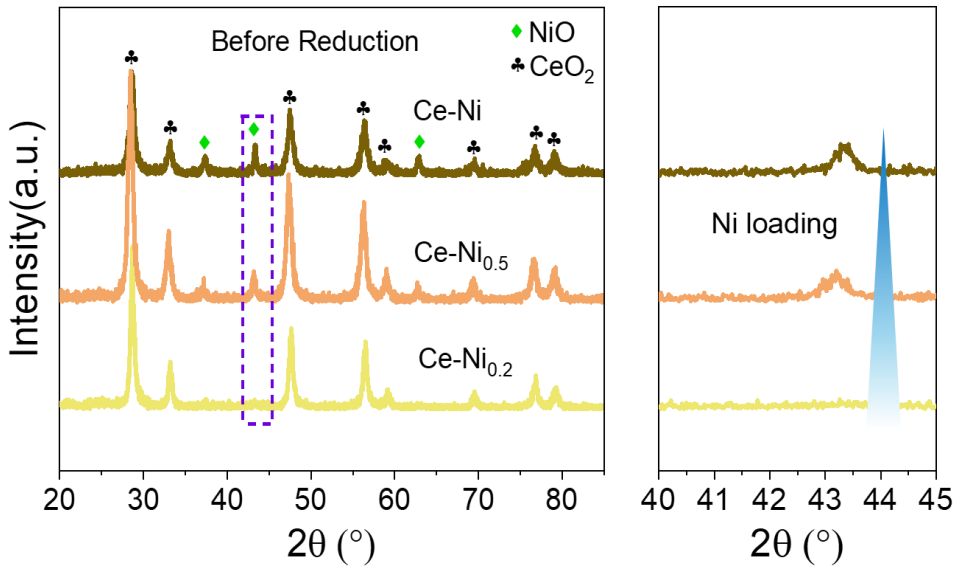

Figure 5.4. XRD patterns of Ce-$Ni_{0.2}$, Ce-$Ni_{0.5}$, and Ce-Ni catalysts prior to reduction.

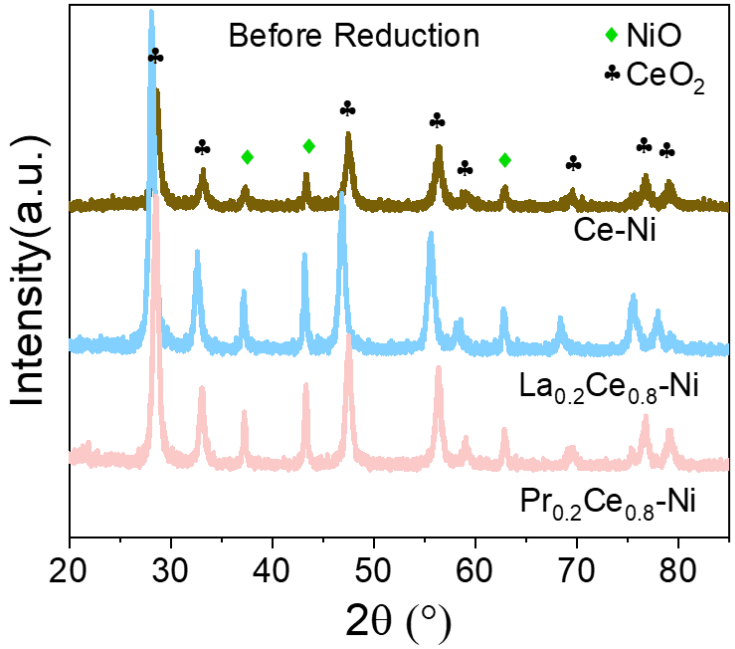

Figure 5.5. XRD patterns of $La_{0.2}Ce_{0.8}$-Ni, $Pr_{0.2}Ce_{0.8}$-Ni, and Ce-Ni catalysts prior to reduction.

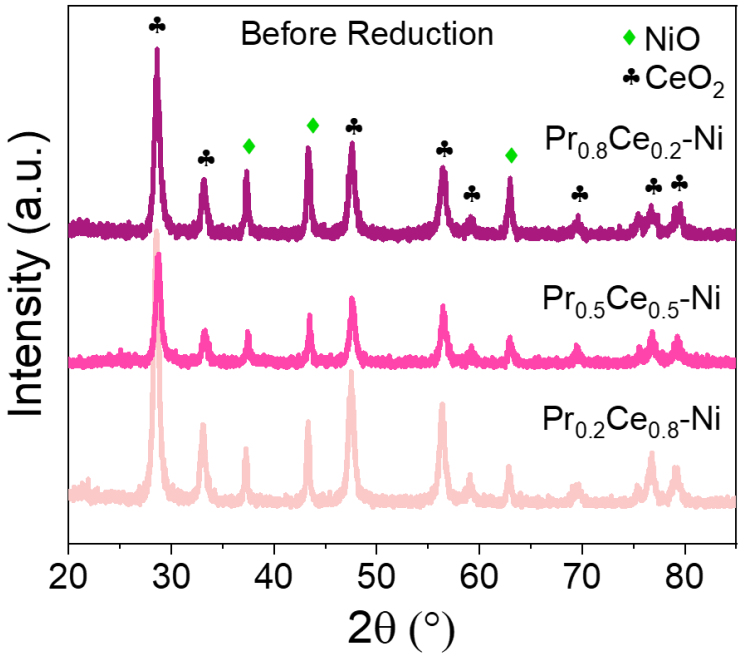

Figure 5.6. XRD patterns of $Pr_{0.2}Ce_{0.8}$-Ni, $Pr_{0.5}Ce_{0.5}$-Ni, and $Pr_{0.8}Ce_{0.5}$-Ni catalysts prior to reduction.

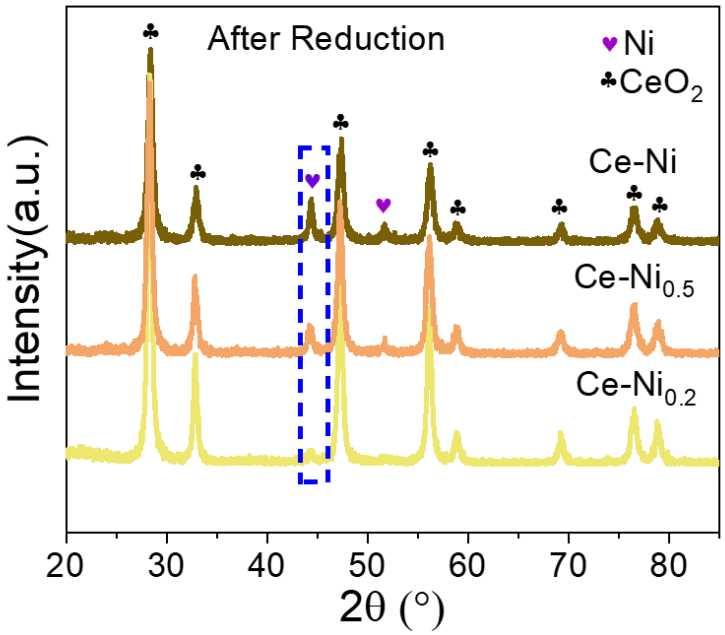

Figure 5.7. XRD patterns of Ce-$Ni_{0.2}$, Ce-$Ni_{0.5}$, and Ce-Ni after reduction.

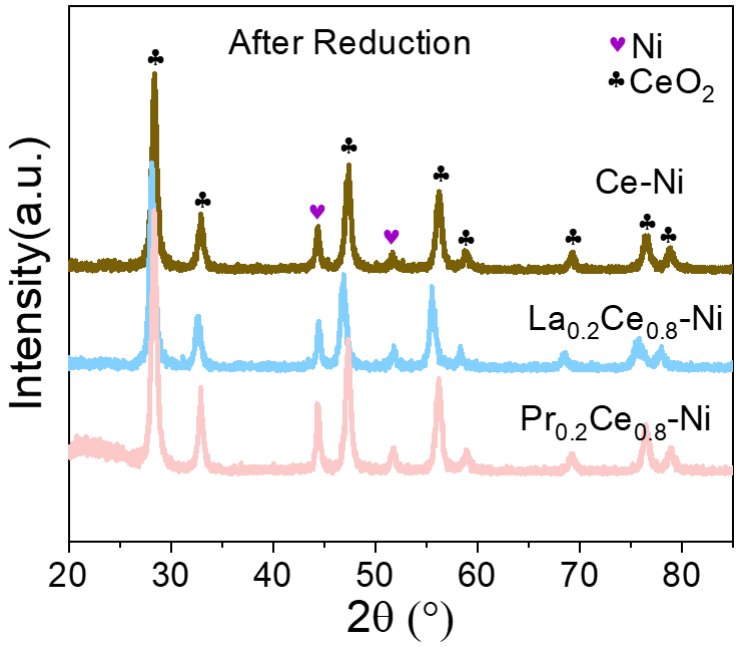

Figure 5.8. XRD patterns of $La_{0.2}Ce_{0.8}$-Ni, $Pr_{0.2}Ce_{0.8}$-Ni, and Ce-Ni after reduction.

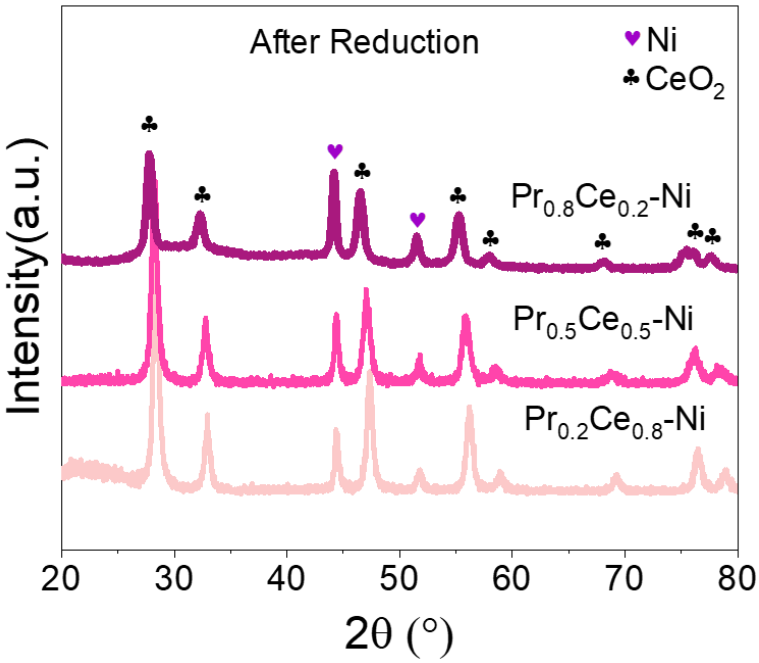

Figure 5.9. XRD patterns of $Pr_{0.2}Ce_{0.8}$-Ni, $Pr_{0.5}Ce_{0.5}$-Ni, and $Pr_{0.8}Ce_{0.5}$-Ni after reduction, showing the phase composition and crystallographic structure of the reduced samples.

The morphology of the reduced $Pr_{0.5}Ce_{0.5}$-Ni catalyst was characterized by EDS and TEM (Figure 5.3c-e and Figure 5.10, Figure 5.11, and Figure 5.12). As shown in Figure 5.3c, the catalyst exhibits a nano-crystalline morphology with particle sizes of 8-30 nm. The Ce (red) and Pr (green) signals largely overlap, with no detectable Pr-rich domains, indicating homogeneous Pr incorporation into the CeO_2 lattice. In contrast, metallic Ni (magenta) appears as discrete nanoparticles dispersed on the oxide support, with sizes of 15-30 nm. High-magnification TEM images from multiple regions (i-iv, Figure 5.3d) further reveal clear lattice fringes for both Pr-doped CeO_2 (PC) and metallic Ni (Figure 5.3e). A distinct interface between the oxide support and Ni phase, highlighted by green dashed lines, indicates intimate metal-support contact that is critical for the interfacial catalysis.[186, 187] The measured interplanar spacings of 0.311 and 0.275 nm are assigned to the (111) and (200) planes of PC, respectively, in good agreement with the XRD Rietveld values (~0.314 and ~0.272 nm). The 0.196 nm spacing corresponds to the (111) plane of face-centered cubic Ni, also consistent with the XRD result (~0.203 nm). Together, these results confirm that $Pr_{0.5}Ce_{0.5}$-Ni consists of well-dispersed Ni nanoparticles strongly anchored to a homogeneous Pr-doped CeO_2 support.

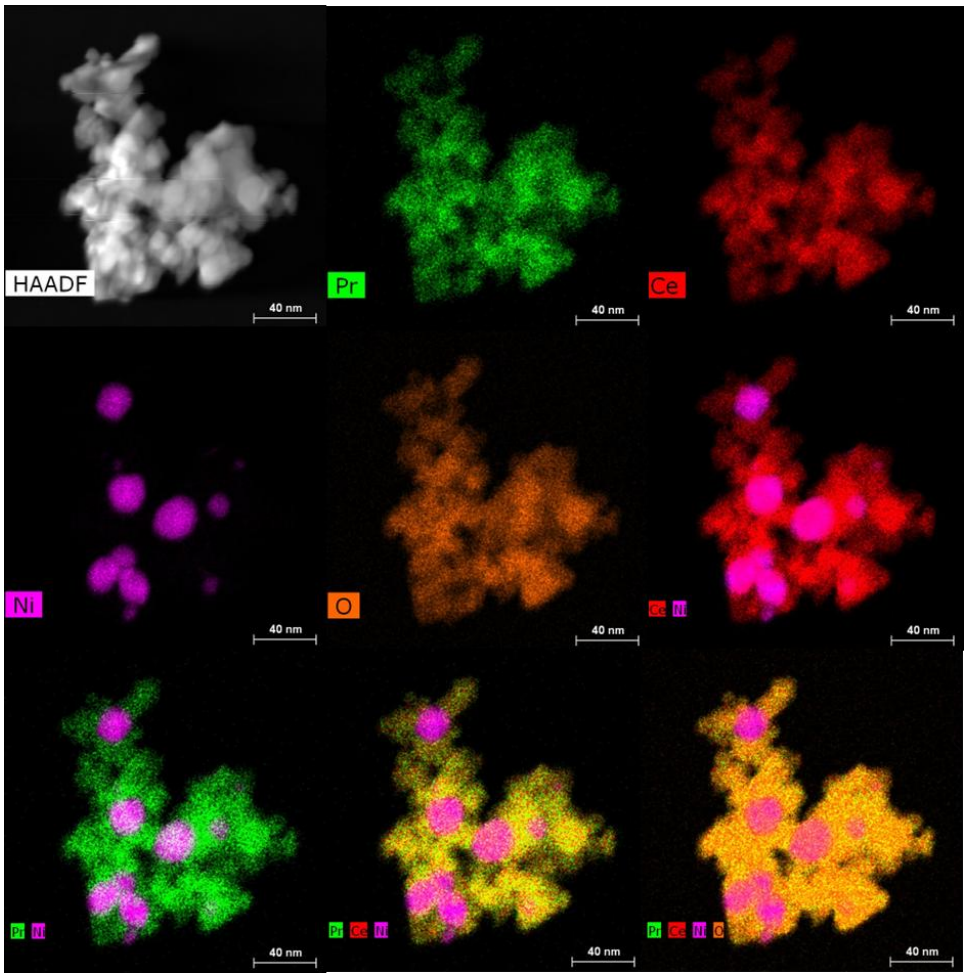

Figure 5.10. High-angle annular dark-field (HAADF) image and EDS mapping of the reduced $Pr_{0.5}Ce_{0.5}$-Ni (area 1).

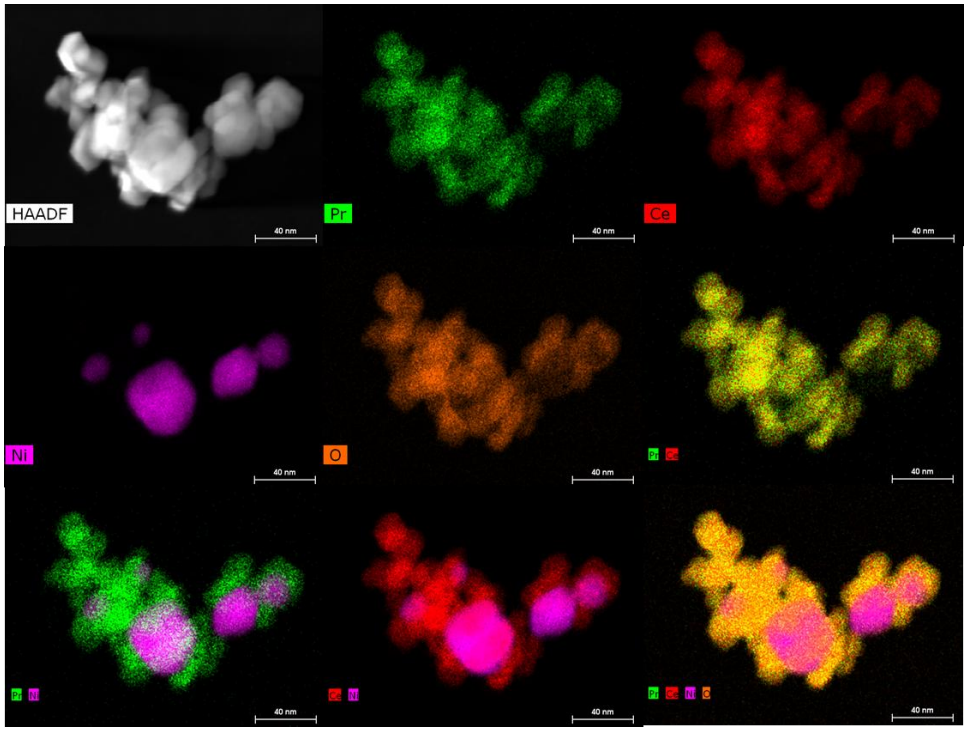

Figure 5.11. High-angle annular dark-field (HAADF) image and EDS mapping of the reduced $Pr_{0.5}Ce_{0.5}$-Ni (area 2).

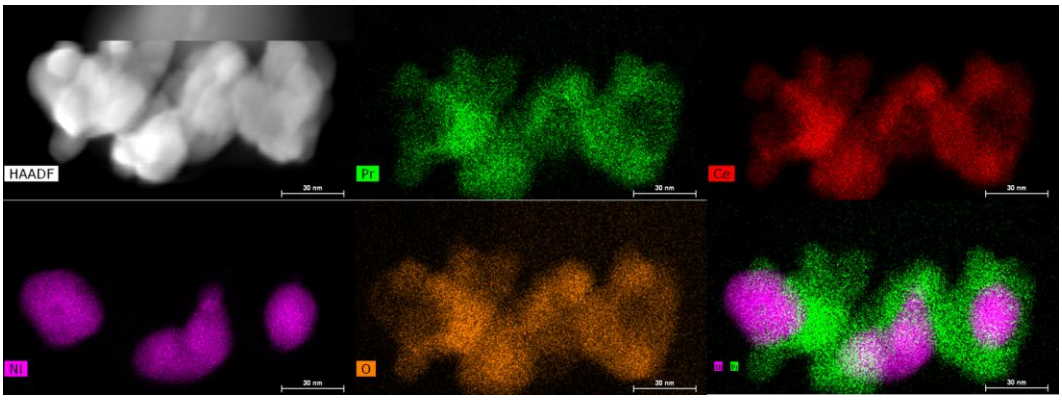

Figure 5.12. High-angle annular dark-field (HAADF) image and EDS mapping of the reduced $Pr_{0.5}Ce_{0.5}$-Ni (area 3).

Figure 5.13 and Figure 5.14, Figure 5.15, Figure 5.16, Figure 5.17, and Figure 5.18 show the catalytic performance of a series of designed catalysts for CO_2 hydrogenation. As shown in Figure 5.13a, the CO_2 conversion increases with an increasing Ni loading on the CeO_2 support. Among the Ce-Ni_x series, Ce-Ni exhibits the highest conversion, representing a relatively 30% improvement over Ce-$Ni_{0.2}$ at 450 °C. This trend may be related to the higher Ni content, which provides adequate Ni sites for H_2 dissociation, thereby enhancing CO_2 hydrogenation.[169] Modifying the support provides another effective strategy to further enhance catalytic activity.[188] As shown in Figure 5.13b, $La_{0.2}Ce_{0.8}$-Ni and $Pr_{0.2}Ce_{0.8}$-Ni both outperform the undoped Ce-Ni catalyst. $Pr_{0.5}Ce_{0.5}$-Ni yields the highest CO_2 conversion across the entire temperature range, particularly at temperatures below 450 °C (Figure 5.13c). Compared with the traditional BZCYYb-Ni CO_2 electrode, the rationally designed $Pr_{0.5}Ce_{0.5}$-Ni has been shown to significantly boost CO_2 conversion and CH_4 selectivity (Figure 5.13d). For example, $Pr_{0.5}Ce_{0.5}$-Ni achieved > 40% improvement of CO_2 conversion at 500 °C (Figure 5.13d). The performance gap widened at reduced temperatures. At 400°C, $Pr_{0.5}Ce_{0.5}$-Ni achieved a CO_2 conversion 3.5-fold higher than that of BZCYYb4411-Ni. Importantly, the $Pr_{0.5}Ce_{0.5}$-Ni catalyst also exhibits significantly higher CH_4 selectivity, achieving 86.1 % CH_4 selectivity at 400 °C, whereas the selectivity of BZCYYb-Ni reaches only 41.7% (Figure 5.13d). The comprehensive CH_4 yield results are presented in Figure 5.15. $Pr_{0.5}Ce_{0.5}$-Ni achieves the highest CH_4 yield across all temperatures, reaffirming its superior catalytic performance for CO_2 methanation. Catalytic performance was also evaluated under a CO_2/H_2 ratio of 1:4 from 400-600 °C and $Pr_{0.5}Ce_{0.5}$-Ni still exhibits the highest CO_2 conversion and CH_4 selectivity among all catalysts (Figure 5.16).

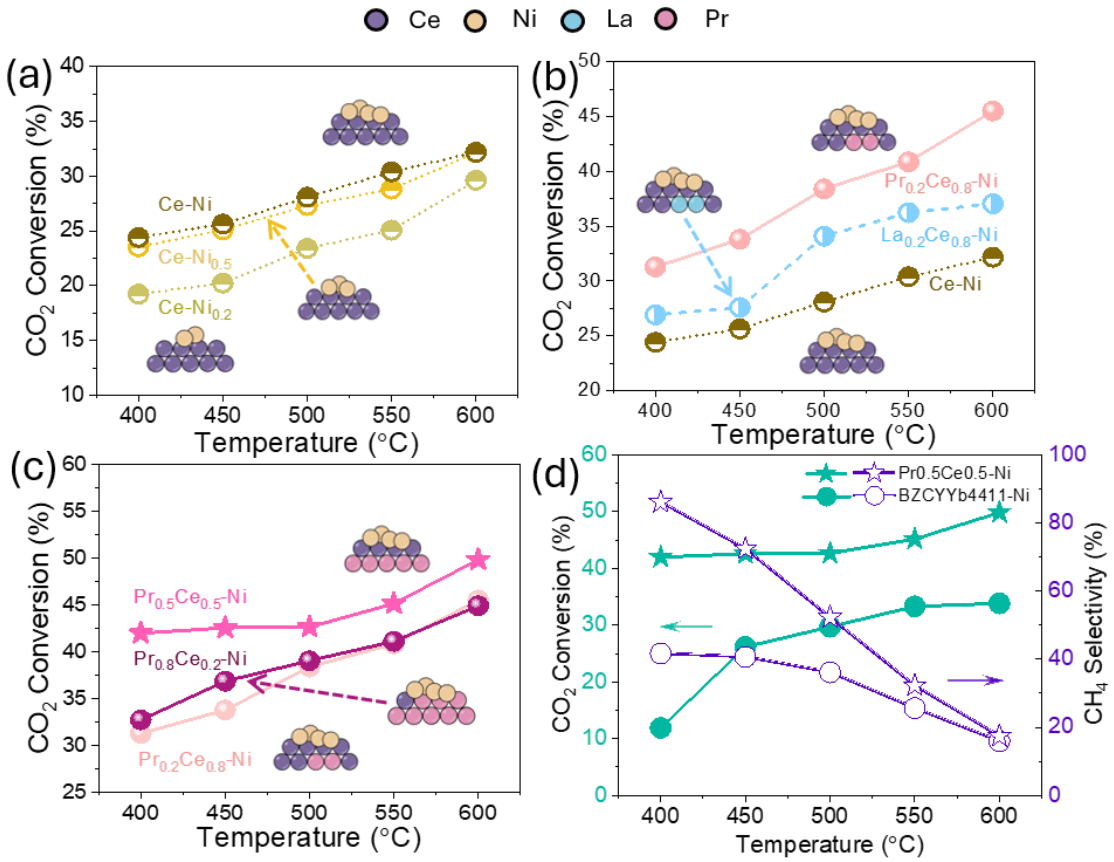

Figure 5.13. CO_2 conversion as a function of temperature (400-600 °C, H_2:CO_2 = 1:1) over Ni-based catalysts with systematically tuned composition. (a) Effects of Ni loading on the CeO_2 support: Ce-$Ni_{0.2}$, Ce-$Ni_{0.5}$, Ce-Ni catalysts; (b) effects of dopant species (La and Pr) on Ce-Ni catalysts including Ce-Ni, $La_{0.2}Ce_{0.8}$-Ni and $Pr_{0.2}Ce_{0.8}$-Ni; (c) the impact of Pr/Ce ratios on CO_2 methanation activity including $Pr_{0.2}Ce_{0.8}$-Ni, $Pr_{0.5}Ce_{0.5}$-Ni and $Pr_{0.8}Ce_{0.2}$-Ni; (d) the comparison of BZCYYb4411-Ni with rationally designed $Pr_{0.5}Ce_{0.5}$-Ni for CO_2 conversion and CH_4 selectivity (CO_2 : H_2=1:1, with the total follow rate as 20 sccm).

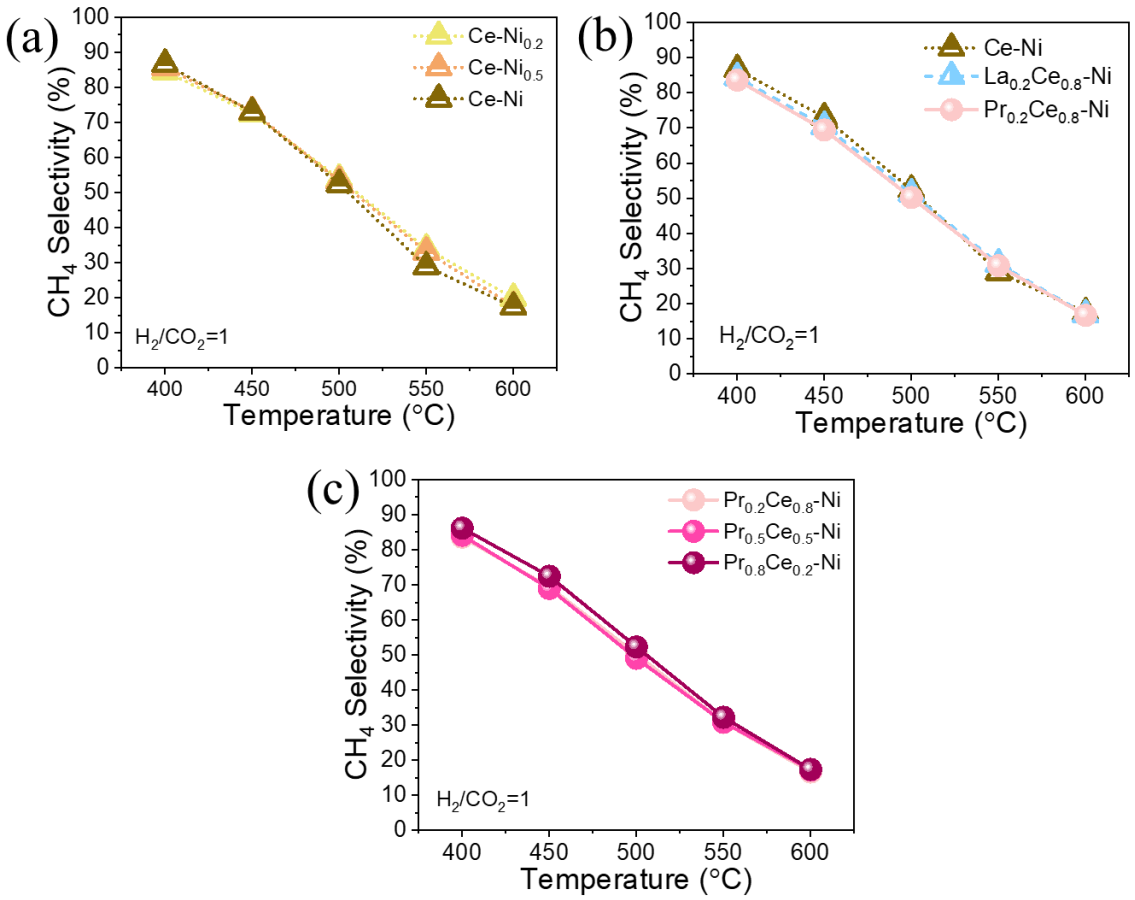

Figure 5.14. CH_4 selectivity as a function of temperature (400-600 °C, H_2/CO_2 = 1:1) over different catalysts with systematically tuned composition, illustrating the effects of (a) Ni loading, (b) dopant species (La and Pr), and (c) Pr/Ce ratios.

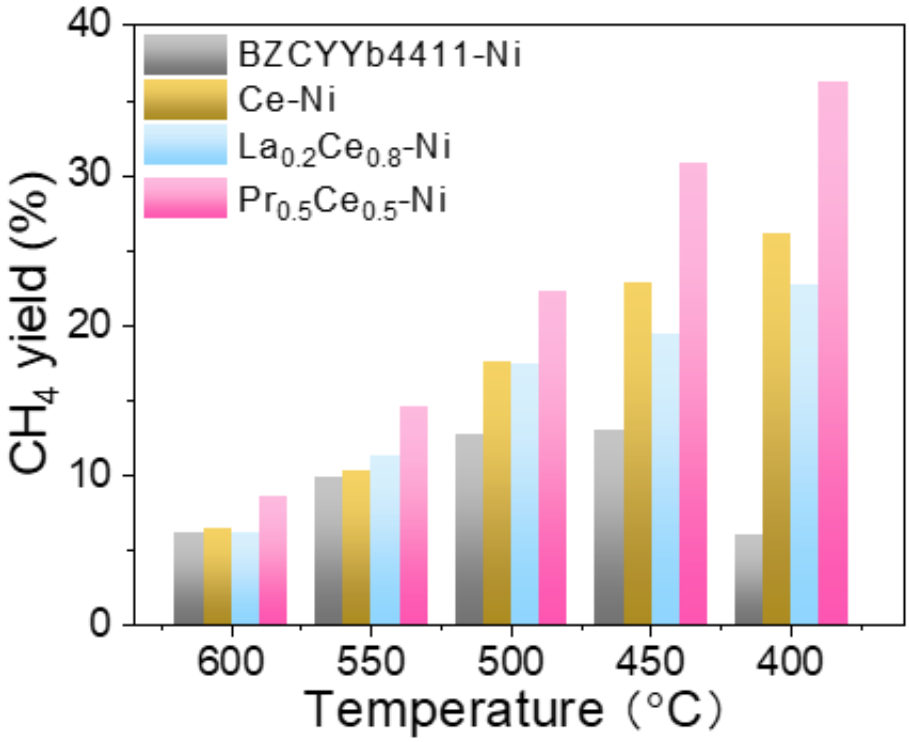

Figure 5.15. CH_4 yield as a function of temperature (400-600 °C) including BZCYYb4411-Ni, Ce-Ni, $La_{0.2}Ce_{0.8}$-Ni, and $Pr_{0.5}Ce_{0.5}$-Ni catalysts.

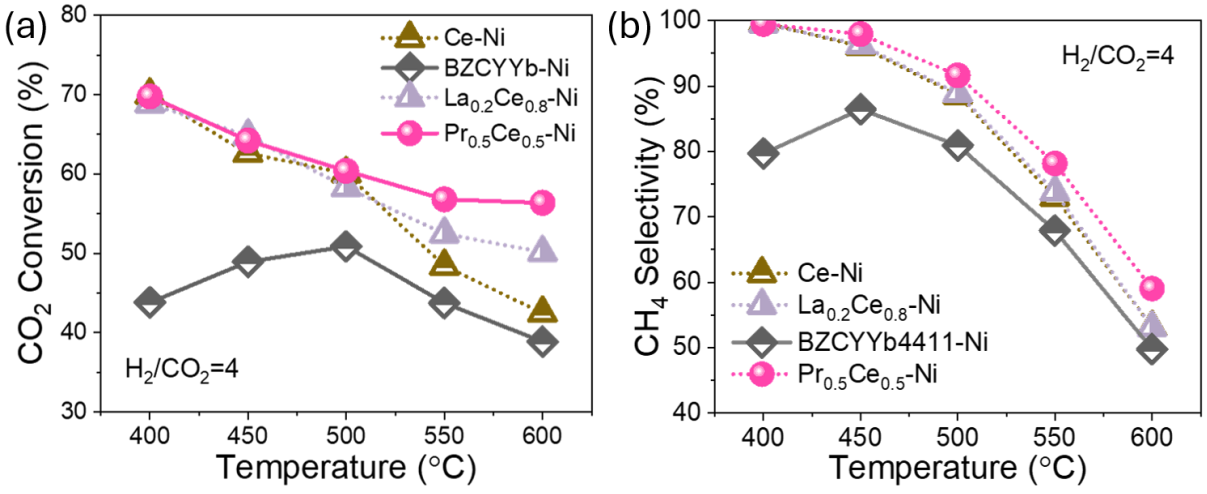

Figure 5.16. Comparison of BZCYYb4411-Ni with designed catalysts (Ce-Ni, $La_{0.2}Ce_{0.8}$-Ni , $Pr_{0.5}Ce_{0.5}$-Ni) for (a) CO_2 conversion and (b) CH_4 selectivity as a function of temperature (400-600 °C, $H_2/CO_2 = 4$).

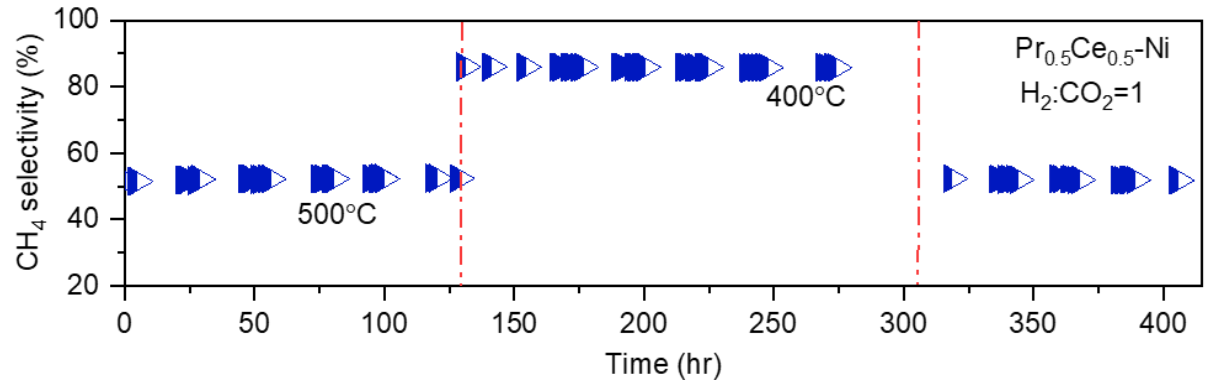

Figure 5.17. Long-term stability of the optimized $Pr_{0.5}Ce_{0.5}$-Ni catalyst at 500 °C and 400 °C (H_2:CO_2=1:1) for CH_4 selectivity.

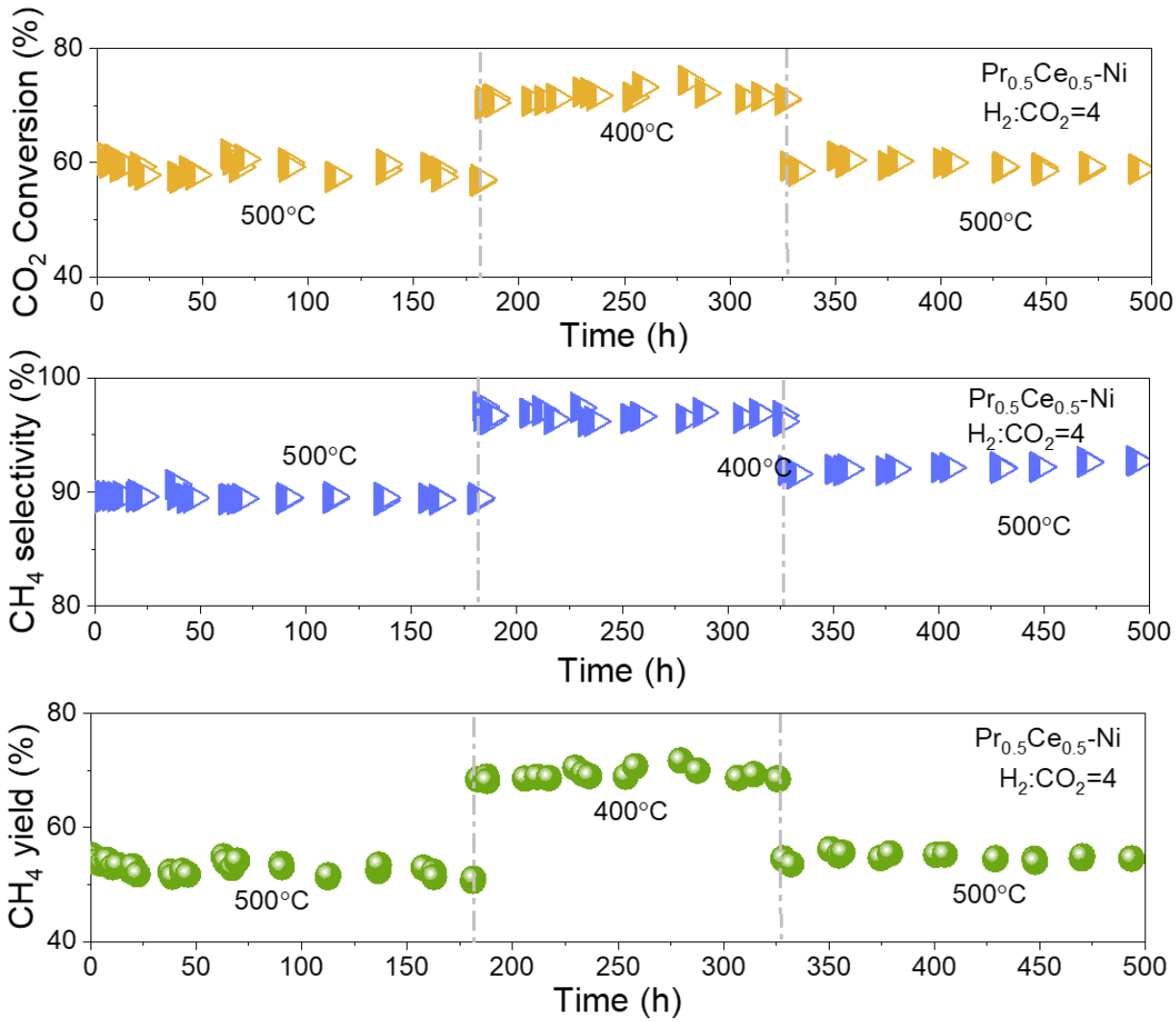

Figure 5.18. Long-term stability of the optimized $Pr_{0.5}Ce_{0.5}$-Ni catalyst at 500 °C and 400 °C (CO_2: H_2=1:4), including (a) CO_2 conversion, (b) CH_4 selectivity and (c) CH_4 yield.

The catalytic stability tests were further conducted on $Pr_{0.5}Ce_{0.5}$-Ni under a CO_2: H_2 ratio of 1:1 at 400-500°C (Figure 5.19a-b, Figure 5.17). As shown in Figure 5.19a, the CH_4 selectivity remains stable at approximately 45% at 500°C for nearly 130 h, and reaches around 40% when the temperature is reduced to 400°C for another 145 h. Upon returning to 500°C, the selectivity recovers to its original value for another 270 h, indicating excellent thermal reversibility and structural robustness. Figure 5.19b shows that the CH_4 yield is also durable. The long-term stability of the optimized $Pr_{0.5}Ce_{0.5}$-Ni catalyst was also evaluated under a CO_2: H_2 ratio of 1:4 (Figure 5.18). The SEM images of the catalyst after stability test are then compared with those of the freshly reduced catalyst (Figure 5.19c), and reveal similar surface morphology and particle distribution, with no apparent structural degradation or carbon deposition observed after such long-term reaction.

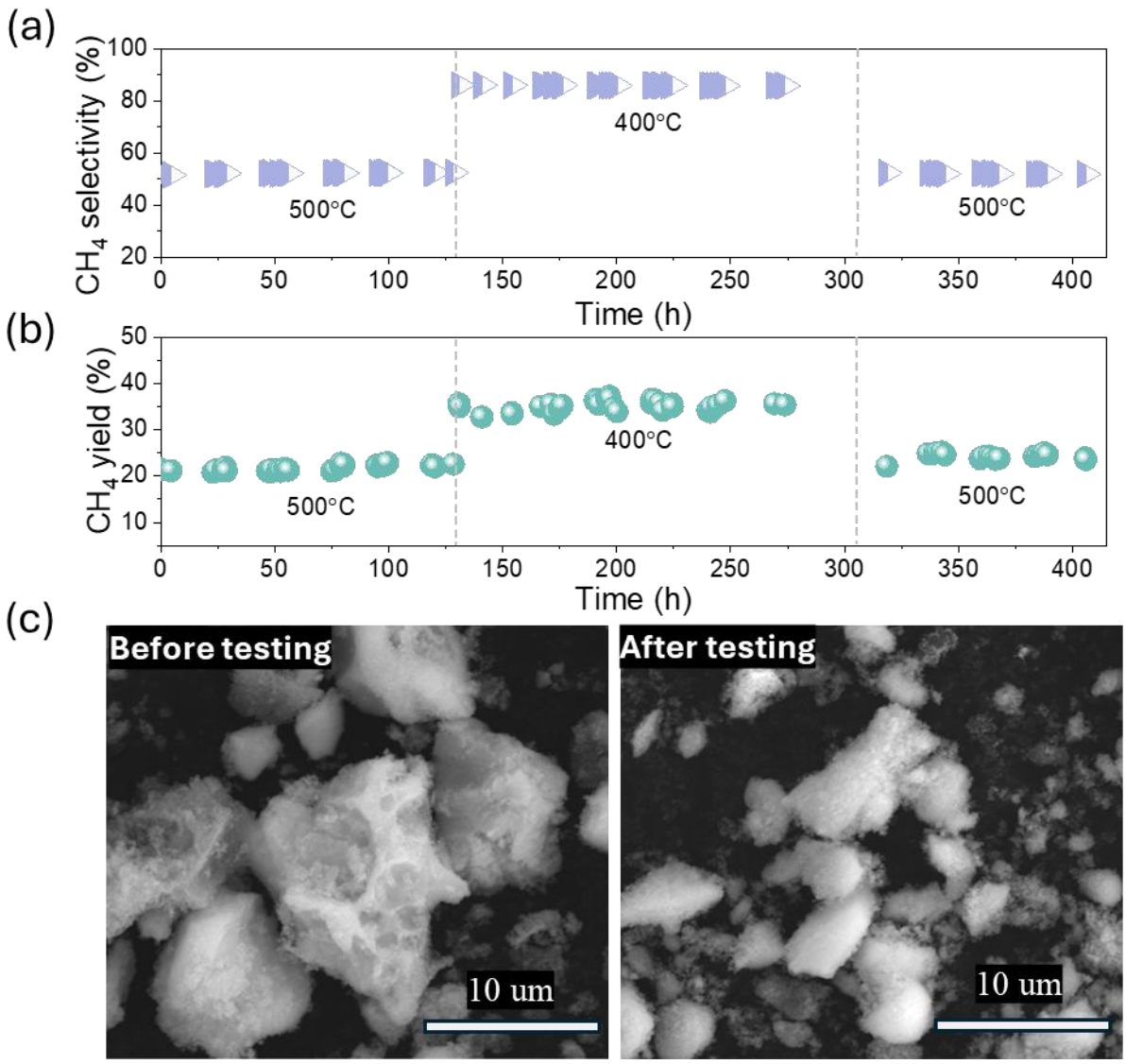

Figure 5.19. Long-term stability of the optimized $Pr_{0.5}Ce_{0.5}$-Ni catalyst at 500 °C and 400 °C (H_2:CO_2 = 1:1), including (a) CH_4 selectivity, (b) CH_4 yield, and (c) SEM images of the $Pr_{0.5}Ce_{0.5}$-Ni catalysts before and after stability testing.

5.3.2 Reducibility of metallic Ni and basic sites on the oxide support

The reduction behavior and metal-support interactions of the synthesized catalysts were investigated by H_2-TPR. As shown in Figure 5.20a-c, all samples exhibit multiple hydrogen consumption peaks, which can be classified into three distinct regions. Peak 1 (P1) (below 350°C)

is typically associated with the reduction of highly dispersed and weakly bound NiO species on the surface.[189-191] Peak 2 (P2) located at intermediate temperature (350-450 °C) corresponds to the bulk reduction of NiO nanoparticles,[189-191] which constitutes the main reduction event. Peak 3 (P3) (above 450 °C) is related to the reduction of strongly bound NiO species that interact intimately with the oxide support, as well as possible reduction of the doped Ni from the lattice from the support itself. [189-191]

BZCYYb4411-Ni (Figure 5.20a) exhibits a dominant reduction peak at high temperature (P2/P3 region). In contrast, the Ce-Ni$_x$ series exhibits a well-defined P1 peak. Notably, $La_{0.2}Ce_{0.8}$-Ni shows a much less pronounced P1 feature (Figure 5.20b), indicating that La incorporation does not significantly enhance low-temperature reducibility. For the Ce-Ni$_x$ series, P2 gradually shifts toward higher temperatures and becomes more intense as the Ni loading increases (Figure 5.20a). The enhanced P2 intensity also reflects an increased amount of reducible Ni species, corresponding to the higher overall Ni content. Upon doping with La or Pr, the reduction behavior changes more noticeably in the high-temperature region (P3) (Figure 5.20b). Increasing Pr content leads to notable changes in the relative intensities of both P2 and P3 (Figure 5.20c). Specifically, $Pr_{0.8}Ce_{0.2}$-Ni exhibits the most intense P2. In contrast, $Pr_{0.2}Ce_{0.8}$-Ni shows comparable contributions from P2 and P3, albeit at lower overall intensities. $Pr_{0.5}Ce_{0.5}$-Ni displays concurrently enhanced P2 and P3 features, revealing a balanced contribution from reducible bulk NiO species and strong Ni-oxide support interactions.[189] Such a balance is key to achieving moderate metal-support interactions for the CO_2/H_2 absorption and reactions.

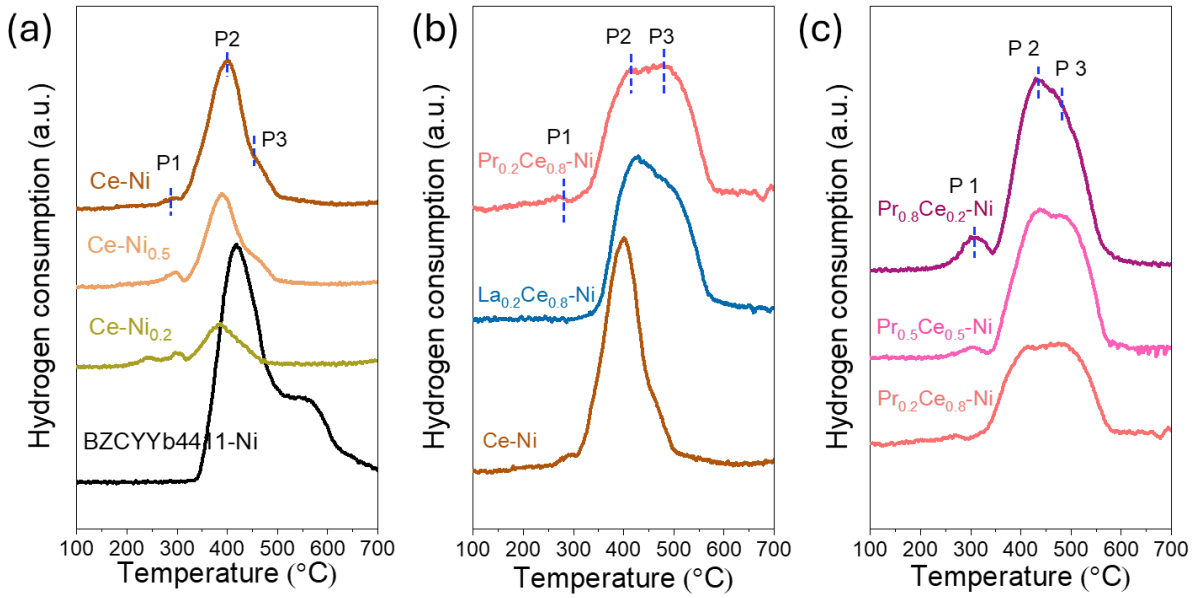

Figure 5.20. H_2-TPR profiles of synthesized catalysts: (a) Ce-Ni$_x$ (x = 0.2, 0.5, 1) catalysts and BZCYYb4411-Ni, (b) Ce-Ni, La- and Pr-doped Ce-Ni catalysts, and (c) Pr$_y$Ce$_{1-y}$-Ni catalysts with different Pr/Ce ratios.

The CO_2 adsorption-desorption behavior was exploited to assess the strength and nature of basic sites on the catalyst surface. As shown in Figure 5.21a, the BZCYYb4411-Ni sample exhibited negligible CO_2 desorption over the entire temperature range. The absence of intrinsic basicity ensures that any observed desorption peaks in other samples originate from the active support rather than the metallic Ni. Ce-Ni$_x$ (Figure 5.21a) and La-doped catalysts (Figure 5.21b) exhibited prominent CO_2 desorption peaks centered below 300°C, indicating a large number of weak basic sites in the low-temperature (LT) region. The weak basic sites typically do not significantly contribute to CO_2 methanation, since CO_2 adsorbed on these sites is not fully activated to break the C-O bond for subsequent hydrogenation.[176, 189, 190] Liu *et al.* have attributed the higher reactivity of Ni catalysts supported by CeO_2 to an increased population of intermediate-strength alkaline sites.[175] Pr$_y$Ce$_{1-y}$-Ni shifts CO_2 adsorption peaks to even higher temperature than Ce-Ni$_x$,

indicating more basic sites for CO_2 binding (Figure 5.21c). More importantly, Pr_yCe_{1-y}-Ni displays significantly enhanced desorption in the intermediate-temperature (IT) region and high-temperature (HT) region. This enhancement is likely related to the substitution of Ce^{4+} with Pr^{3+}, which increases the surface oxygen vacancies that facilitate CO_2 adsorption and activation. In particular, $Pr_{0.5}Ce_{0.5}$-Ni exhibits the most pronounced CO_2 desorption peak in the MT region, which is most relevant for CO_2 methanation.[175, 192]

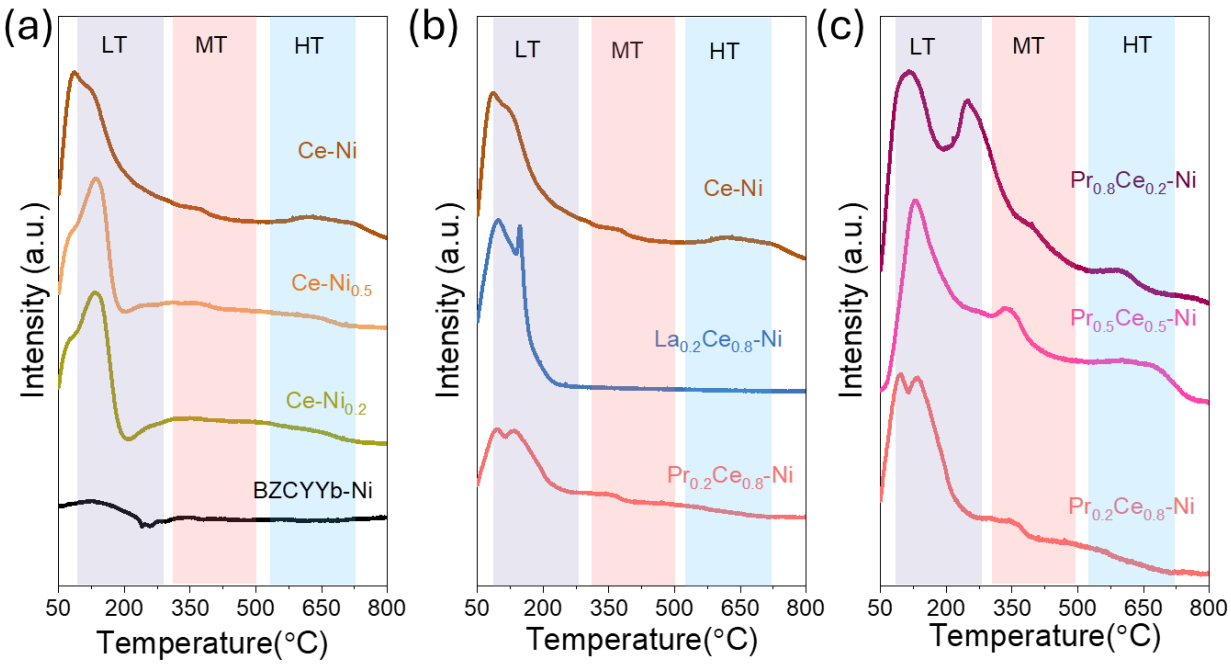

Figure 5.21. CO_2-TPD profiles of synthesized catalysts: (a) Ce-Ni_x (x = 0.2, 0.5, 1)and BZCYYb-Ni, (b) Ce-Ni, La- and Pr-doped Ce-Ni, and (c) Pr_yCe_{1-y}-Ni with different Pr/Ce ratios. CO_2-TPD was conducted by first pre-treating the sample reduced at 600 °C for 2 h, followed by CO_2 adsorption at room temperature, purging with Ar, and finally heating under Ar to monitor CO_2 desorption profiles.

5.3.3 Surface electronic structure of the catalysts by operando spectra

Operando NAP-XPS was employed to probe the surface electronic structure and chemical environment of the catalysts under realistic operating conditions, because most *ex situ* XPS studies show that Ni predominantly exists in oxidized states (Ni^{2+}) in the sub-surface even after high-temperature reduction.[32] The measurements were conducted under a CO_2/H_2 atmosphere at elevated temperatures (~27 °C, 350 °C, and 450 °C) after *in situ* H_2 reduction/activation. The corresponding survey spectra are shown in Figure 5.23 confirming the coexistence of elements on the Ce-Ni and $Pr_{0.5}Ce_{0.5}$-Ni catalysts.

As shown in Figure 5.22a, the Ni 2p peaks at 450 °C indicate the presence of two main types of Ni species, where metallic Ni^0 accounts for the peak centered around 852 eV, and the other peak located at ~853 eV corresponds to oxidized Ni species (Ni^{2+}).[193] The Ni 2p spectra reveal a clear increase in the fraction of metallic Ni species for $Pr_{0.5}Ce_{0.5}$-Ni compared with Ce-Ni, showing that Pr incorporation enhances the reducibility of Ni species, which is consistent to the XRD Rietveld refinement results. Cárdenas-Arenas *et al.*[193]claimed that the Ni-O-Ce interfacial sites are those most active for the initial step of CO_2 dissociation, whereas metallic Ni^0 sites are active for H_2 dissociation. Therefore, the increased Ni^0 fraction in $Pr_{0.5}Ce_{0.5}$-Ni is expected to facilitate hydrogen activation and subsequent hydrogenation steps. In the Ce $3d_{5/2}$ region (Figure 5.22b) at 450 °C, the peaks at ~880 and ~889 eV are assigned to Ce^{4+}, while those at ~883 and ~885 eV correspond to Ce^{3+} species. To present the photoemission feature of Ce $3d_{5/2}$ of $Pr_{0.5}Ce_{0.5}$-Ni and Ce-Ni, the photoemission feature of Ce $3d_{1/2}$ is not shown here. The percentage of Ce^{3+} species is estimated to be ~51% for Ce-Ni and ~56% for $Pr_{0.5}Ce_{0.5}$-Ni. The O 1s peaks at 532-526 eV were assigned to the lattice oxygen, while peaks at 535-526 eV were assigned to surface oxygen (Figure 5.22c).[134] The O 1s spectra show an enhanced contribution from surface-related oxygen

species in $Pr_{0.5}Ce_{0.5}$-Ni, which can be attributed to defect-associated oxygen and surface hydroxyl groups.[134] In addition, the XPS spectra collected at 27 and 350 °C exhibit generally consistent spectral features for the Ce, Ni, Pr, and O species in both Ce-Ni and $Pr_{0.5}Ce_{0.5}$-Ni (Figure 5.25 and Figure 5.26). These results demonstrate that the Pr incorporated into the support lattice modifies the surface chemistry of its host by increasing the concentration of oxygen vacancies and surface-active oxygen species.

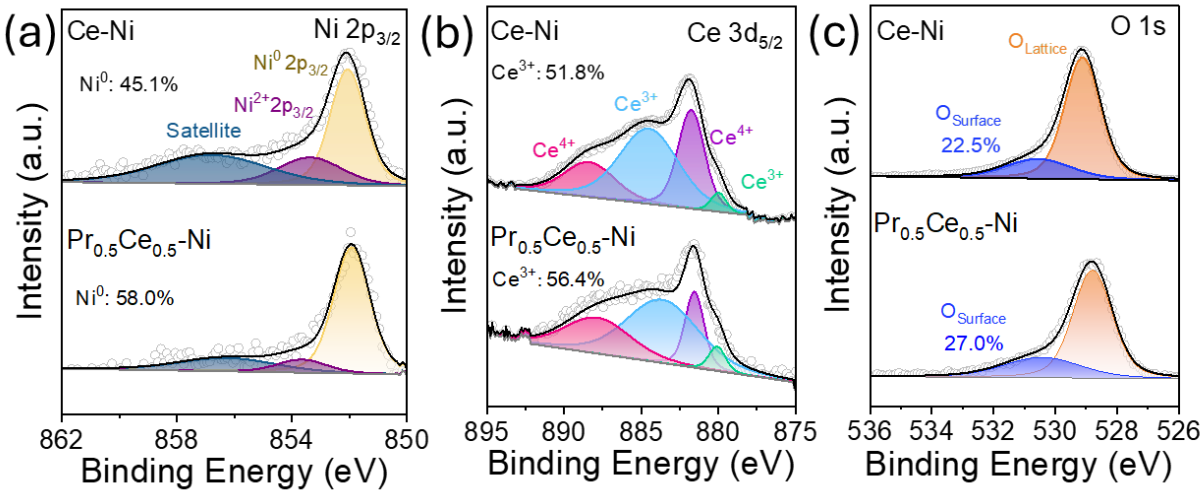

Figure 5.22. *Operando* XPS spectra in the energy region of (a) Ni 2p, (b) Ce 3d, (c) O 1s for Ce-Ni and $Pr_{0.5}Ce_{0.5}$-Ni catalysts measured under CO_2:H_2=1:1 after H_2 reduction at 450 °C.

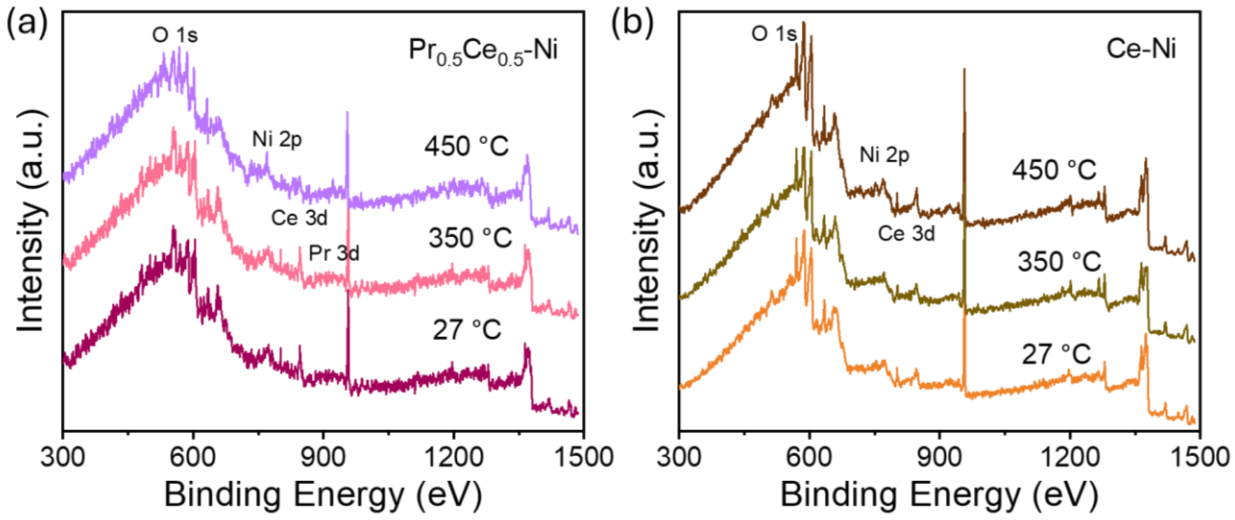

Figure 5.23. *Operando* XPS survey spectra of (a) $Pr_{0.5}Ce_{0.5}$-Ni and (b) Ce-Ni collected under CO_2/H_2 (1:1) at 27 °C, 350 °C, and 450 °C following H_2 reduction at 450 °C.

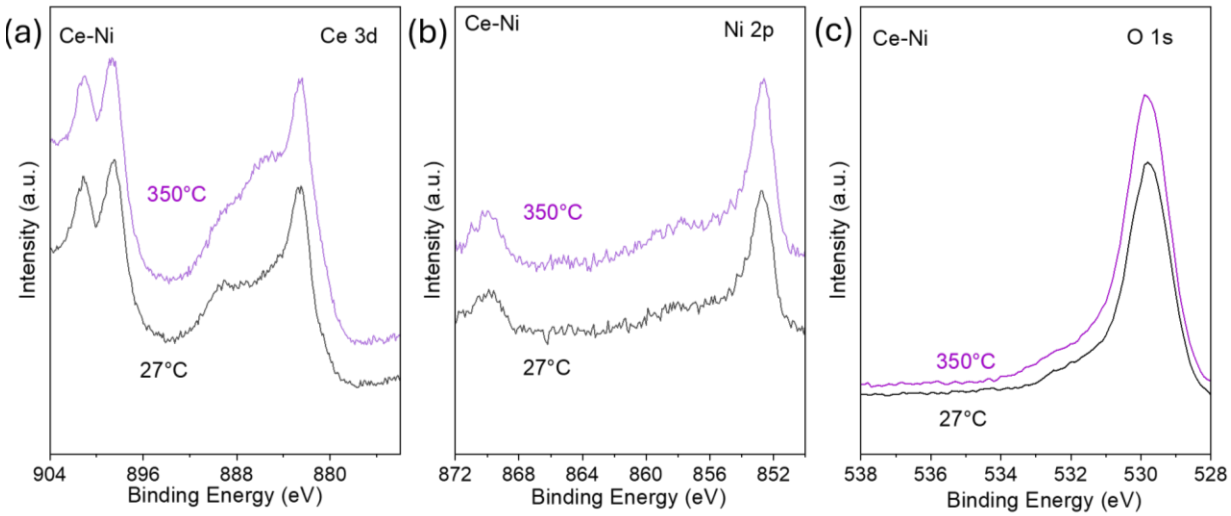

Figure 5.24. *Operando* XPS spectra of Ce-Ni collected in the energy regions of (a) Ce 3d, (b) Ni 2p, and (c) O 1s under CO_2/H_2 (1:1) at 27 and 350 °C after prior reduction in H_2 at 450 °C.

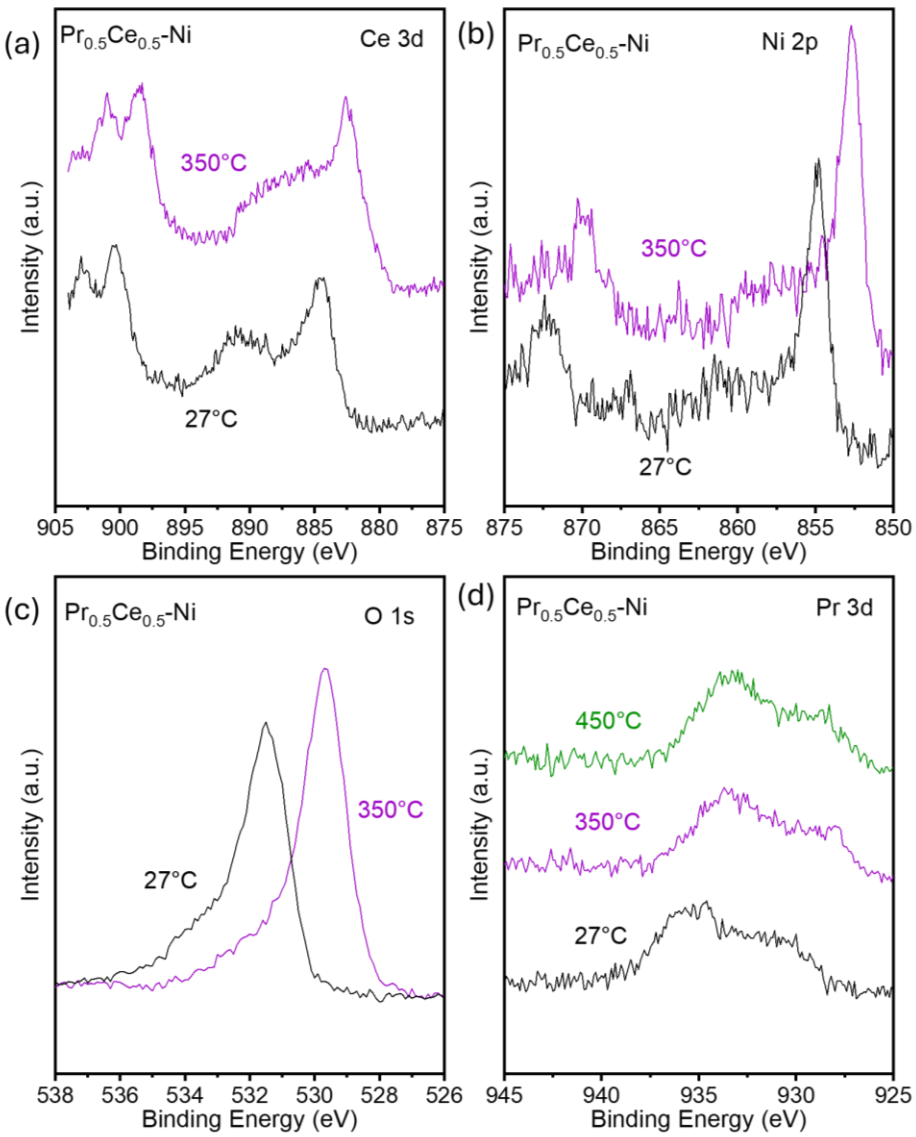

Figure 5.25. *Operando* XPS spectra of $Pr_{0.5}Ce_{0.5}$-Ni collected in the energy regions of (a) Ce 3d, (b) Ni 2p, (c) O 1s, and (d) Pr 3d under CO_2/H_2 (1:1) at 27 and 350 °C after prior reduction in H_2 at 450 °C.

To gain a more comprehensive understanding of the evolution of the electronic structure induced by Pr doping, soft X-ray absorption spectroscopy (XAS) was then employed.[194, 195] Here, three detection modes were applied, including channeltron, drain current (DC), and total

fluorescence yield (TFY) (Figure 5.26, Figure 5.27, Figure 5.28, Figure 5.29 and Figure 5.30), which probe surface (~2-3 nm), subsurface (~10-20 nm), and bulk (~100 nm) information, respectively, enabling depth-resolved characterization of the catalysts. The Ce $M_{4,5}$ spectra of Ce-Ni and $Pr_{0.5}Ce_{0.5}$-Ni split into two prominent peaks in the M4 and M5 regime with the satellite peaks on the higher-energy side (Figure 5.26a). The M4 and M5 spectral peaks arise from the electronic transition from the Ce $3d_{3/2}$ and $3d_{5/2}$ core levels into unoccupied 4f states as per the dipole selection rules.[195] Hence, Ce M_4 for $3d_{3/2}$ and Ce M_5 for $3d_{5/2}$ edges directly reflect the occupancy of the 4f orbital, which are separated by ~17 eV.[195] Compared with Ce-Ni, $Pr_{0.5}Ce_{0.5}$-Ni shows a noticeable decrease in the relative intensity of the M_4 edge and a slight modification of the spectral line shape, evidencing an increased contribution of Ce^{3+} species, which agrees well with the above XPS analysis.

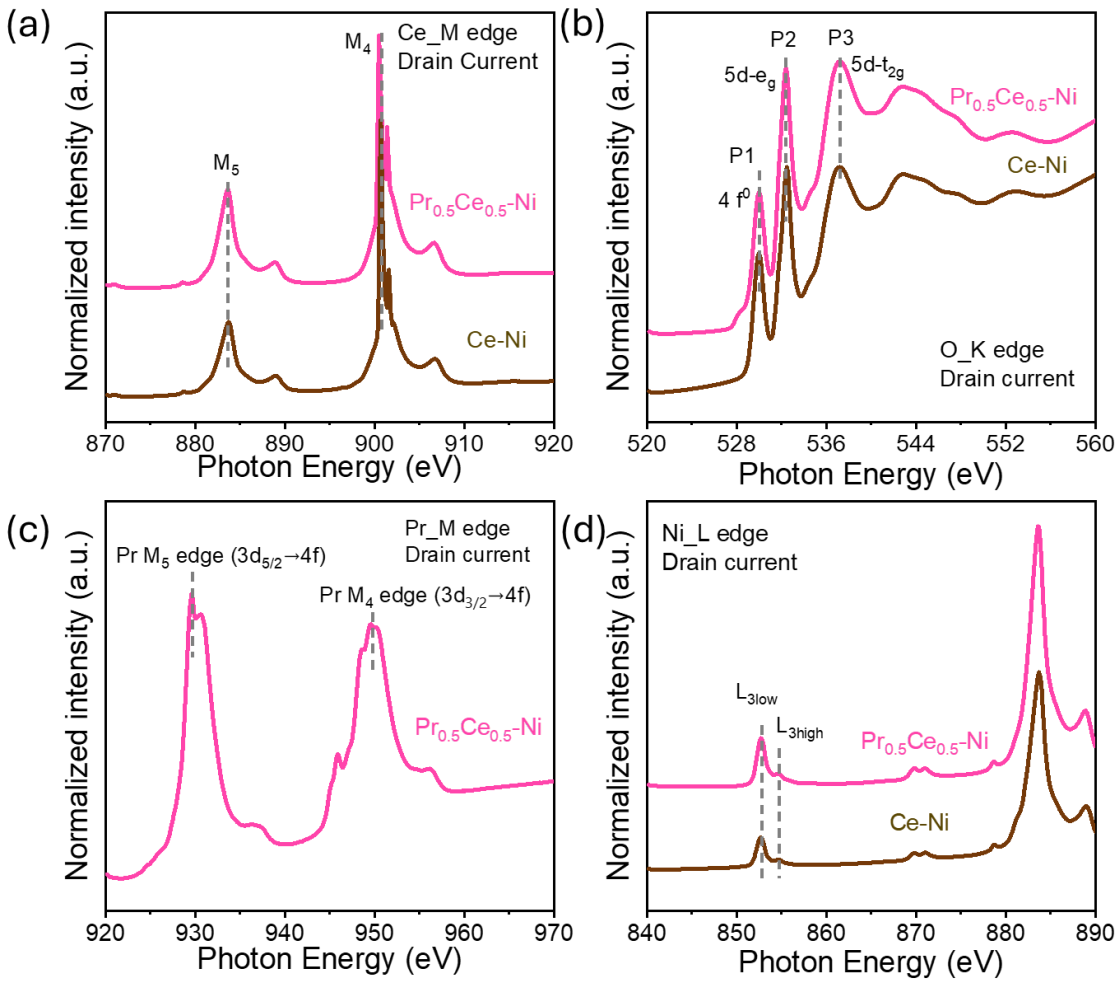

Figure 5.26. Soft XAS spectra for Ce-Ni and $Pr_{0.5}Ce_{0.5}$-Ni in Drain current of (a) Ce $M_{4,5}$ absorption edges, (b) O K-edge, (c) Pr $M_{4,5}$ edge and (d) Ni L-edge.

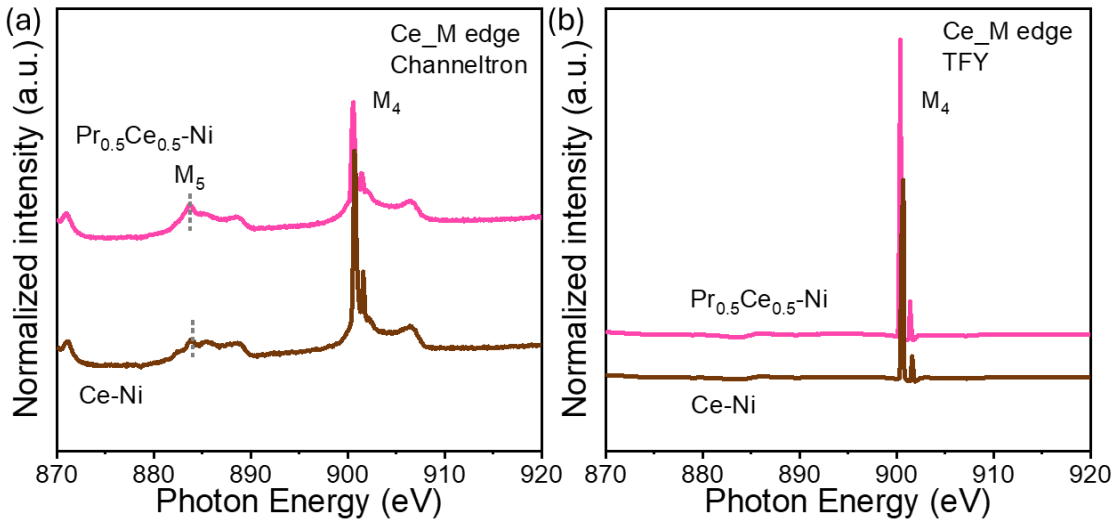

Figure 5.27. Soft XAS spectra of Ce $M_{4,5}$ absorption edges for Ce-Ni and $Pr_{0.5}Ce_{0.5}$-Ni (a) channeltron mode and (b) TFY mode.

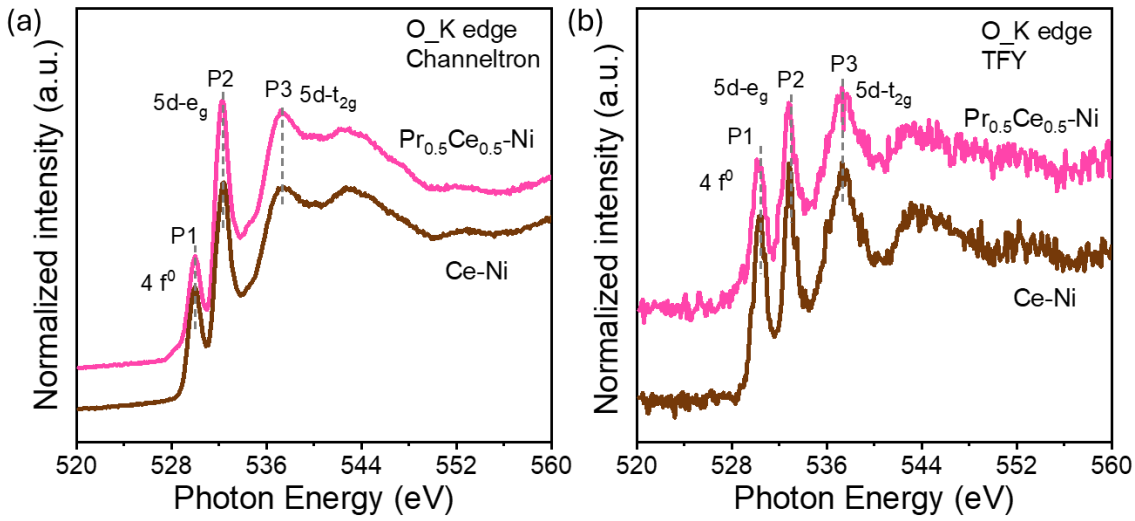

Figure 5.28. Soft XAS spectra of O K-edge for Ce-Ni and $Pr_{0.5}Ce_{0.5}$-Ni (a) channeltron and (b) TFY mode.

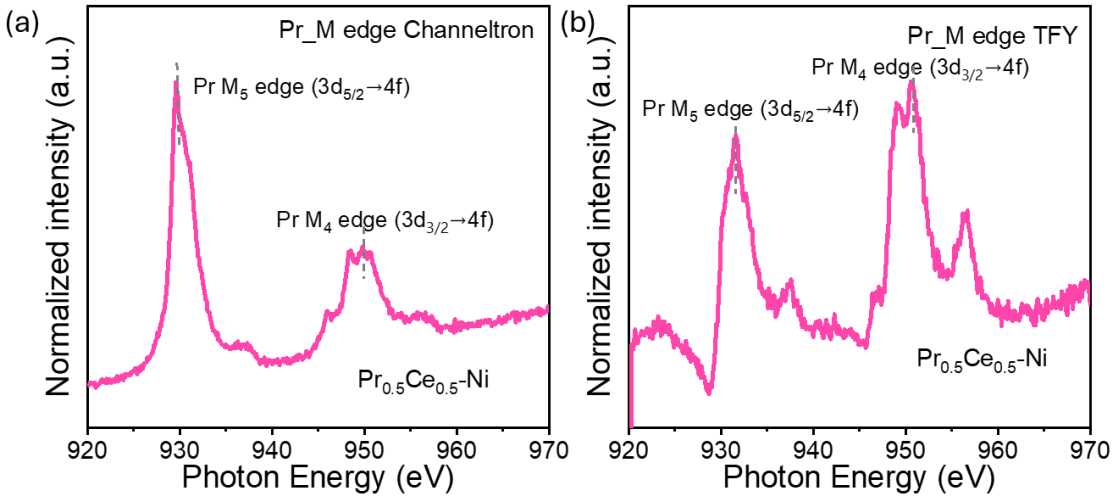

Figure 5.29. Soft XAS spectra of Pr $M_{4,5}$ edge for Ce-Ni and $Pr_{0.5}Ce_{0.5}$-Ni (a) channeltron and (b) TFY mode.

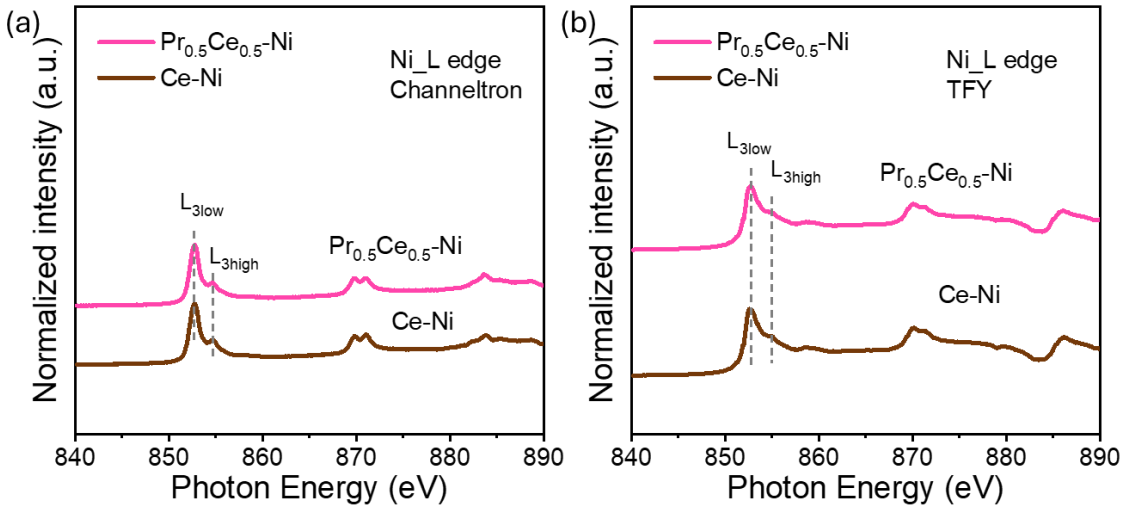

Figure 5.30. Soft XAS spectra of Ni L-edge for Ce-Ni and $Pr_{0.5}Ce_{0.5}$-Ni (a) channeltron and (b) TFY mode.

The O K-edge XAS spectra (Figure 5.26b) further provides insight into the hybridization between O 1s and Ce 4f/5d states. Three main features (Peak 1, Peak 2, Peak 3) were observed.

Peak 1 (P1) (~530 eV) for all samples may be attributed to the transition from O 1s → O 2p states hybridized with the Ce $4f^0$ state, mainly localized at the Ce site, while P2 and P3 correspond to hybridization with the Ce 5d-e_g and 5d-t_{2g} states, due to crystal orbital splitting of the levels in pure and doped CeO_2 nanomaterials.[195] P1 shows minimal difference between the two samples, whereas P2 exhibits a slight shift (~0.1 eV) toward lower energy in $Pr_{0.5}Ce_{0.5}$-Ni, revealing a change in crystal structure.[195] Previous studies have correlated the enhancement of the O 2p-Ce 5d-related features (particularly P2) with increased defect concentration and modified electronic hybridization in non-stoichiometric CeO_2.[194, 195] Therefore, the observed changes suggest that the incorporation of Pr alters the O 2p-Ce electronic coupling.

To directly probe the role of Pr, the Pr $M_{4,5}$-edge XAS was analyzed (Figure 5.26c). The spectra display characteristic multiplet features corresponding to transitions from Pr 3d to the unoccupied 4f states. Pr in ceria-based systems is typically stabilized in the Pr^{3+} state.[196] In the present case, the spectral features are dominated by Pr^{3+} characteristics, supporting that Pr is primarily incorporated into the CeO_2 lattice in the trivalent state.[196] The absence of significant peak shifts suggests that Pr is incorporated into the lattice rather than forming segregated phases. In Figure 5.26c, the peak intensity ratio between the high-energy shoulder (L_{3high}) and the low-energy shoulder (L_{3low}) of the L3-edge is positively correlated to the Ni oxidation state. At a probing near-surface depth (10-20 nm) by the DC mode, the Ce-Ni sample shows a lower L_{3high}/L_{3low} ratio and thereby a lower Ni oxidation state than $Pr_{0.5}Ce_{0.5}$-Ni on the particle surface (Figure 5.26d). The Ni oxidation state remains virtually the same for Ce-Ni and $Pr_{0.5}Ce_{0.5}$-Ni based on the channeltron mode and TFY mode (Figure 5.30), showing a high similarity of Ni oxidation state in the bulk between Ce-Ni and $Pr_{0.5}Ce_{0.5}$-Ni samples.

5.3.4 Probing the CO_2 methanation reaction pathways by operando DRIFTS

To gain insight into the reaction pathway, *Operando* DRIFTS measurements were conducted to compare the CO_2 hydrogenation mechanism over the $Pr_{0.5}Ce_{0.5}$-Ni catalyst with that of the BZCYYb4411-Ni electrode at 400°C (Figure 5.31a-c) under the CO_2 and H_2 working conditions. Unlike the reference electrode, the DRIFTS spectra of $Pr_{0.5}Ce_{0.5}$-Ni show an obvious CH_4-related peak (~3015 cm^{-1}) (Figure 5.31b), suggesting high selectivity of this catalyst toward CH_4 production, consistent with the performance shown in Figure 5.13d. Moreover, strong and well-defined bands corresponding to formate and carbonate species (1600-850 cm^{-1}), which are key catalytic intermediates in CO_2 hydrogenation,[41] were observed while only very weak signals were detected for BZCYYb-Ni. Figure 5.31d highlights the distinct vibrational features associated with surface carbonate and formate species for different catalysts. Compared with BZCYYb-Ni, Ce-Ni and $Pr_{0.5}Ce_{0.5}$-Ni show distinct vibrational bands assigned to formyl (HCO*) species (~1758 cm^{-1} and ~1430 cm^{-1}),[41] formate (HCOO*) species (~1546 and ~1363 cm^{-1}),[134] monodentate carbonate (~1070 cm^{-1}),[32] and carbonate (CO_3*) species (~840 cm^{-1}).[32] In contrast, BZCYYb-Ni exhibits weak, noisy peaks across 1800-1300 cm^{-1}, which might be ascribed to the H_2O produced during the reaction and poor CO_2 adsorption. This observation supports our CO_2-TPD results for BZCYYb-Ni, which show relatively flat, weak signals indicative of limited CO_2 adsorption capability (Figure 5.21a). However, compared with Ce-Ni, $Pr_{0.5}Ce_{0.5}$-Ni shows more pronounced bands of reactive HCOO* and carbonate, but less HCO*. The stronger HCOO* bands and more intense signals in the carbonates signal region (~1758-845 cm^{-1}) demonstrate that these surface species are dynamically involved in CO_2 activation and hydrogenation.

To examine the effect of temperature on this reaction process, the temperature-equilibrium DRIFTS spectra were collected between 300 °C and 500 °C (Figure 5.31e-f). BZCYYb-Ni shows

a much stronger temperature-dependent change in HCO* (~1430 cm^{-1}) and HCO_3* signals (~1646 cm^{-1}) but no observable HCOO* features (Figure 5.31e), implying that the reaction pathway likely does not proceed via formate but instead follows a formyl-related route. The coexistence of HCO_3* and stable CO_3* species also suggests a less dynamic CO_2 adsorption-conversion equilibrium, likely due to the limited surface reducibility on BZCYYb-Ni. Ce-Ni shows weaker temperature dependence (Figure 5.31f), although slight variations are observed in the HCOO* bands. Relative to the $Pr_{0.5}Ce_{0.5}$-Ni, the intensity of HCOO* and CO_3* species on Ce-Ni is much lower. The modest increase in the HCOO* bands with temperature suggests that methanation can still proceed but will be hindered by the formation and decomposition of HCOO*. In addition, the HCO* signal increases with temperature, indicating the likelihood of a competing formyl-related pathway. With increasing temperature, the intensities of the HCOO* and CO_3* bands in $Pr_{0.5}Ce_{0.5}$-Ni (Figure 5.31g) gradually increase, indicating that these species are becoming more stable during hydrogenation. The HCO* band (1430 cm^{-1}) slightly weakens, while the HCOO* bands (1510 and 1360 cm^{-1}) become stronger, suggesting that, at higher temperatures, the reaction pathway on $Pr_{0.5}Ce_{0.5}$-Ni is more likely to proceed via HCOO* rather than HCO*. The pronounced CO_3* signal at ~840 cm^{-1} for $Pr_{0.5}Ce_{0.5}$-Ni also reflects the strong basicity of the Pr-Ce mixed support, which facilitates CO_2 adsorption and conversion into the HCOO* intermediate.

The dynamic evolutions of surface species during CO_2 hydrogenation at 300-500 °C on all catalysts were tracked by the DRIFTS spectra in Figure 5.32. The DRIFTS spectra were collected at 400 °C over a period of 70 minutes to gain time-resolved insights into methane formation of $Pr_{0.5}Ce_{0.5}$-Ni (Figure 5.31h). The gaseous CH_4 band (~3016 cm^{-1}) is barely detectable at the beginning of the reaction (0-10 min) but becomes progressively stronger with time (15-70 min). The continuous growth of this CH_4 band clearly indicates sustained methane production on the

$Pr_{0.5}Ce_{0.5}$-Ni surface under steady CO_2/H_2 flow conditions, suggesting enhanced methanation activity (Figure 5.13d). However, the time-resolved DRIFTS spectra of Ce-Ni (Figure 5.33) show much less pronounced evolution of the CH_4-related peaks, together with no obvious changes in the formate and carbonate regions during the reaction process. On the other hand, Figure 5.31h shows a progressive growth of the CO_3* envelope in the 1300-900 cm^{-1} region, notably monodentate carbonate at ~1070 cm^{-1} and CO_3* at ~840-860 cm^{-1}, which might be attributed to the rapid CO_2 capture on the basic sites of the Pr doped-CeO_2 and the build-up of a CO_3* reservoir during reaction. Moreover, $Pr_{0.5}Ce_{0.5}$-Ni exhibits more obvious changes in the OH*, CO_3*, and HCOO* regimes compared with Ce-Ni (Figure 5.32), indicating more dynamic CO_2 adsorption and intermediate conversion processes during CO_2 hydrogenation.

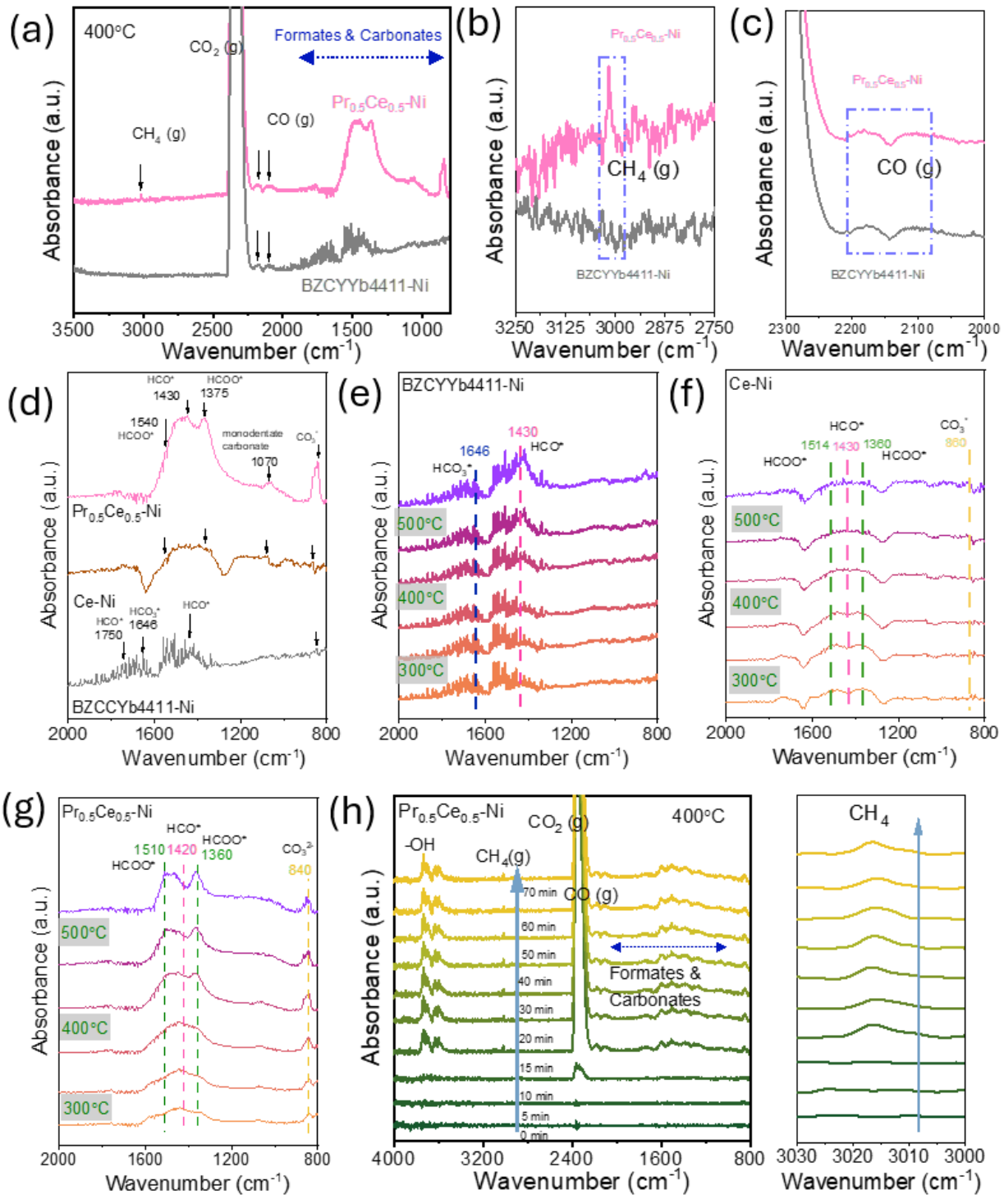

Figure 5.31. (a) DRIFTS spectra of $Pr_{0.5}Ce_{0.5}$-Ni and BZCYYb4411-Ni to probe the products and intermediate species in CO_2 and H_2 atmosphere; The samples were first reduced at 600°C for 1 h and cooled down to 30 °C under H_2. The atmosphere was then changed to ultrahigh purity (UHP)

Ar to collect the background. Then the temperature increased to 400 °C at a ramping rate of 10°/min. The feeding gas was changed from UHP Ar to 10 sccm CO_2, 10 sccm H_2, and 20 sccm Ar. The spectra were collected after reaching equilibrium. (b) enlarged view of the CH_4-related region in (a); (c) enlarged view of the CO-related region in (a); DRIFTS of CO_2 hydrogenation over the carbonate bands in the catalyst of (d) $Pr_{0.5}Ce_{0.5}$-Ni, Ce-Ni, and BZCYYb-Ni at 400°C; (e) temperature-dependent (250 to 500 °C) DRIFTS behavior of (e) $Pr_{0.5}Ce_{0.5}$-Ni,(f) Ce-Ni and (g) BZCYYb-Ni; (h) time-resolved DRIFTS of CO_2 methanation over $Pr_{0.5}Ce_{0.5}$-Ni at 400°C. The samples were first reduced at 600°C for 1 h and cooled down to 30 °C under H_2. The atmosphere was then changed to UHP Ar. Then the temperature was increased to 400 °C at a ramping rate of 10° min^{-1} to collect the background, and the feeding gas was changed from UHP Ar to 10 sccm CO_2, 10 sccm H_2, and 20 sccm Ar.

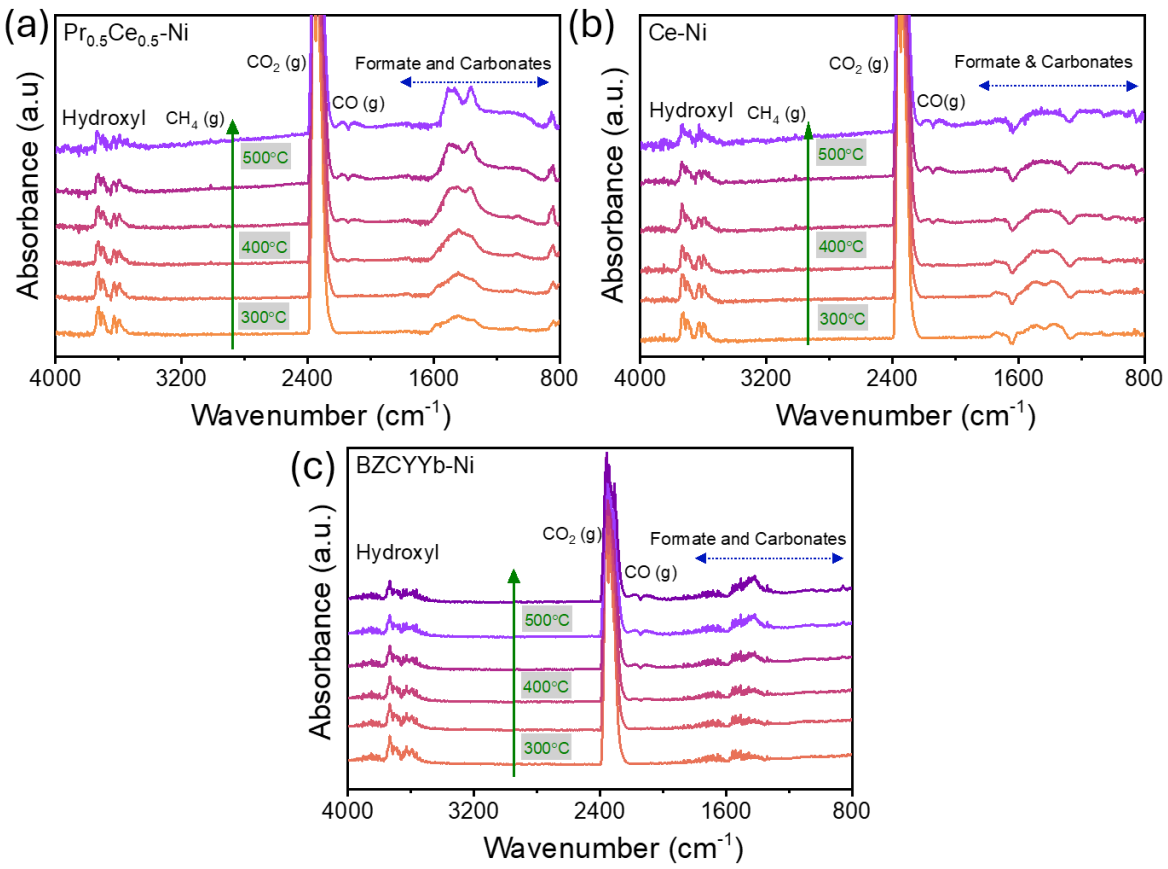

Figure 5.32. DRIFTS spectra of CO_2 hydrogenation over full range (4000-800 cm^{-1}) with temperature of (a) $Pr_{0.5}Ce_{0.5}$-Ni, (b) Ce-Ni and (c) BZCYYb4411-Ni. The samples were first reduced at 600°C for 1 h and cooled down to 30 °C under H_2. The atmosphere was then changed to ultrahigh purity (UHP) Ar to collect the background. Then the temperature increased to testing temperature (from 300 to 500 °C with a temperature interval of 50 °C) at a ramping rate of 10°/min and held at the testing temperature. The feeding gas was changed from UHP Ar to 10 sccm CO_2, 10 sccm H_2, and 20 sccm Ar. The spectra were collected after reaching equilibrium.

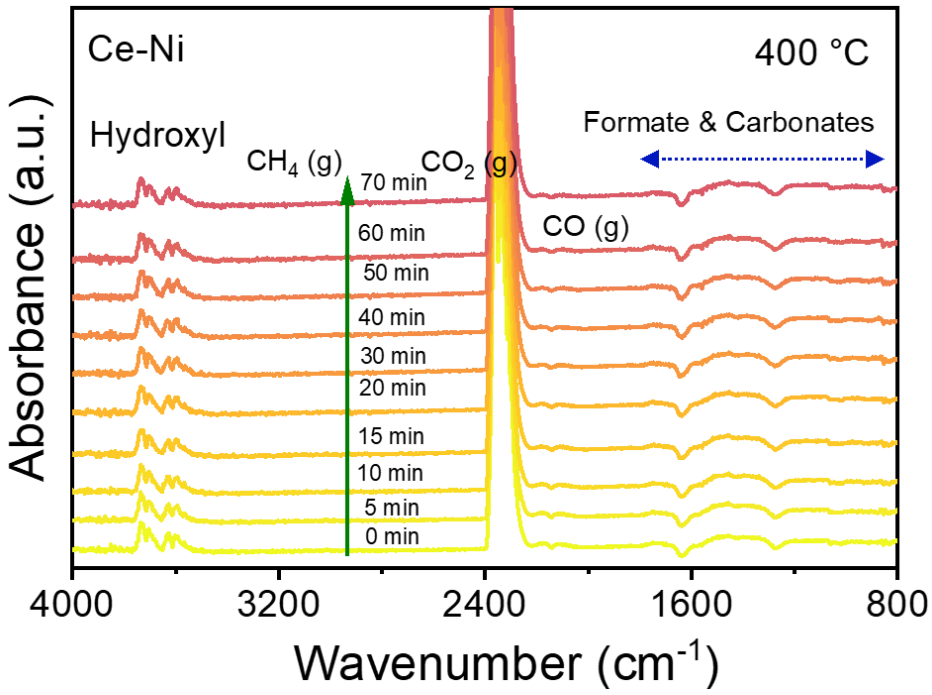

Figure 5.33. time-resolved DRIFTS of CO_2 methanation over Ce-Ni at 400ºC. The atmosphere was then changed to UHP Ar. Then the temperature was increased to 400 °C at a ramping rate of 10° min^{-1} to collect the background, and the feeding gas was changed from UHP Ar to 10 sccm CO_2, 10 sccm H_2, and 20 sccm Ar.

The overall CO_2 methanation pathways can be summarized as two pathways, i.e., CO* pathway (formyl-related) and the formate pathway,[41, 197] as illustrated in Figure 5.34 and Figure 5.35. In the CO* pathway, the adsorbed CO_2* is first converted into a carboxyl intermediate (COOH*) that subsequently dissociates into CO*, followed by stepwise hydrogenation through HCO*, H_2CO*, CH_2*, and CH_3* intermediates toward CH_4 formation. In the formate pathway, CO_2* is hydrogenated to HCOO*, followed by the formation of H_2COO* and H_2COOH intermediates before converging into the common hydrogenation sequence toward CH_4. BZCYYb4411-Ni shows pronounced temperature-dependent variations in HCO* and HCO_3*

species but no observable HCOO* features, suggesting that the formyl-related route dominates on this catalyst and that HCO* likely behaves as a spectator-like intermediate.

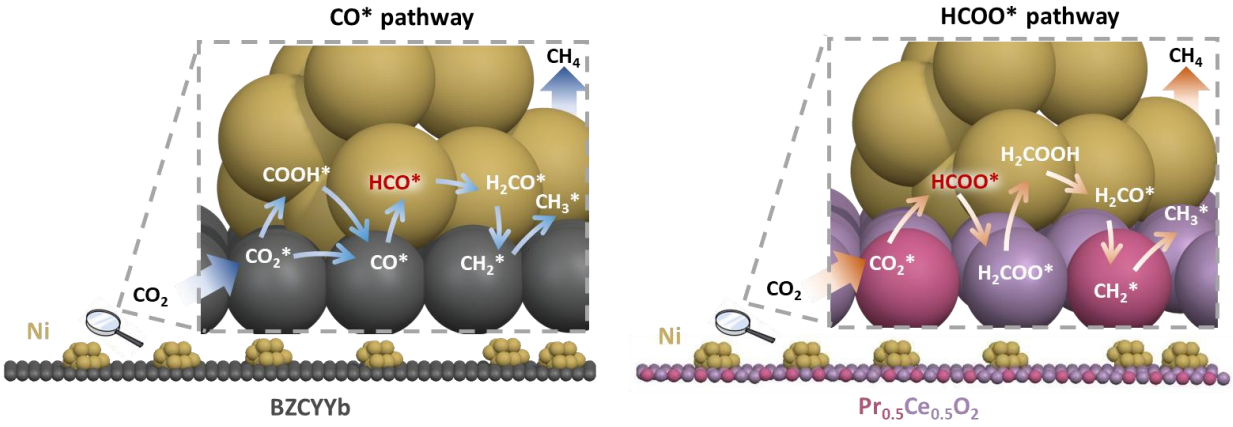

Figure 5.34. Schematic illustrations of the proposed CO_2 hydrogenation pathways over conventional BZCYYb-Ni and $Pr_{0.5}Ce_{0.5}O_2$-supported Ni catalysts, highlighting the distinct CO*-mediated and HCOO*-mediated routes toward CH_4 formation.

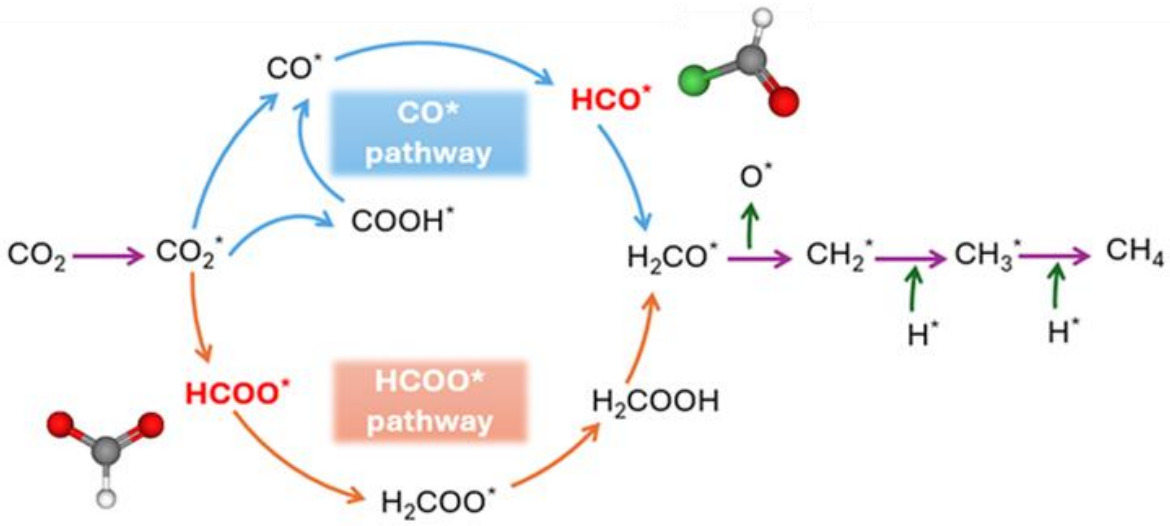

Figure 5.35. Schematic illustration of the proposed CO_2 hydrogenation pathways over catalysts, including the HCOO*-mediated and CO*-mediated reaction routes toward CH_4 formation.

For $Pr_{0.5}Ce_{0.5}$-Ni catalysts, the metallic Ni facilitates efficient H_2 activation, while the enriched oxygen vacancies and stronger basic sites that facilitate CO_2 adsorption and activation. This synergistic metal-support interaction is directly reflected in the DRIFTS spectra.[186] $Pr_{0.5}Ce_{0.5}$-Ni shows a higher concentration of active HCOO* intermediate than BZCYYb-Ni. The HCOO*-related vibrational bands of $Pr_{0.5}Ce_{0.5}$-Ni become progressively more pronounced as temperature increases, indicating that CO_2 hydrogenation proceeds via dual reaction pathways, with a growing preference for the formate-mediated route at elevated temperatures. DRIFTS provided strong evidence of enhanced formation of CO_3* and HCOO* intermediates, consistent with rapid CO_2 adsorption on the basic Pr-doped support and continuous conversion through formate intermediates, while the species involved in the CO* pathway were suppressed. These results demonstrate that Pr doping not only enhances CO_2 adsorption and activation through increased oxygen vacancy concentration and basicity, but also promotes a more efficient formate pathway, thereby leading to the significantly enhanced CH_4 activity and selectivity of $Pr_{0.5}Ce_{0.5}$-Ni.

5.4. Conclusion

A rationally designed Pr-doped CeO_2-supported Ni catalyst was developed for high-performance CH_4-selective CO_2 methanation. Compared with the conventional BZCYYb4411-Ni electrode, it achieves > 3.5-fold higher CO_2 conversion and ~2.1-fold higher CH_4 selectivity at 400 °C under a CO_2:H_2 = 1:1, while maintaining stable performance for over 400 h under continuous operation at 400-500 °C. Beyond performance improvement, this work provides a fundamental understanding of how Pr incorporation regulates catalyst structure and surface chemistry. Comprehensive structural characterization reveals that successful doping of Pr into the CeO_2 lattice balances metal-support interactions, enhances reducibility, and increases the population of moderate and strong

basic sites. More importantly, *Operando* XPS reveals an increased fraction of Ce^{3+} species and an enrichment of surface oxygen-related components in $Pr_{0.5}Ce_{0.5}$-Ni. Complementary soft XAS confirms that Pr is primarily incorporated as Pr^{3+}, inducing oxygen vacancies via charge compensation and tuning the O 2p-Ce hybridization, while moderately modifying the near-surface electronic structure of Ni. DRIFTS measurements demonstrate that these electronic and structural modulations lead to a mechanistic shift in CO_2 methanation. Unlike the conventional BZCYYb4411-Ni electrode, which predominantly follows a CO-mediated pathway, the $Pr_{0.5}Ce_{0.5}$-Ni catalyst promotes the formation and hydrogenation of reactive formate intermediates, enabling a formate-mediated pathway that favors CH_4 production. Overall, this work establishes a clear structure-property-mechanism relationship, providing fundamental insights into the design of advanced catalysts through electronic structure engineering and tuning of metal-support interactions.

Chapter 6 - Conclusion

The overall objective of this dissertation was to develop a fundamental understanding of proton-related processes and catalytic reaction mechanisms in protonic ceramic materials through the integration of operando vibrational spectroscopy, kinetic analysis, and theoretical modeling. By combining DRIFTS, ECR, DFT, and advanced structural and electronic characterization techniques, this dissertation establishes quantitative relationships between local proton chemistry, bulk transport behavior, interfacial reaction pathways, and electrochemical performance. The knowledge gained provides important insights into the rational design of high-performance protonic ceramic electrochemical devices operating at intermediate temperatures.

Chapter 3 established a quantitative operando DRIFTS-ECR-DFT framework to investigate hydration, dehydration, and H_2O/D_2O isotope-exchange processes in BZCYYb4411 proton-conducting electrolytes. Time-resolved DRIFTS measurements demonstrated that both hydration and dehydration follow first-order kinetics, while hydration proceeds substantially faster than dehydration, exhibiting activation energies of 35.8 and 63.7 kJ mol^{-1}, respectively. Combined with DFT calculations, the results revealed the fundamental energetic origins governing proton incorporation and release within the perovskite lattice, providing molecular-level understanding of proton defect formation and migration. H_2O/D_2O isotope-exchange experiments further revealed a clear directional dependence in proton-exchange kinetics, where the replacement of surface hydroxyls by deuteroxyls proceeds more slowly than the reverse process. The persistence of residual O-H signals together with the crossover behavior of normalized O-H and O-D intensities demonstrated the coexistence of two proton populations consisting of rapidly exchanging mobile hydroxyl species and more strongly bound proton species with significantly slower exchange kinetics. DFT calculations further showed that D-containing configurations

consistently possess lower vibrational free energies than their H-containing counterparts and that the magnitude of the isotope effect strongly depends on the local dopant-vacancy environment. Complementary ECR measurements demonstrated that bulk hydration kinetics cannot be described by a simple one-step water diffusion process but instead follow a coupled two-fold diffusion mechanism involving both proton-related and vacancy-related equilibration processes. Collectively, this chapter established a quantitative framework linking surface proton chemistry with bulk proton transport, providing new mechanistic insights into proton transport in proton-conducting oxides.

Building upon the operando methodology established in Chapter 3, Chapter 4 investigated how a commonly used sintering additive, Ni, influences proton transport chemistry in BZCYYb proton-conducting electrolytes. Operando DRIFTS combined with H_2O/D_2O isotope-exchange measurements revealed that Ni addition significantly slows hydration equilibration, prolongs dehydration, and markedly suppresses proton/deuteron exchange kinetics compared with pristine BZCYYb. Quantitative kinetic analysis further showed substantially reduced isotope-exchange rate constants together with a dramatic reduction in the apparent activation energy from 54.75 to 9.70 kJ mol^{-1}. These observations suggest that Ni fundamentally alters the rate-limiting step governing proton/deuteron exchange, resulting in slower overall proton dynamics with considerably weaker temperature dependence. Rather than serving solely as a processing aid for densification, Ni was shown to modify proton transport chemistry at the atomic level, highlighting an often-overlooked coupling between electrolyte processing and proton transport properties. This work therefore extends the operando DRIFTS methodology beyond mechanistic studies toward evaluating processing-induced modifications of proton-conducting electrolytes.

While Chapters 3 and 4 focused primarily on proton transport within electrolyte materials, Chapter 5 expanded the operando spectroscopy approach to investigate catalytic reaction mechanisms at functional electrode interfaces. A rationally designed Pr-doped CeO_2-supported Ni catalyst was developed for highly selective CO_2 methanation. Compared with the conventional BZCYYb4411-Ni electrode, the optimized catalyst achieved more than 3.5-fold higher CO_2 conversion and approximately 2.1-fold higher CH_4 selectivity at 400 °C under a CO_2:H_2 ratio of 1:1, while maintaining stable performance for over 400 hours between 400 and 500 °C. Comprehensive structural characterization demonstrated that Pr incorporation strengthens metal-support interactions, enhances catalyst reducibility, and increases the concentration of moderate and strong basic sites. Operando XPS and soft X-ray absorption spectroscopy further revealed that Pr is predominantly incorporated as Pr^{3+}, generating oxygen vacancies through charge compensation and modifying the electronic structure near the catalyst surface. Operando DRIFTS demonstrated that these structural and electronic changes fundamentally alter the CO_2 methanation pathway. Unlike the conventional catalyst, which primarily follows a CO-mediated mechanism, the Pr-doped catalyst promotes the formation and hydrogenation of reactive formate intermediates, thereby favoring a formate-mediated pathway with significantly enhanced methane selectivity. This chapter establishes a direct structure-property-mechanism relationship that provides important guidelines for catalyst design through electronic structure engineering and metal-support interaction optimization.

Although the three studies address different scientific questions, they collectively demonstrate the capability of operando spectroscopy to quantitatively probe dynamic chemical processes in protonic ceramic materials across multiple length scales. Chapter 3 established the fundamental understanding of proton incorporation, isotope exchange, and bulk transport in

proton-conducting electrolytes. Chapter 4 further demonstrated how processing additives can modify these proton-transfer processes by altering local kinetic pathways. Finally, Chapter 5 extended these mechanistic insights from electrolyte proton chemistry to catalytic surface reactions, revealing how electronic structure engineering governs reaction intermediates and catalytic pathways during CO_2 methanation.

Overall, this dissertation establishes operando DRIFTS as a versatile platform for quantitatively investigating dynamic proton-related and catalytic processes in protonic ceramic systems. More importantly, by integrating operando spectroscopy with kinetic modeling, theoretical calculations, and advanced structural characterization, this work provides a comprehensive methodology for correlating atomic-scale structure, surface chemistry, transport kinetics, and catalytic performance. These findings offer fundamental design principles for developing next-generation protonic ceramic fuel cells, electrolyzers, membrane reactors, and related catalytic energy-conversion technologies.

Chapter 7 - Outlook

DRIFTS can offer insights into surface intermediate species involved in catalytic processes. Its ability to provide real-time surface chemistry information is essential for understanding catalytic reactions and enhancing the overall cell performance of PCCs. However, despite its advantages, several challenges and opportunities remain for advancing DRIFTS as a technique for intermediate-temperature PCC research. This dissertation has significantly advanced the application of operando vibrational spectroscopy for protonic ceramic electrochemical cells by establishing quantitative DRIFTS methodologies, integrating H_2O/D_2O isotope exchange with kinetic analysis, correlating surface proton chemistry with bulk transport through combined DRIFTS–DFT–ECR analysis, and extending operando spectroscopy to catalyst reaction mechanisms under realistic operating conditions. These advances demonstrate the capability of operando spectroscopy to provide quantitative mechanistic insights across multiple functional components of PCCs. Despite these achievements, several important challenges remain and provide opportunities for future research: (i) further achieving quantitative analysis capabilities to extract more accurate information from IR signals; (ii) extending *operando* spectroscopy from half-cell configurations to fully integrated PCC devices under realistic electrochemical operating conditions, including simultaneous current loading, high steam partial pressure, and elevated pressure, and allowing for online analysis; (iii) integrating DRIFTS with complementary techniques such as mass spectrometry (MS), *in situ* Raman spectroscopy, X-ray spectroscopy, and neutron-based characterization to simultaneously monitor gas products, surface intermediates, and bulk structural evolution.; (iv) developing customized DRIFTS devices capable of operating under high temperatures, pressures, and complex gas environments; and (v) integrating modeling and AI

for spectral interpretation and mechanism prediction. These directions collectively aim to deepen mechanistic insights and guide materials optimization in PCC systems (Figure 7.1).

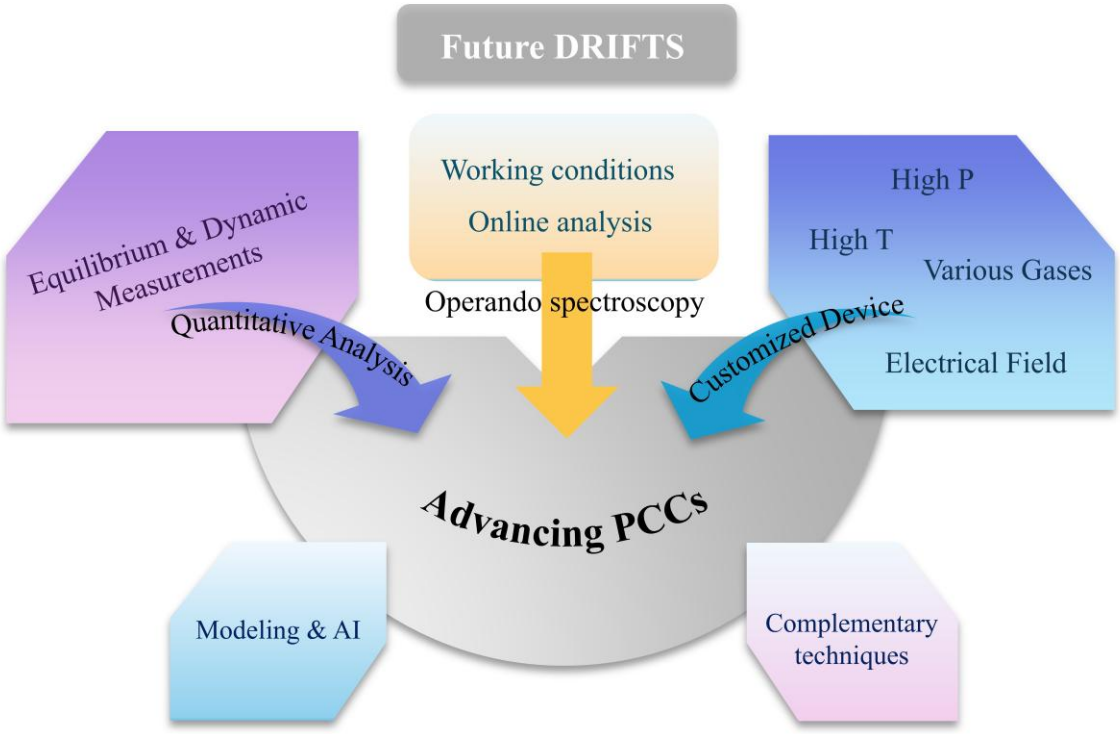

Figure 7.1. Opportunities and challenges for applying DRIFTS to PCC research.

7.1 Quantitative analysis

The previous discussion reviewed DRIFTS applied to PCCs, with DRIFTS mainly being employed as a qualitative method or semi-quantitative in PCCs. . In our work, quantitative operando DRIFTS methodologies were established by integrating time-resolved spectroscopy with kinetic analysis, H_2O/D_2O isotope exchange, and complementary DFT and ECR approaches, demonstrating the capability of DRIFTS to quantitatively investigate proton hydration, dehydration, and surface exchange kinetics. These advances significantly expand the role of DRIFTS beyond qualitative characterization.

Despite this progress, further developments are still needed to fully realize the quantitative potential of operando DRIFTS. DRIFTS can be an accurate quantitative tool for *operando* studies, provided that an appropriate analytical transformation of the diffused intensity is used. For electrochemical catalysis in PCC studies, quantitative analysis enables researchers to integrate spectral data with kinetic models more effectively. However, due to the complexity of diffuse reflectance spectra, such as calibration difficulties, baseline drift, and peak overlap, the relationship between spectral intensity and surface species concentration is often nonlinear. Therefore, calibration curves using reference samples to correlate spectral intensity and eliminate background interference should be carefully constructed.

A sample's absorbance and spectral properties are related and form the basis for many quantitative spectroscopic analyses. For DRIFTS experiments, Kubelka–Munk units and the Kubelka–Munk equation are usually used for quantitative analysis[83, 94]. However, misconceptions about Kubelka–Munk methods still exist in DRIFTS studies involving PCCs, even though alternative approaches like (pseudo-)absorbance have been proposed[83, 94]. Most research either defaults to the Kubelka–Munk function or uses absorbance log(1/R)) without clear justification, and the rationale for selecting a specific intensity transformation function is rarely discussed. Studies by Matyshak and Krylov, supported by subsequent research, show that pseudo-absorbance offers a more linear relationship with surface concentration in the relative reflectance range of 60–100%[83, 198]. This range is relevant to many DRIFTS experiments where absorption by adsorbed species is weak. Additionally, the (pseudo-)absorbance method mitigates issues like baseline drift during measurements, making it preferable under these conditions. Only when reflectance drops significantly (<60%) does the Kubelka–Munk transform become more appropriate[83].

The choice between using the Kubelka–Munk units and absorbance units is highly dependent on the experimental conditions, catalytic reactions, and specific catalysts. For example, in Meunier et al.'s study of the RWGS reaction over a Pt/CeO_2 catalyst, absorbance units are more appropriate when investigating surface species by DRIFTS. The disappearance of the formate band (2948 cm^{-1}) was tracked after replacing the reaction feed (1% CO_2 + 4% H_2 in Ar) with pure argon[199]. When Kubelka–Munk units were used, the formate bands became distorted due to a slight baseline shift. In contrast, the absorbance spectra remained well resolved and showed no significant distortion for the formate band. This discrepancy primarily resulted from the variation in the absorption and scattering properties of the catalyst upon introducing the reaction feed, with the reference spectrum being obtained under Ar.

DRIFTS has been widely used in heterogeneous catalysis to quantitatively analyze surface species, offering valuable insights into catalytic mechanisms. For instance, Meunier et al. demonstrated this by investigating the reactivity of formate species on a $Au/Ce(La)O_2$ catalyst during the WGS reaction[200]. They prepared standard samples with known sodium formate concentrations on a ceria-lanthana support and measured the C-H stretching vibration peak area at 2830 cm^{-1} using DRIFTS (Figure 7.2a). In so doing, they established a calibration curve using standard samples, creating a linear correlation between the peak area and formate concentration (Figure 7.2b) and thereby enabling accurate quantification. Specifically, the peak area of formate's characteristic band (2830 cm^{-1}) is calculated through integration. This peak area is then converted into absolute concentration (e.g., mol/g) using the calibration curve. This method leverages the high sensitivity of DRIFTS and the precise linear relationship of characteristic peaks, making it a reliable technique for the quantitative analysis of surface species. At the same time, it highlights the potential of DRIFTS to not only quantify adsorbed species but also elucidate their roles in

catalytic processes, significantly advancing our understanding of heterogeneous catalysis. However, such comprehensive quantitative analyses are notably absent in the study of PCC systems. Incorporating these methodologies into PCC research could provide deeper insights into surface reactions and intermediates, paving the way for optimizing performance and stability in these systems. This represents a promising direction for future investigations.

7.2 *Operando* DRIFTS

Operando spectroscopy refers to spectroscopic measurements conducted on a sample under working conditions, accompanied by simultaneous online product analysis. This term differentiates studies where online activity measurements are performed alongside spectroscopic measurements (*operando* DRIFTS) from those where only spectroscopic data are collected (*in situ* DRIFTS)[94]. More recently, operando DRIFTS has been extended from catalytic reactors to electrochemical devices. Meng et al.[103] developed an operando DRIFTS platform capable of investigating proton-conducting ceramic electrolytes under realistic high-temperature fuel cell operating conditions. To the best of our knowledge, this represents the first operando DRIFTS study to probe the hydration dynamics of a proton-conducting ceramic electrolyte operating in a single-device configuration, enabling direct observation of surface hydroxyl evolution during electrochemical operation. This work significantly advances operando spectroscopy by bringing spectroscopic characterization closer to practical PCC operating conditions and establishes a foundation for investigating electrolyte surface chemistry under realistic electrochemical environments.

However, despite these advances, the development of integrated online analysis remains limited. Current operando DRIFTS studies in PCCs primarily focus on spectroscopic observations, while simultaneous quantitative analysis of gas-phase products under electrochemical operation is

still lacking. The absence of synchronized online product analysis restricts the direct correlation between surface intermediate evolution, reaction kinetics, and electrochemical performance. Future developments should therefore integrate operando DRIFTS with complementary online analytical techniques, such as MS and GC, to enable simultaneous monitoring of surface species, gaseous products, and electrochemical responses. Such multimodal operando platforms would provide a more comprehensive understanding of reaction mechanisms and degradation processes in protonic ceramic electrochemical cells. While DRIFTS measurements under constant current or voltage conditions are essential for investigating realistic electrochemical surface processes[112], the online analysis of reactor effluents offers additional advantages. Firstly, it enables the collection of kinetic data directly linked to the simultaneously obtained spectroscopic data, regardless of whether the cell operates as an ideal reactor. Secondly, it helps determine whether the activity data gathered in the *operando* reactor are kinetically meaningful by comparing them with data from a conventional "ideal" reactor designed for accurate kinetic measurements. This integrated approach allows for simultaneous monitoring of surface species via DRIFTS and gas-phase products via MS. Such *operando* setups provide real-time insights into reaction mechanisms, bridging the gap between surface processes and catalytic performance. For example, the combination of DRIFTS and MS has been effectively used to correlate the evolution of surface adsorbates with the production rates of reaction products, enabling a more comprehensive understanding of adsorption, desorption, and reaction kinetics on PCC surfaces. In Meunier's study, DRIFTS, with its shallow analysis depth (a few hundred microns), focuses on characterizing surface species at the upper part of the catalyst bed[199]. Meanwhile, MS, located at the reactor exit, detects the effluent's gas-phase composition (Figure 7.2c)[199]. The integration of *in situ* MS during steady-state isotopic transient kinetic analysis (SSITKA) enables differentiation between primary reaction intermediates and

spectator species. This setup simultaneously monitors surface species reactivity via DRIFTS and gas-phase product formation using MS during SSITKA. For example, in a study on the water–gas shift reaction, the reaction product CO_2 was monitored simultaneously via DRIFTS and MS[199]. The DRIFTS signal at the front of the catalyst bed and the MS data at the reactor exit produced identical results, demonstrating the complementary nature of these techniques for providing a unified understanding of reaction dynamics. Since DRIFTS and MS data correspond to different parts of the reactor, ensuring homogeneity in the gas-phase composition along the catalyst bed is essential. This alignment ensures that the gas-phase composition observed by DRIFTS at the front of the bed matches the composition measured by MS at the reactor exit. DRIFTS can provide chemical information and interface with other instruments that offer physical and compositional insights on the same sample, with common instruments including TGA, GC, and MS.

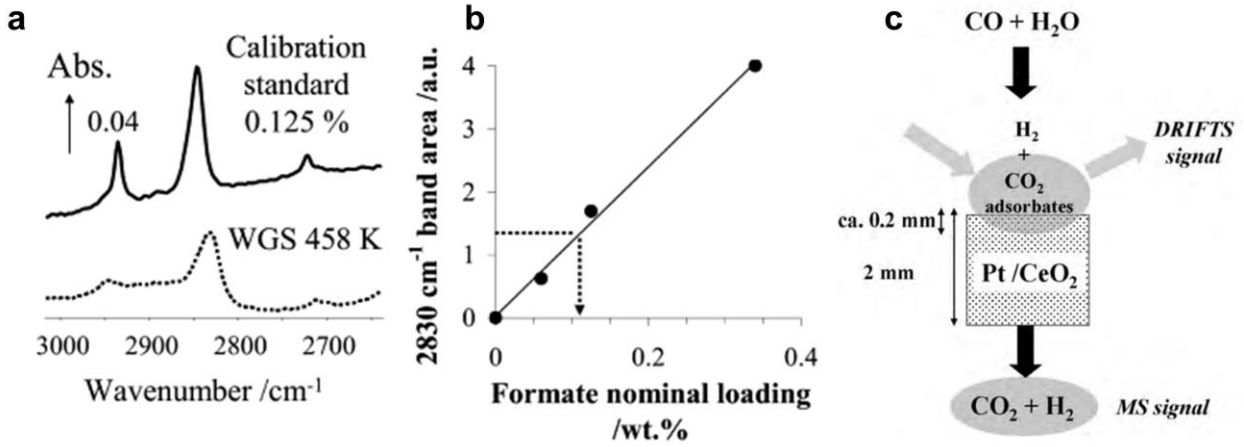

Figure 7.2. (a) DRIFTS curve for an Au-free Ce (La)O_2 material in Ar impregnated with 0.125 wt.% of formate deposited from sodium formate at 373 K (solid line), and DRIFTS curve for 0.6 at. % Au + 7.3 at. % La/CeO_2 under 2% CO + 7% H_2O in Ar at 458 K (dotted line). (b) Calibration plot relating to the formate CH stretching band area of the Ce (La)O_2 sample impregnated with

various loadings of sodium formate. The dotted line is associated with the *in situ* spectrum shown in a. [200]. (c) DRIFTS-MS-SSITKA technique for *operando* investigation. [199].

In addition, direct ammonia protonic ceramic fuel cells (DA-PCCs) have emerged as a promising technology for efficient energy conversion[201, 202]. Ammonia (NH_3) is an attractive fuel alternative to hydrogen, offering several advantages such as easier storage and transportation, high volumetric energy density, and carbon-free composition[203]. Meanwhile, as a cutting-edge electrochemical platform, PCCs can also enable NH_3 synthesis under moderate pressures and low-to-intermediate temperatures, driven by surplus electricity from solar and wind energy[4, 203]. These complementary features make DA-PCC systems highly appealing for affordable energy infrastructures. In DA-PCCs, both ammonia activation and proton transport are central to the cell's operation, leading to complex surface chemistry that is not yet fully understood. As discussed by Liang et al. in a recent review, key mechanistic insights into ammonia decomposition in protonic ceramic fuel cells remain limited, particularly under low-temperature and real operating conditions[203]. In contrast, low-temperature ammonia fuel cells have seen the widespread use of DRIFTS to study transient nitrogen-containing surface intermediates (e.g., $–NH_2$, $–NH_2$, N≡N), providing valuable insights into ammonia oxidation pathways under *operando* conditions[204]. However, DRIFTS applications in DA-PCCs are still extremely limited. This highlights a clear knowledge gap. Applying DRIFTS to DA-PCCs would be instrumental in elucidating surface mechanisms and guiding the rational design of catalytic materials for ammonia-fueled ceramic systems. We believe this represents a timely and important direction for future research.

7.3 Complementary techniques

Combining DRIFTS with other *in situ* techniques is a promising direction for advancing *operando*/*in situ* DRIFTS studies, as it can provide a more comprehensive understanding of surface chemistry. However, the combination of such techniques has rarely been applied in the field of PCCs. Although DRIFTS is a surface-sensitive technique that cannot provide bulk structural information, integrating it with complementary techniques such as XRD, TGA, and TPD can significantly broaden its utility. For instance, while DRIFTS is limited in its ability to probe bulk properties, XRD can effectively provide detailed information about the bulk structure of materials, making the combination of these methods highly valuable for comprehensive material characterization. As a future direction, these integrated approaches can bridge the gap between surface-level DRIFTS data, bulk material characteristics, and theoretical understanding, leading to more significant insights that will advance the existing understanding of their mechanisms and enhance performance.

In addition, despite its numerous successful prior applications, DRIFTS faces several inherent limitations when applied to high-temperature PCC environments. One of the major challenges is thermal radiation from the sample and surroundings, which can introduce significant background interference and complicated spectral interpretation. Additionally, prolonged exposure to elevated temperatures can degrade IR-transparent window materials, reducing optical transmission and decreasing the signal-to-noise ratio. Evidence suggests that KBr and CaF_2 are commonly used as window materials due to their good infrared transparency[81, 82, 143]. However, both exhibit limitations under harsh conditions. KBr is highly hygroscopic, and CaF_2 may undergo structural degradation in reactive atmospheres or elevated temperatures. The choice of window material can thus directly affect the accuracy, stability, and reproducibility of DRIFTS

measurements under *operando* conditions. To ensure reliable spectral acquisition, careful control of environmental parameters and periodic calibration are required. Coupling DRIFTS with complementary techniques such as MS, *in situ* Raman spectroscopy, or synchrotron-based infrared sources may help overcome these limitations. Such multi-modal approaches offer more robust insights into surface reaction mechanisms and can improve confidence in the interpretation of data obtained under realistic PCC operating conditions[205-207].

7.4 Customized equipment

Current commercial DRIFTS equipment is primarily designed for low-temperature systems, posing challenges for studying specific intermediate-temperature PCCs. Generally, PCC operation requires intermediate-temperature conditions, a controlled gas atmosphere, and the simultaneous application of electrical current. Furthermore, PCCs for power generation or energy storage must be sealed within a specialized fixture to ensure gas-tightness and maintain separate working atmospheres for the oxygen and hydrogen electrodes, which introduces additional complexities for designing custom DRIFTS chambers. Therefore, appropriately modified commercial equipment is needed to fully utilize DRIFTS in the analysis of PCCs. For example, the design incorporates a sealable button cell holder that separates the two working electrodes and allows the application of external voltages or currents. By enabling measurements through charging or discharging, this platform helps probe real electrochemical working conditions. It is expected to reveal potential links between surface species behavior and device-level performance and holds strong potential for advancing *operando* spectroscopic techniques in future PCC research.

7.5 Modeling and machine learning

The interpretation of DRIFTS spectra often involves complex, overlapping vibrational features, making it challenging to unambiguously identify surface species and reaction mechanisms using conventional analysis methods. To overcome these limitations, integrating computational modeling and machine learning (ML) with DRIFTS has emerged as a promising approach to enhance interpretability and predictive accuracy, thereby accelerating material discovery and optimization.

Computational modeling methods, particularly DFT, have traditionally provided theoretical benchmarks for assigning vibrational modes observed in DRIFTS experiments[32, 38, 42, 208]. In previous sections of this review, we primarily discussed the use of DFT modeling to calculate reaction pathways and adsorption energies, showing how it significantly aids in revealing catalytic mechanisms. Beyond these applications, DFT also plays a vital role in simulating molecular structures and their corresponding vibrational frequencies. These theoretical simulations confirm the presence and nature of experimentally observed surface species and intermediates, providing additional confidence in spectral assignments. Moreover, DFT enables the prediction of the adsorption geometries, binding energies, and vibrational behavior of molecules adsorbed on surfaces, thus delivering the comprehensive theoretical foundation essential for accurately interpreting experimental DRIFTS spectra. Additionally, advanced simulation techniques such as *ab initio* molecular dynamics (AIMD) can further capture dynamic aspects of surface reactions under realistic operating conditions, thereby deepening the mechanistic understanding derived from *operando* DRIFTS data.

Recently, ML approaches have further advanced this capability by extracting quantitative structural and compositional information directly from experimental spectral data[209-211]. A

representative example is the work by Usoltsev et al., which demonstrated the use of ML algorithms trained on the DRIFT spectra of CO adsorbed on palladium hydride (PdH_x)[212]. Their models successfully predicted key structural descriptors such as hydride stoichiometry and Pd–Pd interatomic distances with high accuracy. Figure 7.3a illustrates the experimental DRIFT spectra collected under varying hydrogen pressures, clearly showing spectral shifts correlated to hydride formation. Figure 7.3b provides an example of the descriptor selection process used for experimental spectra, illustrating how spectral peaks and their positions are identified and parameterized through Gaussian fitting, which serves as a critical preprocessing step enabling the effective training and performance of the ML model. Figure 7.3c validates the high predictive accuracy of the ML model, displaying strong correlations between ML-predicted and experimentally measured structural descriptors, specifically Pd–Pd interatomic distances and lattice constants. The integration of ML in this manner not only automates spectral interpretation but also directly yields quantitative insights into structural transformations, surpassing the limitations of traditional analytical methods.

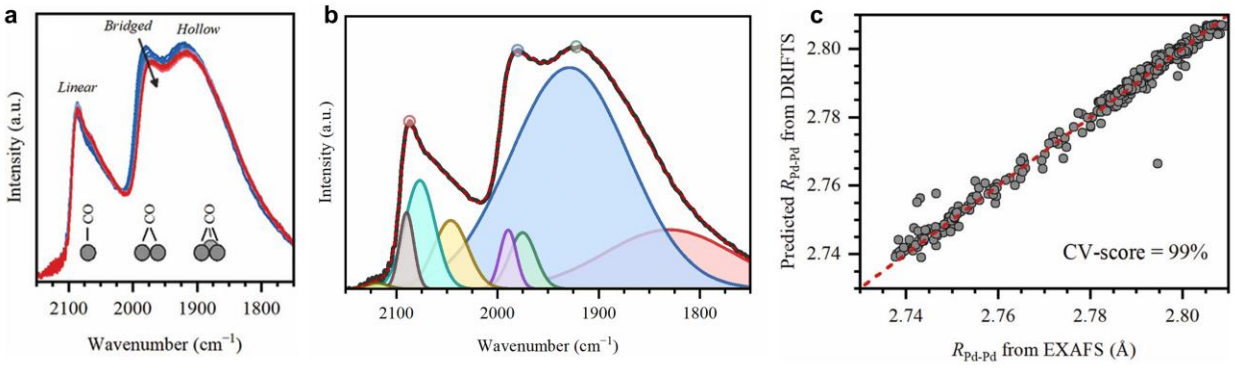

Figure 7.3. Integration of ML with DRIFTS for quantitative structural analysis of PdH_x. (a) Experimental DRIFT spectra collected under varying hydrogen pressures. (b) Descriptor selection and Gaussian fitting of spectral peaks. (c) ML model validation, showing excellent correlation

between predicted and experimentally measured structural descriptors of Pd–Pd interatomic distances. [212].

However, challenges remain before we can fully realize the potential of modeling and ML in DRIFTS analysis. These include the need for large, high-quality training datasets, ensuring the generalizability and robustness of ML models, and developing explainable artificial intelligence approaches to maintain interpretability. Future research should focus on addressing these limitations through improved experimental–computational workflows and interdisciplinary collaboration, unlocking new opportunities for accelerated materials discovery and deeper mechanistic insights into PCCs and related electrochemical systems.

References

(1) Du, Z.; Gong, W.; Xu, K.; Zhu, F.; Zhang, X.; Chen, Y. Protonic ceramic electrochemical cells for hydrogen production from seawater electrolysis. *J. Mater. Chem. A.* **2024**, *12* (41), 28066-28073, 10.1039/D4TA05666C. DOI: 10.1039/D4TA05666C.

(2) Liu, F.; Ding, D.; Duan, C. Protonic Ceramic Electrochemical Cells for Synthesizing Sustainable Chemicals and Fuels. *Adv. Sci.* **2023**, *10* (8), 2206478. DOI: https://doi.org/10.1002/advs.202206478.

(3) Zhu, P.-X.; Wang, L.-C.; Stewart, F.; Ding, D.; Matz, J.; Dong, P.; Ding, H. Direct conversion of natural gases in solid oxide cells: a mini-review. *Electrochem. commun.* **2021**, *128*, 107068. DOI: https://doi.org/10.1016/j.elecom.2021.107068.

(4) Li, M.; Hua, B.; Wu, W.; Wang, L. C.; Ding, Y.; Welander, M. M.; Walker, R. A.; Ding, D. Activating nano-bulk interplays for sustainable ammonia electrosynthesis. *Mater. Today* **2022**, *60*, 31-40. DOI: https://doi.org/10.1016/j.mattod.2022.09.011.

(5) Tsvetkov, N.; Kim, D.; Jeong, I.; Kim, J. H.; Ahn, S.; Lee, K. T.; Jung, W. Advances in materials and interface understanding in protonic ceramic fuel cells. *Adv. Mater. Technol.* **2023**, *8* (20), 2201075. DOI: https://doi.org/10.1002/admt.202201075.

(6) Meng, Y.; Gao, J.; Zhao, Z.; Amoroso, J.; Tong, J.; Brinkman, K. S. Review: recent progress in low-temperature proton-conducting ceramics. *J. Mater. Sci.* **2019**, *54* (13), 9291-9312. DOI: https://doi.org/10.1007/s10853-019-03559-9.

(7) Bartel, C. J.; Sutton, C.; Goldsmith, B. R.; Ouyang, R.; Musgrave, C. B.; Ghiringhelli, L. M.; Scheffler, M. New tolerance factor to predict the stability of perovskite oxides and halides. *Science Advances* **2019**, *5* (2), eaav0693. DOI: doi:10.1126/sciadv.aav0693.

(8) Tarasova, N.; Hanif, M. B.; Janjua, N. K.; Anwar, S.; Motola, M.; Medvedev, D. Fluorine-insertion in solid oxide materials for improving their ionic transport and stability. A brief review. *Int. J. Hydrogen Energy* **2024**, *50*, 104-123. DOI: https://doi.org/10.1016/j.ijhydene.2023.08.074.

(9) Takahashi, T.; Iwahara, H. rev. Chim. Miner. **1980**.

(10) Medvedev, D.; Murashkina, A.; Pikalova, E.; Demin, A.; Podias, A.; Tsiakaras, P. BaCeO3: Materials development, properties and application. *Prog. Mater. Sci.* **2014**, *60*, 72-129. DOI: https://doi.org/10.1016/j.pmatsci.2013.08.001.

(11) Cao, J.; Ji, Y.; Shao, Z. Perovskites for protonic ceramic fuel cells: a review. *Energ. Environ. Sci.* **2022**, *15* (6), 2200-2232. DOI: https://doi.org/10.1039/D2EE00132B.

(12) Ryu, K. H.; Haile, S. M. Chemical stability and proton conductivity of doped BaCeO3–BaZrO3 solid solutions. *Solid State Ion.* **1999**, *125* (1), 355-367. DOI: https://doi.org/10.1016/S0167-2738(99)00196-4.

(13) Guo, Y.; Lin, Y.; Ran, R.; Shao, Z. Zirconium doping effect on the performance of proton-conducting BaZryCe0.8−yY0.2O3−δ (0.0≤y≤0.8) for fuel cell applications. *J. Power Sources.* **2009**, *193* (2), 400-407. DOI: https://doi.org/10.1016/j.jpowsour.2009.03.044.

(14) Nie, H.; Liu, Z.; Xiao, M.; Yang, G.; Li, T.; Starostina, I. A.; Medvedev, D. A.; Wang, W.; Zhou, W.; Ran, R. Recent Advances and Challenges in Perovskite-Based Protonic Ceramic Electrolytes: Design Strategies and Fabrication Innovations. *Adv. Funct. Mater.* **2025**, *35* (10), 2416651. DOI: https://doi.org/10.1002/adfm.202416651.

(15) Bae, K.; Kim, D. H.; Choi, H. J.; Son, J.-W.; Shim, J. H. High-Performance Protonic Ceramic Fuel Cells with 1 μm Thick Y:Ba(Ce, Zr)O3 Electrolytes. *Adv. Energy Mater. Cem.* **2018**, *8* (25), 1801315. DOI: https://doi.org/10.1002/aenm.201801315.

(16) Regalado Vera, C. Y.; Ding, H.; Peterson, D.; Gibbons, W. T.; Zhou, M.; Ding, D. A mini-review on proton conduction of BaZrO3-based perovskite electrolytes. *JPhys Energy* **2021**, *3* (3), 032019. DOI: 10.1088/2515-7655/ac12ab.

(17) Duan, C.; Huang, J.; Sullivan, N.; O'Hayre, R. Proton-conducting oxides for energy conversion and storage. *Appl. Phys. Rev.* **2020**, *7* (1). DOI: https://doi.org/10.1063/1.5135319.

(18) Choi, S.; Kucharczyk, C. J.; Liang, Y.; Zhang, X.; Takeuchi, I.; Ji, H.-I.; Haile, S. M. Exceptional power density and stability at intermediate temperatures in protonic ceramic fuel cells. *Nat. Energy.* **2018**, *3* (3), 202-210. DOI: https://doi.org/10.1038/s41560-017-0085-9.

(19) Yang, L.; Wang, S.; Blinn, K.; Liu, M.; Liu, Z.; Cheng, Z.; Liu, M. Enhanced Sulfur and Coking Tolerance of a Mixed Ion Conductor for SOFCs: BaZr0.1Ce0.7Y0.2–xYbxO3–δ. *Science* **2009**, *326* (5949), 126-129. DOI: doi:10.1126/science.1174811.

(20) Xie, Y.; Shi, N.; Ricote, S.; Chen, M. Zinc triggers favorable hydrogenation reaction in double perovskite PrBaCo2O6-δ: Applications in protonic ceramic cells. *Chem. Eng. J.* **2024**, *492*, 151939. DOI: https://doi.org/10.1016/j.cej.2024.151939.

(21) Ohlin, L.; Bazin, P.; Thibault-Starzyk, F.; Hedlund, J.; Grahn, M. Adsorption of CO2, CH4, and H2O in zeolite ZSM-5 studied using in situ ATR-FTIR spectroscopy. *J. Phys. Chem. C.* **2013**, *117* (33), 16972-16982. DOI: 10.1021/jp4037183.

(22) Xu, Y.; Xu, K.; Zhu, F.; He, F.; Zhang, H.; Fang, C.; Liu, Y.; Zhou, Y.; Choi, Y.; Chen, Y. A low-lewis-acid-strength cation Cs+-doped double perovskite for fast and durable oxygen reduction/evolutions on protonic ceramic cells. *ACS Energy Lett.* **2023**, *8* (10), 4145-4155. DOI: https://doi.org/10.1021/acsenergylett.3c01722.

(23) Ding, H.; Wu, W.; Jiang, C.; Ding, Y.; Bian, W.; Hu, B.; Singh, P.; Orme, C. J.; Wang, L.; Zhang, Y.; et al. Self-sustainable protonic ceramic electrochemical cells using a triple conducting

electrode for hydrogen and power production. *Nat. Commun.* **2020**, *11* (1), 1907. DOI: https://doi.org/10.1038/s41467-020-15677-z.

(24) He, F.; Zhou, Y.; Hu, T.; Xu, Y.; Hou, M.; Zhu, F.; Liu, D.; Zhang, H.; Xu, K.; Liu, M.; et al. An efficient high-entropy perovskite-type air electrode for reversible oxygen reduction and water splitting in protonic ceramic cells. *Adv. Mater.* **2023**, *35* (16), 2209469. DOI: https://doi.org/10.1002/adma.202209469 (acccessed 2024/10/11).

(25) Regalado Vera, C. Y.; Ding, H.; Urban-Klaehn, J.; Li, M.; Zhao, Z.; Stewart, F.; Tian, H.; Liu, X.; Dong, Y.; Li, J.; et al. Improving proton conductivity by navigating proton trapping in high scandium-doped barium zirconate electrolytes. *Chem. Mater.* **2023**, *35* (14), 5341-5352. DOI: https://doi.org/10.1021/acs.chemmater.3c00531.

(26) Andreev, R. D.; Anokhina, I. A.; Korona, D. V.; Gilev, A. R.; Animitsa, I. E. Transport properties of In3+- and Y3+-doped hexagonal perovskite Ba5In2Al2ZrO13. *Russ. J. Electrochem.* **2023**, *59* (3), 190-203. DOI: 10.1134/S1023193523030035.

(27) Wang, M.; Wang, L.-C.; Liu, B.; Ding, Y.; Yang, Y.; Ding, D. Promotional effect of ZnO and ZrO2 in K-doped Fe catalysts for CO2 hydrogenation to light olefins. *ACS Catal.* **2025**, *15* (8), 5954-5967. DOI: 10.1021/acscatal.4c07100.

(28) Alrefae, M.; Es-sebbar, E.-t.; Farooq, A. Absorption cross-section measurements of methane, ethane, ethylene and methanol at high temperatures. *J. Mol. Spectrosc.* **2014**, *303*, 8-14. DOI: https://doi.org/10.1016/j.jms.2014.06.007.

(29) Azzolina-Jury, F.; Thibault-Starzyk, F. Mechanism of low pressure plasma-assisted CO2 hydrogenation over Ni-USY by microsecond time-resolved FTIR spectroscopy. *Top. Catal.* **2017**, *60* (19), 1709-1721. DOI: 10.1007/s11244-017-0849-2.

(30) Guo, L.; Gao, X.; Gao, W.; Wu, H.; Wang, X.; Sun, S.; Wei, Y.; Kugue, Y.; Guo, X.; Sun, J.; et al. High-yield production of liquid fuels in CO2 hydrogenation on a zeolite-free Fe-based catalyst. *Chem. Sci.* **2023**, *14* (1), 171-178, 10.1039/D2SC05047A. DOI: 10.1039/D2SC05047A.

(31) Park, K.; Kim, Y.; Lee, K. J. Analysis of deuterated water contents using FTIR bending motion. *J. Radioanal. Nucl. Chem.* **2019**, *322* (2), 487-493. DOI: 10.1007/s10967-019-06734-z.

(32) Liu, F.; Deng, H.; Ding, H.; Kazempoor, P.; Liu, B.; Duan, C. Process-intensified protonic ceramic fuel cells for power generation, chemical production, and greenhouse gas mitigation. *Joule* **2023**, *7* (6), 1308-1332. DOI: https://doi.org/10.1016/j.joule.2023.05.009.

(33) Meng, Y.; Deng, H.; Wang, L.-C.; Kim, D.; Liu, B.; Liu, F.; Ding, Y.; Ding, D. Highly efficient La/Ni co-doped strontium titanate catalyst for co-production of propylene and hydrogen from propane in protonic ceramic electrochemical cells. *Applied Catalysis B- Environ.* **2024**, *354*, 124111. DOI: https://doi.org/10.1016/j.apcatb.2024.124111.

(34) Kermarec, M.; Delafosse, D.; Che, M. An i.r. study of carbon monoxide fixation by Ni+ ions obtained by photoreduction of a nickel-exchanged silica. *Journal of the Chemical Society, Chemical Communications* **1983**, (8), 411-413, 10.1039/C39830000411. DOI: 10.1039/C39830000411.

(35) Peri, J. B. Infrared studies of Ni held at low concentrations on alumina supports. *J. Catal.* **1984**, *86* (1), 84-94. DOI: https://doi.org/10.1016/0021-9517(84)90350-6.

(36) Galhardo, T. S.; Braga, A. H.; Arpini, B. H.; Szanyi, J.; Gonçalves, R. V.; Zornio, B. F.; Miranda, C. R.; Rossi, L. M. Optimizing active sites for high CO selectivity during CO(2) hydrogenation over supported nickel catalysts. *J Am Chem Soc* **2021**, *143* (11), 4268-4280. DOI: 10.1021/jacs.0c12689 From NLM.

(37) Aleksandrov, H. A.; Zdravkova, V. R.; Mihaylov, M. Y.; Petkov, P. S.; Vayssilov, G. N.; Hadjiivanov, K. I. Precise identification of the infrared bands of the polycarbonyl complexes on Ni–MOR zeolite by 12C16O–13C18O coadsorption and computational modeling. *J. Phys. Chem. C.* **2012**, *116* (43), 22823-22831. DOI: 10.1021/jp304972u.

(38) Xu, Y.; Zhang, H.; Xu, K.; Zhang, X.; Zhu, F.; Deng, W.; He, F.; Liu, Y.; Chen, Y. An Efficient trifunctional spinel-based electrode for oxygen reduction/evolution reactions and nonoxidative ethane dehydrogenation on protonic ceramic electrochemical cells. *Adv. Mater.* **2024**, *36* (40), 2408044. DOI: https://doi.org/10.1002/adma.202408044.

(39) Zhang, W.; Zhang, Q.; Zhu, P.; Meng, Y.; Zhao, Z.; Wang, W.; Ding, Y.; Sun, Q.; Zhang, Y.; Li, M.; et al. An active oxygen electrode for proton-conducting solid oxide electrolysis cells with high faradaic efficiency. *Adv. Energy Mater. Cem.* **2025**, 2500852. DOI: https://doi.org/10.1002/aenm.202500852.

(40) Belhadj, H.; Hakki, A.; Robertson, P. K. J.; Bahnemann, D. W. In situ ATR-FTIR study of H2O and D2O adsorption on TiO2 under UV irradiation. *Phys. Chem. Chem. Phys.* **2015**, *17* (35), 22940-22946, 10.1039/C5CP03947A. DOI: 10.1039/C5CP03947A.

(41) Liu, F.; Fang, L.; Diercks, D.; Kazempoor, P.; Duan, C. Rationally designed negative electrode for selective CO2-to-CO conversion in protonic ceramic electrochemical cells. *Nano Energy* **2022**, *102*, 107722. DOI: https://doi.org/10.1016/j.nanoen.2022.107722.

(42) Hong, K.; Choi, M.; Bae, Y.; Min, J.; Lee, J.; Kim, D.; Bang, S.; Lee, H.-K.; Lee, W.; Hong, J. Direct methane protonic ceramic fuel cells with self-assembled Ni-Rh bimetallic catalyst. *Nat. Commun.* **2023**, *14* (1), 7485. DOI: https://doi.org/10.1038/s41467-023-43388-8.

(43) Wang, Z.; Luo, Z.; Xu, H.; Zhu, T.; Guan, D.; Lin, Z.; Chan, T.-S.; Huang, Y.-C.; Hu, Z.; Jiang, S. P.; et al. New understanding and improvement in sintering behavior of cerium-rich

perovskite-type protonic electrolytes. *Adv. Funct. Mater.* **2024**, *34* (38), 2402716. DOI: https://doi.org/10.1002/adfm.202402716.

(44) Kondo, J.; Abe, H.; Sakata, Y.; Maruya, K.-i.; Domen, K.; Onishi, T. Infrared studies of adsorbed species of H2, CO and CO2 over ZrO2. *J. Chem. Soc., Faraday Trans. 1.* **1988**, *84* (2), 511-519, 10.1039/F19888400511. DOI: 10.1039/F19888400511.

(45) Iwahara, H.; Esaka, T.; Uchida, H.; Maeda, N. Proton conduction in sintered oxides and its application to steam electrolysis for hydrogen production. *Solid State Ion.* **1981**, *3-4*, 359-363. DOI: https://doi.org/10.1016/0167-2738(81)90113-2.

(46) Choi, S.; Davenport, T. C.; Haile, S. M. Protonic ceramic electrochemical cells for hydrogen production and electricity generation: exceptional reversibility, stability, and demonstrated faradaic efficiency. *Energ. Environ. Sci.* **2019**, *12* (1), 206-215, 10.1039/C8EE02865F. DOI: https://doi.org/10.1039/C8EE02865F.

(47) Sozal, M. S. I.; Tang, W.; Das, S.; Li, W.; Durygin, A.; Drozd, V.; Zhang, C.; Jafarizadeh, B.; Wang, C.; Agarwal, A.; et al. Electrical, thermal, and H2O and CO2 poisoning behaviors of PrNi0.5Co0.5O3-δ electrode for intermediate temperature protonic ceramic electrochemical cells. *Int. J. Hydrogen Energy* **2022**, *47* (51), 21817-21827. DOI: https://doi.org/10.1016/j.ijhydene.2022.05.011.

(48) Develos-Bagarinao, K.; De Vero, J.; Kishimoto, H.; Ishiyama, T.; Yamaji, K.; Horita, T.; Yokokawa, H. Multilayered LSC and GDC: an approach for designing cathode materials with superior oxygen exchange properties for solid oxide fuel cells. *Nano Energy* **2018**, *52*, 369-380. DOI: https://doi.org/10.1016/j.nanoen.2018.08.014.

(49) Solovyev, A. A.; Kuterbekov, K. A.; Nurkenov, S. A.; Nygymanova, A. S.; Shipilova, A. V.; Smolyanskiy, E. A.; Rabotkin, S. V.; Ionov, I. V. Anode-supported solid oxide fuel cells with

multilayer LSC/CGO/LSC cathode. *Fuel Cells* **2021**, *21* (4), 408-412. DOI: https://doi.org/10.1002/fuce.202000168.

(50) Lim, Y.; Park, J.; Lee, H.; Ku, M.; Kim, Y.-B. Rapid fabrication of lanthanum strontium cobalt ferrite (LSCF) with suppression of LSCF/YSZ chemical side reaction via flash light sintering for SOFCs. *Nano Energy* **2021**, *90*, 106524. DOI: https://doi.org/10.1016/j.nanoen.2021.106524.

(51) Jiang, S. P. Development of lanthanum strontium cobalt ferrite perovskite electrodes of solid oxide fuel cells – a review. *Int. J. Hydrogen Energy* **2019**, *44* (14), 7448-7493. DOI: https://doi.org/10.1016/j.ijhydene.2019.01.212.

(52) Shi, H.; Yang, G.; Liu, Z.; Zhang, G.; Ran, R.; Shao, Z.; Zhou, W.; Jin, W. High performance tubular solid oxide fuel cells with BSCF cathode. *Int. J. Hydrogen Energy* **2012**, *37* (17), 13022-13029. DOI: https://doi.org/10.1016/j.ijhydene.2012.05.061.

(53) Subhashini, P. V. C. K.; Rajesh, K. V. D. Manufacturing method of BSCF cathode for low-temperature solid oxide fuel cell-A review. *Materials Today: Proceedings* **2022**, *62*, 2357-2361. DOI: https://doi.org/10.1016/j.matpr.2022.04.653.

(54) Duan, C.; Tong, J.; Shang, M.; Nikodemski, S.; Sanders, M.; Ricote, S.; Almansoori, A.; O'Hayre, R. Readily processed protonic ceramic fuel cells with high performance at low temperatures. *Science* **2015**, *349* (6254), 1321-1326. DOI: doi:10.1126/science.aab3987.

(55) Duan, C.; Kee, R. J.; Zhu, H.; Karakaya, C.; Chen, Y.; Ricote, S.; Jarry, A.; Crumlin, E. J.; Hook, D.; Braun, R.; et al. Highly durable, coking and sulfur tolerant, fuel-flexible protonic ceramic fuel cells. *Nature* **2018**, *557* (7704), 217-222. DOI: 10.1038/s41586-018-0082-6.

(56) Duan, C.; Kee, R.; Zhu, H.; Sullivan, N.; Zhu, L.; Bian, L.; Jennings, D.; O'Hayre, R. Highly efficient reversible protonic ceramic electrochemical cells for power generation and fuel production. *Nat. Energy.* **2019**, *4* (3), 230-240. DOI: https://doi.org/10.1038/s41560-019-0333-2.

(57) Liu, F.; Diercks, D.; Kumar, P.; Seong, A.; Jabbar, M. H. A.; Gumeci, C.; Furuya, Y.; Dale, N.; Oku, T.; Usuda, M.; et al. Redesigning protonic ceramic electrochemical cells to lower the operating temperature. *Science Advances* **2025**, *11* (2), eadq2507. DOI: doi:10.1126/sciadv.adq2507.

(58) Zhang, H.; Xu, K.; Xu, Y.; He, F.; Zhu, F.; Zhu, L.; Chen, Y. Improving the performance of the PrBa0.8Ca0.2Co2O5+δ cathode for proton-conducting SOFCs by microwave sintering. *Ceram. Int.* **2024**, *50* (20, Part C), 40384-40390. DOI: https://doi.org/10.1016/j.ceramint.2024.05.299.

(59) Chen, Y.; Yoo, S.; Choi, Y.; Kim, J. H.; Ding, Y.; Pei, K.; Murphy, R.; Zhang, Y.; Zhao, B.; Zhang, W.; et al. A highly active, CO2-tolerant electrode for the oxygen reduction reaction. *Energ. Environ. Sci.* **2018**, *11* (9), 2458-2466, 10.1039/C8EE01140K. DOI: 10.1039/C8EE01140K.

(60) Liu, F.; Deng, H.; Diercks, D.; Kumar, P.; Jabbar, M. H. A.; Gumeci, C.; Furuya, Y.; Dale, N.; Oku, T.; Usuda, M.; et al. Lowering the operating temperature of protonic ceramic electrochemical cells to <450 °C. *Nat. Energy.* **2023**, *8* (10), 1145-1157. DOI: 10.1038/s41560-023-01350-4.

(61) Bian, W.; Wu, W.; Wang, B.; Tang, W.; Zhou, M.; Jin, C.; Ding, H.; Fan, W.; Dong, Y.; Li, J.; et al. Revitalizing interface in protonic ceramic cells by acid etch. *Nature* **2022**, *604* (7906), 479-485. DOI: 10.1038/s41586-022-04457-y.

(62) Tang, W.; Ding, H.; Bian, W.; Regalado Vera, C. Y.; Gomez, J. Y.; Dong, Y.; Li, J.; Wu, W.; Fan, W.; Zhou, M.; et al. An unbalanced battle in excellence: revealing effect of Ni/Co occupancy on water splitting and oxygen reduction reactions in triple-conducting oxides for protonic ceramic electrochemical cells. *Small* **2022**, *18* (30), 2201953. DOI: https://doi.org/10.1002/smll.202201953.

(63) Liu, F.; Duan, C. Direct-hydrocarbon proton-conducting solid oxide fuel cells. *Sustain.* **2021**, *13* (9), 4736.

(64) Du, Z.; He, F.; Gao, H.; Xu, Y.; Zhu, F.; Xu, K.; Xia, J.; Zhang, H.; Huang, Y.; Liu, Y.; et al. An active bifunctional Pd-doped double perovskite air electrode for reversible protonic ceramic electrochemical cells. *Energy Storage Mater.* **2024**, *68*, 103345. DOI: https://doi.org/10.1016/j.ensm.2024.103345.

(65) Park, J. S.; Choi, H. J.; Han, G. D.; Koo, J.; Kang, E. H.; Kim, D. H.; Bae, K.; Shim, J. H. High–performance protonic ceramic fuel cells with a PrBa0.5Sr0.5Co1.5Fe0.5O5+δ cathode with palladium–rich interface coating. *J. Power Sources.* **2021**, *482*, 229043. DOI: https://doi.org/10.1016/j.jpowsour.2020.229043.

(66) Zhu, L.; Cadigan, C.; Duan, C.; Huang, J.; Bian, L.; Le, L.; Hernandez, C. H.; Avance, V.; O'Hayre, R.; Sullivan, N. P. Ammonia-fed reversible protonic ceramic fuel cells with Ru-based catalyst. *Commun. Chem.* **2021**, *4* (1), 121. DOI: 10.1038/s42004-021-00559-2.

(67) Watanabe, K.; Yamaguchi, Y.; Nomura, K.; Sumi, H.; Mori, M.; Mizutani, Y.; Shimada, H. Effect of cobalt content on electrochemical performance for La0.6Sr0.4CoxFe1-xO3-δ and BaZr0.8Yb0.2O3-δ composite cathodes in protonic ceramic fuel cells. *Ceram. Int.* **2023**, *49* (12), 21085-21090. DOI: https://doi.org/10.1016/j.ceramint.2023.03.105.

(68) Michelson, A. A. The relative motion of the earth and the luminiferous ether. *Am. J. Sci.* **1881**, (22), 120-129. DOI: https://doi.org/10.2475/ajs.s3-22.128.120.

(69) Michelson, A. A. M., E.W. . On the relative motion of the earth and the luminiferous ether. *Am. J. Sci.* **1887**, (34), 333-345. DOI: https://doi.org/10.2475/ajs.s3-34.203.333.

(70) Millikan, R. C.; Pitzer, K. S. Infrared spectra and vibrational sssignment of monomeric formic acid. *J. Chem. Phys.* **1957**, *27* (6), 1305-1308. DOI: 10.1063/1.1743996 (acccessed 2/5/2025).

(71) Griffiths, P. R. The early days of commercial FT-IR spectrometry: a personal perspective. *Appl. Spectrosc.* **2017**, *71* (3), 329-340. DOI: 10.1177/0003702816683529 From NLM.

(72) Fan, Q.; Pu, C.; Smotkin, E. S. In situ fourier transform infrared-diffuse reflection spectroscopy of direct methanol fuel cell anodes and cathodes. *J. Electrochem. Soc.* **1996**, *143* (10), 3053. DOI: 10.1149/1.1837163.

(73) Pei, F.; Huang, Y.; Wu, L.; Zhou, S.; Kang, Q.; Lin, W.; Liao, Y.; Zhang, Y.; Huang, K.; Shen, Y.; et al. Multisite crosslinked poly(ether-urethane)-based polymer electrolytes for high-voltage solid-state lithium metal batteries. *Adv. Mater.* **2024**, *36* (49), 2409269. DOI: https://doi.org/10.1002/adma.202409269.

(74) Yan, Y.; Weng, S.; Fu, A.; Zhang, H.; Chen, J.; Zheng, Q.; Zhang, B.; Zhou, S.; Yan, H.; Wang, C.-W.; et al. Tailoring electrolyte dehydrogenation with trace additives: stabilizing the LiCoO2 cathode beyond 4.6 V. *ACS Energy Lett.* **2022**, *7* (8), 2677-2684. DOI: 10.1021/acsenergylett.2c01433.

(75) Zhang, X.-H.; Yao, W.-K.; Zhao, H.-T.; Zhuang, X.-X.; Jin, Y.-Q.; Ding, Y.; Li, M.-J.; Zhou, Z.-Y.; Wang, T.; Sun, S.-G. Enhancing carbon monoxide tolerance in low-temperature PEM fuel cells through carbon nitride surface modification. *ACS Appl. Mater. Interfaces* **2025**, *17* (2), 3257-3264. DOI: 10.1021/acsami.4c15487.

(76) Qin, G.; Bao, J.; Gao, J.; Ruan, F.; An, S.; Wang, Z.; Li, L. Enhanced grain boundary conductivity of Gd and Sc co-doping BaZrO3 proton conductor for proton ceramic fuel cell. *Chem. Eng. J.* **2023**, *466*, 143114. DOI: https://doi.org/10.1016/j.cej.2023.143114.

(77) S.S.Bhokare, V. R. B., R. D. Chakole M.S. Charde. Applications of FTIR spectroscopy: review. *Int. J. Dev. Res.* **2022**, *7* (8), 213-219.

(78) Patrizi, B.; Siciliani de Cumis, M.; Viciani, S.; D'Amato, F. Dioxin and related compound detection: perspectives for optical monitoring. *Int J Mol Sci* **2019**, *20* (11). DOI: https://doi.org/10.3390/ijms20112671.

(79) Saji, R.; Ramani, A.; Gandhi, K.; Seth, R.; Sharma, R. Application of FTIR spectroscopy in dairy products: a systematic review. *Food and Humanity* **2024**, *2*, 100239. DOI: https://doi.org/10.1016/j.foohum.2024.100239.

(80) Smith, B. C. *Fundamentals of Fourier Transform Infrared Spectroscopy (2nd ed.)*; CRC Press, 2011. DOI: https://doi.org/10.1201/b10777.

(81) Mayerhöfer, T. G.; Pahlow, S.; Hübner, U.; Popp, J. CaF2: an ideal substrate material for infrared spectroscopy? *Anal. Chem.* **2020**, *92* (13), 9024-9031. DOI: 10.1021/acs.analchem.0c01158.

(82) Dziarski, K.; Hulewicz, A. Determination of transmittance of IR windows made of CaF2 within operational temperatures of electric devices. *PAR* **2021**, *25* (4), 25-30.

(83) Sirita, J.; Phanichphant, S.; Meunier, F. C. Quantitative analysis of adsorbate concentrations by diffuse reflectance FT-IR. *Anal. Chem.* **2007**, *79* (10), 3912-3918. DOI: 10.1021/ac0702802 From NLM.

(84) Hecht, W. W. a. H. G. *Reflectance Spectroscopy*; Interscience Publishers, 1966.

(85) Kubelka, P. M., Franz An article on optics of paint layers *Z. Tech. Phys* **1931**, *12*, 593–601.

(86) Olinger, J. M.; Griffiths, P. R. Quantitative effects of an absorbing matrix on near-infrared diffuse reflectance spectra. *Analytical Chemistry* **1988**, *60* (21), 2427-2435. DOI: 10.1021/ac00172a022.

(87) Culler, S. R.; McKenzie, M. T.; Fina, L. J.; Ishida, H.; Koenig, J. L. Fourier transform diffuse reflectance infrared study of polymer films and coatings: a method for studying polymer surfaces. *Appl. Spectrosc.* **1984**, *38* (6), 791-795. DOI: 10.1366/0003702844554512.

(88) Kang, L.; Wang, B.; Güntner, A. T.; Xu, S.; Wan, X.; Liu, Y.; Marlow, S.; Ren, Y.; Gianolio, D.; Tang, C. C.; et al. The electrophilicity of surface carbon species in the redox reactions of CuO-CeO2 catalysts. *Angew. Chem. Int. Ed.* **2021**, *60* (26), 14420-14428. DOI: https://doi.org/10.1002/anie.202102570.

(89) Su, B.; Kong, Y.; Wang, S.; Zuo, S.; Lin, W.; Fang, Y.; Hou, Y.; Zhang, G.; Zhang, H.; Wang, X. Hydroxyl-bonded Ru on metallic TiN surface catalyzing CO2 reduction with H2O by infrared light. *J. Am. Chem. Soc.* **2023**, *145* (50), 27415-27423. DOI: 10.1021/jacs.3c08311.

(90) Fahelelbom, K. M.; Saleh, A.; Al-Tabakha, M. M. A.; Ashames, A. A. Recent applications of quantitative analytical FTIR spectroscopy in pharmaceutical, biomedical, and clinical fields: a brief review. *Rev. anal. chem.* **2022**, *41* (1), 21-33. DOI: doi:10.1515/revac-2022-0030 (acccessed 2025-02-11).

(91) Jiang, J.; Zhang, S.; Longhurst, P.; Yang, W.; Zheng, S. Molecular structure characterization of bituminous coal in Northern China via XRD, Raman and FTIR spectroscopy. *Spectrochim Acta A Mol Biomol Spectrosc.* **2021**, *255*, 119724. DOI: https://doi.org/10.1016/j.saa.2021.119724.

(92) Mi, R.; Li, D.; Hu, Z.; Yang, R. T. Morphology effects of CeO2 nanomaterials on the catalytic combustion of toluene: a combined kinetics and diffuse reflectance infrared fourier transform spectroscopy study. *ACS Catal.* **2021**, *11* (13), 7876-7889. DOI: 10.1021/acscatal.1c01981.

(93) Hu, Z.; Tang, Z.; Zhang, T.; Yong, X.; Mi, R.; Li, D.; Yang, X.; Yang, R. T. Synergism between manganese and cobalt on Mn–Co oxides for the catalytic combustion of VOCs: a combined

kinetics and diffuse reflectance infrared fourier transform spectroscopy study. *Ind. Eng. Chem. Res.* **2022**, *61* (14), 4803-4815. DOI: 10.1021/acs.iecr.1c05077.

(94) Meunier, F. C. The power of quantitative kinetic studies of adsorbate reactivity by operando FTIR spectroscopy carried out at chemical potential steady-state. *Catal. Today* **2010**, *155* (3), 164-171. DOI: https://doi.org/10.1016/j.cattod.2009.11.017.

(95) Liu, Z.; Song, Y.; Xiong, X.; Zhang, Y.; Cui, J.; Zhu, J.; Li, L.; Zhou, J.; Zhou, C.; Hu, Z.; et al. Sintering-induced cation displacement in protonic ceramics and way for its suppression. *Nat. Commun.* **2023**, *14* (1), 7984. DOI: 10.1038/s41467-023-43725-x.

(96) Mu, S.; Huang, H.; Ishii, A.; Hong, Y.; Santomauro, A.; Zhao, Z.; Zou, M.; Peng, F.; Brinkman, K. S.; Xiao, H.; et al. Rapid Laser Reactive Sintering for Sustainable and Clean Preparation of Protonic Ceramics. *ACS Omega* **2020**, *5* (20), 11637-11642. DOI: 10.1021/acsomega.0c00879.

(97) Kreuer, K.-D.; Paddison, S. J.; Spohr, E.; Schuster, M. Transport in Proton Conductors for Fuel-Cell Applications: Simulations, Elementary Reactions, and Phenomenology. *Chem. Rev.* **2004**, *104* (10), 4637-4678. DOI: 10.1021/cr020715f.

(98) Nowick, A. S.; Du, Y. High-temperature protonic conductors with perovskite-related structures. *Solid State Ion.* **1995**, *77*, 137-146. DOI: https://doi.org/10.1016/0167-2738(94)00230-P.

(99) Kreuer, K. D. Proton-Conducting Oxides. *Annual Review of Materials Research* **2003**, *33* (Volume 33, 2003), 333-359. DOI: https://doi.org/10.1146/annurev.matsci.33.022802.091825.

(100) Kreuer, K. D.; Fuchs, A.; Maier, J. HD isotope effect of proton conductivity and proton conduction mechanism in oxides. *Solid State Ion.* **1995**, *77*, 157-162. DOI: https://doi.org/10.1016/0167-2738(94)00265-T.

(101) Kreuer, K.-D. Proton Conductivity: Materials and Applications. *Chem. Mater.* **1996**, *8* (3), 610-641. DOI: 10.1021/cm950192a.

(102) Stub, S. Ø.; Vøllestad, E.; Norby, T. Protonic surface conduction controlled by space charge of intersecting grain boundaries in porous ceramics. *J. Mater. Chem. A.* **2018**, *6* (18), 8265-8270, 10.1039/C7TA11088J. DOI: 10.1039/C7TA11088J.

(103) Meng, Y.; Liu, F.; Li, M.; Wang, Z.; Deng, H.; Zhang, Q.; Li, H.; Wang, W.; Sun, Q.; Gomez, J.; et al. Probing the proton exchange kinetics of BaZr0.1Ce0.7Y0.1Yb0.1O3−δ ceramic electrolyte by operando diffuse reflectance infrared Fourier transform spectroscopy. *Energ. Environ. Sci.* **2026**, *19* (3), 828-835, 10.1039/D5EE05957G. DOI: 10.1039/D5EE05957G.

(104) Yu, J. H.; Lee, J.-S.; Maier, J. Peculiar Nonmonotonic Water Incorporation in Oxides Detected by Local In Situ Optical Absorption Spectroscopy. *Angew. Chem. Int. Ed.* **2007**, *46* (47), 8992-8994. DOI: https://doi.org/10.1002/anie.200701765.

(105) Wang, X.; Li, W.; Zhou, C.; Xu, M.; Hu, Z.; Pao, C.-W.; Zhou, W.; Shao, Z. Enhanced Proton Conduction with Low Oxygen Vacancy Concentration and Favorable Hydration for Protonic Ceramic Fuel Cells Cathode. *ACS Appl. Mater. Interfaces* **2023**, *15* (1), 1339-1347. DOI: 10.1021/acsami.2c19343.

(106) Lim, D.-K.; Im, H.-N.; Song, S.-J.; Yoo, H.-I. Hydration of Proton-conducting BaCe0.9Y0.1O3−δ by Decoupled Mass Transport. *Scientific Reports* **2017**, *7* (1), 486. DOI: 10.1038/s41598-017-00595-w.

(107) Grimaud, A.; Mauvy, F.; Marc Bassat, J.; Fourcade, S.; Marrony, M.; Claude Grenier, J. Hydration and transport properties of the Pr2−xSrxNiO4+δ compounds as H+-SOFC cathodes. *Journal of Materials Chemistry* **2012**, *22* (31), 16017-16025, 10.1039/C2JM31812A. DOI: 10.1039/C2JM31812A.

(108) Shi, Y.; Liu, Y.; Dong, H.; Fu, G.; Zhou, H.; Wang, H.; Wang, X.-L.; Yao, Y.-F. Operando nuclear magnetic resonance decodes alkali-tuned proton-electron relay boosting CO2-to-formate conversion. *Nat. Commun.* **2026**, *17* (1), 2136. DOI: 10.1038/s41467-026-68604-z.

(109) Fang, Y.; Li, M.; Wen, Y.; Li, P.; Gao, Y.; Ma, T.; Shan, B. Azobenzene-derived coordination polymers for redox-mediated integration of CO2 capture and electrolysis. *Nat. Catal.* **2026**, *9* (2), 211-222. DOI: 10.1038/s41929-026-01487-x.

(110) Feng, N.; Lin, H.; Song, H.; Yang, L.; Tang, D.; Deng, F.; Ye, J. Efficient and selective photocatalytic CH4 conversion to CH3OH with O2 by controlling overoxidation on TiO2. *Nat. Commun.* **2021**, *12* (1), 4652. DOI: 10.1038/s41467-021-24912-0.

(111) Wang, Z.; Liu, F.; Meng, Y.; Bian, W.; Zhao, H.; Duan, C.; Benson, M. T.; Li, M.; Liu, B.; Ding, D. A comprehensive review of diffuse reflectance infrared Fourier transform spectroscopy (DRIFTS) techniques in protonic ceramic cells (PCCs): Current status and future perspective. *eScience* **2025**, *5* (5), 100437. DOI: https://doi.org/10.1016/j.esci.2025.100437.

(112) Shi, N.; Zhu, K.; Xie, Y.; Huan, D.; Hyodo, J.; Yamazaki, Y. Investigation of water impacts on surface properties and performance of air-electrode in reversible protonic ceramic cells. *Small* **2024**, *20* (36), 2400501. DOI: https://doi.org/10.1002/smll.202400501.

(113) Shi, N.; Xie, Y.; Huan, D.; Yang, Y.; Xue, S.; Qi, Z.; Pan, Y.; Peng, R.; Xia, C.; Lu, Y. Controllable CO2 conversion in high performance proton conducting solid oxide electrolysis cells and the possible mechanisms. *J. Mater. Chem. A.* **2019**, *7* (9), 4855-4864, 10.1039/C8TA12458B. DOI: 10.1039/C8TA12458B.

(114) Gao, J.; Meng, Y.; Benton, A.; He, J.; Jacobsohn, L. G.; Tong, J.; Brinkman, K. S. Insights into the Proton Transport Mechanism in TiO2 Simple Oxides by In Situ Raman Spectroscopy. *ACS Appl. Mater. Interfaces* **2020**, *12* (34), 38012-38018. DOI: 10.1021/acsami.0c08120.

(115) Wang, X.; Cai, Z.; Chen, Z.; Liu, D.; Chen, W.; Zhu, J.; Li, W.; Wang, X.; Zhang, L.; Wang, W.; et al. Highly ionic-dispersed oxygen electrode for reversible proton ceramic electrochemical cells. *Nat. Commun.* **2026**, *17* (1), 3989. DOI: 10.1038/s41467-026-70738-z.

(116) Liu, Z.; Bai, Y.; Sun, H.; Guan, D.; Li, W.; Huang, W.-H.; Pao, C.-W.; Hu, Z.; Yang, G.; Zhu, Y.; et al. Synergistic dual-phase air electrode enables high and durable performance of reversible proton ceramic electrochemical cells. *Nat. Commun.* **2024**, *15* (1), 472. DOI: 10.1038/s41467-024-44767-5.

(117) Kim, E.; Yoo, H.-I. Two-fold -to-single-fold transition of the conductivity relaxation patterns of proton-conducting oxides upon hydration/dehydration. *Solid State Ion.* **2013**, *252*, 132-139. DOI: https://doi.org/10.1016/j.ssi.2013.04.005.

(118) Toby, B. H.; Von Dreele, R. B. GSAS-II: the genesis of a modern open-source all purpose crystallography software package. *Journal of Applied Crystallography* **2013**, *46* (2), 544-549. DOI: https://doi.org/10.1107/S0021889813003531.

(119) Kresse, G.; Hafner, J. Ab initio molecular dynamics for liquid metals. *Physical Review B* **1993**, *47* (1), 558-561. DOI: 10.1103/PhysRevB.47.558.

(120) Kresse, G.; Furthmüller, J. Efficiency of ab-initio total energy calculations for metals and semiconductors using a plane-wave basis set. *Computational Materials Science* **1996**, *6* (1), 15-50. DOI: https://doi.org/10.1016/0927-0256(96)00008-0.

(121) Dong, W.; Kresse, G.; Furthmüller, J.; Hafner, J. Chemisorption of H on Pd(111): An ab initio approach with ultrasoft pseudopotentials. *Physical Review B* **1996**, *54* (3), 2157-2166. DOI: 10.1103/PhysRevB.54.2157.

(122) Blöchl, P. E. Projector augmented-wave method. *Physical Review B* **1994**, *50* (24), 17953-17979. DOI: 10.1103/PhysRevB.50.17953.

(123) Li, M.; Hua, B.; Wang, L.-C.; Sugar, J. D.; Wu, W.; Ding, Y.; Li, J.; Ding, D. Switching of metal–oxygen hybridization for selective CO_2 electrohydrogenation under mild temperature and pressure. *Nature Catalysis* **2021**, *4* (4), 274-283. DOI: 10.1038/s41929-021-00590-5.

(124) Li, M.; Hua, B.; Wu, W.; Wang, L.-C.; Ding, Y.; Welander, M. M.; Walker, R. A.; Ding, D. Activating nano-bulk interplays for sustainable ammonia electrosynthesis. *Mater. Today* **2022**, *60*, 31-40. DOI: https://doi.org/10.1016/j.mattod.2022.09.011.

(125) Perdew, J. P.; Burke, K.; Ernzerhof, M. Generalized Gradient Approximation Made Simple. *Physical Review Letters* **1996**, *77* (18), 3865-3868. DOI: 10.1103/PhysRevLett.77.3865.

(126) Kresse, G.; Joubert, D. From ultrasoft pseudopotentials to the projector augmented-wave method. *Physical Review B* **1999**, *59* (3), 1758-1775. DOI: 10.1103/PhysRevB.59.1758.

(127) Nowick, A. S.; Vaysleyb, A. V. Isotope effect and proton hopping in high-temperature protonic conductors. *Solid State Ion.* **1997**, *97* (1), 17-26. DOI: https://doi.org/10.1016/S0167-2738(97)00081-7.

(128) Antonova, E. P.; Gordeev, E. V.; Fedorova, K. A. Features of electrical transport and H/D isotope effects in the proton-conducting electrolyte BaCe0.7Zr0.1Y0.1Yb0.1O3-δ. *Solid State Sciences* **2024**, *154*, 107625. DOI: https://doi.org/10.1016/j.solidstatesciences.2024.107625.

(129) Bonanos, N.; Huijser, A.; Poulsen, F. W. H/D isotope effects in high temperature proton conductors. *Solid State Ion.* **2015**, *275*, 9-13. DOI: https://doi.org/10.1016/j.ssi.2015.03.028.

(130) Cawkwell, M. J.; Luscher, D. J.; Addessio, F. L.; Ramos, K. J. Equations of state for the α and γ polymorphs of cyclotrimethylene trinitramine. *Journal of Applied Physics* **2016**, *119* (18). DOI: 10.1063/1.4948673 (acccessed 5/10/2026).

(131) Arai, K.; Saito, M.; Suganami, K.; Inada, M.; Hayashi, K.; Motohashi, T. Proton conductive behaviors of Ba(ZnxNb1−x)O3−δ−y(OH)2y studied by infrared spectroscopy. *Journal of Solid State Chemistry* **2022**, *308*, 122913. DOI: https://doi.org/10.1016/j.jssc.2022.122913.

(132) Day, T. J. F.; Schmitt, U. W.; Voth, G. A. The Mechanism of Hydrated Proton Transport in Water. *J. Am. Chem. Soc.* **2000**, *122* (48), 12027-12028. DOI: 10.1021/ja002506n.

(133) Yeon, J. I.; Yoo, H.-I. Hydration kinetics of proton-conducting zirconates upon a change of temperature in wet atmosphere. *Solid State Ion.* **2010**, *181* (29), 1323-1327. DOI: https://doi.org/10.1016/j.ssi.2010.07.030.

(134) Song, C.; Liu, J.; Wang, R.; Tang, X.; Wang, K.; Gao, Z.; Peng, M.; Li, H.; Yao, S.; Yang, F.; et al. Engineering MO_x/Ni inverse catalysts for low-temperature CO_2 activation with high methane yields. *Nat. Chem. Eng.* **2024**, *1* (10), 638-649. DOI: https://doi.org/10.1038/s44286-024-00122-5.

(135) Yamazaki, Y.; Blanc, F.; Okuyama, Y.; Buannic, L.; Lucio-Vega, J. C.; Grey, C. P.; Haile, S. M. Proton trapping in yttrium-doped barium zirconate. *Nat. Mater.* **2013**, *12* (7), 647-651. DOI: 10.1038/nmat3638.

(136) Glerup, M.; Poulsen, F. W.; Berg, R. W. Vibrational spectroscopy on protons and deuterons in proton conducting perovskites. *Solid State Ion.* **2002**, *148* (1), 83-92. DOI: https://doi.org/10.1016/S0167-2738(02)00048-6.

(137) Wen, Y.; Rosnes, A.; Jiang, B.; Prytz, Ø.; Norby, T.; Haugsrud, R.; Polfus, J. M. Nickel-Induced Lattice Defects Limit Proton Uptake in Barium Zirconate Electrolytes. *J. Am. Chem. Soc.* **2026**, *148* (1), 379-387. DOI: 10.1021/jacs.5c13935.

(138) Huang, Y.; Merkle, R.; Zhou, D.; Sigle, W.; van Aken, P. A.; Maier, J. Effect of Ni on electrical properties of Ba(Zr,Ce,Y)O3-δ as electrolyte for protonic ceramic fuel cells. *Solid State Ion.* **2023**, *390*, 116113. DOI: https://doi.org/10.1016/j.ssi.2022.116113.

(139) Peng, C.; Zhao, B.; Meng, X.; Ye, X.; Luo, T.; Xin, X.; Wen, Z. Effect of NiO Addition on the Sintering and Electrochemical Properties of BaCe0.55Zr0.35Y0.1O3-δ Proton-Conducting Ceramic Electrolyte. *Membranes* **2024**, *14* (3), 61.

(140) Chen, M.; Chen, D.; Wang, K.; Xu, Q. Densification and electrical conducting behavior of BaZr0.9Y0.1O3-δ proton conducting ceramics with NiO additive. *J. Alloys Compd.* **2019**, *781*, 857-865. DOI: https://doi.org/10.1016/j.jallcom.2018.12.090.

(141) Tong, J.; Clark, D.; Bernau, L.; Subramaniyan, A.; O'Hayre, R. Proton-conducting yttrium-doped barium cerate ceramics synthesized by a cost-effective solid-state reactive sintering method. *Solid State Ion.* **2010**, *181* (33), 1486-1498. DOI: https://doi.org/10.1016/j.ssi.2010.08.022.

(142) Huang, Y.; Merkle, R.; Maier, J. Effects of NiO addition on sintering and proton uptake of Ba(Zr,Ce,Y)O3−δ. *J. Mater. Chem. A.* **2021**, *9* (26), 14775-14785, 10.1039/D1TA02555D. DOI: 10.1039/D1TA02555D.

(143) Smith, B. C. *Fundamentals of fourier transform infrared spectroscopy* CRC Press., 2011. DOI: https://doi.org/10.1201/b10777.

(144) Cooper, A.; Stokes, T.; Irwin, M.; Dixon, E.; Wilson, A.; Cefali, G. Determining aqueous deuterium detection limits via infrared spectroscopy to understand its capabilities for real-time monitoring of tritiated water. *Fusion Eng. Des.* **2024**, *207*, 114647. DOI: https://doi.org/10.1016/j.fusengdes.2024.114647.

(145) Kelly, T. D.; Petrosky, J. C.; McClory, J. W.; Adamiv, V. T.; Burak, Y. V.; Padlyak, B. V.; Teslyuk, I. M.; Lu, N.; Wang, L.; Mei, W.-N.; et al. Rare Earth Dopant (Nd, Gd, Dy, and Er)

Hybridization in Lithium Tetraborate. *Frontiers in Physics* **2014**, *Volume 2 - 2014*, Original Research. DOI: 10.3389/fphy.2014.00031.

(146) Carmo, M.; Fritz, D. L.; Mergel, J.; Stolten, D. A comprehensive review on PEM water electrolysis. *Int. J. Hydrogen Energy* **2013**, *38* (12), 4901-4934. DOI: https://doi.org/10.1016/j.ijhydene.2013.01.151.

(147) Duan, C. Selective CO_2 electrohydrogenation. *Nat. Catal.* **2021**, *4* (4), 264-265. DOI: https://doi.org/10.1038/s41929-021-00600-6.

(148) Ye, R.-P.; Ding, J.; Gong, W.; Argyle, M. D.; Zhong, Q.; Wang, Y.; Russell, C. K.; Xu, Z.; Russell, A. G.; Li, Q.; et al. CO_2 hydrogenation to high-value products via heterogeneous catalysis. *Nat. Commun.* **2019**, *10* (1), 5698. DOI: https://doi.org/10.1038/s41467-019-13638-9.

(149) Liu, Z.; Gao, X.; Wang, K.; Liang, J.; Jiang, Y.; Ma, Q.; Zhao, T.-S.; Zhang, J. A short overview of Power-to-Methane: Coupling preparation of feed gas with CO_2 methanation. *Chemical Engineering Science* **2023**, *274*, 118692. DOI: https://doi.org/10.1016/j.ces.2023.118692.

(150) Gao, R.; Zhang, L.; Wang, L.; Zhang, X.; Zhang, C.; Jun, K.-W.; Ki Kim, S.; Park, H.-G.; Gao, Y.; Zhu, Y.; et al. A comparative study on hybrid power-to-liquids/power-to-gas processes coupled with different water electrolysis technologies. *Energy Conversion and Management* **2022**, *263*, 115671. DOI: https://doi.org/10.1016/j.enconman.2022.115671.

(151) Zhong, D.; Fang, Q.; Du, R.; Jin, Y.; Peng, C.; Cheng, D.; Li, T.; Zhao, T.; Zhang, S.; Zheng, Y.; et al. Selective Electrochemical CO_2 Reduction to Ethylene or Ethanol via Tuning *OH Adsorption. *Angew. Chem. Int. Ed.* **2025**, *64* (32), e202501773. DOI: https://doi.org/10.1002/anie.202501773.

(152) Wei, D.; Wang, Y.; Dong, C.-L.; Nga, T. T. T.; Zhou, H.; Hu, C.; Shi, Y.; Wang, J.; Guo, L.; Shen, S. Plasmon-Assisted Tandem Electrocatalysis for CO_2-to-C_2H_5OH Conversion. *Angewandte Chemie* **2025**, *137* (39), e202512179. DOI: https://doi.org/10.1002/ange.202512179.

(153) Li, H.; Qin, X.; Zhang, X.-G.; Jiang, K.; Cai, W.-B. Boron-Doped Platinum-Group Metals in Electrocatalysis: A Perspective. *ACS Catal.* **2022**, *12* (20), 12750-12764. DOI: https://doi.org/10.1021/acscatal.2c04358.

(154) Hou, X.; Jiang, Y.; Wei, K.; Jiang, C.; Jen, T.-C.; Yao, Y.; Liu, X.; Ma, J.; Irvine, J. T. S. Syngas Production from CO_2 and H_2O via Solid-Oxide Electrolyzer Cells: Fundamentals, Materials, Degradation, Operating Conditions, and Applications. *Chem. Rev.* **2024**, *124* (8), 5119-5166. DOI: https://doi.org/10.1021/acs.chemrev.3c00760.

(155) Qiu, P.; Li, C.; Liu, B.; Yan, D.; Li, J.; Jia, L. Materials of solid oxide electrolysis cells for H_2O and CO_2 electrolysis: A review. *Journal of Advanced Ceramics* **2023**, *12* (8), 1463-1510. DOI: https://doi.org/10.26599/JAC.2023.9220767.

(156) Song, Y.; Zhang, X.; Xie, K.; Wang, G.; Bao, X. High-Temperature CO_2 Electrolysis in Solid Oxide Electrolysis Cells: Developments, Challenges, and Prospects. *Adv. Mater.* **2019**, *31* (50), 1902033. DOI: https://doi.org/10.1002/adma.201902033.

(157) Skafte, T. L.; Guan, Z.; Machala, M. L.; Gopal, C. B.; Monti, M.; Martinez, L.; Stamate, E.; Sanna, S.; Garrido Torres, J. A.; Crumlin, E. J.; et al. Selective high-temperature CO_2 electrolysis enabled by oxidized carbon intermediates. *Nat. Energy.* **2019**, *4* (10), 846-855. DOI: https://doi.org/10.1038/s41560-019-0457-4.

(158) Li, W.; Wang, H.; Shi, Y.; Cai, N. Performance and methane production characteristics of H_2O–CO2 co-electrolysis in solid oxide electrolysis cells. *Int. J. Hydrogen Energy* **2013**, *38* (25), 11104-11109. DOI: https://doi.org/10.1016/j.ijhydene.2013.01.008.

(159) Xie, K.; Zhang, Y.; Meng, G.; Irvine, J. T. S. Direct synthesis of methane from CO_2/H_2O in an oxygen-ion conducting solid oxide electrolyser. *Energ. Environ. Sci.* **2011**, *4* (6), 2218-2222, 10.1039/C1EE01035B. DOI: https://doi.org/10.1039/C1EE01035B.

(160) Chen, L.; Chen, F.; Xia, C. Direct synthesis of methane from CO_2–H_2O co-electrolysis in tubular solid oxide electrolysis cells. *Energ. Environ. Sci.* **2014**, *7* (12), 4018-4022, 10.1039/C4EE02786H. DOI: https://doi.org/10.1039/C4EE02786H.

(161) Wang, Y.; Zhang, H.; Cao, J.; Xu, K.; Pei, K.; Chen, Y. Highly selective reduction of CO_2 through a protonic ceramic electrochemical cell. *J. Power Sources.* **2022**, *524*, 231101. DOI: https://doi.org/10.1016/j.jpowsour.2022.231101.

(162) Wang, C.; Miao, X.; Luo, T.; Zhu, X.; Ye, X.; Wen, Z. Synergistic construction of nano nickel and lanthanum tungstate matrix for CO_2-tolerant PCEC: Achieving stable CO_2 methanation. *J. Energy Chem.*. **2026**, *114*, 146-155. DOI: https://doi.org/10.1016/j.jechem.2025.09.086.

(163) Ye, Y.; Lee, W.; Pan, J.; Sun, X.; Zhou, M.; Li, J.; Zhang, N.; Han, J. W.; Chen, Y. Tuning the product selectivity of CO_2/H_2O co-electrolysis using CeO_2-modified proton-conducting electrolysis cells. *Energ. Environ. Sci.* **2023**, *16* (7), 3137-3145, 10.1039/D3EE01468A. DOI: https://doi.org/10.1039/D3EE01468A.

(164) Li, J.; Lin, Y.; Pan, X.; Miao, D.; Ding, D.; Cui, Y.; Dong, J.; Bao, X. Enhanced CO_2 Methanation Activity of Ni/Anatase Catalyst by Tuning Strong Metal–Support Interactions. *ACS Catal.* **2019**, *9* (7), 6342-6348. DOI: https://doi.org/10.1021/acscatal.9b00401.

(165) Hong, K.; Sutanto, S. N.; Lee, J. A.; Hong, J. Ni-based bimetallic nano-catalysts anchored on $BaZr_{0.4}Ce_{0.4}Y_{0.1}Yb_{0.1}O_{3-\delta}$ for internal steam reforming of methane in a low-temperature proton-conducting ceramic fuel cell. *J. Mater. Chem. A.* **2021**, *9* (10), 6139-6151, https://doi.org/10.1039/D0TA11359J. DOI: 10.1039/D0TA11359J.

(166) Pan, Z.; Duan, C.; Pritchard, T.; Thatte, A.; White, E.; Braun, R.; O'Hayre, R.; Sullivan, N. P. High-yield electrochemical upgrading of CO_2 into CH_4 using large-area protonic ceramic electrolysis cells. *Applied Catalysis B- Environ.* **2022**, *307*, 121196. DOI: https://doi.org/10.1016/j.apcatb.2022.121196.

(167) Miao, X.; Feng, J.; Dai, Z.; Zhu, X.; Wen, J.; Zhang, L.; Ye, X.; Zhou, Y.; Wen, Z. A Regenerative Coking-resistant CO_2 Hydrogenation Reactor using a Protonic Ceramic Electrolysis Cell with Thin and Robust Fuel Electrode. *Adv. Energy Mater. Cem.* **2024**, *14* (42), 2402208. DOI: https://doi.org/10.1002/aenm.202402208.

(168) Tommasi, M.; Degerli, S. N.; Ramis, G.; Rossetti, I. Advancements in CO_2 methanation: A comprehensive review of catalysis, reactor design and process optimization. *Chem. Eng. Res. Des.* **2024**, *201*, 457-482. DOI: https://doi.org/10.1016/j.cherd.2023.11.060.

(169) Ju, Y.; Bae, D.; Kim, M.; Ryu, T.; Hazlett, M. J.; Min, H.; Park, J.; Kim, Y. J.; Kang, S. B. Low-temperature catalytic CO_2 methanation over nickel supported on praseodymium oxide. *J. Environ. Chem. Eng.* **2025**, *13* (2), 116129. DOI: https://doi.org/10.1016/j.jece.2025.116129.

(170) Fan, W. K.; Tahir, M. Recent trends in developments of active metals and heterogenous materials for catalytic CO_2 hydrogenation to renewable methane: A review. *J. Environ. Chem. Eng.* **2021**, *9* (4), 105460. DOI: https://doi.org/10.1016/j.jece.2021.105460.

(171) Cárdenas-Arenas, A.; Cortés, H. S.; Bailón-García, E.; Davó-Quiñonero, A.; Lozano-Castelló, D.; Bueno-López, A. Active, selective and stable NiO-CeO_2 nanoparticles for CO_2 methanation. *Fuel Process. Technol.* **2021**, *212*, 106637. DOI: https://doi.org/10.1016/j.fuproc.2020.106637.

(172) Zhou, G.; Liu, H.; Cui, K.; Jia, A.; Hu, G.; Jiao, Z.; Liu, Y.; Zhang, X. Role of surface Ni and Ce species of Ni/CeO_2 catalyst in CO_2 methanation. *Appl. Surf. Sci.* **2016**, *383*, 248-252. DOI: https://doi.org/10.1016/j.apsusc.2016.04.180.

(173) Ni, Z.; Djitcheu, X.; Gao, X.; Wang, J.; Liu, H.; Zhang, Q. Effect of preparation methods of CeO_2 on the properties and performance of Ni/CeO_2 in CO_2 reforming of CH_4. *Scientific Reports* **2022**, *12* (1), 5344. DOI: https://doi.org/10.1038/s41598-022-09291-w.

(174) Du, Y.; Qin, C.; Xu, Y.; Xu, D.; Bai, J.; Ma, G.; Ding, M. Ni nanoparticles dispersed on oxygen vacancies-rich CeO_2 nanoplates for enhanced low-temperature CO_2 methanation performance. *Chem. Eng. J.* **2021**, *418*, 129402. DOI: https://doi.org/10.1016/j.cej.2021.129402.

(175) Liu, K.; Xu, X.; Xu, J.; Fang, X.; Liu, L.; Wang, X. The distributions of alkaline earth metal oxides and their promotional effects on Ni/CeO_2 for CO_2 methanation. *J. CO2 Util.* **2020**, *38*, 113-124. DOI: https://doi.org/10.1016/j.jcou.2020.01.016.

(176) Li, S.; Liu, G.; Zhang, S.; An, K.; Ma, Z.; Wang, L.; Liu, Y. Cerium-modified Ni-La_2O_3/ZrO_2 for CO_2 methanation. *J. Energy Chem.*. **2020**, *43*, 155-164. DOI: https://doi.org/10.1016/j.jechem.2019.08.024.

(177) Chen, J.; Pham, H. N.; Mon, T.; Toops, T. J.; Datye, A. K.; Li, Z.; Kyriakidou, E. A. Ni/CeO_2 Nanocatalysts with Optimized CeO_2 Support Morphologies for CH_4 Oxidation. *ACS Applied Nano Materials* **2023**, *6* (6), 4544-4553. DOI: https://doi.org/10.1021/acsanm.2c05496.

(178) Mei, D. First-principles characterization of formate and carboxyl adsorption on stoichiometric CeO_2(111) and CeO_2(110) surfaces. *J. Energy Chem.*. **2013**, *22* (3), 524-532. DOI: https://doi.org/10.1016/S2095-4956(13)60069-8.

(179) Gao, P.; Tang, S.; Han, X.; Hao, Z.; Chen, J.; Pan, Y.; Zhang, Z.; Zhang, H.; Zi, X.; Chen, L.; et al. Boosting CO2 methanation via tuning metal-support interaction over hollow Ni/CeO_2. *Chem. Eng. J.* **2024**, *498*, 155784. DOI: https://doi.org/10.1016/j.cej.2024.155784.

(180) Kildgaard, J. V.; Hansen, H. A.; Vegge, T. DFT + U Study of Strain-Engineered CO2 Reduction on a CeO_{2-x} (111) Facet. *J. Phys. Chem. C.* **2021**, *125* (26), 14221-14227. DOI: https://doi.org/10.1021/acs.jpcc.1c01019.

(181) Farmer, J. A.; Campbell, C. T. Ceria Maintains Smaller Metal Catalyst Particles by Strong Metal-Support Bonding. *Science* **2010**, *329* (5994), 933-936. DOI: https://doi.org/10.1126/science.1191778.

(182) Ma, W.; Morales-Vidal, J.; Tian, J.; Liu, M.-T.; Jin, S.; Ren, W.; Taubmann, J.; Chatzichristodoulou, C.; Luterbacher, J.; Chen, H. M.; et al. Encapsulated Co–Ni alloy boosts high-temperature CO_2 electroreduction. *Nature* **2025**, *641* (8065), 1156-1161. DOI: https://doi.org/10.1038/s41586-025-08978-0.

(183) Liu, F.; Deng, H.; Wang, Z.; Hussain, A. M.; Dale, N.; Furuya, Y.; Miura, Y.; Fukuyama, Y.; Ding, H.; Liu, B.; et al. Synergistic Effects of In-Situ Exsolved Ni–Ru Bimetallic Catalyst on High-Performance and Durable Direct-Methane Solid Oxide Fuel Cells. *J. Am. Chem. Soc.* **2024**, *146* (7), 4704-4715. DOI: https://doi.org/10.1021/jacs.3c12121.

(184) Chen, T.; Zheng, G.; Liu, K.; Zhang, G.; Huang, Z.; Liu, M.; Zhou, J.; Wang, S. Application of CuNi–CeO_2 fuel electrode in oxygen electrode supported reversible solid oxide cell. *Int. J. Hydrogen Energy* **2023**, *48* (26), 9565-9573. DOI: https://doi.org/10.1016/j.ijhydene.2022.11.236.

(185) Escudero, M. J.; Maffiotte, C. A.; Serrano, J. L. Long-term operation of a solid oxide fuel cell with MoNi–CeO_2 as anode directly fed by biogas containing simultaneously sulphur and

siloxane. *J. Power Sources.* **2021**, *481*, 229048. DOI: https://doi.org/10.1016/j.jpowsour.2020.229048.

(186) Zhou, J.; Gao, Z.; Xiang, G.; Zhai, T.; Liu, Z.; Zhao, W.; Liang, X.; Wang, L. Interfacial compatibility critically controls Ru/TiO_2 metal-support interaction modes in CO_2 hydrogenation. *Nat. Commun.* **2022**, *13* (1), 327. DOI: https://doi.org/10.1038/s41467-021-27910-4.

(187) Wang, T.; Hu, J.; Ouyang, R.; Wang, Y.; Huang, Y.; Hu, S.; Li, W.-X. Nature of metal-support interaction for metal catalysts on oxide supports. *Science* **2024**, *386* (6724), 915-920. DOI: https://doi.org/10.1126/science.adp6034.

(188) van Deelen, T. W.; Hernández Mejía, C.; de Jong, K. P. Control of metal-support interactions in heterogeneous catalysts to enhance activity and selectivity. *Nat. Catal.* **2019**, *2* (11), 955-970. DOI: https://doi.org/10.1038/s41929-019-0364-x.

(189) Siakavelas, G. I.; Charisiou, N. D.; AlKhoori, S.; AlKhoori, A. A.; Sebastian, V.; Hinder, S. J.; Baker, M. A.; Yentekakis, I. V.; Polychronopoulou, K.; Goula, M. A. Highly selective and stable nickel catalysts supported on ceria promoted with Sm_2O_3, Pr_2O_3 and MgO for the CO_2 methanation reaction. *Applied Catalysis B- Environ.* **2021**, *282*, 119562. DOI: https://doi.org/10.1016/j.apcatb.2020.119562.

(190) Tsiotsias, A. I.; Charisiou, N. D.; AlKhoori, A.; Gaber, S.; Stolojan, V.; Sebastian, V.; van der Linden, B.; Bansode, A.; Hinder, S. J.; Baker, M. A.; et al. Optimizing the oxide support composition in Pr-doped CeO_2 towards highly active and selective Ni-based CO_2 methanation catalysts. *J. Energy Chem..* **2022**, *71*, 547-561. DOI: https://doi.org/10.1016/j.jechem.2022.04.003.

(191) Hongmanorom, P.; Ashok, J.; Chirawatkul, P.; Kawi, S. Interfacial synergistic catalysis over Ni nanoparticles encapsulated in mesoporous ceria for CO_2 methanation. *Applied Catalysis B-Environ.* **2021**, *297*, 120454. DOI: https://doi.org/10.1016/j.apcatb.2021.120454.

(192) Zhao, K.; Wang, W.; Li, Z. Highly efficient Ni/ZrO_2 catalysts prepared via combustion method for CO_2 methanation. *J. CO2 Util.* **2016**, *16*, 236-244. DOI: https://doi.org/10.1016/j.jcou.2016.07.010.

(193) Cárdenas-Arenas, A.; Quindimil, A.; Davó-Quiñonero, A.; Bailón-García, E.; Lozano-Castelló, D.; De-La-Torre, U.; Pereda-Ayo, B.; González-Marcos, J. A.; González-Velasco, J. R.; Bueno-López, A. Design of active sites in Ni/CeO2 catalysts for the methanation of CO_2: tailoring the Ni-CeO_2 contact. *Applied Materials Today* **2020**, *19*, 100591. DOI: https://doi.org/10.1016/j.apmt.2020.100591.

(194) Beaumont, S. K. Soft XAS as an in situ technique for the study of heterogeneous catalysts. *Phys. Chem. Chem. Phys.* **2020**, *22* (34), 18747-18756, 10.1039/D0CP00657B. DOI: https://doi.org/10.1039/D0CP00657B.

(195) Soni, S.; Dave, M.; Dalela, B.; Alvi, P. A.; Kumar, S.; Sharma, S. S.; Phase, D. M.; Gupta, M.; Dalela, S. Effect of defects and oxygen vacancies on the RTFM properties of pure and Gd-doped CeO_2 nanomaterials through soft XAS. *Applied Physics A* **2020**, *126* (8), 585. DOI: https://doi.org/10.1007/s00339-020-03777-y.

(196) Krishna Kumar, K. P.; Chiou, J. W.; Tsai, H. M.; Pao, C. W.; Jan, J. C.; Hsu, P. C.; Ling, D. C.; Chien, F. Z.; Pong, W. F.; Tsai, M. H.; et al. Electronic and local atomic structures of $(La_{1-x}Pr_x)_{0.85}Zr_{0.15}MnO_3$ studied by x-ray absorption spectroscopy. *Journal of Physics: Condensed Matter* **2005**, *17* (26), 4197. DOI: https://doi.org/10.1088/0953-8984/17/26/017.

(197) Zhang, G.; Liu, M.; Fan, G.; Zheng, L.; Li, F. Efficient Role of Nanosheet-Like Pr_2O_3 Induced Surface-Interface Synergistic Structures over Cu-Based Catalysts for Enhanced Methanol Production from CO_2 Hydrogenation. *ACS Appl. Mater. Interfaces* **2022**, *14* (2), 2768-2781. DOI: https://doi.org/10.1021/acsami.1c20056.

(198) Matyshak, V. A.; Krylov, O. V. In situ IR spectroscopy of intermediates in heterogeneous oxidative catalysis. *Catal. Today* **1995**, *25* (1), 1-87. DOI: https://doi.org/10.1016/0920-5861(95)00067-P.

(199) Meunier, F. C.; Goguet, A.; Shekhtman, S.; Rooney, D.; Daly, H. A modified commercial DRIFTS cell for kinetically relevant operando studies of heterogeneous catalytic reactions. *Appl. Catal. A Gen.* **2008**, *340* (2), 196-202. DOI: https://doi.org/10.1016/j.apcata.2008.02.034.

(200) Meunier, F. C.; Reid, D.; Goguet, A.; Shekhtman, S.; Hardacre, C.; Burch, R.; Deng, W.; Flytzani-Stephanopoulos, M. Quantitative analysis of the reactivity of formate species seen by DRIFTS over a Au/Ce(La)O2 water–gas shift catalyst: first unambiguous evidence of the minority role of formates as reaction intermediates. *J. Catal.* **2007**, *247* (2), 277-287. DOI: https://doi.org/10.1016/j.jcat.2007.02.013.

(201) Yun, J.; Xiong, G.; Kim, S.; Bardgett, D.; Choi, S.; Haile, S. M. Understanding direct-ammonia protonic ceramic fuel cells: high-performance in the absence of precious metal catalysts. *ACS Energy Lett.* **2024**, *9* (11), 5520-5528. DOI: 10.1021/acsenergylett.4c02263.

(202) Liu, Z.; Tao, M.; Xiao, M.; Li, J.; Xu, R.; Chen, B.; Li, T.; Yang, G.; Zhang, Y.; Shi, N.; et al. Direct ammonia protonic ceramic fuel cells through heterogeneous interfaces engineering. *Chem Catalysis* **2025**, 101365. DOI: https://doi.org/10.1016/j.checat.2025.101365.

(203) Liang, M.; Kim, J.; Xu, X.; Sun, H.; Song, Y.; Jeon, S.; Shin, T. H.; Shao, Z.; Jung, W. Electricity-to-ammonia interconversion in protonic ceramic cells: advances, challenges and

perspectives. *Energ. Environ. Sci.* **2025**, *18* (8), 3526-3552, 10.1039/D4EE06100D. DOI: 10.1039/D4EE06100D.

(204) Fang, F.; Cheng, Q.; Wang, M.; He, Y.; Huan, Y.; Liu, S.; Qian, T.; Yan, C.; Lu, J. Identifying upper d-band edge as activity descriptor for ammonia oxidation on PtCo alloys in low-temperature direct ammonia fuel cells. *ACS Nano* **2025**, *19* (1), 1260-1270. DOI: 10.1021/acsnano.4c13451.

(205) O'Nolan, D.; Zhao, H.; Chen, Z.; Grenier, A.; Beauvais, M. L.; Newton, M. A.; Nenoff, T. M.; Chupas, P. J.; Chapman, K. W. A multimodal analytical toolkit to resolve correlated reaction pathways: the case of nanoparticle formation in zeolites. *Chem. Sci.* **2021**, *12* (41), 13836-13847, 10.1039/D1SC04232G. DOI: 10.1039/D1SC04232G.

(206) Hanson, J. C.; Si, R.; Xu, W.; Senanayake, S. D.; Mudiyanselage, K.; Stacchiola, D.; Rodriguez, J. A.; Zhao, H.; Beyer, K. A.; Jennings, G.; et al. Pulsed-reactant in situ studies of ceria/CuO catalysts using simultaneous XRD, PDF and DRIFTS measurements. *Catal. Today* **2014**, *229*, 64-71. DOI: https://doi.org/10.1016/j.cattod.2013.10.087.

(207) Yao, S.; Mudiyanselage, K.; Xu, W.; Johnston-Peck, A. C.; Hanson, J. C.; Wu, T.; Stacchiola, D.; Rodriguez, J. A.; Zhao, H.; Beyer, K. A.; et al. Unraveling the dynamic nature of a CuO/CeO2 catalyst for CO oxidation in operando: a combined study of XANES (fluorescence) and DRIFTS. *ACS Catal.* **2014**, *4* (6), 1650-1661. DOI: 10.1021/cs500148e.

(208) Song, Y.; Liu, J.; Wang, Y.; Guan, D.; Seong, A.; Liang, M.; Robson, M. J.; Xiong, X.; Zhang, Z.; Kim, G.; et al. Nanocomposites: a new opportunity for developing highly active and durable bifunctional air electrodes for reversible protonic ceramic cells. *Adv. Energy Mater. Cem.* **2021**, *11* (36). DOI: https://doi.org/10.1002/aenm.202101899.

(209) Margenot, A.; O' Neill, T.; Sommer, R.; Akella, V. Predicting soil permanganate oxidizable carbon (POXC) by coupling DRIFT spectroscopy and artificial neural networks (ANN). *Comput. Electron. Agric.* **2020**, *168*, 105098. DOI: https://doi.org/10.1016/j.compag.2019.105098.

(210) Wang, Y.; Sun, Y.; Liu, X.; Dong, F. Predicting and understanding photocatalytic CO2 reduction reaction with IR spectroscopy-based interpretable machine learning framework. *PNAS Nexus* **2024**, *3* (9). DOI: 10.1093/pnasnexus/pgae339 (acccessed 5/16/2025).

(211) McCall, M. A.; Watson, J. S.; Tan, J. S. W.; Sephton, M. A. Biochar stability revealed by FTIR and machine learning. *ACS SRM* **2025**. DOI: 10.1021/acssusresmgt.5c00104.

(212) Usoltsev, O.; Tereshchenko, A.; Skorynina, A.; Kozyr, E.; Soldatov, A.; Safonova, O.; Clark, A. H.; Ferri, D.; Nachtegaal, M.; Bugaev, A. Machine learning for quantitative structural information from infrared spectra: the case of palladium hydride. *Small Methods* **2024**, *8* (7), 2301397. DOI: https://doi.org/10.1002/smtd.202301397.